

DIRECTED ENERGY WEAPONS (DEW) HIGH POWER MICROWAVE (HPM) 6.1, 6.2 AND SBIR PROGRAMS FY24 ANNUAL REPORT

Mr. Ryan Hoffman, Program Manager

DISTRIBUTION STATEMENT A. Approved for public release; distribution is unlimited.
DCN#: 2025-4-11-835

Directed Energy Weapons (DEW) High Power Microwave (HPM) Program

Annual Report for FY24

Table of Contents

Title	Pages
Introduction to ONR's HPM Program by Program Officer Ryan Hoffman, Office of Naval Research	3-4
ONR Grants	
Long slot arrays for high power microwaves – <i>Dr. Mauro Ettore</i>	6-18
Improving Performance of Crossed-Field Amplifiers Through Modulation Injection – <i>Dr. Allen Garner</i>	19-32
Surface Breakdown and Plasma Formation in Cross-Field High Power Microwave Sources – <i>Dr. Ken Hara</i>	33-47
High Power, High Frequency, Repetitively Pulsed Oscillators – <i>Dr. Nicholas Jordan</i>	48-65
New Anode Materials for High Lethality HPM Sources – <i>Dr. Ravi Joshi</i>	66-87
Enhanced Free Recovery for Kilohertz Operation of Spark Gaps – <i>Dr. Jane Lehr</i>	88-102
Distributed Coordination of Aerial Swarms for High-Gain Wireless Transmission – <i>Dr. Jeffrey Nanzer</i>	103-117
An Accessible Platform for Simultaneous Macro, Meso and Microscopic Measurements of Polymeric Materials at High Loading Rates and Temperatures – <i>Dr. Sal Portillo</i>	118-129
High Power Electromagnetic Sources from X-Band to Ka-Band – <i>Dr. Edl Schamiloglu</i>	130-146
Novel HPM source topologies for high power microwave and millimeter wave generation – <i>Dr. Jacob Stephens</i>	147-159
Elucidating Plasma Formation Near Dielectric Interfaces in High Power Microwave Systems – <i>Dr. Thomas Underwood</i>	160-176
Pulsed Dielectric Breakdown of Solid Dielectric Insulation Materials – <i>Dr. David Wetz</i>	177-191
ONR Young Investigator Program (YIP)	
Direct Generation of Electromagnetic Radiation with a Compact, Air-Stable, Optically Modulated Electron Emitter – <i>Dr. Rehan Kapadia</i>	193-218
Multi-frequency High Power Microwave Generation and Amplification via Optically Gated Electron Beams, MSU – <i>Dr. Peng Zhang</i>	219-235

Directed Energy Weapons (DEW) High Power Microwave (HPM) Program

Annual Report for FY24

Table of Contents

ONR Early Career Grant (ECG)	
Infrared Optics with Engineered Materials – <i>Dr. Mikhail Kats</i>	237-251
ONR Industry contracts	
Implementation of Tunable Dielectric and Multiferroic Materials For High Power Microwave Applications, Powerhouse Consulting – <i>Dr. Somnath Sengupta</i>	253-256
SBIRs/STTRs contracts	
Low Profile, Foldable, High Power Microwave Antenna – <i>EngeniusMicro, LLC</i>	258
Collapsible Radiating Antenna For Trivial Easy Deployment (CRAFTED) – <i>MaXentric Technologies</i>	258
Innovative Low Profile, Foldable, High Power Microwave Antenna – <i>Nanohmics Inc.</i>	259
Deployable High-Power Microwave Reflectarray – <i>Physical Sciences Inc.</i>	259
Low-Void Density Additive Ferroic Composites – <i>Nanohmics Inc</i>	259
Additive Manufacturing of Multi-functional Ferroic Composites – <i>NanoVox LLC</i>	260
Jet based Additive Manufacturing of Ni-Zn Ferrite Composites Enabling High Power Microwave (HPM) Directed Energy Weapons (DEW) – <i>Hepburn and Sons LLC</i>	260
Digital Design and Additive Manufacturing Strategy for Ferroelectric-Polymer Composites – <i>Corvid Technologies</i>	261
High Impedance Ferro-materials for use in Additive Manufacturing (HIFAM) – <i>United Protective Technologies, LLC</i>	261
Next-Gen Solid-State Power Module for High Power Microwave Drivers – <i>Scientific Applications & Research Assoc., Inc. (SARA)</i>	262
Solid-state, Sub-nanosecond Pulse Sharpener for Generating High Power Impulses, <i>Transient Plasma Systems Inc.</i>	262
Improved Marx Pulse Generator for HPM Systems (Dr. Sam Dickerson – <i>Scientific Applications & Research Assoc., Inc. (SARA)</i>	263

Introduction

Ryan Hoffman

Division Director and HPM Program Officer, Office of Naval Research

The Directed Energy Weapons (DEW) Program of the Office of Naval Research (ONR) was initiated in response to the rapid development and growing threat of directed energy technologies by adversaries. Directed energy weapons are defined as electromagnetic systems capable of converting chemical or electrical energy to radiated energy and focusing it on a target, resulting in physical damage that degrades, neutralizes, defeats, or destroys an adversarial capability. The U.S. Navy uses HPM to gain and sustain tactical, operational, and strategic advantage in the arena of EM Maneuver Warfare and Integrated Defense for U.S. forces across the full range of military operations, including power projection and integrated defense missions. The ability to focus radiated energy reliably and repeatedly at range, with precision and controllable effects, while producing measured physical damage, is the measure of DEW system effectiveness. In anticipation of DEW advancements, the ONR HPM Program comprises a portfolio of initiatives and research projects which seek to provide the science and engineering basis for means and methodologies to provide the Navy advanced HPM technologies, systems, and techniques enabling a new class of weapons that will be highly effective in the battlespace. The goal is to be the most effective steward of DEW systems.

Asymmetric threats are proliferating worldwide and likely will continue to do so until such time as effective countermeasures are deployed. Often enough, Rules of Engagement will restrict kinetic engagement with asymmetric threats contingent on the particulars of the scenario. DEW systems – or more specifically for this report, HPM weapons – are expected to allow Naval commanders significantly more flexible responses to a number of asymmetric threats, including various small surface craft and unmanned aerial vehicle (UAV) threats. This flexibility is possible since the restrictions on engaging targets might be removed or reduced based on recognition of 1) the low collateral damage and 2) the non-lethal and reversible effects associated with HPM weapons.

HPM weapons create pulses of electromagnetic energy over a broad spectrum of known radio and microwave frequencies, causing either temporary or permanent results on electronics within targeted systems at scalable effects. HPM weapon systems can be used to disrupt, disable, or potentially destroy critical electronic circuitry in target systems, even in restricted scenarios, while also having the advantage of low cost per shot. HPM weapons deliver electromagnetic energy through coupling of the electromagnetic wave to target circuits through aperture or cable points of entry, thereby inducing currents in the circuitry capable of causing a variety of effects. Potential effects include erroneous signals, system lock-up, shutdown, loss of communications between systems, and physical damage.

As DEW falls within the Fundamental Research part of the broad ONR Science & Technology (S&T) investment portfolio, projects funded are long-term initiatives, covering basic research or applied science. These investigations can have a five to twenty year horizon. Across the HPM technology thrust areas, research projects within the program include performers from academia, industry, government laboratories, and small businesses. Moreover, the program includes performers whose research is financed through Navy SBIR/STTR funding. In addition, S&T solutions from an international technical community are afforded through ONR Global, which

funds projects that foster cooperation in areas of mutual interest with global partners. The program encourages the cross-pollination of ideas and collaboration among performers worldwide, and offers an annual review where performers provide updates on the status of their research and present results to their DEW peers. Furthermore, data and facilities sharing are encouraged within the program. This approach contributes to increased success for the program and for the Navy.

Focus areas cover HPM sub-systems that optimize power and/or energy density at the electronic target for a variety of platform sizes and capabilities while minimizing size, weight, power and cost. Examples of related areas for S&T investment and research include supporting technologies such as power electronics, pulsed power drivers, power modulators, as well as frequency agile RF sources and antennas.

Additional research focus areas include research into electronic system coupling, interaction, and effects with the first goal of enabling development of predictive effects tools for current systems. A second goal of this work includes an exploration of in band and out of band coupling and interaction mechanisms. This exploration will exploit developing advances in frequency and bandwidth agility both to identify new potential weapon system possibilities as well as to achieve significant improvements in size, weight, power, and cost in new variants of existing systems.

Research Challenges and Opportunities

- RF coupling and modeling tools to capture complex EM wave interactions with electronics and associated enclosures, RF component disruption, along with novel techniques for experimental validation. Prediction of effects on electronics with improved techniques for HPM lethality testing and analysis. Analysis of HPM coupling mechanisms, electronic device interaction physics, and component level effects validated through experiment. Development of tools and techniques for more efficient identification and utilization of novel RF waveforms.
- Pulsed power/power electronics; including high energy density capacitors, power conditioning, high voltage switches, dielectric insulators, 3D printed/novel materials and power modulator pulse forming networks that enable higher duty cycle operation
- Solid state and vacuum electronic based HPM sources that provide frequency and waveform parameter tunability and are reconfigurable to adapt to changing requirements; computer codes for modelling HPM physics to enable the next generation of devices
- Wide bandwidth high power amplifiers that provide the ability of very rapid waveform adjustment.
- High power, low profile, or conformal antenna designs and capable radome materials, novel array concepts, high power beam steering techniques and distributed beam forming approaches.
- Novel HPM sensors, instrumentation and algorithms are of interest for measurement of waveforms and diagnosing system performance as well as applied to Electronic battle damage indication (eBDI).

ONR Grant Reports

Long slot arrays for high power microwaves

Grant No. N00014-24-1-2201

Annual Report for Fiscal Year 2024

Period of Performance: March 1, 2024 to September 30, 2024

Prepared by:

Dr. Mauro Ettore, Principal Investigator
Michigan State University
428 S Shaw Lane, Room 2120 Engineering
East Lansing, MI 48824
Tel: 517-353-4970
Email: ettore@msu.edu



Acknowledgement/Disclaimer: This work was sponsored by the Office of Naval Research (ONR), under grant/contract number N00014-24-1-2201. The views and conclusions contained herein are those of the authors only and should not be interpreted as representing those of ONR, the U.S. Navy or the U.S. Government.

Section I: Project Summary

1. Overview of Project

Executive Summary:

This report presents an overview of our progress in analyzing and modeling long slot arrays for high-power microwave (HPM) applications. Long slot arrays utilize the strong mutual coupling among the radiating slots and a compact true-time delay (TTD) beamforming network that feeds these slots to achieve extremely wide bandwidths and a large field of view. These characteristics, combined with their compact design, make them appealing for next-generation HPM antennas. In this report, we summarize our preliminary findings on modeling long slot arrays for HPM applications in the X-band. We discuss their ability to handle high power within a small form factor and the stability of their phase center for transmitting short pulses. Additionally, we introduce the concept of virtual quasi-optical systems, which allows for mechanically steering the antenna's main beam direction.

Objective:

This effort considers long slot arrays fed by a TTD beamforming network for HPM applications. We will leverage the TTD operation of the array to explore its capability to radiate high-power microwaves in X-band over a wide field of view, wideband operation with a reduced form factor to outperform the current state of the art and propose a novel antenna solution for HPM applications. This research effort has the following scientific objectives:

- Develop a Green's function framework to address the electromagnetic problem associated with long slot arrays. This framework will assess the array's capability to propagate and radiate high electromagnetic power across a wide frequency band and large field of view. Vacuum-based systems will be considered to maintain high electric fields and minimize the risk of breakdown effects. Additionally, the array's geometrical features will be connected to its capability to radiate pulses and high power while avoiding high field intensities and simplifying design complexity.
- Develop a TTD beamformer with a compact form factor using a corporate feed network and a quasi-optical system to efficiently feed an array of long slots while minimizing losses and size. We will employ physical optics to analyze and optimize the quasi-optical system, ensuring minimal variation of its phase center for pulsed radiation and wideband operation. Additionally, we will investigate gap waveguide technology to facilitate electrical contact between moving parts within the antenna structure to enable mechanical steering.
- Experimental validation of a high-power microwave long slot array operating across the entire X-band (8-12 GHz), demonstrating superior power handling capabilities with a compact radiating structure.

Naval Relevance:

The proposed solution offers a compact, flat HPM antenna alternative to conventional, high-performance space-fed reflectors. This antenna is designed to operate efficiently with short pulses and low-frequency dispersion while providing a wide field of view and a compact profile compared to other TTD solutions. The successful development of this antenna will introduce a new concept

for HPM systems in next-generation directed energy weapons (DEW) for the U.S. Navy, resulting in significant benefits in terms of size, weight, and cost.

Introduction/Background:

Antennas play a crucial role in the development of HPM technology. Current research focuses on achieving ultra-wideband (UWB) operation with minimal dispersion for short pulse sources and shifting systems toward higher frequency bands (from X to K bands). In this context, HPM antennas must meet strict requirements regarding gain, steering capability in both azimuth and elevation, pattern shaping, efficiency, size, and weight. The chosen technology must also withstand harsh environments and intense electric fields necessary for the radiation of gigawatt-level powers. Existing HPM antenna solutions utilize well-established designs such as Vlasov and COBRA antennas, horns, space-fed reflectors, radial line slot (RLSA) and helixes arrays to meet these stringent requirements partially. Novel concepts, such as transmit and reflect arrays, have also been introduced to steer the main beam of HPM antennas. Space-fed reflectors remain an exceptional choice for creating TTD systems that can instantaneously illuminate a radiating aperture. The TTD feature enables very wide band operation with low dispersion, although it comes at the cost of increased size and weight of the radiating device. Mechanical rotation of the entire antenna in azimuth and elevation is also necessary for steering the main beam, which may have limitations regarding steering speed and pointing accuracy. Steering can alternatively be achieved by positioning multiple sources in the focal plane of the reflector (a beam-switching scheme). In this research endeavor, we leverage the capabilities of long slot arrays fed by a corporate feed network and quasi-optical systems. This approach aims to achieve the advantages of space-fed reflectors while satisfying the current requirements for HPM antennas with a compact and low-profile design. The long slots in the array are non-resonant radiating elements, ensuring wide-band operation over a broad field of view. Our group has validated this antenna architecture for telecommunications applications in the Ka-band and beyond, demonstrating wide fields of view and an overall thickness of just a few wavelengths. This effort addresses the challenge of analyzing and validating long slot arrays fed by a corporate feed network and quasi-optical systems specifically for HPM applications. We aim to harness the TTD operation of the array to explore its capabilities for radiating gigawatt-level microwave power across a wide field of view in the entire X-band, all while maintaining a reduced form factor that surpasses the current state of the art.

2. Activities and Accomplishments

In this report, we have focused on analyzing and designing long slot arrays for high-power radiation and defining the quasi-optical system and corporate feed network for TTD illumination of the radiating aperture. Specifically, we will detail our progress in the following areas:

- **Modeling of The Unit Cell of the Array and Corporate Feed Network:** We have studied the unit cell of the array and corporate feed network to operate across the entire X-band while adhering to geometrical restrictions necessary for supporting high-intensity fields.
- **Phase Center Stability:** We have examined the stability of the phase center for the array, the corporate feed network, and the quasi-optical system for pulse radiation.
- **Virtual Quasi-Optical Systems:** We have introduced the concept of virtual quasi-optical systems enabled by gap waveguide technology.

Each of these topics is discussed in a dedicated section of the report.

2.1 Modeling of The Unit Cell of the Array and Corporate Feed Network

The general architecture of a long slot array fed by a quasi-optical system (e.g., pillbox transition) is shown in Figure 1. The long slots are non-resonant radiating elements sampling the aperture with a periodicity smaller than λ_0 (λ_0 is the free space wavelength at the higher frequency of operation). A corporate-feed network made in Parallel-Plate-Waveguide (PPW) technology feeds the long slots in parallel. The geometrical size of the PPWs, the distance between the parallel plates, is set smaller than $\lambda_0/2$ to allow the propagation of the TEM mode for wideband operation without frequency dispersion or cut-off frequency. The corporate feed network is illuminated by a pillbox coupler (quasi-optical system) made by a parabolic 180° bend. The pillbox coupler transforms the cylindrical wavefront of the TEM mode launched by the input horn in its focal plane to a planar one, illuminating the array. The corporate feed network and pillbox coupler illuminate the slots of the array simultaneously with a TTD behavior with high efficiency and a reduced form factor.

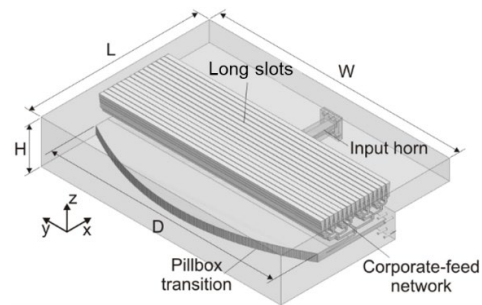


Figure 2: Perspective view of a long slot array.

The considered array geometry is graphically reported in Figure 2. The slots are characterized by a width a and periodicity d_x and are located on a Perfect Electric Conductor (PEC) ground plane. The TEM mode of the feeding PPWs illuminates the slots for radiation simultaneously. The array is considered in vacuum to sustain high electric fields for high power radiation. Matching layers or a covering radome may be introduced. Long slot arrays present sharp edges within their unit cell and beam-forming network. The unit cell of a long slot array has been revisited for HPM applications. In particular, smooth edges have been introduced to reduce the possibility of breakdown effects, as shown in Figure 3(a). The periodicity of the unit cell along the x-axis, d_x , can exceed the classical limit of half wavelength since the main beam of the array is steered in the yz-plane in Figure 3(a). However, d_x should be limited to values smaller

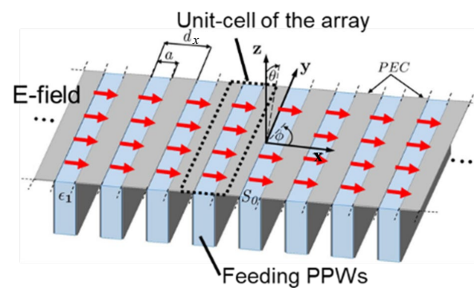


Figure 1: Array geometry. PEC stands for Perfect Electric Conductor.

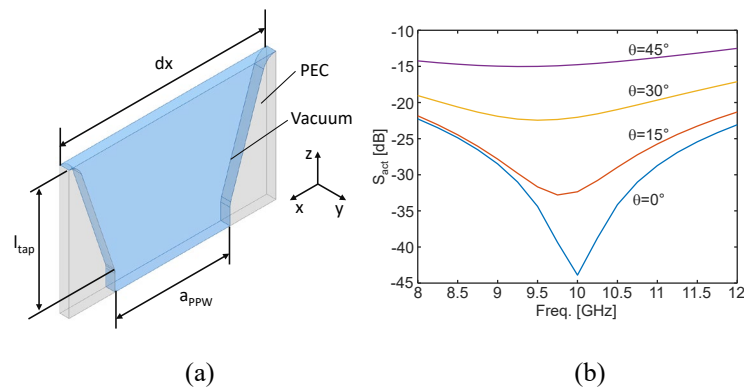


Figure 3: (a) Unit cell with smooth edges; (b) Active reflection coefficient for different steering angles in the yz-plane.

than λ_m at the higher frequency of operation ($\lambda_m=25$ mm at 12 GHz) to avoid scan blindness. Here we choose $d_x=22.5$ mm= $0.9\lambda_m$.

Once the periodicity is fixed, the slot width should be chosen to provide matching over the band of interest. An in-house Mode Matching (MM) tool provides the preliminary design. A PPW structure then feeds the slot. The PPW structure should be chosen to limit high electric field levels. Larger spacing between the metallic plate of the PPW should be then preferred. However, the spacing should not exceed half wavelength at 12 GHz to preserve the single-mode operation of the PPW. Here, we chose the spacing, a_{PPW} , equal to 10.16 mm to be compatible with the height of standard rectangular waveguides in X-band. Note that rectangular waveguides are generally used to feed long slot arrays. However, other feeding structures may be considered during this activity to ease the integration with HPM sources. A smooth matching transition of length l_{tap} connects the feeding PPW to the radiating aperture. l_{tap} is equal to 12 mm ($0.48 \lambda_m$). The active reflection coefficient is shown in Figure 3(b). The unit cell is matched in the band 8-12 GHz for steering angles up to 45° in elevation.

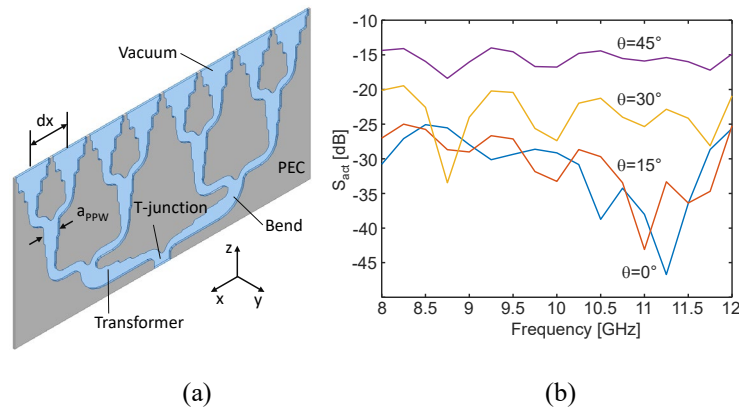


Figure 5: (a) Array of 8 slots with smooth edges; (b) Active reflection coefficient for different steering angles in the yz -plane.

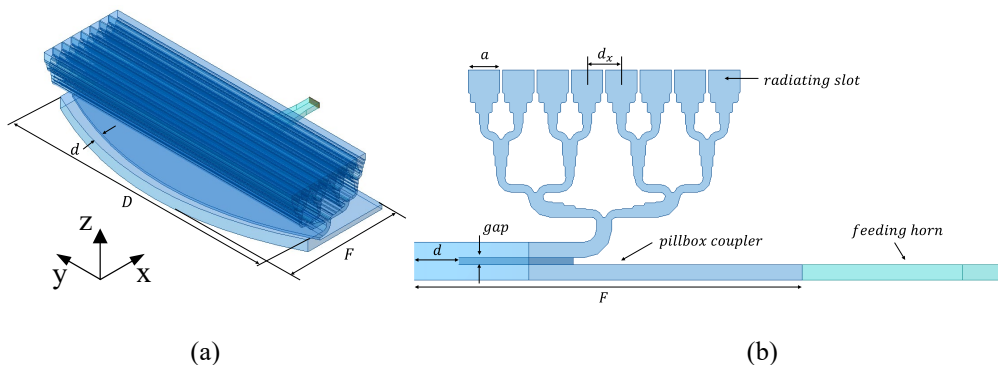


Figure 4: Long slot array of 8 slots with corporate network, pillbox coupler, and an integrated H-plane horn. (a) Perspective view; (b) Side view along the xz -plane.

Long slot arrays are fed by a corporate feed network (CFN), as shown in Figure 1 and Figure 4(a). The building blocks of the CFN have been revisited for HPM applications by introducing smooth edges to reduce the possibility of breakdown events. The CFN's feeding mode is the TEM mode of the PPW. Figure 4a reports the CFN for an array of 8 slots with a periodicity $dx = 22.5$ mm. The maximum spacing of the CFN (a_{PPW} in Figure 4a) equals 10.16 mm, while the minimum height is 5.08 mm. The various building blocks are highlighted. In particular, T-junctions, bends, and impedance transformers made up the CFN. The preliminary design of the building blocks is based

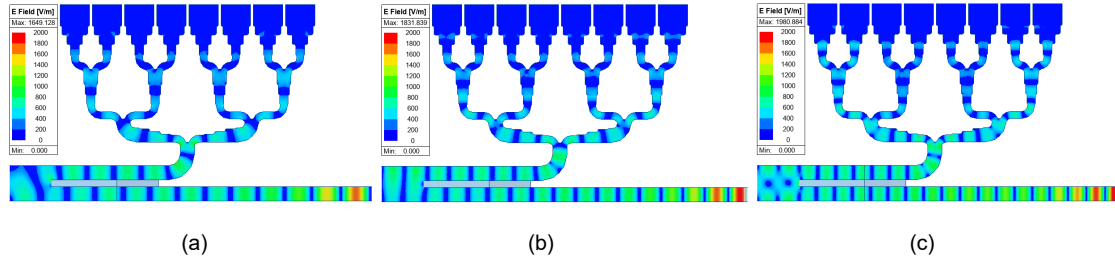


Figure 6: Electric field distribution in the pillbox system, corporate feed network, and an array of slots at (a) 8 GHz (Max: 1649 V/m); (b) 10 GHz (Max: 1831 V/m); (c) 12 GHz (Max: 1980 V/m).

on circuitual models without fillets. A fillet with a minimum radius of 1 mm is considered to smooth the angles without affecting the scattering performances of the structure.

Figure 4(b) shows the active reflection coefficient for an array of 8 slots. The array is matched in the band 8-12 GHz for steering angles up to 45° in elevation. The vertical profile of the array can be further reduced by considering PPWs with smaller heights or sub-array configurations. At the moment, vacuum and PEC have been considered for the materials of the unit cell. A corporate feed network feeds the array of 8 long slots through a quasi-optical beam former made by a pillbox transition, as shown in Figure 5. The quasi-optical system was analyzed with a Physical Optics (PO) tool to derive a trade-off between the size, efficiency, and stability of the focal point of the finite array with frequency. The pillbox beam former presents a small F/D of 0.7 (Figure 5). The H-plane feeding horn provides the required -10-dB edge tapering over the pillbox reflector. The radiating aperture of the horn is $1.5 \lambda_0$, with λ_0 the wavelength at 10 GHz. The pillbox transition's focal length is equal to 300 mm ($10 \lambda_0$) to fulfill far-field conditions for the integrated horn. The finite array of slots fed by a classical quasi-optical system has been used to derive preliminary results on the proposed antenna's power handling capability by tracking the electric field's maxima within the structure. The electric field distribution of the finite array is plotted in Figure 6 for an input power of 1W. A maximum of 2 kV/m has been observed at the feeding point of the quasi-optical system. For a breakdown voltage of 50 MV/m in vacuum, the antenna's power handling capacity is estimated to be over 600 MW. The observed maxima of the electric field need to be reduced to increase the power handling capacity of the antenna. However, such preliminary results show the potential of such a solution for HPM systems.

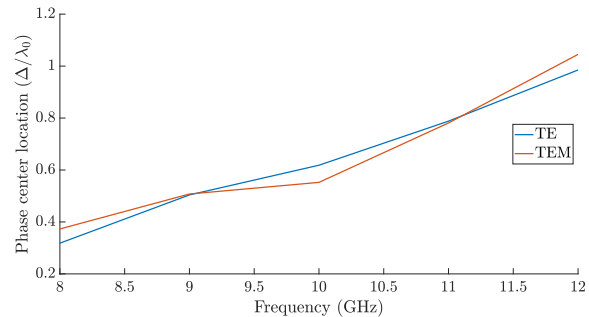


Figure 7: Normalized phase center location of the finite array with corporate feed network for different mode illuminations.

2.2 Phase Center Stability

We have investigated the stability of the phase center in the band of interest by first analyzing the various building blocks of the antenna: the finite array of long slots with its corporate feed network and the quasi-optical system. The geometrical dimensions of the finite array and its corporate feed network are those in Figure 5, with a width $D = 420$ mm. The variation of the phase center location along the H-plane (yz -plane) has been analyzed with full-wave simulations. The reference system is considered centered on the radiating aperture. A Transverse Electric (TE_{10}) and TEM mode have been considered to illuminate the corporate feed network. These two modes provide a different field distribution along the y -axis. The normalized phase center variation (Δ/λ_0) is shown in Figure 7. Positive/negative variations correspond to positions above/below the radiating aperture. The normalized phase center variation (Δ/λ_0) is smaller than $0.42 \lambda_0$ and $0.40 \lambda_0$ for TE and TEM mode, respectively. Future studies will consider corporate feed networks with a thinner profile to better understand the effect of the vertical size of the corporate network on the phase center location.

The quasi-optical system (pillbox coupler) is then analyzed with an in-house PO tool to evaluate the variation of the phase center position as a function of the F/D ratio of the quasi-optical system. The geometry of the system is the one in Figure 5. The phase center location is normalized to focal distance (F) to relate its variation to the ideal location of the phase center at the focus of the quasi-optical system. The variation of the phase center location is smaller than $0.20 \lambda_0$ and $0.16 \lambda_0$ for F/D values of 0.59 and 0.7, respectively, as shown in Figure 8. Larger F/D ratios should be considered to reduce the phase center variation within the band of interest.

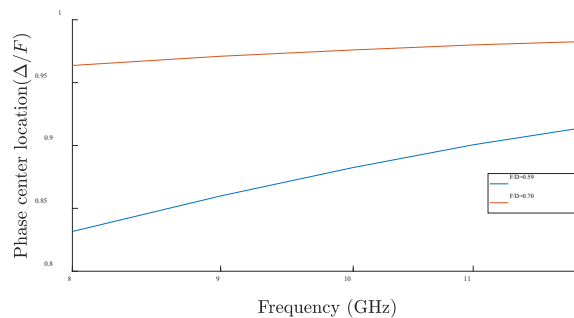


Figure 8: Normalized phase center location of the quasi-optical system for different F/D ratios.

The complete antenna was then analyzed considering a diameter $D = 715$ mm. Note that smaller D could be used without affecting the general conclusions. The focus of the antenna has been retrieved

by analyzing the antenna in reception by shining a plane wave toward the antenna aperture and searching for the maximum of the received field over the axis of the quasi-optical system. The plane wave is coming toward the antenna from the broadside direction (z -axis in Figure 5) with the electric field orthogonal to the slots along the x -axis. The energy induced by the plane wave propagates as a TEM mode through the corporate feed network, and the parabolic surface of the pillbox coupler focuses it toward the focal plane. The

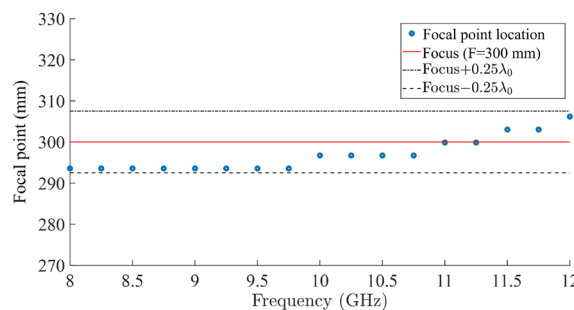


Figure 9: Location of the focus of the antenna in the band 8-12 GHz with a frequency step of 0.25 GHz. The variation is smaller than $0.5 \lambda_0$.

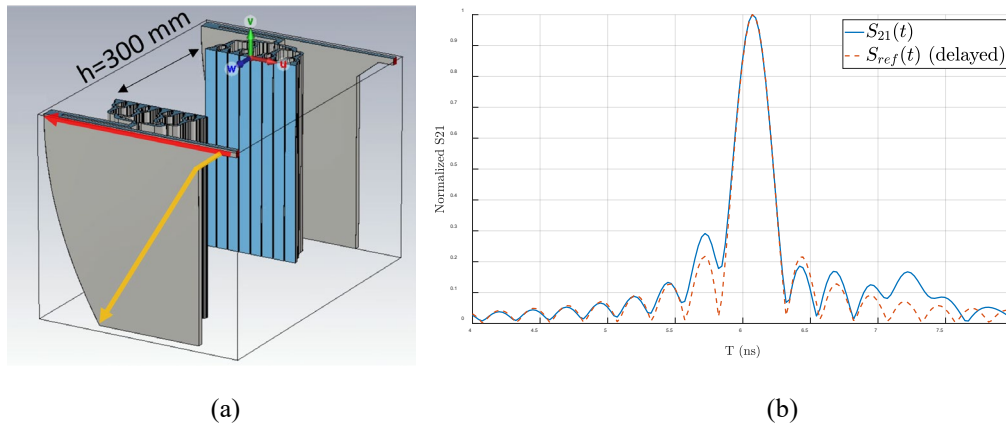


Figure 10: (a) Wireless link setup; (b) Received and transmitted signal. For comparison, the reference signal is delayed by 6.076 ns.

focus is retrieved by searching for the maximum of the TEM mode electric field along the axis of the quasi-optical system. It is worth mentioning that a more accurate analysis should consider the aperture field distribution over the feeding horn and derive the electromagnetic reaction of such distribution with the received field. However, the location of the maximum of the received field provides a good estimation of the position and variation of the focus. The ideal geometrical focus is located 300 mm from the apex of the parabolic reflector of the quasi-optical system. Figure 9 shows the location of the focus with a frequency step of 0.25 GHz. The focus variation is $0.42 \lambda_0$ in X-band (λ_0 is the free space wavelength at 10 GHz). It is worth mentioning that quasi-optical systems with larger F/D ratios will provide smaller variations, as previously reported. This result proves the stability of the phase center of the complete antenna system.

Finally, the pulse propagation in a wireless link made by two long slot arrays has been analyzed. The geometry is shown in Figure 10(a). The link between a transmitting and receiving long slot array can be characterized in terms of its complex transfer function $H(\omega) = U_{RX}(\omega)/U_{TX}(\omega)$, where $U_{RX}(\omega)$ and $U_{TX}(\omega)$ are the spectra of the received and transmitted signals. $H(\omega)$ is related to the scattering parameter $S_{21}(\omega)$ of the wireless link. The pulse response of a wireless link to an input signal can be then derived by means of the Inverse Fourier transform $S_{21}(t)$ of $S_{21}(\omega)$ in the band of interest (8-12 GHz). The distortion of the received signal due to the dispersive behavior of the antennas is quantified by the fidelity factor (F) given by:

$$F = \max_{\tau} \frac{\int_{-\infty}^{\infty} s_{ref}(t) S_{12}(t-\tau) dt}{\sqrt{\int_{-\infty}^{\infty} |s_{ref}(t)|^2 dt \int_{-\infty}^{\infty} |S_{12}(t)|^2 dt}}$$

where $s_{ref}(t)$ and $S_{12}(t)$ are the reference and received signal, respectively. We considered a *sinc* signal in the band 8-12 GHz as reference signal. The reference and received signals in time domain are shown in Figure 10(b). The peak of the received signal is at 6.076 ns, corresponding to 1823 mm of equivalent free space propagation. Figure 10(a) illustrates the optical path length with red and yellow lines for two rays coming from the quasi-optical system. The average of the two optical paths is 1826 mm, in close agreement with the derived distance. The fidelity factor is equal to 0.97 validating the non-dispersive behavior of the antennas. It is worth mentioning that in the considered wireless link the receiving antenna is located within the Fresnel zone of the transmitting antenna due to computational limitations.

2.3 Virtual Quasi-Optical Systems:

In classical quasi-optical systems, vertical conducting walls are used as mirrors to reflect and phase the energy or to reduce the size of the overall beam-forming network. Beam steering is achieved by either placing several sources in the focal plane of the quasi-optical system or by moving the source. Vertical conducting walls, especially in mechanical steering systems, require stringent fabrication requirements for multi-layer structures to provide good electrical contact and reduce losses or leakage in the PPW environment.

We have introduced the concept of virtual quasi-optical systems. Such a novel idea is part of a provisional patent application, as reported below. This invention aims to provide a quasi-optical system based on virtual magnetic walls. The TEM mode of a PPW structure is considered the only propagating mode. Figure 11 shows the equivalent structure for the quasi-optical systems (pillbox transition) in Figure 1 and Figure 5 using a perfect magnetic wall. The perfect magnetic wall is engineered by introducing perfect magnetic conductors (PMC) over the top and bottom plates of the PPWs (blue layers in Figure 11). The PMCs are shaped on one side with a parabolic profile to mimic the parabolic reflector of the initial quasi-optical system. Figure 12 compares the radiation

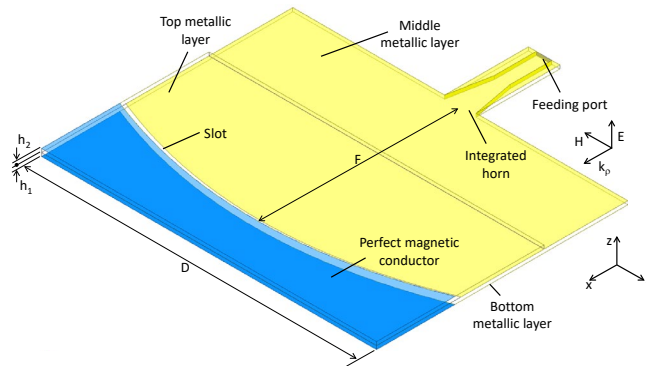


Figure 11: Example of a quasi-optical system made by a pillbox transition with PMCs to create a virtual magnetic wall replacing the metallic mirror in Figure 1. $F=300$ mm and $D=480$ mm.

performance of the proposed concept and a classical system with the same optics and a vertical metallic mirror in X-band. Equivalent performances are achieved at 10 GHz in the xy-plane. The pointing direction of the radiated beam is stable with frequency, as shown in Figure 12(b) in X-band. This is expected from a quasi-optical system behaving as a TTD network. In addition, the displacement of the source along the focal plane of the virtual mirror provides different pointing directions, as shown in Figure 13, for two locations of the input source. It is worth mentioning that

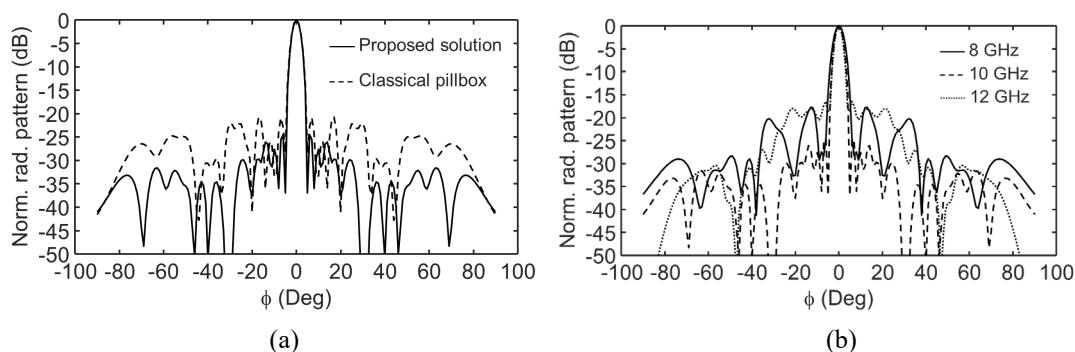


Figure 12: (a) Normalized radiation patterns of the proposed and classical pillbox systems at 10 GHz along the xy-plane. (b) Radiation patterns in the band 8-12 GHz for the proposed solution.

performance of the proposed concept and a classical system with the same optics and a vertical metallic mirror in X-band. Equivalent performances are achieved at 10 GHz in the xy-plane. The pointing direction of the radiated beam is stable with frequency, as shown in Figure 12(b) in X-band. This is expected from a quasi-optical system behaving as a TTD network. In addition, the displacement of the source along the focal plane of the virtual mirror provides different pointing directions, as shown in Figure 13, for two locations of the input source. It is worth mentioning that

the pointing direction of the radiated pattern can be retrieved as $\varphi \approx \tan^{-1} d_s/F$. The equivalence in operation between the two systems can be considered verified. However, a PMC is introduced here on the top and bottom plate of the PPW structure to cancel the magnetic field and thus reflect the TEM mode. The benefits of the virtual magnetic wall can be understood for mechanical steering and fabrication constraints. The virtual magnetic walls do not require any physical connection between the PPWs, and thus, any displacement or rotation does not require any RF choke or particular technology to avoid leakage among the various layers. In addition, the steering of the main beam can be achieved by rotating or moving the equivalent parabolic reflector instead of the feeding horn without affecting the system's operation. The physical implementation of the PMCs and, thus, the magnetic wall is now presented.

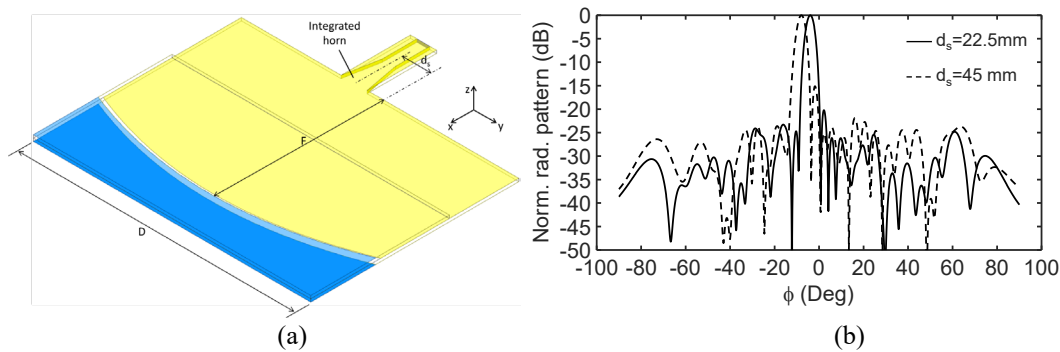


Figure 14: (a) Proposed solution with a source displaced along the y-axis at a distance d_s from the focus of the virtual parabolic mirror. (b) Normalized radiation patterns for two source positions at $d_s=22.5$ mm and 45 mm. For $d_s=22.5$ mm and 45 mm the system radiates at 4° and 8° , respectively.

PMCs can be realized by using gap-waveguide technology in a PPW environment, as shown in Figure 14a. In particular, a periodic structure made by pins is engineered to prevent propagation (stopband) of the TEM mode between the metallic plate and the bed of nails. The dispersion diagram of the structure can be retrieved by using full-wave simulations of the unit cell in the reduced Brillouin zone of the structure, shown in red in Figure 14(b). The dispersion diagram is shown in Figure 14(c), validating the capability of this structure to prevent the propagation of the TEM mode in the stopband independently of its impinging direction. This concept supports the

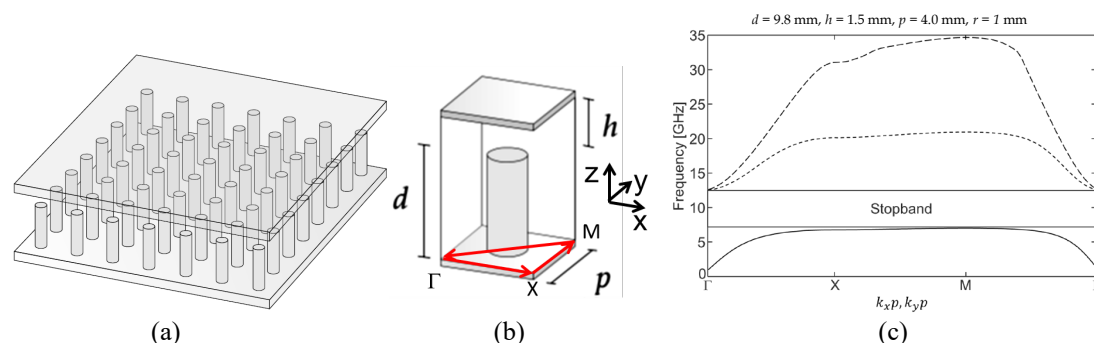


Figure 13: (a) Isometric view of a bed of nails implementing a PMC. The grey parts are metal. (b) Isometric view of the unit cell of the bed of nails. In red, the reduced Brillouin zone is used to derive the dispersion diagram of the structure. (c) Dispersion diagram. The unit-cell geometrical dimensions are provided at the top of the figure. A stopband is achieved in the band 6.3-12.5 GHz.

physical implementation of the PMCs required by the proposed solution. Future works will consider the implementation of the virtual mirror with a bed of nails and its integration into the proposed antenna structure. The operation of the virtual optics as a TTD system and its operation for high-power applications require further investigations.

3. Findings and Conclusions

This report demonstrates that arrays of long slots can operate effectively over a wide bandwidth and a broad field of view. We have numerically validated this concept for X-band operation with a 45° field of view in elevation while achieving a reduced form factor. However, there is a possibility of extending the bandwidth further to enhance the capability and impact of the proposed concept, for example, for communication systems in need of high data rates and wide instantaneous bandwidths. Additionally, we established the stability of the antenna's phase center and confirmed the array's ability to transfer pulses with high-fidelity factors in a wireless link. The stability of the phase center is crucial for the radiation of short pulses for radar applications and sensing. We also introduced and numerically validated the concept of virtual quasi-optical systems with gap waveguide technology. These virtual optics can replace traditional quasi-optical systems, which rely on vertical metallic mirrors, facilitating implementation and mechanical steering of the antenna's main beam. With a breakdown voltage of 50 MV/m in a vacuum, the antenna's estimated power handling capacity exceeds 600 MW, showing the potential of this solution for next-generation HPM systems.

4. Plans and Upcoming Events

In the next year, we will focus on consolidating the results on pulse radiation for HPM applications, investigating the limitations in power handling of the proposed structure and pointing out the critical physical mechanisms associated with the antenna operation and architecture, evaluating the capability of gap waveguide technology to support high power and support mechanical steering of the antenna main beam.

5. Transitions and Impacts

No information to report.

6. Recommendations for Future Work:

Future activities may consider low-dispersive antenna solutions for short-pulse radiation.

7. Personnel

Principal Investigator			
Full Name	Approximate Level of Effort – LOE - (Hours This FY)	Country of Residence	National Academy Member? (Y/N)
Mauro Ettore	160 Hours	U.S.	N
Co-Investigator(s) or Co-PI(s)			
Full Name	Approximate Level of Effort – LOE - (Hours This FY)	Country of Residence	National Academy Member? (Y/N)

N/A	N/A	N/A	N/A
Performer Business Contact(s)			
Full Name	Role	Country of Residence	
Katherine Cook	10 hours	U.S.	N
Additional (Non-Student) Team Members			
Full Name	Approximate Level of Effort – LOE - (Hours This FY)	Country of Residence	National Academy Member? (Y/N)
N/A	N/A	N/A	N/A
Subcontractors			
Full Name and Organization	Approximate Level of Effort – LOE - (Hours This FY)	Country of Residence	National Academy Member? (Y/N)
N/A	N/A	N/A	N/A

8. Collaborations

Full Name	Organization	Collaboration Summary
N/A	N/A	N/A

9. Students

Doctoral Student(s)			
Full Name	University	Graduated?	Graduation Year
Woohyung Jeon	Michigan State University	N	N/A
Ethan Neitzke	Michigan State University	N	N/A
Masters Student(s)			
Full Name	University	Graduated?	Graduation Year
N/A	N/A	N/A	N/A
Undergraduate Student(s)			
Full Name	University	Graduated?	Graduation Year
N/A	N/A	N/A	N/A

10. Technology Transfer

Provisional patent application

Title of invention: Virtual quasi-optical systems in parallel plate waveguide technology

Authors: Mauro Ettore, Woohyung Jeon, Ethan Neitzke

Application #: 63/698,135

Date: 9/24/2024

11. Products, Publications, Patents, License Agreements, etc.

Publications resulting from this project for the reporting period:

Archival Publications

No information to report.

Conference Papers

#	Citation	Acknowledged ONR Support Received? (Y/N)	Peer Reviewed? (Y/N)
1	Ethan Neitzke, Woohyung Jeon, and Mauro Ettorre, "Low-profile virtual quasi-optical systems," 2025 European Conference on Antennas and Propagation (EuCAP 2025), March 30 – April 4, 2025. (Invited paper)	Y	Y

Books

No information to report.

Book Chapter

No information to report.

Theses

No information to report.

Websites

No information to report.

Patents

No information to report.

Other Products:

No information to report.

12. Point of Contact in U.S. Navy / Marine Corps

No information to report.

Improving Performance of Crossed-Field Amplifiers Through Modulation Injection

Grant No. N00014-21-1-2024

Annual Report for Fiscal Year 2024

Period of Performance: October 1, 2023 to June 10, 2024

Prepared by:

Dr. Allen L. Garner, Principal Investigator
Professor and Undergraduate Program Chair, School of Nuclear Engineering
Purdue University
363 N. Grant St.
West Lafayette, IN 47907
Tel: (765) 494-0618
Email: algarner@purdue.edu

Co-Principal Investigator(s):

Jim Browning, jimbronwing@bsu.edu, Boise State University
Jack Watrous, jack.watrous@confluentsciences.com, Confluent Sciences, LLC



This work was sponsored by the Office of Naval Research (ONR), under grant number N00014-21-1-2024. The views and conclusions contained herein are those of the authors only and should not be interpreted as representing those of ONR, the U.S. Navy or the U.S. Government.

Section I: Project Summary

1. Overview of Project

Executive Summary: Crossed-field devices, such as crossed-field amplifiers (CFAs), offer high efficiency, high power density, and robust performance. Improved CFA gain-bandwidth product and reduced noise would contribute to greater use and operational capabilities. This report highlights our progress toward benchmarking the particle-in-cell (PIC) codes ICEPIC and VSim to assess a commercial CFA, our completion of theoretical models describing the maximum current in two-dimensional (2D) crossed-field devices, our assessment of the maximum current allowed in a collisional crossed-field diode, and our work on changes in 2D maximum current with ion emission from the anode. This work is important for developing a testbed for crossed-field device modeling to aid future development and better understanding limitations that may be extended to practical devices.

Objective: This effort studies the effects of electron modulation on a high power (1 MW) L-Band CFA using theory (Purdue University) and simulation using the particle-in-cell codes ICEPIC (Confluent Sciences) and V-Sim (Boise State University and Tech-X). The first task entails developing and validating a CFA model using thermionic emission models. This result will next be combined with secondary emission models and theories and validated. This will subsequently permit the examination of the causes of drive saturation and gain-bandwidth limitations. This combined theory and simulation will then be used to characterize the effects of electron modulation with and without secondary emission on gain, bandwidth, saturation, and noise on CFA efficiency, pulse width, output power, bandwidth, and frequency timing. Finally, an assessment on the impact of noise in the CFA will be performed by examining how particle orbits are impacted based on the thermionic and secondary emission models and the impact of space-charge on the electromagnetic properties of the device.

Naval Relevance: The Navy is accustomed to having complete control of the electromagnetic spectrum, but as a warfare domain, the electromagnetic spectrum is becoming both congested and contested. This necessitates much greater flexibility in our electromagnetic sources. As platforms become much more loaded with electronics and technology, individual electromagnetic sources must be more compact (to physically fit in confined spaces), more efficient (to ease system engineering concerns), more capable (to achieve multiple missions), and more controllable (both to achieve more missions and mitigate the risk for friendly fire on blue team forces). This effort strives to both maintain the high amplitude operation associated with directed energy technology and elucidate the ways in which directed energy devices can provide information rich signals with both choices in center band frequency, high bandwidth frequency modulation, and exquisite phase control. The effort primarily explores the fundamental knowledge and applied science needed to advance the state of the art in electromagnetic maneuver.

Introduction/Background: Crossed-field devices, such as crossed-field amplifiers (CFAs), offer high efficiency, high power density, and robust performance. Improved CFA gain-bandwidth product and reduced noise would contribute to greater use and operational capabilities. Currently, there are no high-power CFA models available for public research studies at universities. This gap is especially important as we try to realize the promise of higher power devices represented by Directed Energy High-Power RF (HPRF) devices. Almost every type of high-power radiofrequency (HPRF) device is an oscillator. While these sources produce very high-power pulses, the waveform control, typically measured in the bandwidth, is insufficient for radar or

communications. This restricts these directed energy (DE) sources to jamming and counter-electronics missions, rather than the more information-intense full-fledged electronic warfare. This proposal goes to the heart of the question “what are the limits to high power amplifiers?” The university community currently lacks the well characterized, high power sources with intense space-charge that can mimic a HPRF device to address these questions. This problem becomes more acute for CFAs. CFAs are the highest power amplifiers widely used; however, they suffer from the limits of the gain-bandwidth product. The lack of a publicly available CFA model using first-principles, particle-in-cell simulations to serve as a benchmark for research hinders the examination of potential methods to improve design.

We use a model of the L3 Technologies L4953 CFA (discontinued) that was operated by the Federal Aviation Administration (FAA). Because this model is discontinued and unclassified, L3 Technologies is willing to allow our team to use the design to develop a high-power CFA model. This CFA model would become a benchmark for CFA research in universities, industry, and national laboratories to allow comparing future simulations and modifications to CFAs and other amplifiers. After developing the model, we would then study the effects of electron modulation on gain, bandwidth, and noise. We can study, via simulation, the saturation effects that occur in CFAs and determine whether techniques such as current modulation can improve the gain-bandwidth performance including performance at higher input powers. This would include studying the cause of saturation and techniques to maintain/increase gain-bandwidth product for HPRF production. Table 1 summarizes our team’s overall research concept. We propose using VSim and ICEPIC and theoretical analysis to (1) develop and validate CFA models using emission-based cathodes, (2) extend the validated model using a combined thermionic emission and simple secondary emission model to approximate the secondary emitting component, (3) apply simulation and theory to analyze the saturation of gain-bandwidth in high power CFAs, (4) study the effects of a modulated cathode and electron back-bombardment on the gain-bandwidth product, and (5) analyze the effects of electron modulation and electron back-bombardment on noise generation and noise reduction with simulation and theory.

From this effort, studying the back-bombardment of field emission cathodes and out of band noise suppression will enhance the effectiveness of radar/communications/electronic warfare by removing spurious signals that degrade source performance for a given application and providing a signature to adversarial platforms. By providing high power, multi-frequency operation, this study could reduce SWAP-C (size, weight, power and cost) of the system.

2. Activities and Accomplishments

Boise State University extended its work from FY23 to assess spoke wobble. VSim simulations showed Brillouin-like and cycloid-like electron flow during space-charge limited emission (SCLE) and non-SCLE, respectively. Two distinct oscillations arose within the spoke: spoke transit wobble, caused by the 360° transit from input to output back to input, and sideband noise. While transit wobble is the dominant oscillation within the spoke, it does not arise on the output. Fig. 1 summarizes the process used for spatial-temporal/spectral visualizations in VSim to perform this assessment. Fig. 2 shows the RF output spectrum the spatial-spectral assessment. The sideband noise that shows up in the spatial-spectral assessment on the left clearly shows up in the RF output spectrum on the left; however, the transit wobble that dominates the spatial-spectral assessment is not visible in the RF output spectrum. Transit wobble is caused by the spoke transiting 360° in the re-entrant design, making it $1/3$ of the operating frequency. The spoke moves forward at output and

recovers before the input. While each spoke has a similar phase shape, the phase difference between each spoke is 120° .

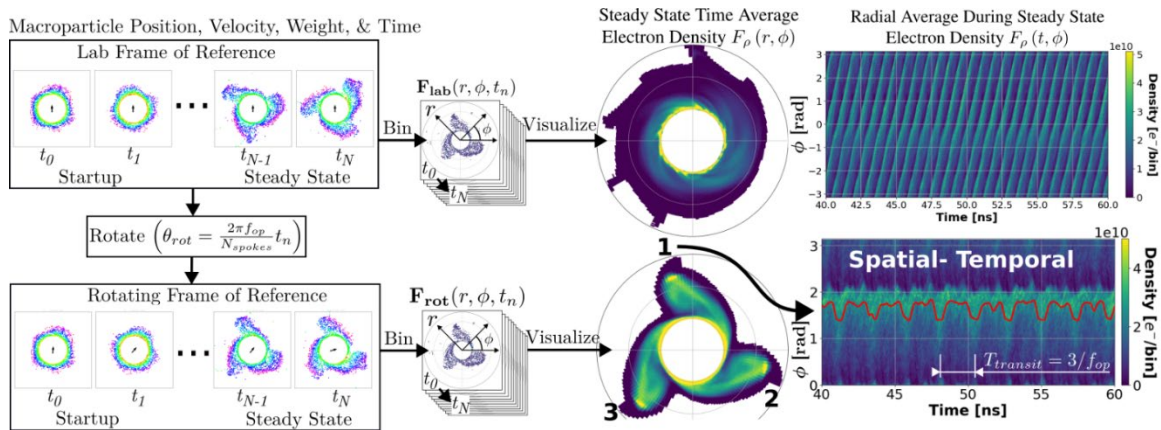


Fig. 1. Procedure to generate spatial and spatial-temporal visualizations. Macroparticle data is dumped for N timesteps in the lab frame of reference. The rotation operator converts to the rotating frame of reference. The macroparticle data (electron density and velocities) are binned to produce the structured dataset $F(r, \phi, t_n)$. Spatial and spatial-temporal visualizations are obtained by averaging in time and radius during steady state, respectively. The rotating frame of reference shows three spokes labeled in both spatial and spatial-temporal visualizations.

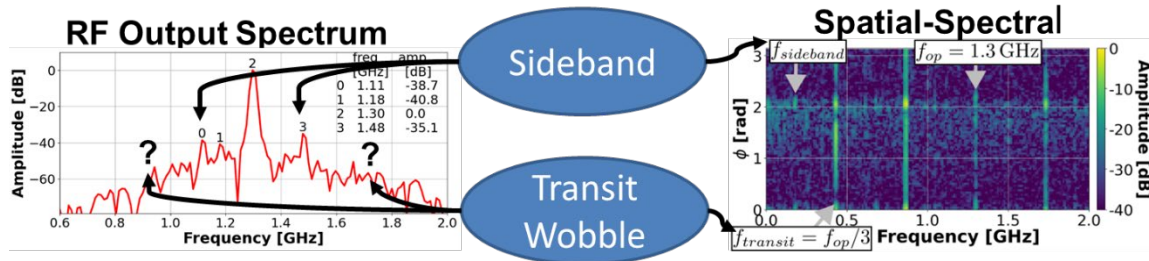


Fig. 2. (left) RF output spectrum and (right) spatial-spectral analysis demonstrating that the sideband noise is present in both analyses, but the transit wobble does not clearly appear in the RF output spectrum despite its dominance in the spatial-spectral analysis.

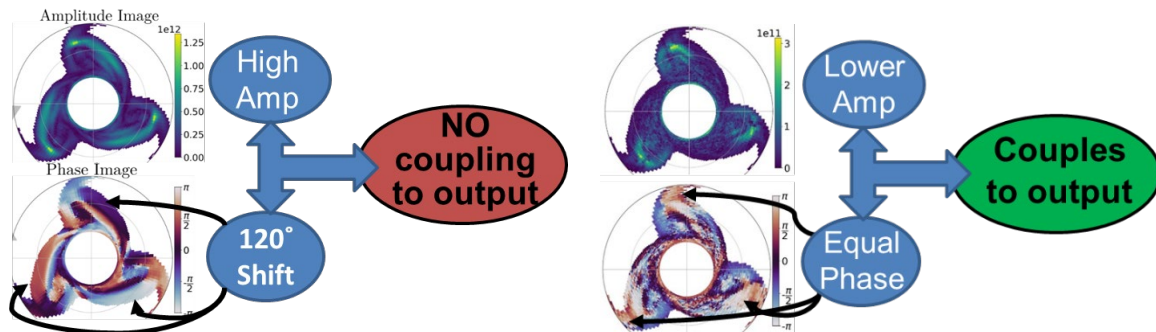


Fig. 3. Left: Spatial-tonal amplitude (top) and phase (bottom) of the transit wobble in the rotating frame of reference showing a 120° shift. **Right:** Spatial-tonal amplitude (top) and phase (bottom) of the sideband noise in the rotating frame of reference showing equal phase and a lower amplitude compared to the transit wobble.

Fig. 3 shows spatial-tonal amplitude and phase images that confirm the absence of coupling to the output for transit wobble and the coupling to output for sideband noise. The sideband noise has a lower amplitude, while the phases are shifted by 120° for the transit wobble and exhibit equal phase for the sideband noise.

Confluent Sciences used ICEPIC, a parallel, three-dimensional electromagnetic particle-in-cell code developed by the Air Force Research Laboratory (AFRL) for modeling high-power microwave devices, in parallel to provide a comparison to VSim. One of the challenges through the early years of the project was diagnosing discrepancies between the two codes. A major challenge was how the two codes report the geometry of the device being modeled. ICEPIC commonly captures intersections of the geometry with specified planes isometrically and to a given scale, permitting comparisons between different realizations of the same geometry. This allows rapid debugging of a newly constructed geometry. VSim generally uses more sophisticated graphical representation techniques, such as Paraview. This led to different representations of the geometry and errors that were often not discerned until after simulations. The final error was discovered in one of the straps.

Upon correcting the geometry, IV-traces for the calculations corresponding to the five different frequencies used for the tuning procedure. The 1280 MHz calculation experienced an instability before it reached the operating point 1 current target (98 A). The other four frequencies (1300, 1315, 1330, and 1350 MHz) achieved the 98 A target. Fig. 4 compares time-averaged voltage and output power from ICEPIC with analogous data from VSim and from actual laboratory measurements of the device. The ICEPIC results are in good agreement with both the laboratory measurements and the VSim results. No obvious systematic deviation separates the ICEPIC results data from the VSim and laboratory data. The 1280 MHz calculations may be having trouble due to the Q-value of the simulated device being too high. Experiments with the value of surface conductivity used in the calculations would be of benefit to test this hypothesis.

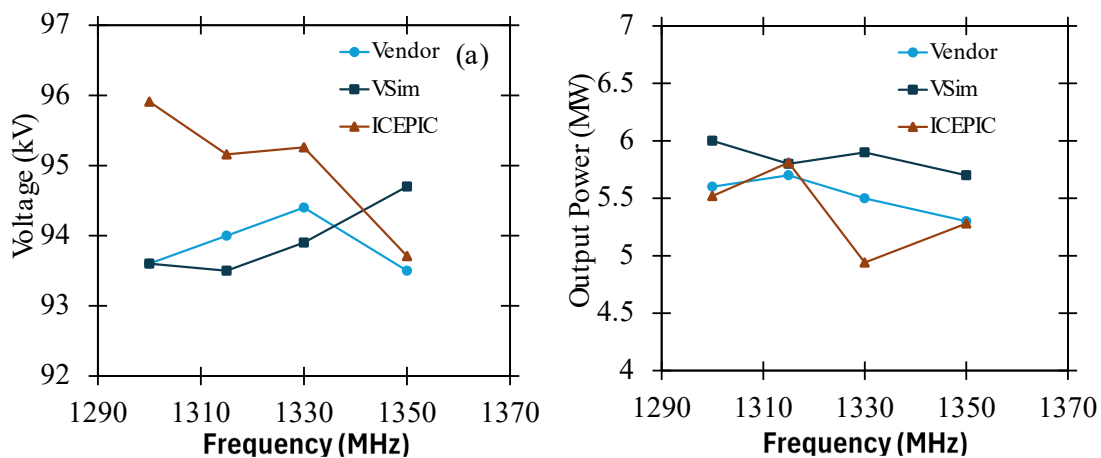


Fig. 4. Tuning procedure results for (a) voltage and (b) output power.

For the gain curve calculations, we used a 5-ns ramp to introduce the AK voltage into the computational domain. A 1-ns ramp was used to introduce the input power signal. This difference in ramp values allows the injected signal to fill the device prior to the onset of electron emission. Although we did not test whether this influenced the development of the electron behavior, it

seemed judicious based on experience. First, we demonstrated that the gain calculated using ICEPIC agreed with VSim, as shown in Fig. 5. Fig. 6 shows the gain curve calculations to date. The gain is referenced to an input power P_{in} that varies with the injection frequency over the range $457 \text{ kW} \leq P_{in} \leq 465 \text{ kW}$. The gain for each frequency is thus referenced to the injected power for that given frequency. All calculations presented in this chart used an applied magnetic field value of 1300 G. The gain is not nearly as flat with respect to frequency as VSim calculations indicated, yet it does have essentially the correct maximum value. For future work, the ICEPIC model has, through the multiple corrective iterations described above, compared well with both experimental data and VSim calculations. It is at this point that calculations of the effect on gain of modulation of the electron emission should begin. Calculations of this nature would likely show paths forward for improving the gain characteristics of the tube.

While the simulations above have focused on crossed-field physics in a vacuum with a emission from the cathode, Purdue has focused its theory in FY24 to conditions involving bipolar flow (simultaneous emission of ions from the anode in addition to electrons from the cathode) to increase the maximum permissible current in the gap and collisions in the gap, which can arise due to imperfect vacuum or electrode erosion.

While prior studies had examined the impact of emitting ions from the anode on the maximum current permissible in a one-dimensional crossed-field gap, no detailed assessment of the implications of extending to two-dimensions, as described in our FY23 report for crossed-field gaps both above and below the Hull cutoff, has been carried out. Thus, we assessed 2D bipolar flow using XOOPIC. Specifically, we investigated focused ion beams targeted at the expected location where the initial virtual cathode is expected to form. We considered a diode with gap distance $D = 0.00216 \text{ m}$ and width $W = 8D$ with particles emitted along the differing

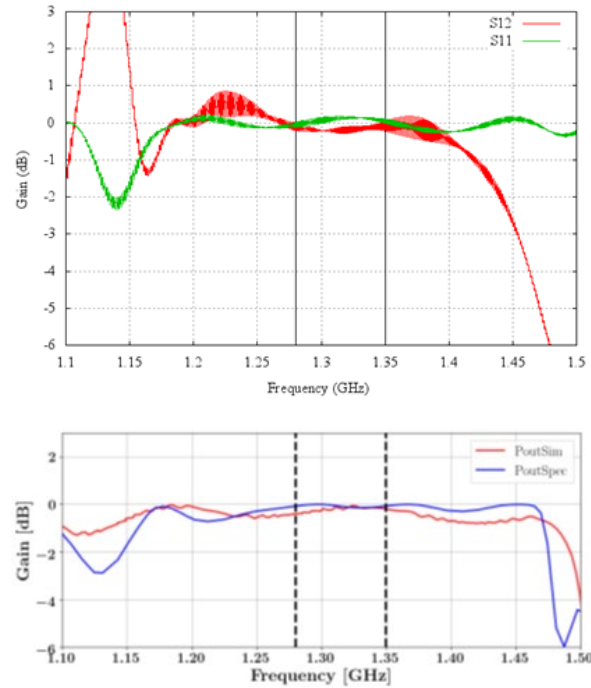


Fig. 5. Demonstration of the agreement of gain calculated using (top) ICEPIC and (bottom) VSim.

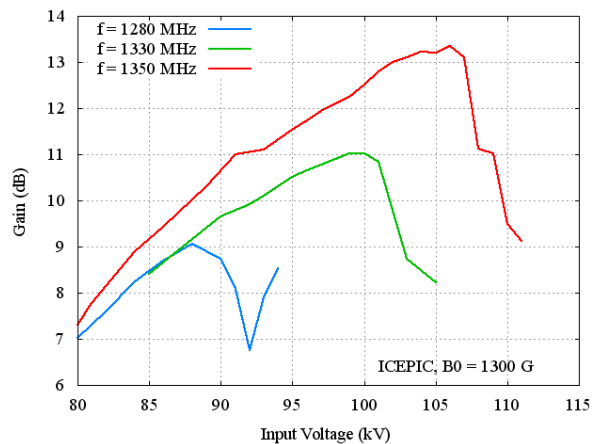


Fig. 6. L-4953 gain for three different frequencies within the operating band as determined from ICEPIC calculations (applied magnetic field value was 1300 G).

fractions of this length. A uniform static magnetic field $B = 1.57B_{H,e} = 0.27$ T and anode-cathode voltage of 12 kV were used, based on the U. S. Navy's Aegis CFA.

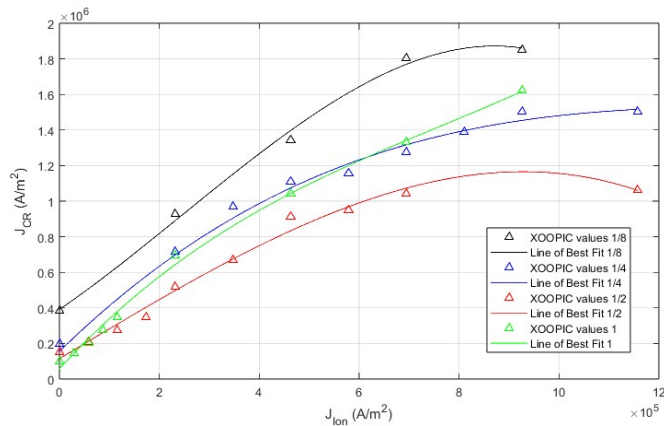


Fig. 7. Critical current J_{CR} as a function of ion emission current J_{ion} for different geometries. The accuracy of each of these critical current values is within 100 A. The electrons were injected with a kinetic energy of 0.5 eV; the H^+ ions were injected with a kinetic energy of 9000 eV to achieve the same initial velocity as the electrons. The diode had gap distance $D = 0.00216$ m and width $W = 8D$ with particles emitted along the differing fractions of this length. A uniform static magnetic field $B = 1.57B_{H,e} = 0.27$ T and anode-cathode voltage of 12 kV were used.

Fig. 7 shows that the critical current increases to a point before plateauing, just like aimed beams. Thus, it appears that targeted beams are optimal for achieving more efficient but smaller increases; however, thinner beams cause the plateau to occur for a lower ion current. For example, an electron emitter with a width 4 times the gap distance and an aimed beam of width 2 times the gap distance will achieve the same SCLC with half the current at a SCLC of 1800 A for both. However, we can achieve a SCLC of 3000 A with a 1500 A parallel beam, but we cannot accomplish this SCLC with any targeted half width beam. The logical extension from here is to aim beams of equal width and investigate the impact of such beams. This work will need to be extended using other grant opportunities in the future.

In the sections above, we assessed the electron trajectories and the transition to turbulence for vacuum crossed-field gaps. Even with magnetic field $B > B_H$, where B_H is the Hull cutoff magnetic field for magnetic insulation, crossed-field devices can undergo gap closure, where electrons emitted from the cathode reach the anode despite the diode technically being magnetically insulated. Previous theories and simulations showed that introducing ions at any location in a crossed-field gap always increased the electrons' excursions toward the anode and that the transit time decreased with increasing pressure. Introducing collision frequency ν as a friction term in the electron force law in a crossed-field gap eliminated magnetic insulation and the resulting trajectories, which neglected space-charge, resembled those from the misaligned crossed-field gap, which also introduced loops in the velocity/position phase space.

Introducing collisions into a nonmagnetic diode changes the limiting current allowed as a function of collision and initial velocity, recovering vacuum limits as the collisions vanish and collisional limits (i.e., the Mott-Gurney law) for infinite collisions [19]. This section highlights the extension of these techniques to a crossed-field gap. We obtain the limiting current by incorporating the collisions into the electron force law as a friction term dependent on the collision frequency ν .

Because the cyclotron frequency Ω is our time scale, $\bar{\nu} < 1$ corresponds to $\nu < \Omega$, meaning that the magnetic field dominates over collisions, and $\bar{\nu} > 1$ corresponds to collisions dominating over magnetic field. Fig. 7 shows \bar{J}_c/\bar{J}_g as a function of B/B_H for various $\bar{\nu}_0$ for four different $\bar{\nu}$.

However, increasing $\bar{\nu}$ reduces the impact of \bar{v}_0 on \bar{J}_c/\bar{J}_g , most likely because this causes the electrons to travel more directly across the gap such that collisions dominate the limiting current rather than trajectory curvature induced by the magnetic field. Fig. 8(a) show that \bar{J}_c/\bar{J}_g decreases more rapidly with increasing \bar{v}_0 at relatively low collisionality, respectively. Fig. 8(b) shows that the change in \bar{J}_c/\bar{J}_g with increasing \bar{v}_0 decreases with increasing collisionality. For $\bar{\nu} = 5$, \bar{v}_0 has no effect on \bar{J}_c/\bar{J}_g .

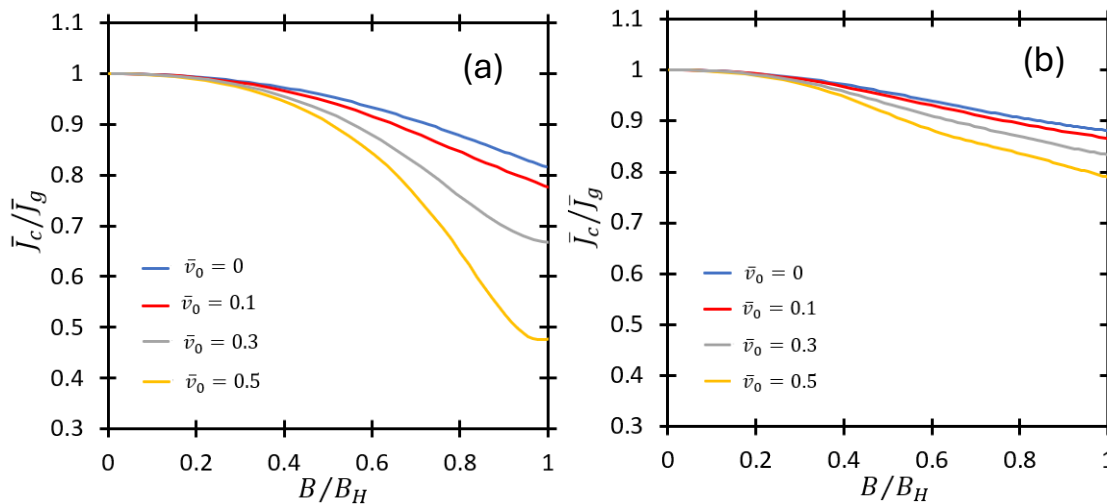


Fig. 8. Nondimensional limiting current \bar{J}_c normalized to the general space-charge limited current \bar{J}_g with injection velocity as a function of the magnetic field B scaled to the Hull cutoff B_H for various injection velocities \bar{v}_0 and collision frequencies of (a) $\bar{\nu} = 1$ and (b) $\bar{\nu} = 2$.

Working with Tech-X, the developer of VSim and a subcontractor on this effort, we used VSim to extend Purdue's other DoD-funded efforts assessing the space-charge limited current for nonplanar and multidimensional diodes to include nonzero initial velocity, which correlates to thermal emission. incorporating nonzero initial velocity means that the virtual cathode no longer corresponds with the cathode. Instead, it appears between the cathode and anode. Moreover, a new limiting current is introduced that corresponds to the electrons having zero initial velocity at the virtual cathode, akin to the condition of the classical Child-Langmuir law. This condition is often referred to as the bifurcation current density J_B , which is less than the Child-Langmuir limit of J_{CL} . This limit is important because it introduces hysteresis into the operation of the diode. Initially, raising the emission current raises the current that reaches the anode; however, increasing the current J_{CL} no longer yields more collected current. Moreover, one cannot simply reduce the current to return to this linear regime. Instead, one must reduce the current to or below J_B to return to J_{CL} . Tech-X demonstrated this bifurcation and hysteresis behavior using VSim in Fig. 9. Purdue has extended these calculations to nonplanar diodes in one-dimension. Purdue is also leveraging these efforts by Tech-X to extend the calculations to multiple dimensions, as well as leveraging the work described above using XOOPIC. These results have clear applications to thermionic emitters for high-power microwave devices, but also to thermionic energy converters.

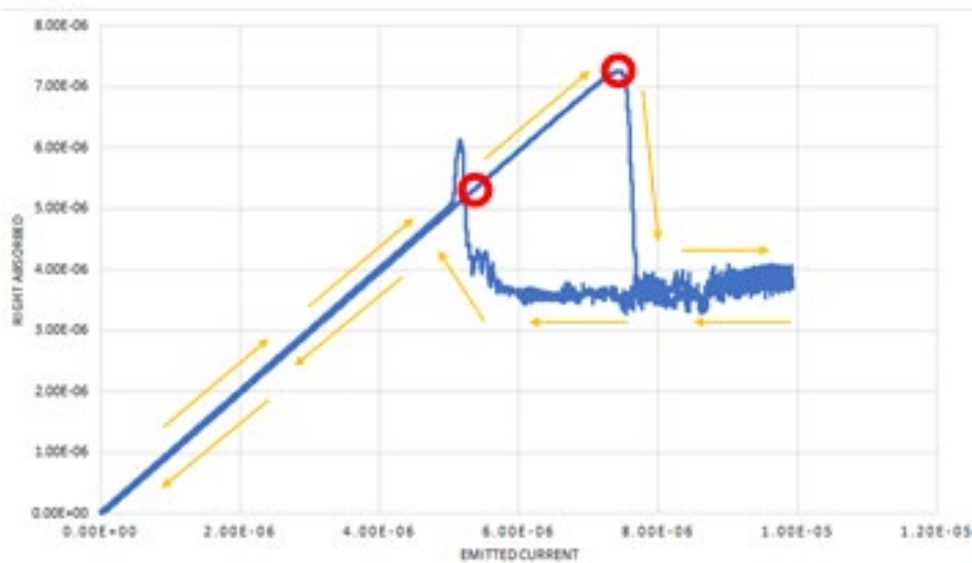


Fig. 9. VSim results of absorbed current as a function of emitted current. The two values are equal up to the space-charge limited current (SCLC), where exceeding the current results in a decrease in absorbed current. Emitting more current fails to appreciably increase the absorbed current and results in oscillations due to the virtual cathode. Increasing the absorbed current requires decreasing the emitted current until reaching the bifurcation current density, at which point the current may be increased to the SCLC.

3. Findings and Conclusions

Since this is the final year of the effort, we will first summarize the efforts during FY24 before briefly summarizing key accomplishments over the entire grant. Boise State's (BSU's) major contribution in FY-24 was the development of spatial-temporal and spatial-spectral visualizations to analyze noise. While this was critical for assessing CFAs, it provides a useful approach and tool for examining other high-power microwave (HPM) devices. For re-entrant CFAs, BSU demonstrated spoke wobble caused by 360° transit and spurious emission (sidebands) caused by spoke oscillations. For the U.S. Navy and Marine Corps, this capability would provide flexibility for simulating CFA performance under nonstandard operating conditions to extend the application window before performing experiments to confirm. Moreover, BSU developed spatial-tonal visualizations that showed that spoke oscillations only coupled to the output if the phase was equal in each spoke. Over the entire grant, BSU accurately predicted operating voltages using VSim within 3% of the Stellant systems L-4953 CFA and output power within 10% except for an outlier at 1.28 GHz. Thus, VSim could be used as a testbed for simulating modifications in CFA design. BSU also developed a new emission technique using a modulated end hat that improved end hat performance and showed that cathode offset matched the CFA performance.

In FY24, Confluent Sciences successfully benchmarked ICEPIC to VSim and experiment for the dispersion relation and both output voltage and power. This provides an important confirmation to BSU's VSim results and another tool, particularly for DoD users familiar with ICEPIC, which is an AFRL code.

In FY24, Purdue completed and published the exact analytic solution for the maximum current in a collisional crossed-field gap, which provides an important limit for practical devices that may

have an imperfect vacuum or for devices that may undergo electrode erosion, which introduces an imperfect vacuum. Purdue also began exploring bipolar flow in a two-dimensional crossed-field gap to increase the maximum current. Over the full effort, Purdue first applied “nexus theory” to a crossed-field diode (both magnetically insulated and non-insulated) to derive the conditions for the transitions between the limiting current, field emission, and thermal emission. They then derived the exact analytic solution and a semi-empirical model for limiting current based on over-injection for a nonmagnetic diode and compared to 2D OOPIC simulations as a first step to assessing crossed-field diodes. This enabled the derivation of the exact analytic solution and a semi-empirical model for limiting current based on over-injection and compared to 2D OOPIC simulations for 2D, non-magnetically insulated diodes. Finally, Purdue derived a semi-empirical model for limiting current and compared the results to 2D OOPIC simulations based on electron trajectories for 2D, magnetically insulated diodes. These final two efforts were published in FY24.

4. Plans and Upcoming Events

The effort has concluded. The team is currently completing manuscripts based on this grant. Purdue University is working on two manuscripts in collaboration with partners from this grant. One effort applies techniques developed under other DoD funded grants to derive the space-charge limited current for multiple dimensions to show the presence of “hot wings” in agreement with ICEPIC simulations from Confluent for a 2D cylindrical diode. This manuscript further shows the recovery of the 1D solution derived by Purdue rather than the traditional Langmuir-Blodgett as a limit of the 2D solution. This provides an important benchmark for PIC. The second manuscript, briefly alluded to above, addresses thermionic emission and benchmarks results from Purdue using OOPIC and from TechX using VSim. A final manuscript extends the concept of electron emission mechanisms for crossed-field diodes to incorporate collisions into an earlier paper funded under this grant that incorporated thermionic and field emission.

Also, from discussions with Stellant Systems, we discovered that NSWC Crane has a working 15 MW variation of the L-4953 CFA. BSU has received operational data for the CFAs that Stellant built for NSWC Crane. Dr. Garner, the PI from Purdue, is participating in a separate DoD funded effort that is managed through NSWC Crane and is working to set up a seminar there. This could provide an additional opportunity for collaboration.

5. Transitions and Impacts

None.

6. Recommendations for Future Work:

We have modeled spurious emission in a CFA and located the oscillations within the spoke that cause spurious emission. The new visualization capabilities offer a way to characterize the noise in more detail to develop a theory of spurious emission. While the L-4953 CFA model was validated against specification, spectral data for stable and unstable operating conditions is required. Future work could include collaborating with NSWC Crane, which has a working 15 MW variation of the L-4953 CFA. NSWC Crane could provide CFA spectra for various voltages, magnetic fields, and input powers that could be used to assess the simulation’s ability to accurately model the spurious emission physics. A validated model would provide a way to develop and validate theory of spurious emission formation.

Preliminary results also show reduced noise with modulated emission from the end hats (EHs), which allow steady output at lower RF input powers to improve the gain. Characterizing this improvement requires a huge amount of data because of the large and sensitive parameter space: voltage, magnetic field, input power, EH emission phase, and EH emission profile. EH emission also provides an additional way to study electron-RF interaction physics. EH emission can be used to inject noise, counteract noise, or to couple to specific RF modes in the device during operation. An additional benefit is that EH emission can be implemented experimentally to further validate theory and simulation.

An unexplored avenue during our effort was the possibility of coaxing higher power out of the L-4953. While the gain curve (Fig. 5) limits the device's output, it might be possible to increase the output power by modifying the device's interior. Padding the interior surface of the device with resistive material (e.g., Eccosorb) might dampen the reflections off the interior boundaries enough to permit operation with higher input power. The device already has a fairly low Q ($8 < Q < 30$), but that is all diffractive loss. Adding a slight resistive loss might open a pathway to working at higher power. Even moving the gain curve in Fig. 5 to the right would increase the output power. The change in electron dynamics due to change in voltage could likely be accommodated by a concomitant change in applied magnetic field strength. The overall result could provide a well-characterized power amplification capability for effects applications.

Finally, extensions of the theory developed during this effort could further inform the simulations and guide both system optimization and design when coupled with the particle-in-cell (PIC) codes used in this study.

7. Personnel

Principal Investigator			
Full Name	Approximate Level of Effort – LOE - (Hours This FY)	Country of Residence	National Academy Member? (Y/N)
Allen L. Garner	100	USA	N
Co-Investigator(s) or Co-PI(s)			
Full Name	Approximate Level of Effort – LOE - (Hours This FY)	Country of Residence	National Academy Member? (Y/N)
Jim Browning	100	USA	N
Jack Watrous	460	USA	N
Performer Business Contact(s)			
Full Name	Role	Country of Residence	
Brin Reed	Business Manager, Purdue Nuclear Engineering	USA	N
Priya Rajendran	Research Account Specialist, College of Engineering, Purdue	USA	N
Additional (Non-Student) Team Members			

Full Name	Approximate Level of Effort – LOE - (Hours This FY)	Country of Residence	National Academy Member? (Y/N)
Marcus Pearlman	400	USA	N
Subcontractors			
Full Name and Organization	Approximate Level of Effort – LOE - (Hours This FY)	Country of Residence	National Academy Member? (Y/N)
David Smithe	130	USA	N

8. Collaborations

Full Name	Organization	Collaboration Summary
John Luginsland	AFOSR	Technical Discussion
John Petillo	Leidos	We worked with him using MICHELLE to assess thermionic emission for nonplanar diodes. While that work was not useful for this grant, it will be valuable for one of our other DoD-funded efforts.
Vlad Podolsky	Avalanche	We discussed applications of crossed-field diodes for their fusion systems, which use thermionic emitters and crossed-field geometries. There may be future collaborations applying the techniques developed here for fusion studies.
Mike Worthington	Stellant Systems	Provided technical expertise and information concerning the L-4953 CFA.

9. Students

Doctoral Student(s)			
Full Name	University	Graduated?	Graduation Year
Xiaojun Zhu	Purdue University	Y	12/31/2023
Lorin Breen	Purdue University	N	
Nilesh Manker	Boise State University	N	
Masters Student(s)			
Full Name	University	Graduated?	Graduation Year
Jack Wright	Purdue University	Y	08/31/2024
Undergraduate Student(s)			
Full Name	University	Graduated?	Graduation Year
None			

10. Technology Transfer

We have had discussions with Dr. Andrew Fairbanks at NSWCDD concerning CFAs that they may have for future testing. Dr. Browning from BSU had discussions with Drs. John Luginsland and Brad Hoff from AFRL concerning the purchase of CFA through a DURIP for future research.

11. Products, Publications, Patents, License Agreements, etc.

Publications resulting from this project for the reporting period:

Archival Publications

#	Citation	Acknowledged ONR Support Received? (Y/N)	Peer Reviewed? (Y/N)
1	<u>L. I. Breen</u> ^G , K. L. Cartwright, A. M. Loveless, and A. L. Garner, "Limiting current in a collisional crossed-field gap," <i>Physics of Plasmas</i> 31 , 092108 (2024).	Y	Y
2	M. Pearlman, D. Smithe, M. Worthington, J. Watrous, A. L. Garner, and J. Browning, "Spoke Characterization in Re-Entrant Backward Wave Crossed-Field Amplifiers via Simulation," <i>IEEE Trans. Electron Devices</i> 71 , 5020-5027 (2024).	Y	Y
3	<u>X. Zhu</u> ^G , <u>J. K. Wright</u> ^G , <u>N. R. Sree Harsha</u> ^G , and A. L. Garner, "Critical current in a two-dimensional non-magnetically-insulated crossed-field gap with monoenergetic emission," <i>Physics of Plasmas</i> 31 , 072101 (2024).	Y	Y
4	<u>X. Zhu</u> ^G , <u>J. K. Wright</u> ^G , <u>N. R. Sree Harsha</u> ^G , J. Browning, and A. L. Garner, "Electron Trajectories and Critical Current in a Two-Dimensional Planar Magnetically Insulated Crossed-field Gap," <i>IEEE Access</i> 12 , 11378-11387 (2024).	Y	Y

Conference Papers

#	Citation	Acknowledged ONR Support Received? (Y/N)	Peer Reviewed? (Y/N)
1	M. Pearlman, J. Watrous, D. Smithe, M. Worthington, A. Garner, and J. Browning, "Simulation Analysis of Noise Generation in a Re-Entrant Crossed-Field Amplifier," 2024 IEEE International Vacuum Electronics Conference, Monterrey, CA, 23 April 2024, https://doi.org/10.1109/IVECIVESC60838.2024.10694825	Y	Y

Books

No Information to report.

Book Chapter

No Information to report.

Theses

#	Citation	Acknowledged ONR Support Received? (Y/N)	Peer Reviewed? (Y/N)
1	J. K. Wright, "Coordinate Invariant Calculations of Space-Charge Limited Current and Tumor Growth," Ph.D. Dissertation, School of Aeronautics and Astronautics, Purdue University, August 2024.	Y	N
2	N. R. Sree Harsha, "Calculating space-charge-limited current density in nonplanar and multi-dimensional diodes," Ph.D. Dissertation, School of Nuclear Engineering, Purdue University, May 2024.	Y	N
3	X. Zhu, "Modeling and Characterization of Solid-State and Vacuum High-Power Microwave Devices," Ph.D. Dissertation, Elmore Family School of Electrical and Computer Engineering, Purdue University, December 2023.	Y	N

Websites

No information to report.

Patents

No information to report.

Other Products:

#	Product Description	Acknowledged ONR Support Received? (Y/N)	Peer Reviewed? (Y/N)
1	<i>J. K. Wright</i> ^G , <i>X. Zhu</i> ^G , and A. L. Garner , "Limiting current in a two-dimensional crossed-field gap with bipolar flow," 2024 IEEE International Power Modulator and High Voltage Conference, Indianapolis, IN, 30 May 2024.	Y	N

12. Point of Contact in U.S. Navy / Marine Corps

<u>Navy Point(s) of Contact Student(s)</u>			
Full Name	Organization	Email	Date of Last Contact
Andrew Fairbanks	NSWCDD	N	08/14/2024
Zachary Drikas	NRL	N	12/13/2023

Surface Breakdown and Plasma Formation in Cross-Field High Power Microwave Sources

Grant No. N00014-21-1-2698

Annual Report for Fiscal Year 2024

Period of Performance: October 1, 2023 to June 1, 2024

Prepared by:

Professor Ken Hara, Principal Investigator
Assistant Professor, Department of Aeronautics and Astronautics
Stanford University
DURAND 252
Stanford, CA 94305
Tel: (650) 725-6309
Email: kenhara@stanford.edu



This work was sponsored by the Office of Naval Research (ONR), under grant/contract number N00014-21-1-2698. The views and conclusions contained herein are those of the authors only and should not be interpreted as representing those of ONR, the U.S. Navy or the U.S. Government.

Section I: Project Summary

1. Overview of Project

Executive Summary:

In this annual report, we summarize the activities on the recently awarded ONR (YIP) grant “Surface breakdown and plasma formation in cross-field high power microwave sources” covering the period October 01, 2023 – June 1, 2024. During the three-year project, we have accomplished the proposed objectives listed below.

Objective:

The goal of this research project is to advance the understanding of surface breakdown and plasma formation in cross-field HPM devices. Specific research objectives include: (R-I) to develop and test electromagnetic plasma fluid and kinetic models; (R-II) to characterize the space charge limited sheath due to the plasma formation near explosive emission cathodes; and (R-III) to investigate the anode plasma formation and radiofrequency wave-driven surface breakdown mechanisms.

Naval Relevance:

Plasma dynamics in high power microwave (HPM) sources are considered a detriment to the operation of vacuum electronic devices (VED) to generate electromagnetic signals. The formation and existence of the plasma flows become more and more critical, particularly when operating the HPM sources at a high-frequency range, which is of great interest to the future of U.S. naval missions.

The research outcomes can help (i) address existing issues in the HPM sources developed and deployed by the U.S. Navy, and (ii) improve the optimization and design processes of the future HPM sources using the predictive modeling capabilities developed through this project. In addition, advancing the fundamental understanding of the interaction between plasma flows, electromagnetic waves, and plasma-immersed materials possesses further immense impacts to other DoD applications and missions, including space propulsion, fusion energy, space weather, aerodynamics, combustion, and material processing.

Introduction/Background:

While HPMs theoretically must operate in high vacuum conditions, outgassing can occur from materials due to available materials and operating conditions. This issue becomes more problematic for compact HPM devices because the volume-to-area ratio worsens, and the plasma-wall interactions greatly influence the electromagnetic wave properties. For instance, pulse shortening of the microwave output signal due to gap closure and lifetime of the device can highly depend on the charged particles¹. A self-consistent plasma simulation model is required to understand the power scaling of these devices as they operate at higher applied voltages up to a few hundred volts or megavolts.

¹ Hadas et al., *J. Appl. Phys.* 104, 064125 (2008); Rose et al., *Phys. Plasmas* 20, 034501 (2013)

2. Activities and Accomplishments

a. Plasma formation due to explosive emission in anode-cathode gaps

To study the plasma formation and expansion, a 1D particle-in-cell Monte Carlo collision (PIC-MCC) simulation model is developed, assuming that a thin neutral layer of gas forms near the cathode due to the surface flashover mechanism. Specifically, we investigate the effect of the outgassed neutral layer, collisions (electron-neutral, ion-neutral, and Coulomb collisions), and different waveforms on plasma formation and expansion. Coulomb collisions are included using the Langevin approach. The 1D PIC-MCC simulation includes a self-consistent Fowler-Nordheim field emission (FNFE) current² from the velvet cathode, which ionizes the outgassed neutral layer from the velvet material, forming plasma. The development of the model is aligned with R-I (development of a plasma model) and the study conducted using the PIC-MCC model is aligned with R-II (the investigation of cathode plasma formation).

We report the simulations assuming the following assumptions. Neutral layer³ is atomic hydrogen and 100 μm thick with density of $1.3 \times 10^{23} \text{ m}^{-3}$. Field enhancement parameter (β) is assumed to be 500⁴. It was observed from our simulation that FNFE cannot ignite plasma without the inclusion of a field enhancement factor (β) to account for micro-protrusions. The anode-cathode gap is 1 cm and we varied the cell size from 400 to 24000 for grid convergence. Voltage pulse has a 20 ns ramp up, 40 ns flat top at 600 kV, and 40 ns ramp down. While we have also changed the pulse waveform, the physics remains similar for the cathode plasma formation and expansion study, so we focus on this particular waveform.

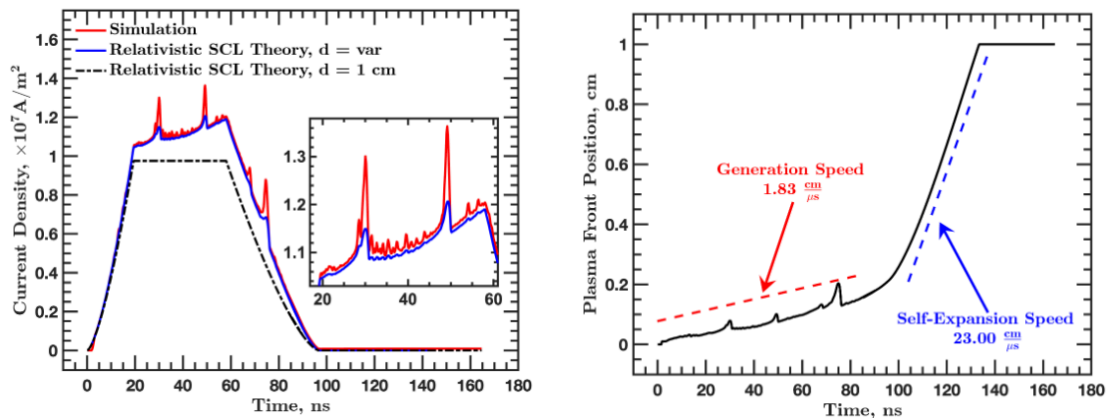


Figure 1. Cathode plasma formation and expansion: (a) Extracted current density; (b) Plasma front location, showing the plasma expansion speed.

In this reporting period, we have been refining the simulations for a peer-reviewed journal article. There are various output functions, post-processing functions, and code improvement implemented. Figure 1(a) shows that the net current extracted from the anode-cathode gap is in good agreement with the relativistic space charge limited (SCL) current theory⁵, when accounting

² Feng et al., Phys. Plasmas, 15, 043301 (2008)

³ Miller, J. Appl. Phys. 84, 3880–3889 (1998)

⁴ Kobayashi et al., Appl. Surf. Science 146, 148-151 (1999)

⁵ Greenwood et al., Physics of Plasmas 23, 072101 (2016)

for the fact that the effective anode-cathode gap is decreasing due to the plasma expansion near the cathode. The temporal change of the effective anode-cathode gap, shown in Fig. 1(b), is used to calculate the SCL theory in Fig. 1(a). The plasma expansion speed is comparable to the previous experimental observations⁶.

One of the interesting outputs is shown in Figure 2. The electron and ion velocity distribution functions (VDFs) are plotted for different time snapshots. As can be seen from Fig. 2(a)-(c), a quasineutral plasma whose bulk velocity is close to zero is formed near the cathode ($x = 0$) and there is a beam-like pattern observed for the extracted electron beam toward the anode ($x = 1$ cm). The ions on the other hand show some features of large-amplitude oscillations, as can be seen from the zoomed-up figures in Figs. 2(a2-c2). It can also be seen from the Figs. 2(a2-c2) that the expansion speed of the ions near the edge of the quasineutral plasma region is the same as that in Fig. 1(b), i.e., approximate 1-2 cm/ μ s. It can be considered that this plasma expansion speed is on the order of the ion acoustic speed. Figure 2(d)-(f) shows the results when the voltage pulsed is turned off. Here, the quasineutral plasma diffuses in both anode and cathode directions.

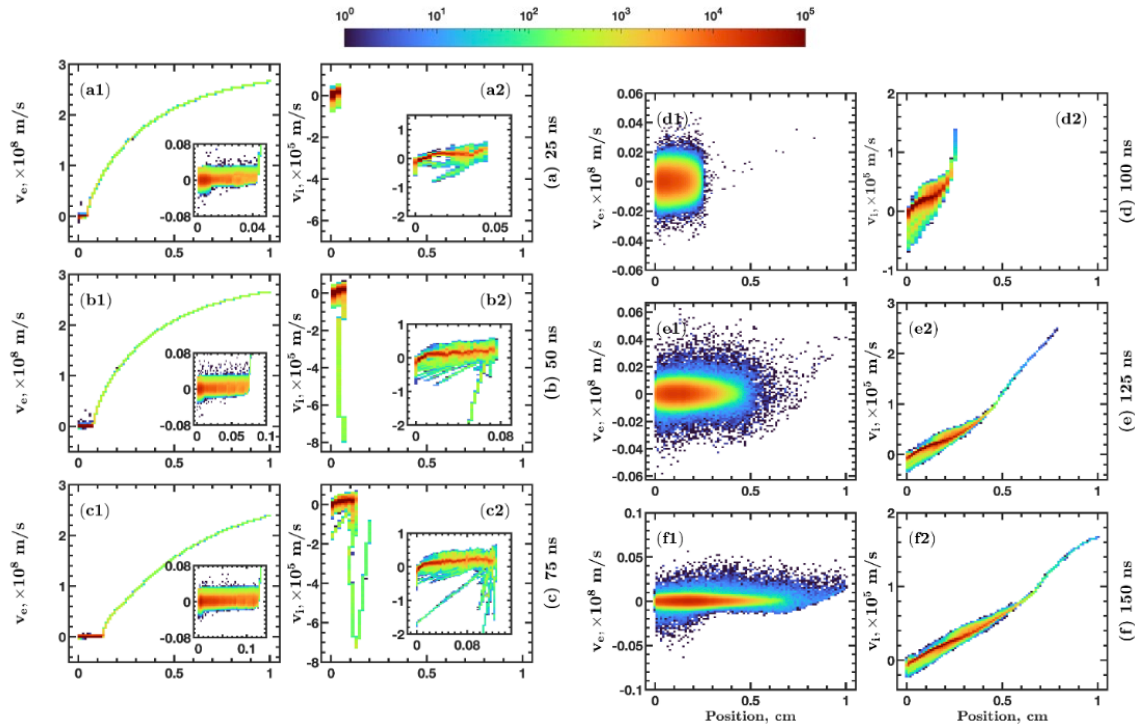


Figure 2: Electron velocity distribution functions (a1-f1) and ion velocity distribution functions (a2-f2) for different time of the anode cathode voltage pulse.

We also investigate the current spike instability, which has been well observed in experiments of high voltage, pulsed powered systems⁷. However, there have been limited simulation and

⁶ Friedman and Ury, *Rev. Sci. Instrum.* 43, 1659–1661 (1972)

⁷ Coleman and Howard, *Journal of Applied Physics* 135, 223302 (2024).

theoretical studies. From the present 1D PIC-MCC simulations, there have been cases where we observed plasma and current oscillations, as shown in Figure 3(a1-a3). It can be seen from Figures 3(a2-a3) that there is a clear local quasineutral plasma structure that is generated near the edge of the cathode plasma. Either from a physical or numerical oscillation, such current spikes can occur. Compared to Figure 1(a), it can be seen from Figure 3(b) that there are some moments during the pulse where a spike is observed, which is about 80-100% larger than the steady-state current extraction. The locally quasineutral plasma structure results in a burst of current toward the anode as electrons and toward the cathode as ions.

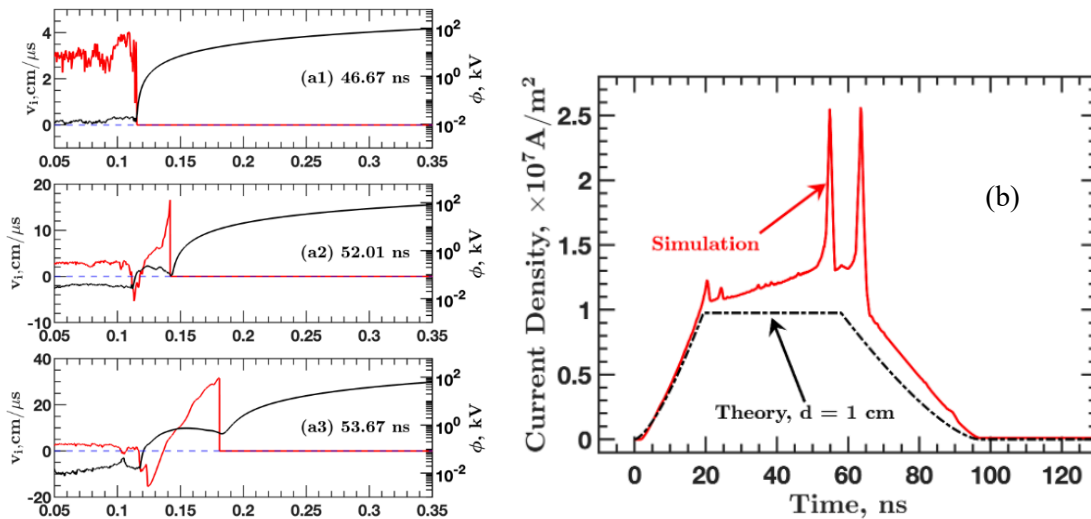


Figure 3. Current spike instability. (a1-a3) Snapshots of plasma profile before and during the first current spike around $t = 55$ ns. (b) (Left) Extracted current, showing two current spike instability.

The current spike instability shown in Figure 3 is modeled using the present 1D PIC-MCC simulation. However, it is worth noting that actual experiments are 2D or 3D in nature. For instance, there can be impurity or imperfection on the electrode surfaces and the plasma discharge may favor a different current path for least resistance. Hence, in the presence of a large current “arc” type discharge, there can be anode spots and cathode spots that may be dynamic. In addition, depending on the operation modes, anode and cathode surfaces are visually affected, such as discoloring, evaporation, sputtering, etc. In the case where 2D/3D plasma oscillations are slower than the formation of the current spike instability, we can speculate that the current spike instability is physical. Such high current operation may lead to increased ion current and energy flux at the cathode as well as increased electron current that can lead to anomalously high temperature which may chemically modify the anode surface characteristics. We are currently writing a journal article, summarizing the cathode plasma formation and expansion.

b. Anode plasma formation in anode-cathode gap

Anode plasma is formed due to the outgassing of the anode metal, e.g., hydrogen outgassing. When such outgassing occurs, it can be considered that the high-energy electrons when reaching the anode surface can ionize the gaseous particles (R-IIIa). Due to a quasineutral plasma formation near the anode, this also results in a decrease of the effective anode-cathode gap. Using

the same 1D PIC-MCC simulation, we included electron stimulated desorption and thermal desorption model proposed by Cuneo et al.⁸. The plasma injection current density (A/cm²) from the anode can be written as

$$j_{i,e} = -en_a v_{th} \exp\left(-\frac{Q_a}{RT_a}\right) - n_a j_e \sigma,$$

where n_a is the instantaneous surface coverage (10¹⁵ cm⁻²), j_e is the current density of incident electrons on anode, σ is the simulated desorption cross-section (10⁻¹⁸ cm²), v_{th} is the desorption rate (10¹³ s⁻¹), Q_a is the binding energy of adsorbate (23 kcal/mol), R is the universal gas constant (0.0019858 kcal/mol/K), and T_a is the anode temperature. Mike Cuneo's paper suggests second order desorption rates for hydrogen, i.e., hydrogen molecule.

Figure 4 shows a good agreement between the PIC-MCC results and the bipolar-relativistic SCL theory proposed by Langmuir⁹ and Choi et al.¹⁰ It is found from the simulation results that the electron stimulated desorption rate is orders of magnitude smaller than the thermal desorption rate, when the anode temperature exceeds 800 °C. We are currently writing a journal article about this model and physics.

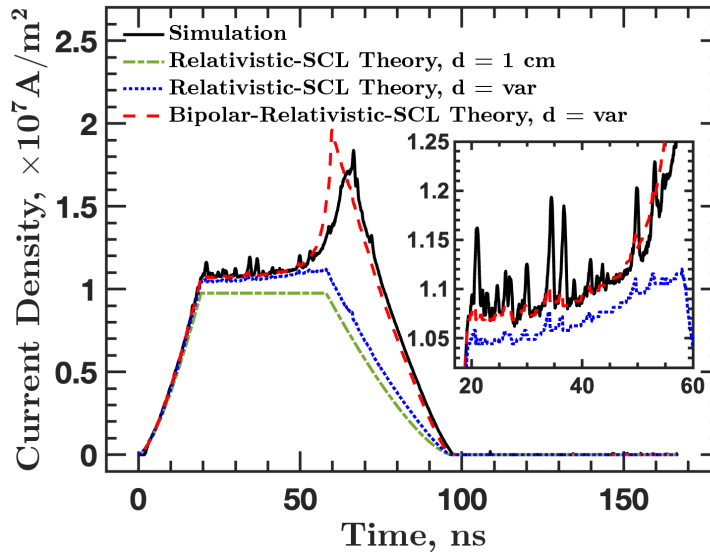


Figure 4. Increased current extraction can be seen from the simulation at $t > 60$ ns. The relativistic SCL theory (accounting for cathode plasma only) starts to deviate and the bipolar-relativistic SCL theory shows good agreement with the simulation result.

c. Hysteresis effects in DC breakdown

In conjunction with the plasma formation studies, we worked on DC and RF breakdown studies (R-IIIb). This work resulted in a study regarding the hysteresis between Townsend and glow discharges using an in-house PIC-MCC simulation code. This phenomenon has been studied and observed for centuries. The common understanding is that negative differential resistivity is

⁸ Cuneo et al., IEEE Transactions on Plasma Science 25, 229–251 (1997)

⁹ Langmuir, Physical Review 33, 954 (1929)

¹⁰ Choi et al. *J. Appl. Phys.* 61, 2160–2165 (1987)

leading to a hysteresis. However, there has not been a simulation activity that clearly shows how the transition between Townsend and glow discharges. What we did was to include a ballast resistor.

$$V_d = V_{app} - IR,$$

where V_d is the anode-cathode discharge voltage, V_{app} is the applied voltage, and I is the current, and R is the resistance of the ballast resistor. This work was accepted and published in Physics of Plasmas as an Editor's pick. This was a collaboration with Saravanapriyan Sriraman at Lam Research.¹¹

Figure 5(a) shows the concepts of gas breakdown (happening when the seed plasma density is small) and sustaining discharge (when the seed plasma density is large, or when the plasma already exists). Figure 5(b) is the self-sustaining discharge voltage, V_d , as a function of the current density that is normalized with pressure squared. When the applied discharge is increased from the breakdown condition, the plasma forms, which increases the discharge current and decreases the discharge voltage. The circuit resistance automatically serves to reduce the discharge voltage when current increases. It is interesting to note that when decreasing the applied voltage, now due to the presence of the plasma, the plasma does not extinguish at the breakdown voltage and can be self-sustained even at lower discharge voltage. Thus, this curve indicates that there is a hysteresis between the breakdown (Townsend discharge) and self-sustaining glow discharge.

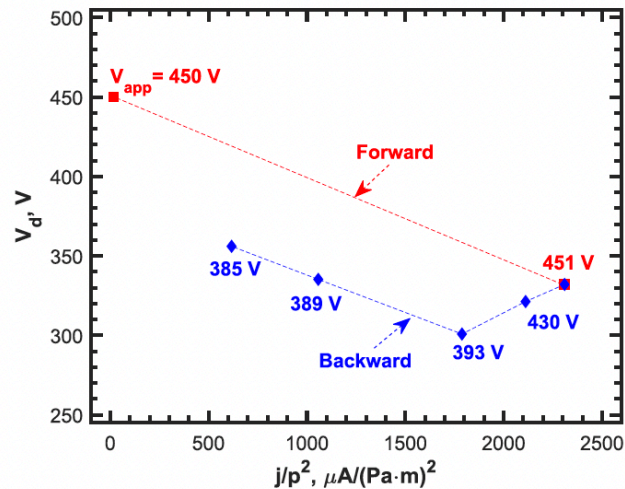


Figure 5: (left) breakdown with and without the plasma; (right) PIC-MCC simulation results of the forward and backward voltage sweep.

d. Fluid moment model development

We have developed several fluid moment approaches for plasma applications. Since the fluid models were developed from scratch for the first time, we have spent some time in developing the

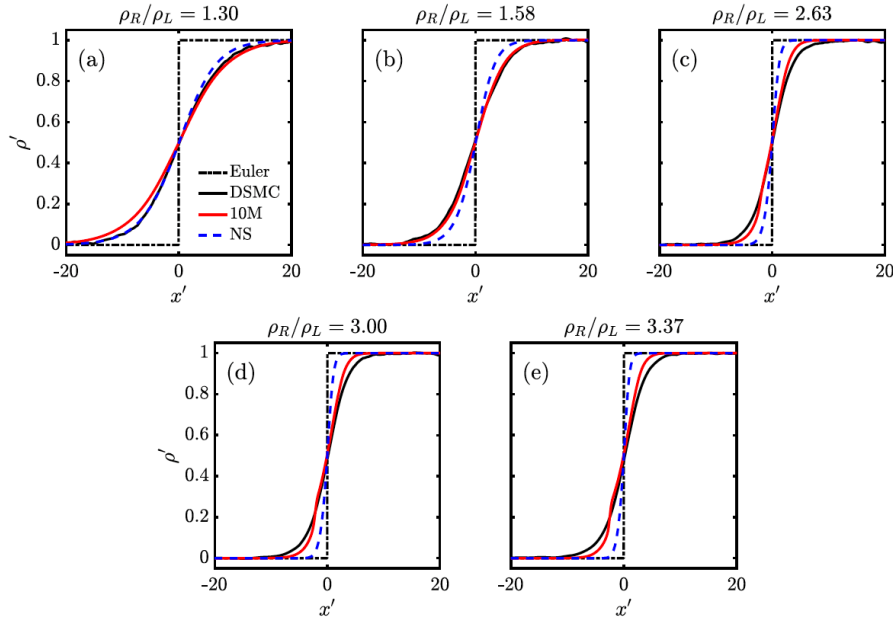
¹¹ Yamashita, Hara, and Sriraman, Physics of Plasmas 31, 073510 (2024)

numerical schemes and test cases to show the utility of the fluid moment approaches. The basic idea for a fluid moment model is to obtain the fluid equations by taking the moments of the Boltzmann solver. For instance, 5-moment approaches solve the full conservation of mass, momentum, and energy¹²:

$$\begin{aligned}\frac{\partial \rho}{\partial t} + \nabla \cdot (\rho \vec{u}) &= S_c \\ \frac{\partial}{\partial t} (\rho \vec{u}) + \nabla \cdot (\rho \vec{u} \otimes \vec{u} + p \vec{I}) &= Z e n (\vec{E} + \vec{u} \times \vec{B}) + S_m \\ \frac{\partial}{\partial t} (\rho \epsilon) + \nabla \cdot \left[\rho \left(\epsilon + \frac{p}{\rho} \right) \vec{u} + \vec{q} \right] &= \vec{j} \cdot \vec{E} + S_\epsilon,\end{aligned}$$

where $\rho = mn$ is the mass density, m is the mass of the atom/molecule, n is the number density, \vec{u} is the bulk velocity, S_c is the source and sink of mass, p is the pressure, Z is the charge state, e is the elementary charge, \vec{E} is the electric field, \vec{B} is the magnetic field, S_m is the collisional drag, ϵ is the mean energy, \vec{q} is the heat flux, $\vec{j} = Zen\vec{u}$ is the current density, and S_ϵ is the energy source and sink due to collisions.

For the 10-moment approach, the 2nd moment equation considers the anisotropic pressure tensor instead of the mean energy, which is equivalent to taking the trace of the pressure tensor. We have developed the 10-moment model with the support of this ONR project, with the goal to apply such moment models for plasma formation in anode-cathode gaps. Figure 6 shows a normal shock test case where the 10-moment model shows better agreement with the direct simulation Monte Carlo (DSMC) results than the 5-moment Navier-Stokes equation.¹³ The 10-moment model is currently used for other applications, e.g., low-temperature magnetized plasmas and Weibel instability.



¹² Mansour, Vialetto, Yamashita, and Hara, Plasma Sources Science and Technology 33 115018 (2024)

¹³ Kuldinow, Yamashita, Mansour, and Hara, Journal of Computational Physics 508, 113030 (2024)

Figure 6: Steady state shock that satisfied the Rankine-Hugoniot equations for different incoming Mach numbers, which result in different density ratio between pre- and post-shock regions.

3. Findings and Conclusions

A high-fidelity PIC-MCC simulation including the ionization and collisional processes sheds light into the plasma formation and expansion in pulsed power systems. The electrons are emitted from the cathode and if simultaneously outgassing of neutral particles occurs from the surface, the outgassed particles can be ionized and form a quasineutral plasma.

The simulations revealed the physical mechanisms of the quasineutral plasma formation and expansion. A quasineutral plasma near the cathode forms a strong space charge effect that cancels the potential exerted between the anode and cathode, hence generating a plateau in the plasma potential that essentially traps the quasineutral plasma. The electrons in the quasineutral plasma are repelled from reaching the cathode due to the cathode sheath, and the ions only can reach the cathode. Assuming that the time rate change of the space charge in the quasineutral plasma is negligible, the current balance shows that the electron current toward the anode must equal the ion current toward the cathode. Now, if we consider that the ion current toward the cathode can be written as $en_0\sqrt{\frac{k_B T_e}{M_i}}$, where e is the elementary charge, n_0 is the plasma density, k_B is the Boltzmann constant, T_e is the electron temperature, m_i is the ion mass, the ionization rate must be equal to the ion loss rate, i.e., $\sqrt{\frac{k_B T_e}{M_i}} = k_{ion}(T_e)N\Delta$, where $k_{ion}(T_e)$ is the ionization rate coefficient, N is the neutral number density, and Δ is the spatial extent to which the neutral atoms exist. Using the number in the simulation, $N = 1.3 \times 10^{23} \text{ m}^{-3}$ and $\Delta = 0.1 \text{ mm}$, the electron temperature can be obtained to be on the order of a few electron-volts.

The development of high-order (five- and ten-moment) fluid models can have immense impact for the plasma studies, as particle-based kinetic models are usually much more computational expensive to run. If the fluid models work, this will significantly accelerate any plasma formation/expansion investigations in the future. Such findings can also be directly implemented in existing codes that are of interest to the DOD (e.g., Magic, ICEPIC, CST Studio).

The research outcomes can help (i) address existing issues in the HPM sources developed and deployed by the U.S. Navy, and (ii) improve the optimization and design processes of the future HPM sources using the predictive modeling capabilities developed through this project. In addition, advancing the fundamental understanding of the interaction between plasma flows, electromagnetic waves, and plasma-immersed materials possesses further immense impacts to other DoD applications and missions, including space propulsion, fusion energy, space weather, aerodynamics, combustion, and material processing.

4. Plans and Upcoming Events

While the present ONR project ended on June 30, 2024, we are still continuing this work. The PIC-MCC results for the cathode and anode plasma formation will be reported in peer-reviewed journals. One of the papers is now in the final phase of the preparation and we have started

writing the other anode plasma paper. The results will be presented in different plasma conferences, such as the IEEE ICOPS and APS DPP.

5. Transitions and Impacts

Graduate student Andy Castillo was selected as an intern at Sandia National Laboratories, where he worked on plasma global model for high-voltage power switches. The work supported by this ONR project also helped Andy Castillo win the Laboratory Residency Graduate Fellowship (LRGF) from Department of Energy, National Nuclear Security Administration. The key hypothesis of the LRGF project is that the shear flow instabilities lead to increased plasma expansion in the MITL gap, which is detrimental to the system. The current approach is to use a 1D magnetostatic PIC code to generate 1D profiles in relevant properties, such as charge and current density and the electric and magnetic fields. Linear stability analysis can be performed (informed by these profiles), and the susceptibility of the system to these instabilities can be determined for a wide range of parameters. The next step will involve a 2D magnetostatic or electromagnetic code to model the instability itself in an idealized configuration.

Work resulting from this ONR project is contributing to the research collaboration with Lam Research and Applied Materials to study physical processes in semiconductor manufacturing devices. In addition, PI is involved in collaborative projects with Sandia National Laboratories on gas breakdown. These collaborations have been successful leading to journal articles, conference presentations, and various invited talks.

6. Recommendations for Future Work:

Plasma formation study sheds light into the physical processes associated with plasma expansion that is one of the limiting factors in HPM devices. The numerical results that show good agreement with experimental observation is promising. The 1D model development has given us more confidence in the 2D development if resources are available. Throughout this ONR project, the model has been elevated to a level where it can be used to study emission physics in pulsed power systems in detail (cf. collaboration with Sandia).

The key recommendation from this project is to continue the theoretical and simulation activities on plasma formation and expansion. The existing simulation tools used for HPM design and characterization often do not capture the plasma formation and expansion, limiting their use for understanding the operation in the presence of anode and cathode plasmas. Considering that the HPMs will be more compact and higher power, the plasma formation is an essential problem for the future HPM devices. The developed plasma simulations can be coupled with more high-fidelity material simulation codes, e.g., molecular dynamics, to study the plasma-electrode coupling in more details.

7. Personnel

Principal Investigator			
Full Name	Approximate Level of Effort – LOE - (Hours This FY)	Country of Residence	National Academy Member? (Y/N)
Ken Hara	120 hours	USA	N
Additional (Non-Student) Team Members			

Full Name	Approximate Level of Effort – LOE - (Hours This FY)	Country of Residence	National Academy Member? (Y/N)
Yusuke Yamashita	480 hours	USA	N

8. Collaborations

Full Name	Organization	Collaboration Summary
Matthew Hopkins, Nicki Bennett	Sandia National Laboratories	Plasma formation in magnetically insulated transmission lines
Matthew Hopkins	Sandia National Laboratories	Plasma chemistry for high-voltage pulsed power switches
Saravanapriyan Sriraman	Lam Research	Plasma breakdown in DC and RF systems
Shahid Rauf, Jason Kenney, Kallol Bera	Applied Materials	Development of particle-in-cell Monte Carlo collision (PIC-MCC) simulations and fluid models
Sedina Tsikata	Georgia Institute of Technology	Low temperature magnetized plasma physics

9. Students

Doctoral Student(s)			
Full Name	University	Graduated?	Graduation Year
Adnan Mansour	Stanford University	N	12/31/2024
Andy Castillo	Stanford University	N	12/31/2025
Derek Kuldinow	Stanford University	N	12/31/2026
Vedanth Sharma	Stanford University	N	12/31/2027
Masters Student(s)			
Full Name	University	Graduated?	Graduation Year
Undergraduate Student(s) [Add Rows Below as Needed]			
Full Name	University	Graduated?	Graduation Year
Satoki Shimamune	University of Cambridge	N	5/30/2025

10. Technology Transfer

We discussed our research with Joe Schumer, Ian Rittersdorf, Alexander Vlasov, and Simon Cooke at NRL before the proposal. PI visited NRL in September 2022. We hope to continue the relationship. PI visited the Air Force Research Laboratory to visit the ICEPIC team in Albuquerque in 2021. PI has strong connection with AFRL in Edwards AFB (In-space propulsion branch), e.g. Christine Greve and David Bilyeu.

11. Products, Publications, Patents, License Agreements, etc.

Publications resulting from this project for the reporting period:

Archival Publications

#	Citation	Acknowledged ONR Support Received? (Y/N)	Peer Reviewed? (Y/N)
1	Y. Yamashita, K. Hara, and S. Sriraman, "Hysteresis between gas breakdown and plasma discharge", <i>Physics of Plasmas</i> (Special Issue: Plasma Sources for Advanced Semiconductor Applications) 31, 073510 (2024) [Editor's pick]	Y	Y
2	D. A. Kuldinow, Y. Yamashita, A. R. Mansour, and K. Hara, "Ten-Moment Fluid Model with Heat Flux Closure for Gasdynamic Flows", <i>Journal of Computational Physics</i> 508, 113030 (2024)	Y	Y
3	A. M. Castillo and K. Hara, "Loss cone effects and monotonic sheath conditions of a partially magnetized plasma sheath", <i>Physics of Plasmas</i> 31, 030701 (2024)	Y	Y
4	Y. Yamashita, R. Lau, and K. Hara, "Inertial and anisotropic pressure effects on cross-field electron transport in low-temperature magnetized plasmas", <i>Journal of Physics D: Applied Physics</i> (Special Issue: Emerging Leaders) 56, 384003 (2023)	Y	Y

Conference Papers

#	Citation	Acknowledged ONR Support Received? (Y/N)	Peer Reviewed? (Y/N)
1	A. M. Castillo, M. M. Hopkins, A. Lietz, and K. Hara, "Plasma chemistry modelling of SF6 replacement gas for high voltage switches", 76th Annual Gaseous Electronics Conference, Ann Arbor, MI, October 2023.	Y	N
2	A. R. Mansour, Y. Yamashita, and K. Hara, "Revisiting Paschen Theory for DC Breakdown", 76th Annual Gaseous Electronics Conference, Ann Arbor, MI, October 2023.	Y	N
3	D. A. Kuldinow Y. Yamashita, and K. Hara, "A 10-Moment Multi-Fluid Model for Low-Temperature Partially Magnetized Plasmas", 76th Annual Gaseous Electronics Conference, Ann Arbor, MI, October 2023.	Y	N
4	Y. Yamashita, K. Hara, and S. Sriraman, "One-dimensional and two-dimensional particle-based kinetic simulations of DC and RF gas breakdown",	Y	N

	76th Annual Gaseous Electronics Conference, Ann Arbor, MI, October 2023.		
5	V. Sharma, A. M. Castillo, Y. Yamashita, and K. Hara, "Modeling of plasma formation and expansion in a high-voltage anode-cathode gap", 65th Annual Meeting of the APS Division of Plasma Physics, Denver, CO, November 2023.	Y	N
6	K. Hara, A. R. Mansour, and S. Tsikata, "Gradient-drift instability in partially ionized, partially magnetized plasmas", 65th Annual Meeting of the APS Division of Plasma Physics, Denver, CO, November 2023.	Y	N
7	D. A. Kuldinow Y. Yamashita, and K. Hara, "A 10-moment multi-fluid model for partially ionized, partially magnetized plasmas", 65th Annual Meeting of the APS Division of Plasma Physics, Denver, CO, November 2023.	Y	N
8	A. R. Mansour, Y. Yamashita, and K. Hara, "Full-fluid Moment Modeling and Theory of DC Breakdown", 65th Annual Meeting of the APS Division of Plasma Physics, Denver, CO, November 2023.	Y	N
9	A. M. Castillo and K. Hara, "Monotonic sheath conditions of partially magnetized plasma sheaths", 65th Annual Meeting of the APS Division of Plasma Physics, Denver, CO, November 2023.	Y	N
10	A. R. Mansour, L. Vialetto, Y. Yamashita, and K. Hara, "Modified Theory and Fluid Modeling for DC Breakdown", 11th International Workshop on the Mechanisms of Vacuum Arcs (MeVArc), Tahoe City, CA, March 2024	Y	N
11	V. Sharma, A. M. Castillo, Y. Yamashita, and K. Hara, "Relativistic 1D PIC-MCC modeling and simulation of impedance collapse in high-voltage diodes," 11th International Workshop on the Mechanisms of Vacuum Arcs (MeVArc), Tahoe City, CA, March 2024	Y	N
12	D. A. Kuldinow, Y. Yamashita, and K. Hara, "Development of a 10-moment multi-fluid model for low temperature magnetized plasmas", 33rd Symposium on Rarefied Gas Dynamics, Gottingen, Germany, July 2024.	Y	N
13	K. Hara, Y. Yamashita, and S. Sriraman, "Computational modeling of hysteresis between Townsend and glow regimes", 77th Annual Gaseous Electronics Conference, San Diego, October 2024.	Y	N

14	V. Sharma, K. Bera, S. Rauf, and K. Hara, "Plasma dynamics of RF multi-trench hollow cathode discharge using hybrid plasma model", 77th Annual Gaseous Electronics Conference, San Diego, October 2024.	Y	N
15	V. Sharma, A. M. Castillo, Y. Yamashita, and K. Hara, "Impedance collapse in a high-voltage diode due to anode and cathode plasma formation and expansion", 77th Annual Gaseous Electronics Conference, San Diego, October 2024.	Y	N
16	A. R. Mansour, K. Hara, and Y. Jo, "RF Plasma Simulations using Full-Fluid Moment Model", 77th Annual Gaseous Electronics Conference, San Diego, October 2024. (poster)	Y	N
17	Y. Yamashita, V. Sharma, S. Sriraman, and K. Hara, "Particle-based kinetic simulations of dual-frequency RF breakdown", 77th Annual Gaseous Electronics Conference, San Diego, October 2024. (poster)	Y	N
18	A. R. Mansour and K. Hara, "Full-Fluid Moment Model for Gas Breakdown and Low Temperature, Partially Magnetized Plasmas", 77th Annual Gaseous Electronics Conference, San Diego, October 2024.	Y	N

Books

No information to report

Book Chapter

No information to report

Theses

A. R. Mansour, "*Fluid Moment Modeling for Low Temperature, Partially Magnetized Plasmas*" (Defended November 14, 2024)

Websites

No information to report

Patents

No information to report

Other Products:

No information to report

12. Point of Contact in U.S. Navy / Marine Corps

Full Name	Organization	Date of Last Contact
Joe Schumer	Naval Research Laboratory	11/2023
Ian Rittersdorf	Naval Research Laboratory	11/2023

High Power, High Frequency, Repetitively Pulsed Oscillators

Grant No. N00014-23-1-2143

Annual Report for Fiscal Year 2024

Period of Performance: October 1, 2023 to September 30, 2024

Prepared by:

Professor Nicholas Jordan, Principal Investigator
Associate Research Professor
University of Michigan Plasma Physics, Pulsed Power, and Microwave Lab
112 NAME Building
2600 Draper Dr.
Ann Arbor, MI 48109
Work: (734) 763-0213
Email: jordann@umich.edu

Co-Principal Investigator:

Ryan McBride,
University of Michigan
mcbrider@umich.edu,



This work was sponsored by the Office of Naval Research (ONR), under grant/contract number N00014-23-1-2143. The views and conclusions contained herein are those of the authors only and should not be interpreted as representing those of ONR, the U.S. Navy or the U.S. Government.

Section I: Project Summary

1. Overview of Project

Executive Summary:

We designed, simulated, manufactured, and tested an overmoded X-band MILO for operation at 8.5 GHz. This MILO was designed to operate in a higher-order mode, increasing the feature sizes within the device to avoid breakdown. In experiments, it produced ~1 MW at 8.1 GHz. Evidence of cathode misalignment and anode-cathode arcing was observed.

We investigated a Brillouin flow step discontinuity in particle-in-cell simulations using CST Microwave Studio. The Brillouin flow is a rectilinear, sheared electron fluid flow in a crossed electric and magnetic field, with zero flow velocity and zero electric field at the surface with which the flow is in contact. It is broadly considered as the equilibrium electron flow in high power crossed-field devices including the magnetron and relativistic magnetron, magnetic insulated line oscillator, and magnetically insulated transmission line. We analyzed Brillouin flow in two dimensions, in a cylindrical geometry where the anode radius changes abruptly at a single axial location while the cathode surface has a constant radius. Our simulation reveals that this change in the anode radius introduces novel bunching of the electrons within the Brillouin hub. This bunching occurs at low frequencies (~250 MHz) and is much more pronounced if the Brillouin flow is from the small gap region to the large gap region, than if the Brillouin flow is from the large gap region to the small gap region. These simulations provided new insight into the physical processes that initiate and sustain the bunching processes that are unique for a crossed-field diode, as compared with a non-magnetized diode.

We also conducted initial simulations of the MADCAP high power microwave source, and began laying the groundwork for experimental tests in year 3.

Objective:

Our goal is to address, via high power microwave (HPM) research, some of the critical problems facing Navy operations due to asymmetric electronic threats. We propose to develop an X-band (8-12 GHz) Magnetically Insulated Line Oscillator (MILO) driven by a 1.6 kJ, 25-30 Ohm, pulsed power source capable of producing highly-repeatable 20-400 kV, 100-200 ns voltage pulses with a 50 ns rise-time and flat-top voltage stability of $\pm 5\%$ at repetition rates of 1 Hz (10 Hz in burst fire operation).

Additionally, the analytic solution for Brillouin flow transitions even under the electrostatic, non-relativistic assumption is hardly explored. Careful analysis of this problem could elucidate the proper definition of the AK gap in the treatment of crossed-field flow. It is conventionally defined as the distance from the tip of the anode vanes to the edge of the cathode, but could also be considered as the distance to the back of the cavity, particularly as the vane tips narrow and the cavity width increases. This definition is critical to most efficiency calculations in crossed-field theory. We will investigate this problem through a combination of analytic theory and 2D/3D simulations. The MADCAP compact recirculating planar magnetron (RPM) source was developed and fabricated at AFRL, but was not exhaustively tested due to time and budget limitations. With our extensive experience designing and testing RPMs, UM is well suited to demonstrate and publish

the capabilities of this source. We will integrate the source with one of our existing pulsed power systems, characterize it, and publish the results.

Naval Relevance:

This X-band MILO research will extend Navy HPM capabilities to higher frequency and repetition rate, enabling a broader range of possible targets and system configurations.

Introduction/Background:

In a recent effort, funded by the Office of Naval Research, we successfully developed a dual-frequency harmonic magnetically insulated line oscillator (MILO) requiring only 10 kA for operation in L- and S-band, and a first-principles theory of MILO operation and insulation requirements. Building on this successful program, we will extend this design to X-band.

2. Activities and Accomplishments

X-band MILO

We designed an initial X-band MILO for operation at 10 GHz and ~10 kA at 300 kV. The dimensions of this initial design were small, and we were concerned it would suffer from severe plasma closure and arcing during the experiment. To increase the feature sizes, we focused on developing an Over-moded X-band MILO (OXMILO), which would operate around 8.5 GHz.

We initially developed a design targeting the HEM₁₁ mode, which proved to operate in a circular polarization (CP). We have now tweaked that design so that the MILO runs in a linearly polarized mode (LP). The geometry for both models is shown in the left side of Figure 1. The OXMILO can operate in either a TE₂₁-Vertical or TE₂₁-Horizontal mode, as shown in the right side of Figure 1.

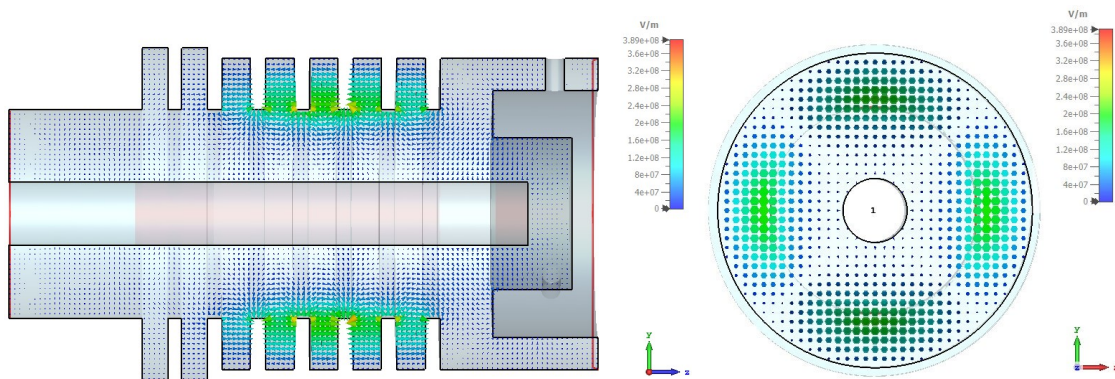


Figure 15: OXMILO eigenmode electric field pattern in a side-view (left) and front-view (right).

Using ANSYS HFSS, we designed a directional field adapter for the OXMILO (Figure 2), to couple the TM₀₁, HEM₁₁, and HEM₂₁ modes into waveguide to make calibrated power measurements. The electric field patterns within the device for each mode are shown in Figure 3 and Figure 4. Focusing on the bottom port (Port 1) as an example, we see that the TM₀₁, HEM₁₁-V, and HEM₂₁ modes successfully couple out, while HEM₁₁-H and HEM₂₁-45d (45 degree rotation) do not. This is confirmed by the S parameters, which indicate a 6 dB reduction for TM₀₁ and HEM₂₁ (which are divided among 4 waveguides), only a 4 dB reduction for HEM₁₁-V (which is divided between

two waveguides, and a 37-42 dB reduction for HEM11-H and HEM21-45d (which do not couple into the waveguides).

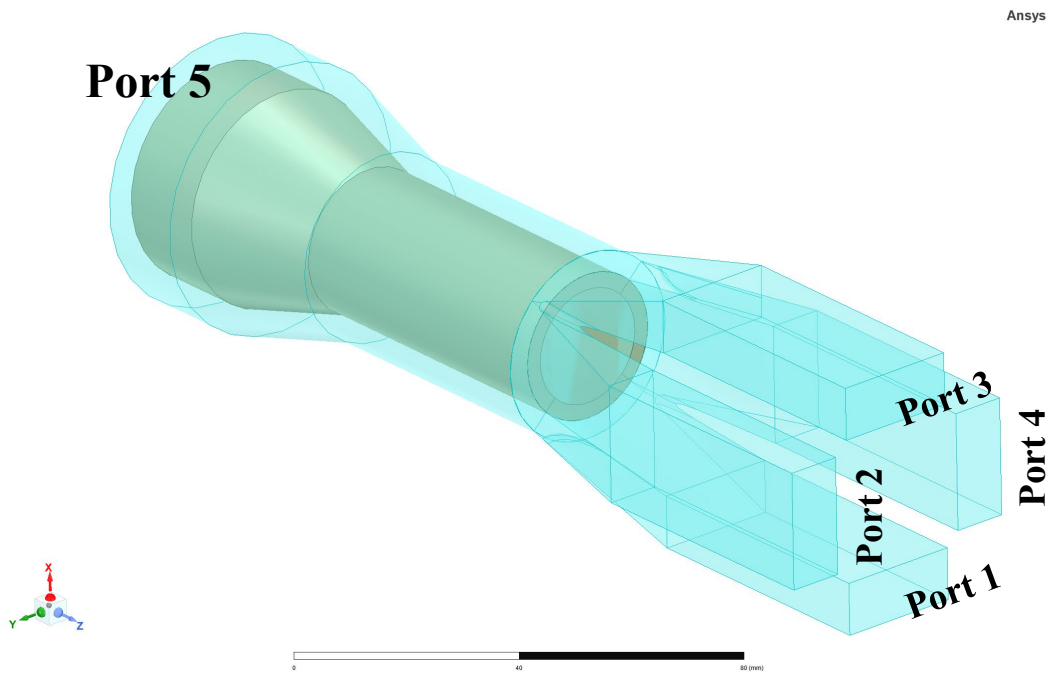


Figure 16: OXMILO directional field adapter (DFA), quad coaxial to WR90 with ports labeled.

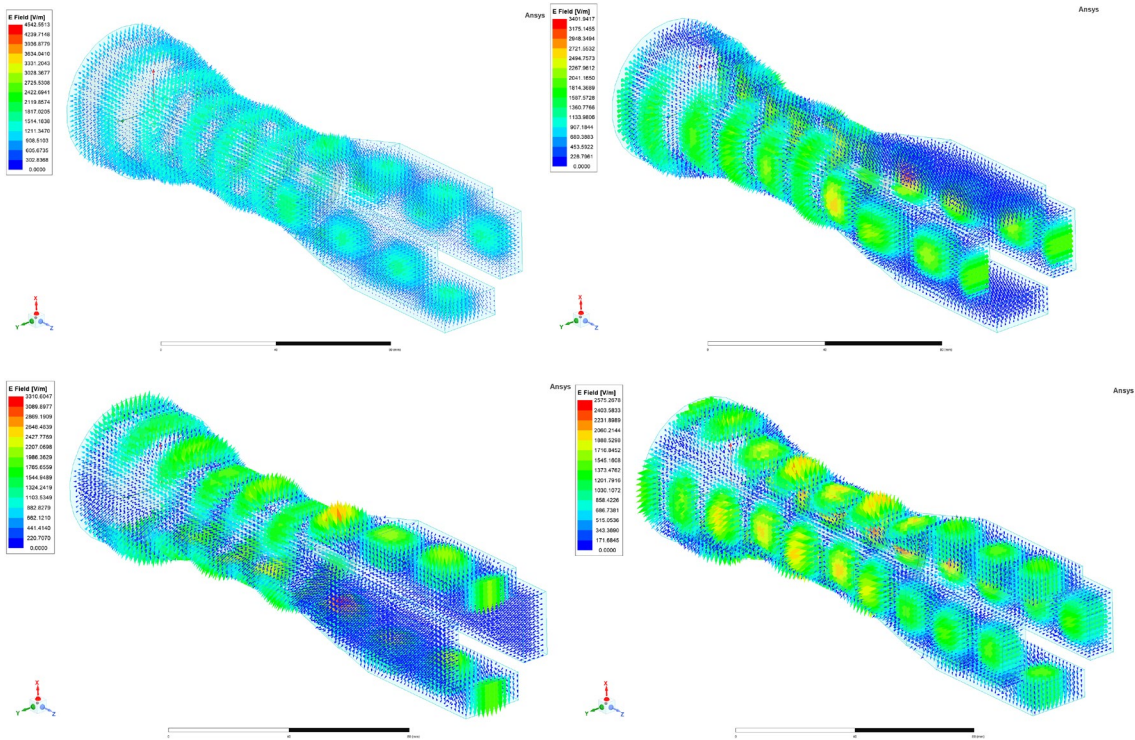


Figure 17: (top left) TM01/TEM01 Mode at 8.1 GHz; (top right) HEM11-H/TE11-H Mode at 8.6 GHz; (bottom left) HEM11-V/TE11-V Mode at 8.6 GHz; (bottom right) HEM21-HV/TE21-HV Mode at 9.6 GHz

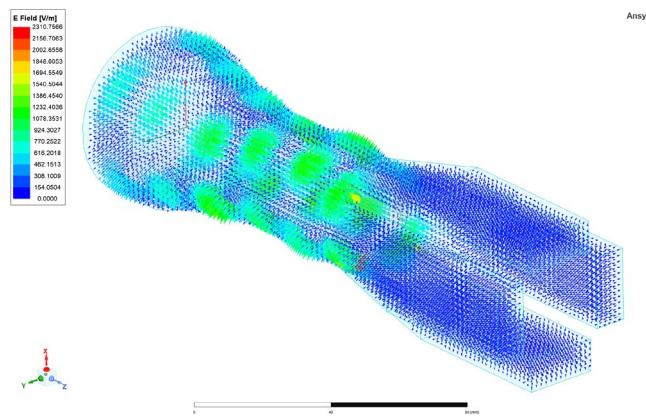


Figure 18: HEM21-45d/TE21-45d Mode at 9.6 GHz

Once the electromagnetic design of the output coupler was complete, the entire OXMILO (Figure 5) was sent out for machining. The coupler was very complex and had to be 3D printed, as it could not be conventionally machined.

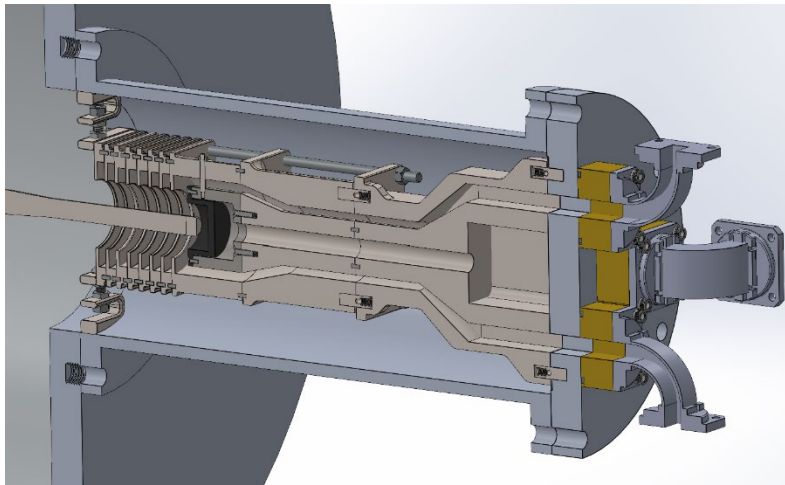


Figure 19: CAD model of OXMILO with extractor, vacuum windows, and waveguide. The downstream diode / beam dump is adjustable by replacing the graphite cup, shown in black.

With then completed the initial experiments with the OXMILO prototype. Power was measured from each of the four ports of the extractor using Schottky diodes with approximately 80 dB inline attenuation. The RF signal from port 1 was also fed into a 40 GS/s oscilloscope to obtain frequency information which could determine the mode of operation.

The first set of experiments used a velvet coated cathode, which arced due to a gap between the end of the cathode and sides of the beam dump of less than 5 mm.

The next experiment attempted to correct this error by using the bare aluminum cathode - increasing the gap on the sides of the cathode to 7.8 mm in the beam dump region. This improved the shape of the voltage pulse and brought the voltage close to 150 kV, shown, but no RF was observed in these experiments, and the tail of the pulse shows signs of an arc due to gap closure.

To further reduce arcing, the tip of the cathode which protrudes into the beam dump was reduced in diameter such that the gap between the cathode and walls was increased to 9 mm. This brought the Marx voltage to 160-180 kV and significantly increased pulse duration. RF output power was observed from ports 2 and 3 (left and top) totaling approximately 38 kW. Unfortunately, high attenuation on the port being fed into the fast oscilloscope prevented frequency data from being obtained for this dataset.

In the final set of experiments, the cathode diameter was further reduced, so that the cathode to wall gap was 10.5 mm. Inline attenuation was reduced and frequency data was obtained from port 3. Several shots resulted in RF only from ports 2 and 4, with powers ranging from 20 to 30 kW. These shots had a frequency between 8.4 and 8.5 GHz, which indicates the MILO was operating in the HEM_{11} mode - a hybrid mode analogous to TE_{11} mode in coaxial cable. Unlike with the previous configuration, several shots were obtained which saw greater than 1 MW of total power, with measured power on all 4 ports, which can be seen in Figure 6. These shots had frequencies from 8.05 to 8.15 GHz, which (along with non-zero power on all ports) is indicative of the fundamental TEM-like mode. In both modes, the RF was produced with the input voltage and current at approximately 180 kV and 4 kA, which suggests the device was not fully magnetically insulated. Nearly all of the power was measured on port 2, which was most likely due to uneven

emission on the bare cathode, and a subsequent inspection of the cathode revealed signs of arcing observed on the left side (where port 2 is located). The directional couplers used for ports 1 and 3 were also of a slot type, and may have suffered from RF breakdown.

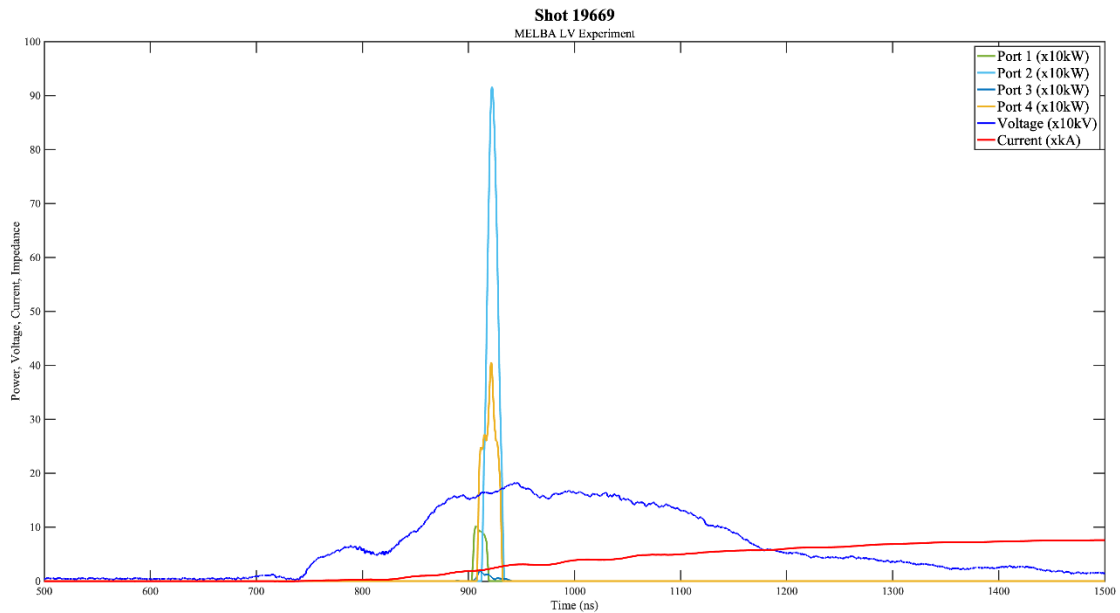


Figure 20: Using a reduced diameter cathode to achieve a 10.5-mm AK gap in the beam dump region improves peak power and emission uniformity with power measured in all ports, indicating operation in the HEM_{11} mode.

Brillouin Flow Discontinuity

We conducted a range of fundamental simulations of Brillouin flow, using CST Particle Studio (CST-PS). In these simulations, a step discontinuity was introduced in the anode, and steady-state electron motion was observed. We found that when the electron flow was from a region of small anode radius to large anode radius (left to right in Figure 7), periodic bunching of the electron flow would occur. This effect was not observed when the direction of electron flow was reversed.

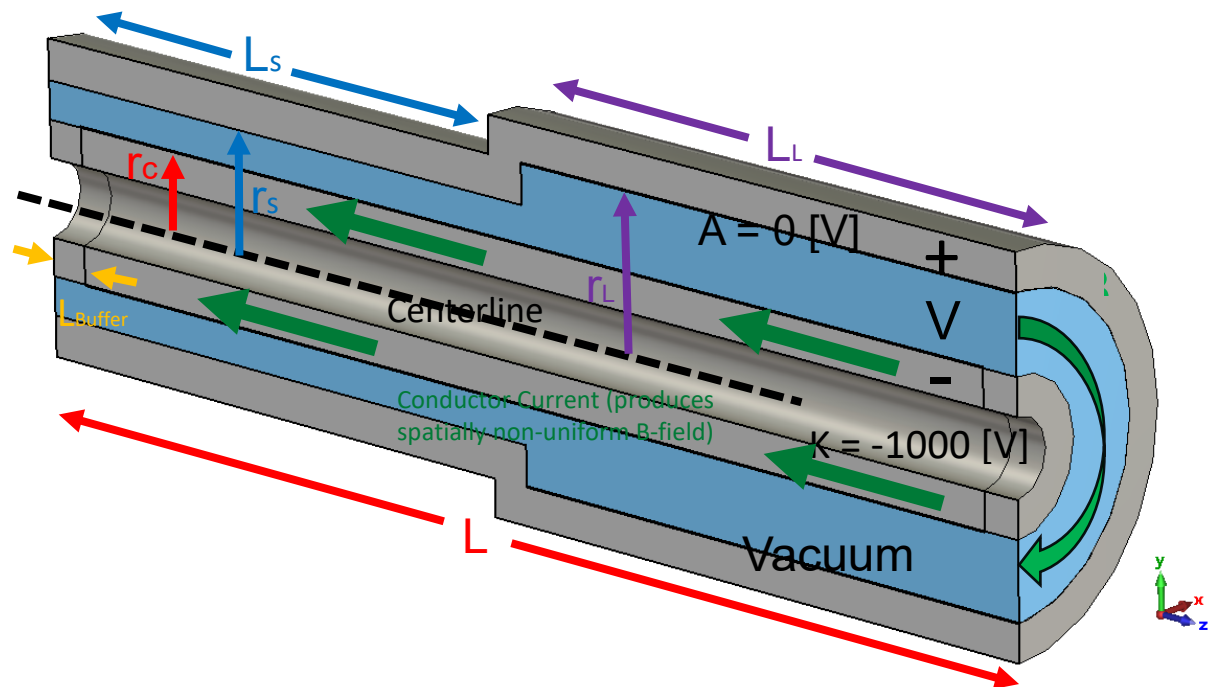


Figure 21: Model of the cylindrical step discontinuity simulation in CST-PS. Electrons are uniformly emitted across the cathode, and flow from left to right. A constant, spatially non-uniform magnetic field is applied.

The overall length of the cylinder, L , is 300 mm, with a cathode radius, r_c , of 20 mm, an anode radius, r_s , of 30 mm in the small gap region and 40 mm in the large gap region, r_L . The cathode explosively emits across its entire surface, with the exception of a 10 mm long buffer region on each end, at a threshold field of 100 V/m. Using the CST Magnetostatic solver and a 2.59 kA current drive on the cathode, a constant but spatially non-uniform magnetic field is calculated, and then applied to the CST-PS simulation. The length of the small and large anode radius sections, L_s and L_L , are identical and each equal to half the total length.

As noted in the previous report, we observe that an instability forms at the radial step discontinuity, and electron bunching occurs. This occurs because the average electron velocity in the small gap is greater than the average electron velocity in the large gap due to the difference in the electric field in the two gaps. In the nominal case, the electron beam in the small gap will overtake the slower electron beam in the large gap near the discontinuity resulting in the initial spatial bunching (seen in Figure 8b). The local increase in space charge near the discontinuity due to this bunching causes a distended virtual cathode to form within the gap (seen in Figure 9b). The virtual cathode is defined as the location where the total electric field is zero in the gap.

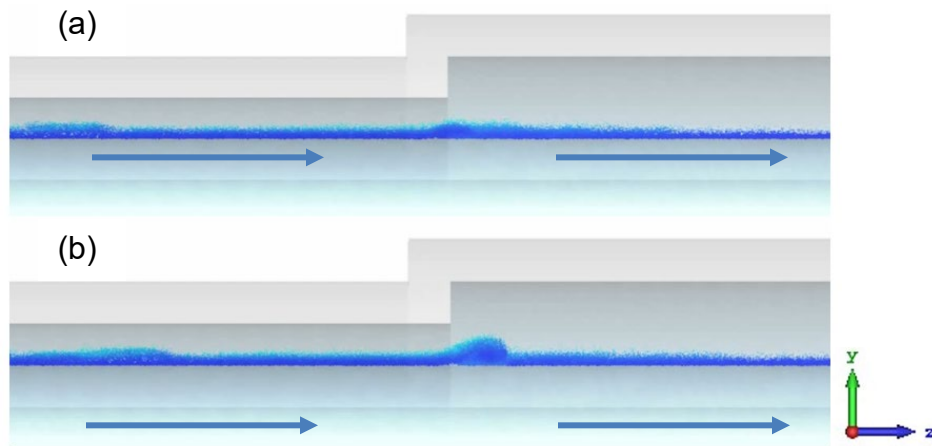


Figure 22: The electron beam is travelling in the $+z$ direction. The $E \times B$ velocity of the electron beam in the small gap is greater than the large gap electron beam $E \times B$ velocity which results in spatial bunching at the discontinuity seen by the particle monitor at (a) 6.5 ns where the initial electron bunching can be seen at the discontinuity and at (b) 7 ns where the initial bunch has developed, and a large virtual cathode has formed.

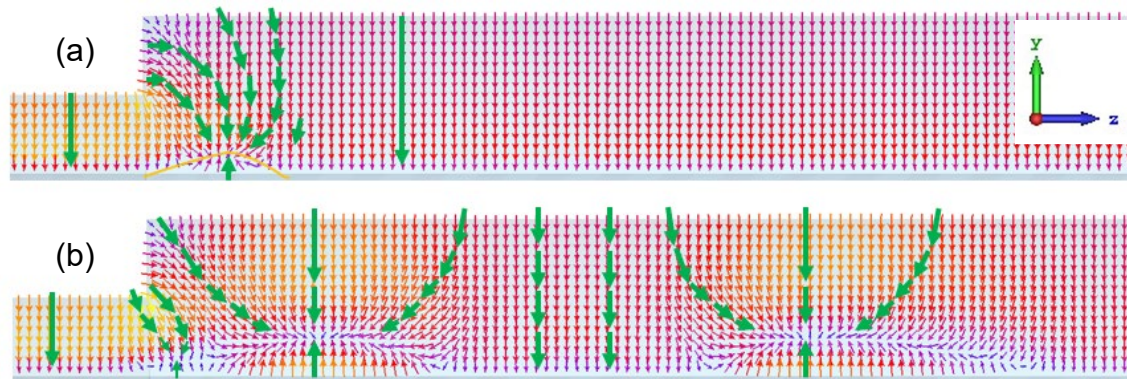


Figure 23: The electric fields in the gap near the discontinuity are depicted. (a) The electric field is altered by the spatial bunching and a large virtual cathode is formed where the initial bunch formed. Notably, the electric field changes direction below the virtual cathode, thus the $E \times B$ in that region would be in the $-z$ direction and vortical motion will occur around this virtual cathode. (b) Development of the virtual cathode when multiple bunches are present.

The vortex motion seen in these bunches is predicted by the Lorentz Force. When the large virtual cathode forms, the local electric field shape changes considerably as seen in Figure 9. The electric field lines point towards the virtual cathode which results in a curved electric field. From this new electric field shape, the motion of the electron beam depends on the position of the particle in the electric field and the velocity of the particle. Assuming an initial Brillouin Flow profile, the particle trajectories around the virtual cathode will be vortical and back-streaming; (electron flow in the $-z$ direction) is possible below the virtual cathode where the electric field now points in the $+y$ direction and the $E \times B$ direction is opposite to the equilibrium drift direction.

As the vortical electron bunch moves axially down the gap in the $+z$ direction, a portion of the electron bunch is back-streaming (moving in the $-z$ direction) and will eventually interact with the

downstream electron beam that is moving in the $+z$ direction, which is seen in Figure 10. The electron beam downstream of the electron bunch will begin to overtake the back-streaming electrons from the previous bunch and the local space charge will increase where the electron beam and the back-streaming electrons meet. This leads to the formation of another large virtual cathode seen in Figure 9. Another vortical electron bunch will form due to the existence of the large virtual cathode as stated earlier. Therefore, each bunch helps prime the subsequent bunch and the back-streaming electrons from each bunch impact the formation and dynamics of the next bunch. The large virtual cathode formed by the electron bunch also prevents electron emission and a reduction in electron density can be observed in the wake of the initial bunches (Figure 10) which results in discrete bunches.

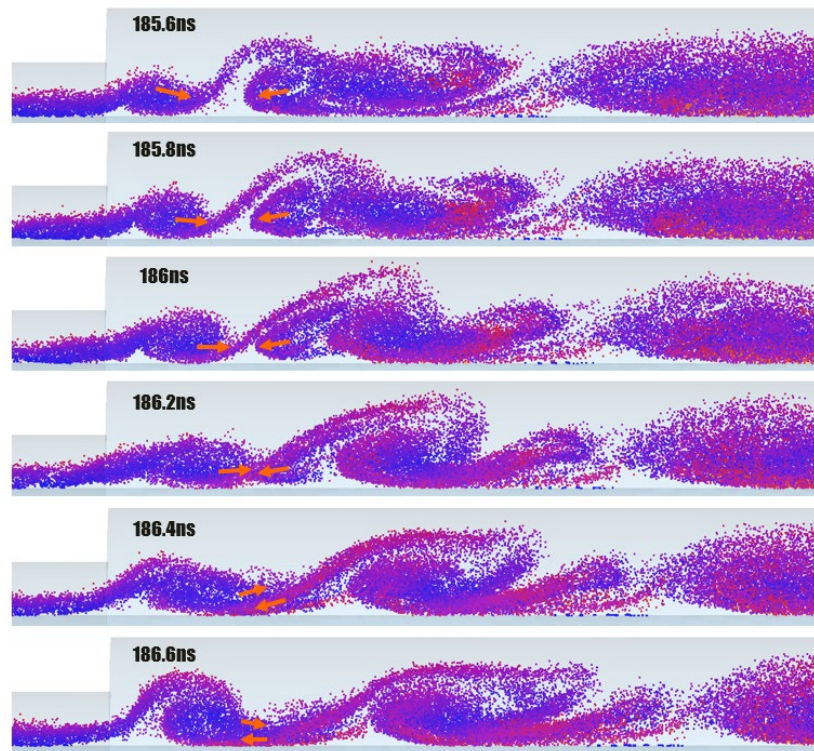
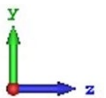


Figure 24: Particle monitors of the electron bunch formation and dynamics at steady state. An electron bunch further downstream ($+z$ direction) will impact the formation and dynamics of the subsequent electron bunch. The back-streaming ($-z$ direction) electrons interact with the electron beam from the small gap and an increase in local space charge is observed resulting in the formation of another electron bunch which interacts with the downstream bunch.



This work was published in PoP and selected as an Editor's Pick. Subsequently, we have found this geometry can be used to generate high power, broadband EM radiation, and have filed a provisional patent on the proposed device. A paper on this application is still in development.

The generation of vortices and virtual cathodes at the discontinuity promotes electron bunching with a variable frequency. In the model shown in Figure 11, we use a cathode radius of 7 mm, an initial anode radius of 22 mm, a large anode radius of 47 mm, and small/large gap lengths of 175 mm.

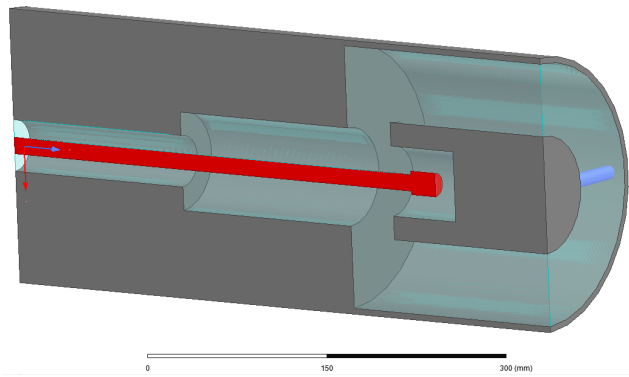


Figure 25: HFSS/CST model of noise generator with 1 steel quarter-wave stub, and 2 polyethylene stubs. Not shown in the coaxial extractor used for our previous L-band MILO experiments.

Applying a -300 kV voltage, bunches form as shown in Figure 12 and the simulated steady state current is ~10.5 kA. Repeated microwave pulses of 5-10 MW (Figure 13) are observed with broad frequency content ranging from 0.1-1.5 GHz (Figure 14).

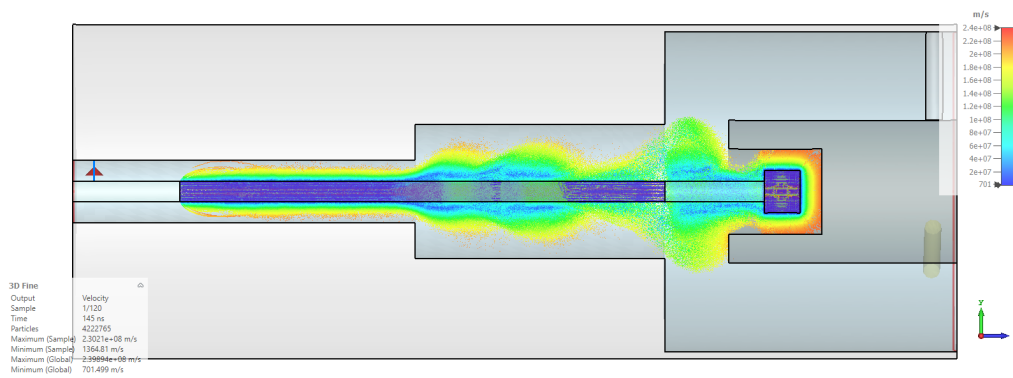


Figure 26: Particle monitor at t=145 ns for CST-PS simulations of the broadband noise generator, showing bunches and vortices forming downstream of the AK-gap discontinuity.

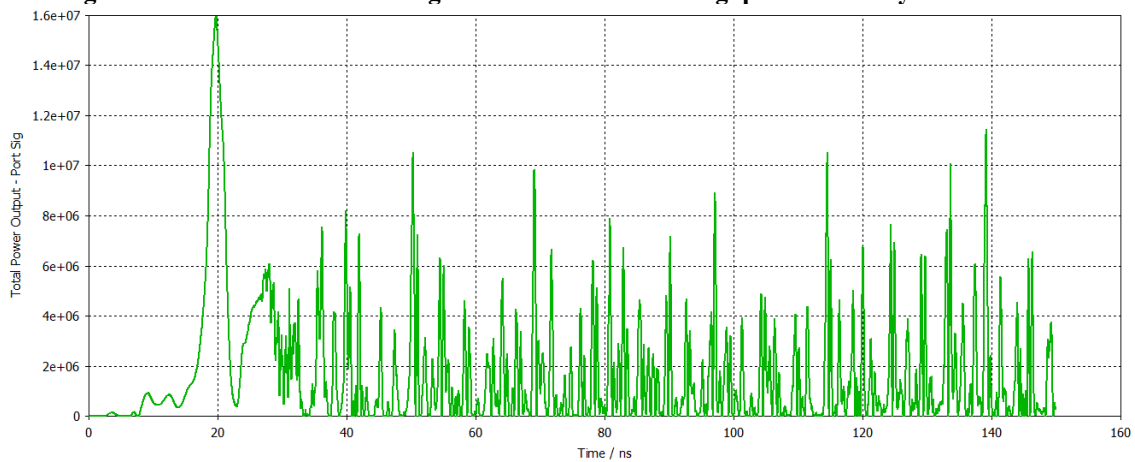


Figure 27: Total power output of broadband noise generator, showing continuous generation of 5-10 MW bursts

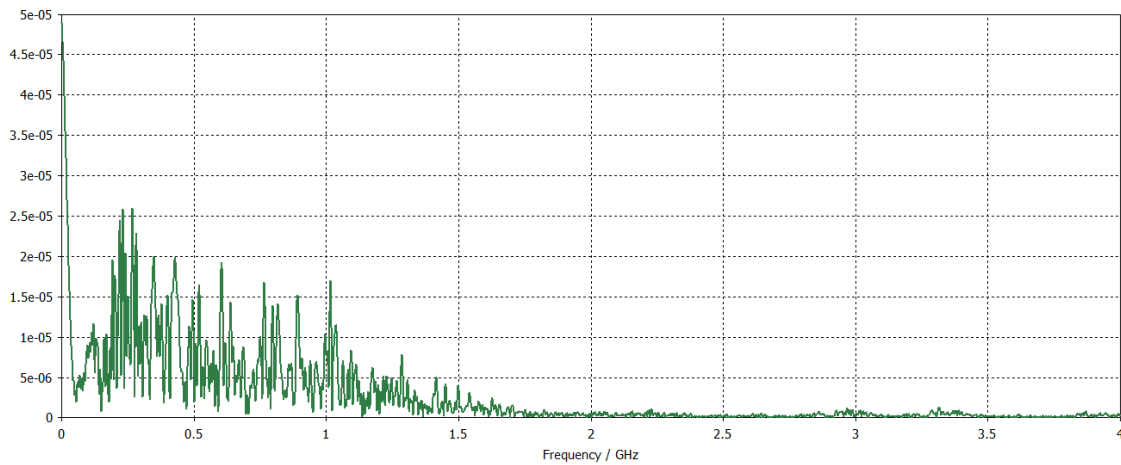


Figure 28: FFT of noise generator, showing broadband frequency content peaking at ~250 MHz. Higher frequency content may be present, but is not able to effectively couple out of the device.

Initial experimental tests of this device were unsuccessful due to issues with the pulsed power driver, but those issues have been resolved and subsequent experiments will be conducted soon.

REP Pulser

Collins Clark visited our lab in late October 2023, and with his help we were able to identify the issues with the REP pulser. These issues were addressed and testing resumed. We established a switch pressure curve for REP (Figure 15), based on the current gas mix and conditions.

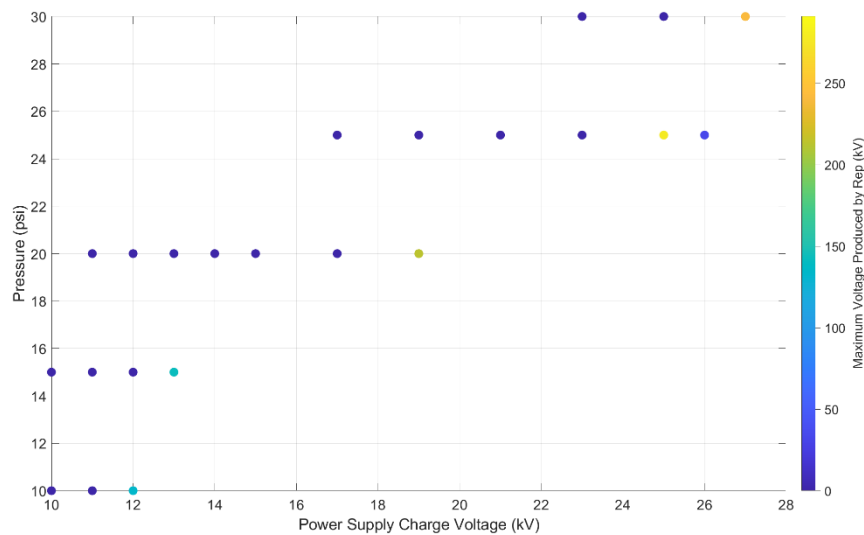


Figure 29: Switch pressure curve for REP, Nov 2023. The dark blue points indicate that REP did not properly erect (low output voltage). Lighter colors indicate increasing output voltage with increased charge voltage, as expected.

After completing the resistive load tests, we installed the Metal Oxide Varistor (MOV) pulse shaping module within REP. Initial tests of this did not work at all due to the load impedance of

the resistive load we had been using. Following consultation with Collins Clark, we increased the load resistance from 17 to 111 Ohms (the inductance was unchanged at 9.8 μH) and retested the MOV module. These tests were successful, though as we increased the output voltage to 150 kV, we observed large voltage reversals at the output and discovered the inductive load was arcing to the surface of the MOVs. The MOV stack and inductive load were sent back to CCT for repair.

During subsequent testing of REP, we encountered an issue with the grounding relay that resulted in the power supply current continuously dumping to ground. This overheated the grounding resistors and melted the nylon rods holding them in place. The insulation on the HV input was also damaged. We have cleaned and replaced the affected resistors, but are investigating issues with the power supplies.

MADCAP

Ian Rittersdorf at NRL supplied us with existing ICEPIC input decks of MADCAP. We conducted these simulations using ICEPIC at 400 kV, pulling ~ 6 kA of current and generating ~ 0.8 GW at 1.22 GHz (Figure 16).

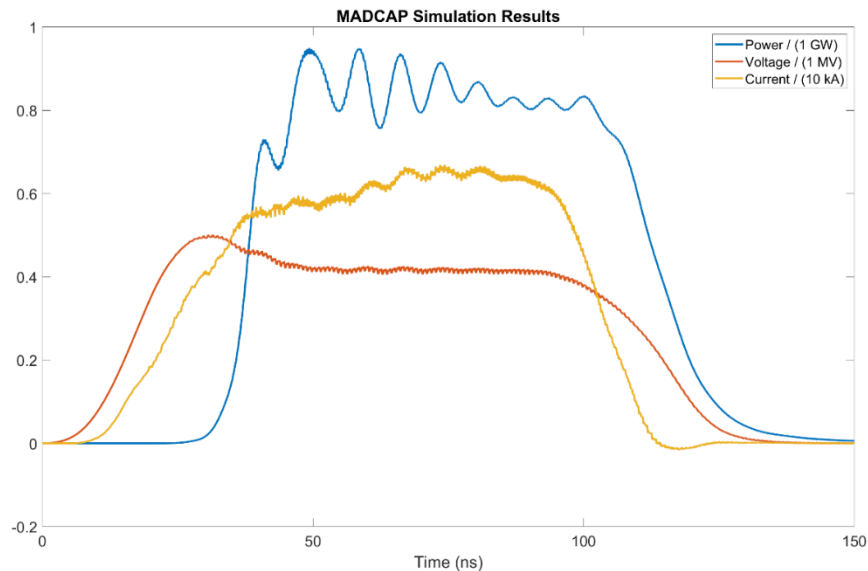


Figure 30: Initial MADCAP simulation results in ICEPIC, producing ~ 800 MW.

MADCAP shipped with two cathode variants: a bare stainless steel cathode, and a stainless steel cathode with brazed carbon fabric emitters. We have assembled the latter version for initial tests. The output of MADCAP is a ~ 2 ft x 1.5 ft aperture, so we are currently working out methods for making a calibrated power measurement. Additionally, we are testing the electromagnet integrated into MADCAP to determine the magnetic field strength and time-to-peak field.

MELBA/REP Control System

A significant portion of student time this year was spent rebuilding the MELBA control system. The old power supplies contained relays and diode protection circuits. We believe the diode in one of the power supplies failed during our 500 kV tests, and was shorted to ground, preventing the capacitors from charging. This necessitated replacement of these 40+ year old power supplies, relays, and diodes, as well as a complete rework of the control system. The new control system is

operated via LabVIEW, and enables repetitive operation (not possible on MELBA, but necessary for the REP pulser).

3. Findings and Conclusions

We designed, simulated, manufactured, and tested an overmoded X-band MILO for operation at 8.5 GHz. This MILO was designed to operate in a higher-order mode, increasing the feature sizes within the device to avoid breakdown. In experiments, it produced ~1 MW at 8.1 GHz. So while it did oscillate at roughly the design frequency, the power output was far below expectations. We think this was due to a mis-aligned cathode causing internal arcs. In meetings with Sem Sol, they indicated that cathode alignment was a critical (and challenging) component of their design. Our initial simulations of a mis-aligned cathode had indicated this wasn't an issue, but the early experimental results match those of Sem Sol. Consequently, we are currently working on ways to improve cathode-anode concentricity in future experiments.

We also observed significant ablation of the graphite beam dump after the initial experiments. While the damage to the beam dump was minor, the ablated graphite coated the entire inside of our vacuum system, including the high voltage insulator. This has not yet caused issues, but continued ablation of carbon will likely lead to catastrophic failure of our ceramic insulating stack. This is an important consideration for continued operation of any repetitive MILO.

We investigated a Brillouin flow step discontinuity in particle-in-cell simulations using CST Microwave Studio. We analyzed Brillouin flow in two dimensions, in a cylindrical geometry where the anode radius changes abruptly at a single axial location while the cathode surface has a constant radius. Our simulation reveals that this change in the anode radius introduces novel bunching of the electrons within the Brillouin hub. These simulations provided new insight into the physical processes that initiate and sustain the bunching processes that are unique for a crossed-field diode, as compared with a non-magnetized diode.

4. Plans and Upcoming Events

- Test of our REP pulser with metal-oxide varistor (MOV) stack and at max operating voltage.
- Experimental testing and optimization of the Overmoded X-band Magnetically Insulated Line Oscillator (OXMILO).
- Complete LabVIEW software for automated control of oscilloscopes, allowing rapid data collection in repetitive operation.
- Conduct simulations of MADCAP magnetron using HFSS and CST microwave studio at the possible operating voltages for our pulsed power driver (300-400 kV).
- Explore viable techniques for MADCAP experimental power and frequency measurement.

Conduct experimental tests of broadband noise generator based on existing simulations. Conduct additional simulations on Brillouin flow at a step discontinuity. We are seeking to better understand what governs the formation of vortices, including their frequency and magnitude. We will vary both the amplitude and sharpness of the electric field transition.

5. Transitions and Impacts

As a basic research program, our transition impacts are largely through the publication of our results and citation of that work (which indicates that other groups have utilized our results). Our recently published papers will, therefore, have a growing transition impact over time.

6. Recommendations for Future Work:

The behavior observed in our simple Brillouin flow step discontinuity studies has proven to be a surprisingly large parameter space for future research. We believe are making progress toward a greater understanding of crossed-field electron flow and the basic limits of MILO efficiency. MILO literature currently has a conflicting view of some basic details, such as whether the electrons transfer their potential energy (like a magnetron) or kinetic energy (like a TWT or other linear-beam tubes) to the RF wave. The insights pertaining to magnetically insulated electron flow are even relevant to our recently submitted publication “Stability of Crossed-Field Amplifiers”.

Discussions with Sem Sol indicated they have an existing X-band MILO and corresponding Marx bank driver that are no longer in use. With modifications to the driver to improve the driver/load impedance match, they believe large performance gains are possible. I would like to explore ways to conduct this work at UM.

7. Personnel

Principal Investigator			
Full Name	Approximate Level of Effort – LOE - (Hours This FY)	Country of Residence	National Academy Member? (Y/N)
Nicholas Jordan	500	USA	N
Co-Investigator(s) or Co-PI(s)			
Full Name	Approximate Level of Effort – LOE - (Hours This FY)	Country of Residence	National Academy Member? (Y/N)
Ryan McBride	40	USA	N

8. Collaborations

Full Name	Organization	Collaboration Summary
David Robie, Dave Hidinger, and Braxton Bragg	Lockheed Martin	Discussed possible collaboration on a desired X-band source with 100’s MW output power and 20% bandwidth
Han Lin, Kiran Raj, and Michael Herndon	Epirus	Discussed Phase II SBIR collaboration on an X-band antenna and provided a letter of support to their Phase I effort.
Brad Hoff, David Simon, Steve Exelby, Wilkin Tang	AFRL	Visited AFRL and hosted a visit to UM to discuss future HPM efforts on high power antennas.
Josh Pompeii and Jack Chen	NSWCDD	Hosted a visit to detail our capabilities and show off current research efforts on magnetrons, MILOs, and CFAs.

Billy Schaefer and Arthur Mabbett	Leidos	Discussed directed energy areas where they can leverage our recent research to address warfighter needs
Collins Clark	CCT	Visited CCT to pulsed power development opportunities related to our REP pulser
Peter Duselis	Sem Sol	Discussion of lessons learned from Sem Sol's X-band MILO design, manufacture, and test

9. Students

Doctoral Student(s)			
Full Name	University	Graduated?	Graduation Year
Adam Brusstar	University of Michigan	N	2027
Zachary Rabine	University of Michigan	N	2029
Ryan Revolinsky	University of Michigan	N	2025
Emma Guerin	University of Michigan	N	2026
Masters Student(s)			
Full Name	University	Graduated?	Graduation Year
Webber Qu	University of Michigan	Y	2024
Undergraduate Student(s)			
Full Name	University	Graduated?	Graduation Year
Georgia Adams	University of Michigan	N	2027
Milo Parrott	University of Michigan	N	2028

10. Technology Transfer

R.A. Revolinsky, C.J. Swenson, N.M. Jordan, Y.Y. Lau, R.M. Gilgenbach, "CROSSED-FIELD DEVICE", US Provisional Patent 63/634,825, Apr 16, 2024.

Visited AFRL to meet with Brad Hoff and David Simon and discuss future HPM research efforts on high power antennas

Hosted a visit for Josh Pompeii and Jack Chen from NSWCCD to detail our capabilities and show off current research efforts on magnetrons, MILOs, and CFAs.

11. Products, Publications, Patents, License Agreements, etc.

Publications resulting from this project for the reporting period:

Archival Publications

#	Citation	Acknowledged ONR Support Received? (Y/N)	Peer Reviewed? (Y/N)
1	R. Revolinsky, C. Swenson, N. Jordan, Y. Y. Lau, and R. Gilgenbach, "On the two-dimensional Brillouin flow," <i>Physics of Plasmas</i> , vol. 31, no. 5, p. 053109, May 2024, doi: 10.1063/5.0205430 .	Y	Y

Conference Papers

#	Citation	Acknowledged ONR Support Received? (Y/N)	Peer Reviewed? (Y/N)
1	A. Brusstar, R. Revolsinky, C. Swenson, E. Guerin, N.M. Jordan, R. Gilgenbach, Y.Y. Lau, "Design of an Overmoded X-band MILO," IVEC 2024, Monterey, CA, April 2024.	Y	N
2	R. Revolinsky, C. Swenson, N.M. Jordan, Y.Y. Lau, R.M. Gilgenbach, "Investigations of Two-dimensional Brillouin Flow through a Cylindrical Step Discontinuity," IVEC 2024, Monterey, CA, April 2024.	Y	N
3	E.N. Guerin, A.N. Brusstar, R.A. Revolinsky, C.J. Swenson, N.M. Jordan, "Initial Testing of Compact Rep-Rate Pulsed Power System", IPMHVC, Indianapolis, IN, May 2024.	Y	N
4	N.M. Jordan, R.A. Revolinsky, C.J. Swenson, E.N. Guerin, A.N. Brusstar, Y.Y. Lau, R.D. McBride, R.M. Gilgenbach, "High Power Microwave Research at the University of Michigan", IPMHVC, Indianapolis, IN, May 2024.	Y	N
5	R. Revolinsky, C. Swenson, N.M. Jordan, Y.Y. Lau, R.M. Gilgenbach, "Simulations of Brillouin Flow with Abrupt Change in Gap Width", EAPPC, Amsterdam, Netherlands, Sept 2024.	Y	N
6	N.M. Jordan, R.A. Revolinsky, A.N. Brusstar, E.N. Guerin, C.J. Swenson, Y.Y. Lau, R.M. Gilgenbach, "Design and Demonstration of an Overmoded X-band MILO", EAPPC, Amsterdam, Netherlands, Sept 2024.	Y	N

Books

No information to report

Book Chapter

No information to report

Theses

No information to report

Websites

No information to report

Patents

#	Citation	Acknowledged ONR Support Received? (Y/N)	Peer Reviewed? (Y/N)
1	R.A. Revolinsky, C.J. Swenson, N.M. Jordan, Y.Y. Lau, R.M. Gilgenbach, "CROSSED-FIELD DEVICE", US Provisional Patent 63/634,825, Apr 16, 2024.	Y	N

Other Products:

#	Product Description	Acknowledged ONR Support Received? (Y/N)	Peer Reviewed? (Y/N)
1	"On the two-dimensional Brillouin flow," Physics of Plasmas Webinar, Sept 20, 2024.	Y	Y

12. Point of Contact in U.S. Navy / Marine Corps

<u>Navy Point(s) of Contact Student(s)</u>			
Full Name	Organization	Email	Date of Last Contact
Matt McQuage	NSWCDD	Y	10/22/2024

New Anode Materials for High Lethality HPM Sources

Grant No. N00014-22-1-2483

Annual Report for Fiscal Year 2024

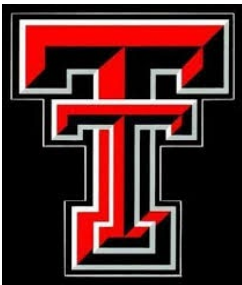
Period of Performance: October 1, 2023 to September 30, 2024

Prepared by:

Professor Ravi P Joshi, Principal Investigator
Texas Tech University
Department of Electrical and Computer Engineering
2500 Broadway MS 3102/Campus
Lubbock TX 79424
Tel: 806-834-7979
Email: ravi.joshi@ttu.edu

Co-Principal Investigator(s):

Mahdi Sanati, Email: m.sanati@ttu.edu
Texas Tech University, Lubbock, TX 79424



This work was sponsored by the Office of Naval Research (ONR), under grant N00014-22-1-2483. The views and conclusions contained herein are those of the authors only and should not be interpreted as representing those of ONR, the U.S. Navy or the U.S. Government.

Section I: Project Summary

1. Overview of Project

Executive Summary: The major goals and objectives of this research are to carry out fundamental research directly tied to the advancement of effective high lethality high power microwave (HPM) sources. It involves assessing and then developing anode materials or material treatment techniques that would help reduce outgassing during active HPM operation. The strategies are being examined as part of this project: (i) use of laser surface treatment to blow off surface adsorbates, (ii) surface layer compression to block or reduce outflow from deep within the anode past the compressed surface layer, (iii) use of surface coatings to act as a physical block for outgassing from the anode interior, and (iv) densification of the layer at or near the surface to potentially “seal” the surface escape route for out-gassing.

This work is a joint collaborative effort between Texas Tech University (TTU) and the University of New Mexico (UNM). The work at TTU will involve simulations based on the Molecular Dynamics (MD), Monte Carlo and first principles Density Functional Theory (DFT) to diffusive outflow of dissolved gases from the anode bulk, and possible bond breakage of contaminant molecules followed by desorption of surface adsorbates.

The overall goal is to reduce contaminants and surface desorption by using different anode treatment techniques (such as surface laser heating), and/or the use of surface coatings, or isentropic compression at the surface.

Objectives: TTU in collaborative partnership with UNM is working to explore new ways to reduce outgassing and desorption from the anode as it can ultimately lead to ion and plasma production in beam-driven high power microwave (HPM) devices. A central objective is to understand and attempt to mitigate anode-initiated ion production due to desorption of neutrals. Appropriate collaborations with UNM on their parallel ONR-supported effort would provide for meaningful comparisons between predictions and measured data. Careful modeling work (coupled with complementary experimental measurements at UNM for validation, model verification and fine-tuning) will enable progress towards this project objective.

Introduction: Simulations based on Molecular Dynamics have been carried out to specifically probe: (i) The possibility of a surface coating that is durable, resistant to degradation, and will resist surface adsorption. With much lower adsorption than the conventional anode materials, the scope for desorption will greatly diminish. (ii) The coating will also have the dual purpose of acting as a physical barrier to stop out-gassing from within the anode bulk region. (iii) Use of isentropic compression to increase the local density at and near the surface to reduce the potential for dissolved gases to escape out through the compacted material. (iv) Finally, obtain quantitative predictions of threshold temperatures for desorption of different adsorbate species, such as carbon and related carbides, oxygen and related oxides, as well as nitrogen from surfaces.

Background: The dynamics of HPM devices during the radiation production phase are dominated by large electron currents periodically impinging on anode surfaces. This leads to heating of the anode, which then facilitates outgassing and desorption of surface contaminants. Here, our

aim is to model gas outflow based on kinetic atomistic models and evaluate the effect of various strategies mentioned above in the Introduction.

2. Activities and Accomplishments

(A) Adsorption and Penetration of Oxygen in Copper and Platinum Slabs

The main results from the simulations reported and discussed in this section is given below.

A platinum (Pt) sample would be far superior to copper (Cu) at *resisting oxygen attachment*, and would also block penetration of the oxygen from the surface into the material. With oxygen remaining at or near the surface for the case of Pt, it would be far easier to have the impurity purged based on surface laser heating. However, for copper, the oxygen may remain especially if it has penetrated deeper into the host. Such residual oxygen incopper would then lead to strong outgassing during HPM device operation.

Detailed results and given and discussed next. LAMMPS-based Molecular Dynamics (MD) calculations were carried out for copper with oxygen atoms placed above the metallic slab. The initial configuration and placement of oxygen is shown in Fig. 1(a) for Cu and Fig. 1(b) for Pt.

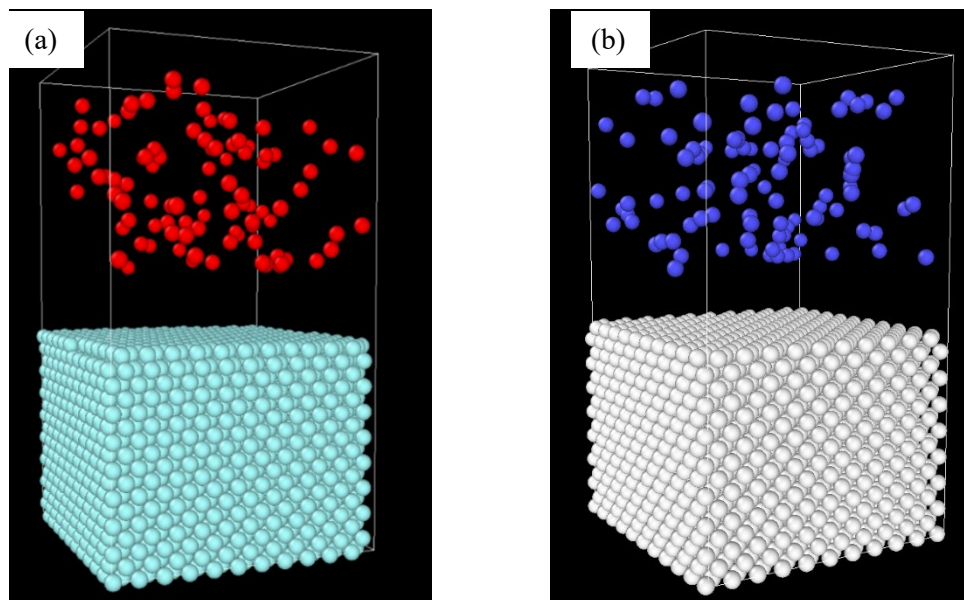


Fig. 1. The initial configuration and placement of oxygen atoms for LAMMPS-based Molecular Dynamics (MD) simulations. (a) Oxygen atoms (red spheres) initially placed above a copper (light green spheres) and, (b) oxygen atoms (purple) placed above platinum (white spheres) slab.

After running MD simulations for the two systems at a temperature of 1100K, the configurations and atomic positions after a 20 ps time interval are shown in Figs. 2(a)-2(b). As evident from the result, the copper is seen to adsorb the oxygen atoms more readily as seen in Fig. 2(a) than for the case of Pt in Fig. 2(b). All the oxygen atoms are predicted to be adsorbed at the surface of the copper in Fig. 2(a). On the hother hand, some oxygen atoms (about 22%) are still completely

detached and seen to be moving freely in the space above the platinum in Fig. 2(b), even after 20 ps.

Another set of snapshots at the later time instant of 39.04 ps at the same 1100K temperature, are presented in Figs. 3(a) and 3(b) for the copper and platinum systems, respectively. At this time the oxygen atoms all remain attached to the copper in Fig. 3(a). Furthermore, some of the oxygen atoms have actually penetrated deeper into the copper anode. In the case of the platinum material at this time, some oxygen atoms are still completely detached and moving freely in the space above the platinum. Those oxygen atoms that are adsorbed seem to remain at the surface with minimal penetration into the Pt metal.

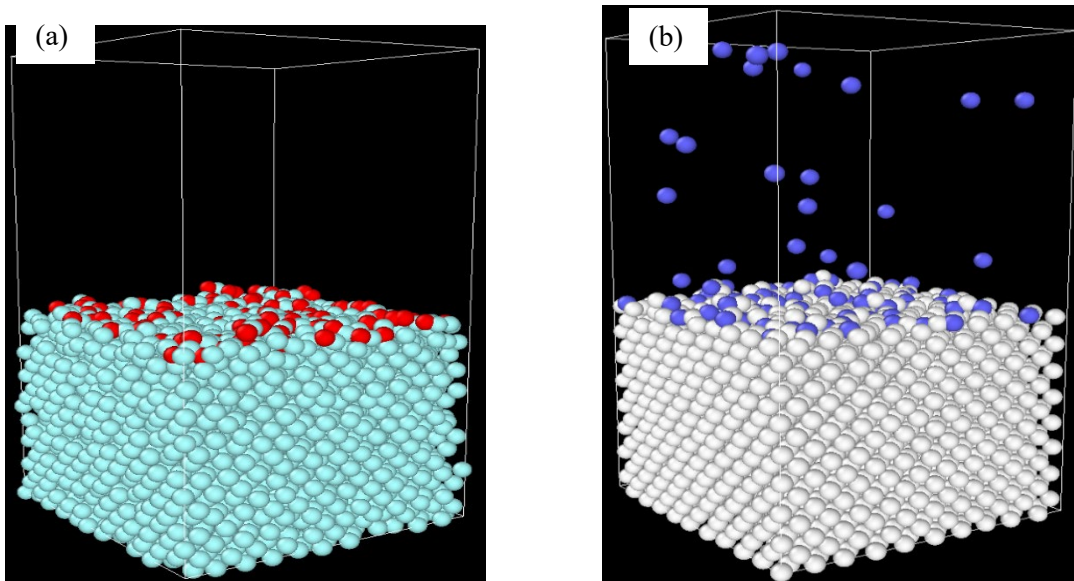


Fig. 2. A 20 ps snapshot of the configuration and placement of oxygen atoms from MD simulations. (a) Oxygen atoms (red spheres) are all adsorbed on the copper (shown as light green spheres) slab and, (b) partial adsorption of oxygen atoms (purple) on to the platinum (white spheres) slab. Some oxygen atoms (about 22%) are still completely detached and moving freely in the space above the platinum.

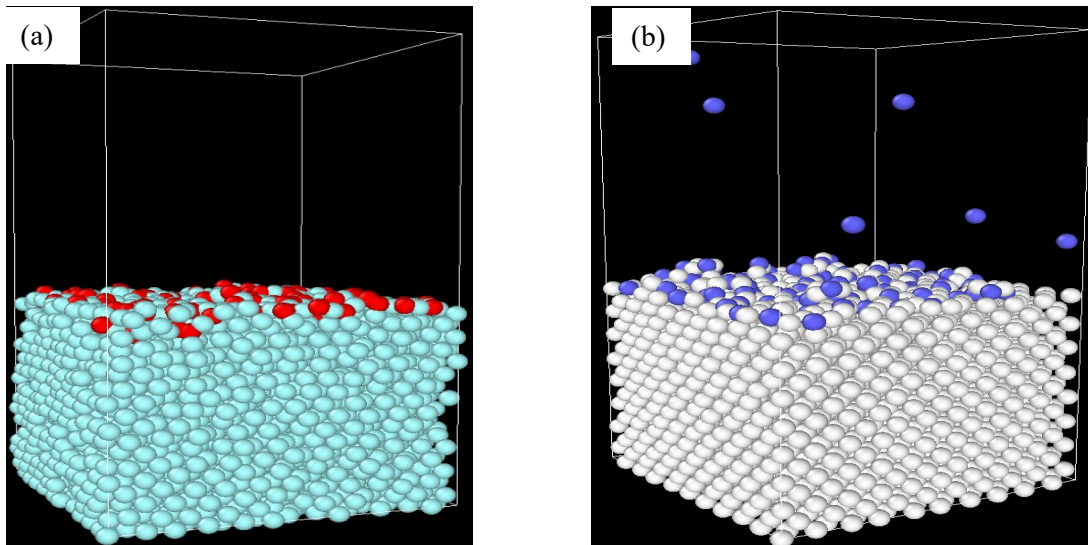


Fig. 3. A 39.04 ps snapshot from MD simulations. (a) Oxygen atoms remain adsorbed at the Cu surface and some even penetrate deeper in. (b) Partial adsorption of oxygen atoms. Some oxygen atoms are still completely detached and moving freely in the space above the platinum.

Results from a final set of snapshots taken at 40 ps are shown on Figs. 4(a) and 4(b) at the same 1100K temperature for comparing Cu with Pt. The results are similar to those for the previous 39.04 ps snapshots. In Fig. 4(a) for copper, the oxygen atoms can be seen to penetrate up to 6 monolayers into the Cu material. By comparison, some oxygen atoms still remain free, while the majority, though attached to the surface, do not penetrate into the platinum.

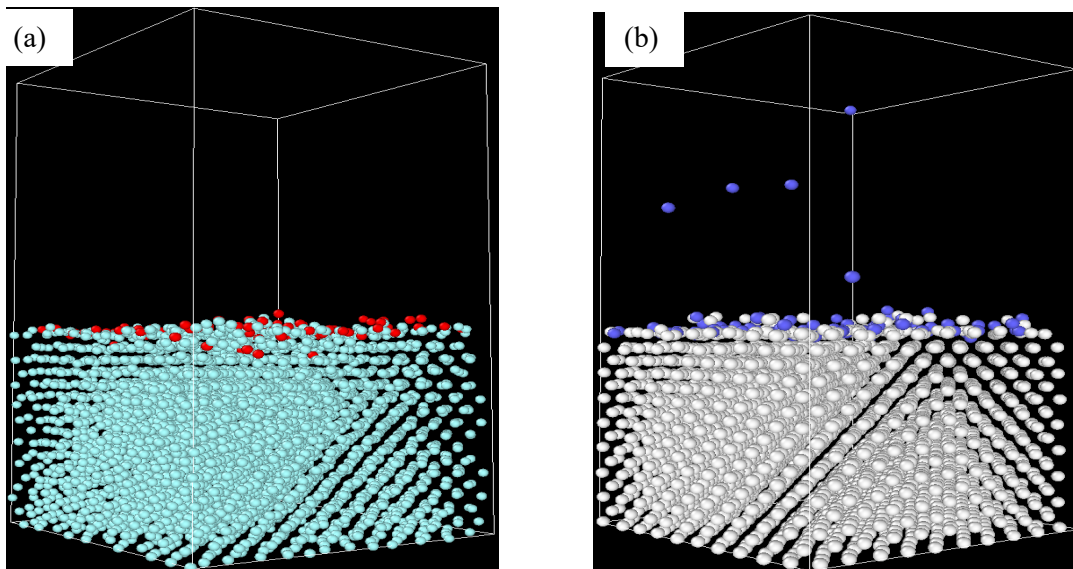


Fig. 4. A 40 ps snapshot of the configuration and placement of oxygen atoms from MD simulations. (a) Oxygen atoms can be seen to penetrate up to 6 monolayers into the Cu material. (b) Partial adsorption of oxygen atoms with a few oxygen atoms still unabsorbed and floating above the platinum surface. Of the adsorbed oxygen atoms, all are seen to stay at the surface with negligible

penetration. The above set of results in Figs. 1-4 clearly show the advantage of Pt in resisting adsorption, and also in preventing deep penetrations into the host metal.

(B) MD Results for Surface Adsorbate Drive-Off From Copper Through Heating

Thermal driven desorption of surface impurities was probed based on MD simulations. Our study attempted to obtain temperature thresholds for desorbing different surface contaminants such as C_2 , O_2 , CO , and CO_2 . The results have shown that carbon-based adsorbates on copper (chosen as an example anode material) could be ejected at a relatively modest surface temperature of 650K. On the other hand, reactive species such as oxygen are very stable due to their large cohesive energies. Our calculations further suggest the benefit of using a platinum coating layer, as the noble metal is robust with strong resistance to oxidation.

The initial structural set up for CO molecules adsorbed on the surface of a copper anode, with the atomic level arrangement, is given in Fig. 5(a) with the copper atoms shown in grey, the oxygen in yellow, and carbon atoms in red. The slab was maintained at a 650 K temperature. A snapshot of the simulated structure at the 3.8 ns instant is given in Fig. 5(b). Some of the CO molecules are seen to detach and move away from the copper slab in this snapshot. While the detached CO molecule is positioned at the top, the release of a couple of other nearby molecules is also predicted to be starting at one of the boundaries. Finally, Fig. 5(c) shows a 4.2 ns snapshot. In this frame, two CO molecules can be clearly seen to have detached from the copper. However, no dissociation of the carbon from the oxygen is predicted at these temperatures for any of the cases. In any event, the results confirm that the 650 K temperature will support the desorption of CO molecular species from the copper surface. Thus, surface heating of copper at or above 650 K is predicted to eliminate CO from the surface and contribute to a cleaner anode sample.

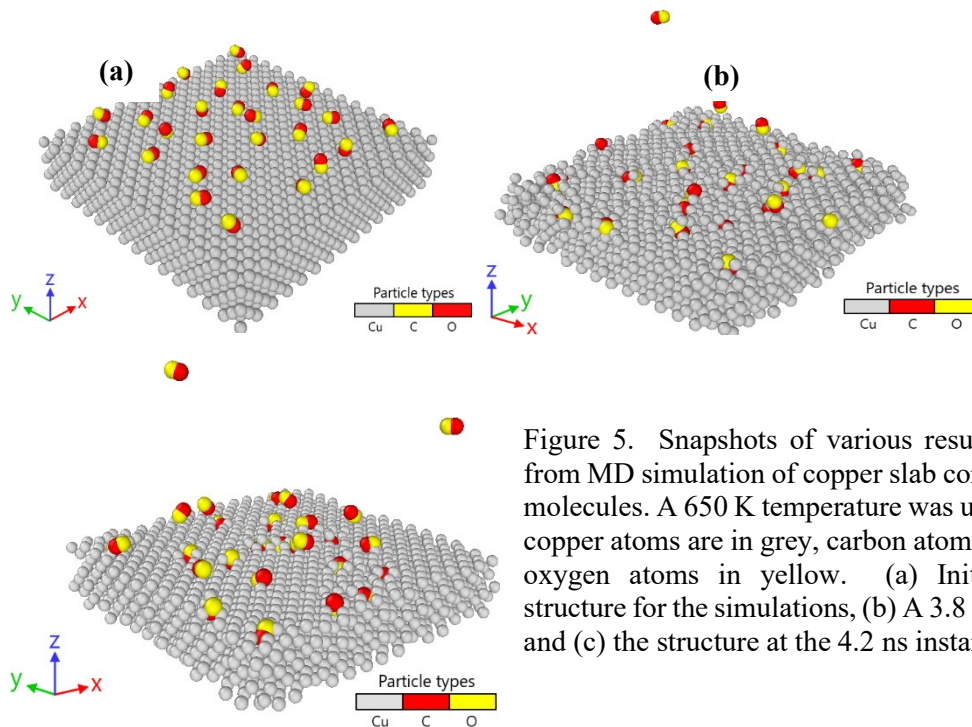


Figure 5. Snapshots of various results obtained from MD simulation of copper slab containing CO molecules. A 650 K temperature was used with the copper atoms are in grey, carbon atoms in red, and oxygen atoms in yellow. (a) Initial starting structure for the simulations, (b) A 3.8 ns snapshot, and (c) the structure at the 4.2 ns instant.

Having obtained results for CO, the presence of CO₂ was simulated next. The focus on carbon-related compounds stems from the fact that despite best efforts, the two most prevalent contaminants found on surfaces are carbon and oxygen. It has also been shown previously that the formation of CO and CO₂ layers on surfaces can significantly enhance the secondary electron yield of the system. Therefore, even from the perspective of reducing secondary electron generation, one needs to clean and remove CO, CO₂, and other such detrimental contaminants that may be present from the surface.

For the CO₂ surface adsorbates, our simulation results yielded a slightly lower requisite surface temperature of 550K to initiate the desorption. The starting configuration of CO₂ molecules placed randomly on the copper surface is shown in Fig. 6(a). In this set of figures, the copper atoms are shown in blue, carbon in red, and oxygen atoms in yellow. The 3.0 ns snapshot of the system configuration is given in Fig. 6(b). In this figure, two CO₂ molecules can be seen to have become detached from the surface and are being blown upwards. The process is predicted to continue, with more CO₂ molecules being ejected over time. The 3.8 ns snapshot shows over four different molecules in flight above the surface. The results thus conclusively indicate that a 550K surface temperature would be adequate to cleanse the CO₂ adsorbate molecules from copper. Also, as in the previous case, dissociation of the CO₂ molecules is not predicted.

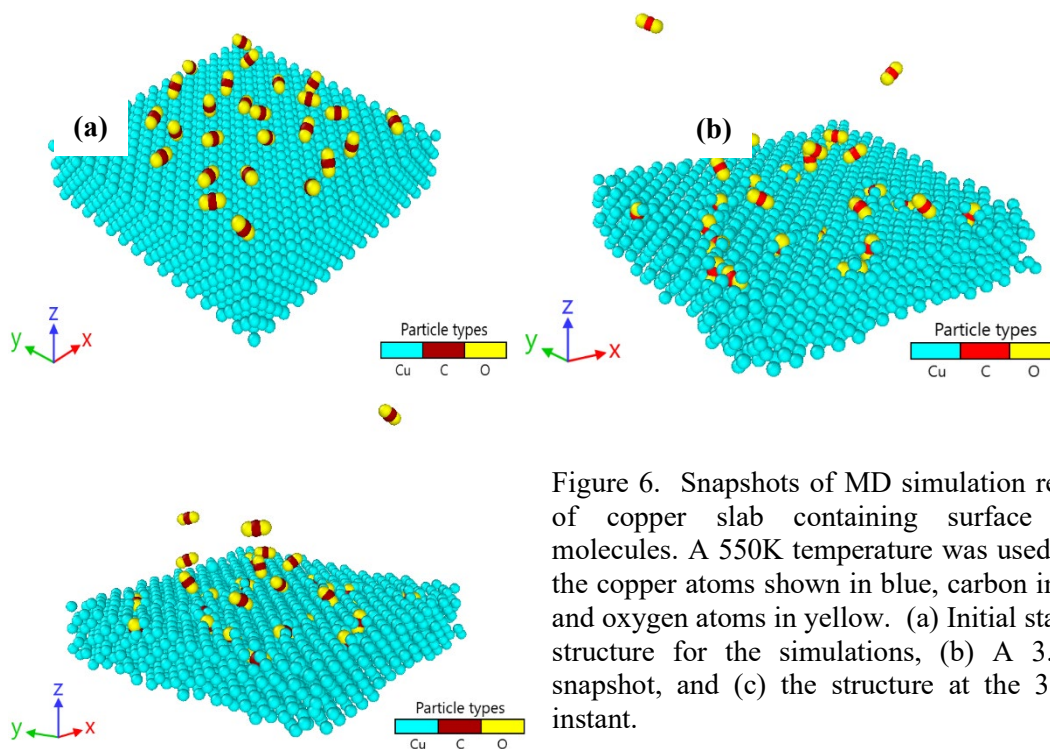


Figure 6. Snapshots of MD simulation results of copper slab containing surface CO₂ molecules. A 550K temperature was used with the copper atoms shown in blue, carbon in red, and oxygen atoms in yellow. (a) Initial starting structure for the simulations, (b) A 3.0 ns snapshot, and (c) the structure at the 3.8 ns instant.

Next, individual carbon atoms were placed randomly on the copper surface to probe the possibility of their thermally driven cleansing. Figure 7(a) shows the geometric configuration and placement of carbon atoms (red spheres) on the copper slab represented by the blue spheres. A temperature of 650K was chosen to probe the time-dependent dynamics for this initial structure. A snapshot at the 12 ns instant obtained from the MD simulations is shown in Fig.

7(b). An important development can be seen to be the binding of individual carbon atoms with the resulting formation of C_2 molecules. Furthermore, many of the C_2 molecules thus formed are predicted to move deeper into the copper host. A few carbon molecules are seen to remain at the surface and have formed attachments to the copper. Finally, at this chosen temperature, none of the carbon impurities at the surface are seen likely to be driven off by thermal heating. A number of other scenarios with the host copper slab maintained at different temperatures were also simulated, each starting with carbon atoms placed at the surface. Temperatures as high as 1300K were used, so that all chosen temperature values always remained below the melting point of copper. In all cases, no ejection of the carbon impurity was predicted. A physical explanation for this difference in requisite temperatures for ejection and/or dissociation associated with the different molecular species is discussed later in this section.

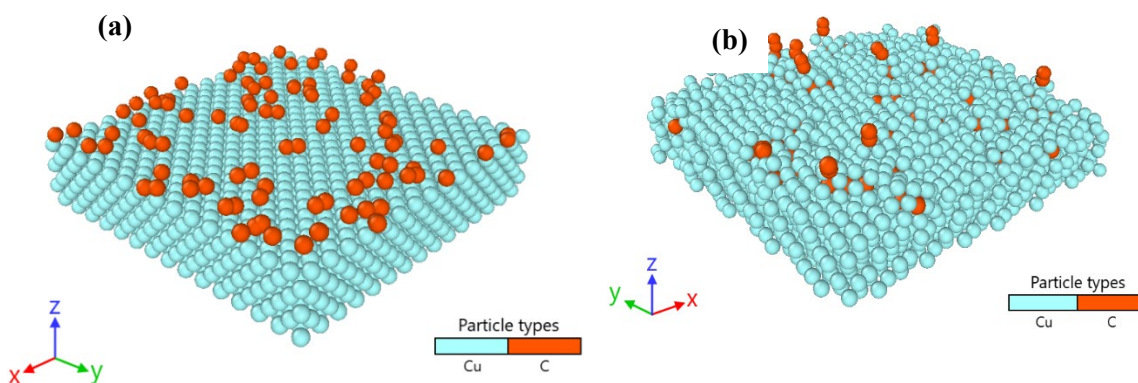


Figure 7. MD simulation results for the structure of a copper slab containing carbon atoms positioned randomly at the surface. A 650K temperature was used with the copper atoms in blue, and oxygen atoms represented by red spheres. (a) Initial starting structure for the simulations, and (b) a 12 ns snapshot.

For completeness, the presence of oxygen atoms on the copper surface was also simulated. Figure 4 shows the structure and placement of atoms for the copper-oxygen system used for the MD simulations. The atoms of the copper slab are shown in grey, while randomly positioned oxygen atoms at the surface are shown in purple. A 650K temperature was used. Figure 8(a) shows the initial starting structure for the simulations, while the structural arrangement of the atomic system obtained after 12 ns is given in Fig. 8(b). The structure at the later 12 ns time instant reveals the oxygen is not predicted to be released from the surface, despite the total simulation time being almost four times larger than the previous cases for carbon. On the contrary, the oxygen atoms are predicted to bond with the copper and either remain at the surface, or in some instances, be located deeper in the copper host. As with the previous case of carbon, simulations at higher temperatures were also carried out. However, at all temperatures attempted, the oxygen remained attached to the copper. This is simply indicative of strong copper-oxygen bonding in this system.

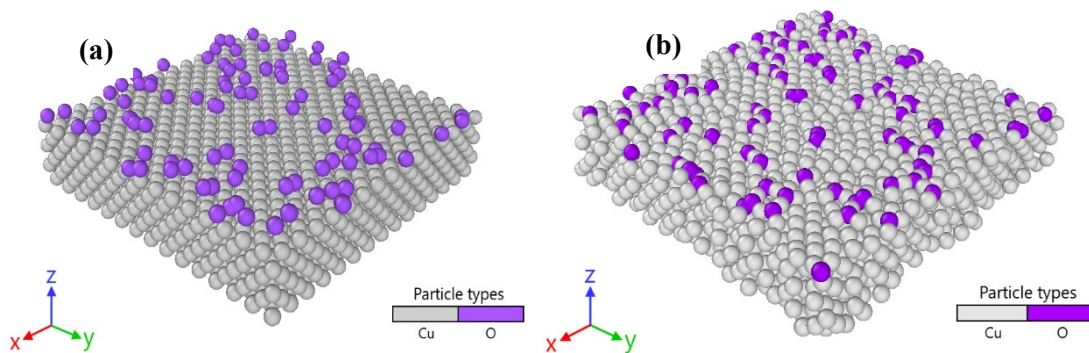


Figure 8. Results showing the structure and placement of copper-oxygen system from MD simulations. The atoms of the copper slab are shown in grey, while randomly positioned oxygen atoms at the surface are shown in purple. A 650K temperature was used. (a) Initial starting structure for the simulations, and (b) a 12 ns snapshot.

(C) Oxidation to Blow Off Surface Carbon and Oxygen Impurities on Platinum Coating

The main result obtained are summarized below.

- (i) Oxygen could be driven off from platinum coated copper at a temperature of $\sim 800\text{K}$.
- (ii) Carbon impurities are predicted to be very hard to dislodge and would remain at the surface up to temperatures of $\sim 1250\text{K}$, which is near the melting point of copper.
- (iii) Since carbon adsorbates were seen to be difficult to dislodge, the possibility of exposing the surface to oxygen was probed. (This could be done by flowing oxygen gas on the anode samples). The point was to determine whether the oxygen could then convert the carbon to CO_2 or CO , which then could be dislodged. As already shown for copper, the presence of CO_2 adsorbates can be dislodged and blown away at temperatures around 650K .
- (iv) Our results also showed that oxidizing carbon atoms at the surface of a Pt coated anode, could lead to surface cleaning with blow-off at temperatures at or above 400K . Thus, any adsorbed carbon that might be present could be eliminated through exposure to oxygen-rich environment followed by surface heating.
- (v) MD simulations also showed that oxygen attachment to Pt surfaces would be much less than the adhesion of oxygen to copper. Hence, Pt coating presents a good solution towards lowering surface adsorbates. Furthermore, the possibility to dissociate or blow-off such surface oxygen at a temperature of around 800K also provides another strategy of securing a cleaner surface via the Pt coating.

The results are presented and discussed next. Figure 9 shows an initial (time $t=0$) snapshot of the initial configuration used in our simulations of oxygen atoms (red spheres) located at the surface of a Pt slab (atoms shown in blue) at 800K . This represents the adsorbed oxygen species on a platinum coating.

Next, Figure 10 shows the same system at a later time instant of 178 ps. The release of a bonded oxygen (O_2) pair can be seen. This underscores the release and ejection of paired O_2 molecules at the 800 K temperature. At this temperature, the solitary oxygen atoms could move around on the surface to form stable bonds with other oxygen atoms that could be encountered. The resulting oxygen molecules were predicted to then be blown away from the surface. Thus, a clean surface free of the oxygen adsorbates is predicted at this 800K operating temperature.

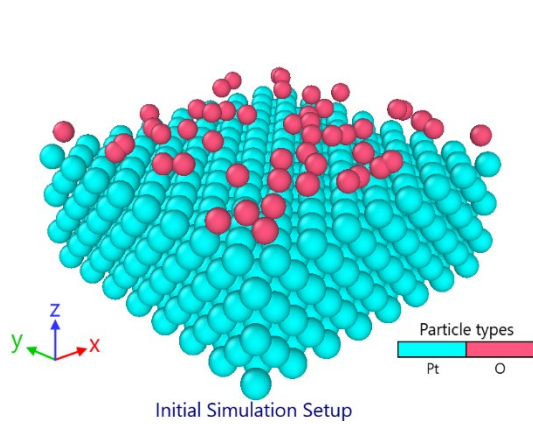


Figure 9. Snapshots of initial (time $t=0$) configuration of oxygen atoms (red spheres) at the surface of a Pt slab (atoms in blue) at

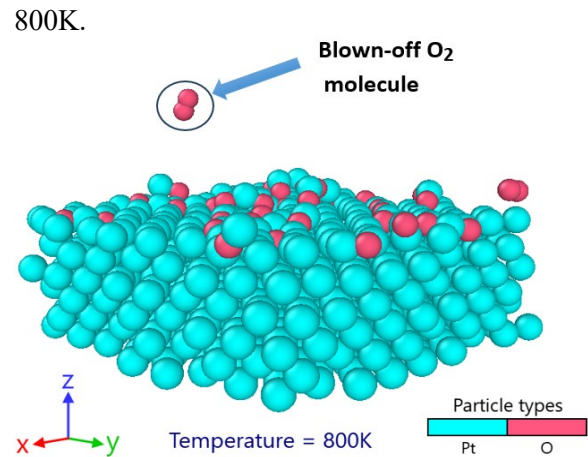


Figure 10. Snapshots of the configuration of Fig. 9 at a later time instant of 178 ps. The release of a bonded oxygen (O_2) pair is seen in the above picture. This underscores the release and ejection of paired O_2 molecules at the 800 K temperature. At this temperature, the solitary oxygen atoms could move around on the surface to form stable bonds with other oxygen atoms.

It is very likely that a surface laser scan or surface heating could conceivably clear the Pt coated surface of the oxygen impurities. Next, the situation of carbon adsorbates at the surface of Pt was examined. The initial starting configuration (time $t=0$) is shown in Figure 11. A total of 50 carbon atoms are shown by purple spheres to lie at the surface of Pt slab (light grey spheres).

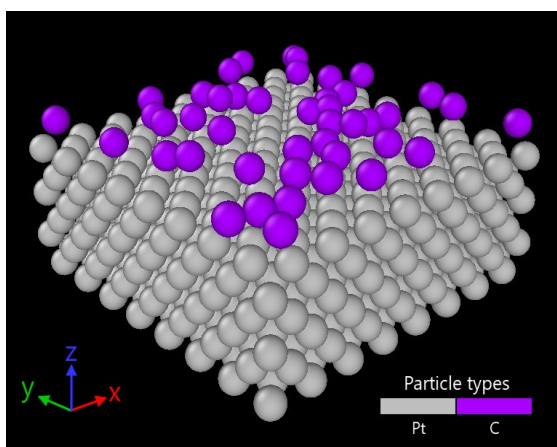


Figure 11. Snapshots of initial (time $t=0$) configuration of carbon atoms (purple spheres) lying at the surface of Pt slab (shown by light grey spheres). A total of 50 carbon atoms were used in this MD simulation.

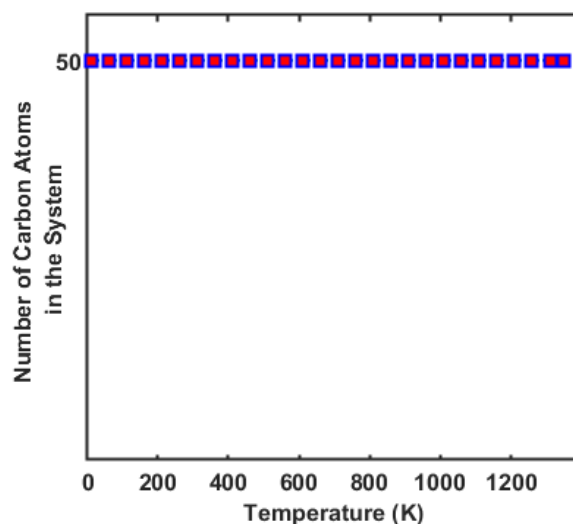


Figure 12. Number of carbon atoms at the Pt surface as a function of Pt temperature. Each value was obtained after running the simulation at that temperature for a long time of 5 ns.

The result of running the MD simulations for a long time for different cases of operating temperature is given in Fig. 12. The number of carbon atoms at the Pt surface is plotted as a function of the Pt temperature. As evident from the plot of Fig. 12, even at the highest simulated temperature of 1250 K, all the carbon atoms are predicted to remain firmly at the surface. No “blow-off” or release of any carbon atom from the surface is predicted. Thus, carbon on Pt forms a very stable structure. We predict it would not be possible to clean the Pt surface of the carbon atoms even after raising the surface temperature up to 1250 K.

Since we have assumed the Pt to be a coating on a copper anode, and since the melting point of copper is roughly 1350 K, the temperatures here were kept well below the Cu melting point. Hence, a maximum temperature of about 1250 K was used in the MD simulations. The carbon adsorbate was shown to be resilient to release from the surface, thus implying a strong bond between carbon and Pt atoms. To possibly overcome this tight coupling between C and Pt atoms, we ran simulations wherein oxygen was deliberately introduced at the surface to force the possible creation of an oxide such as CO_2 . One of our results obtained previously for copper had shown detachment of CO_2 at a temperature of $\sim 650\text{K}$. Hence, the expectation was of a similar detachment of CO_2 from the Pt surface. To test this hypothesis, numerical simulations were carried out by introducing oxygen atoms above the surface of the Pt slab containing the carbon adsorbates. Figure 13 shows the initial configuration of such a system. A snapshot of initial (time $t=0$) configuration of carbon atoms (green spheres) lying at the surface of Pt slab (shown by light grey spheres), and oxygen atoms placed close to the surface. The temperature was chosen to be 380 K.

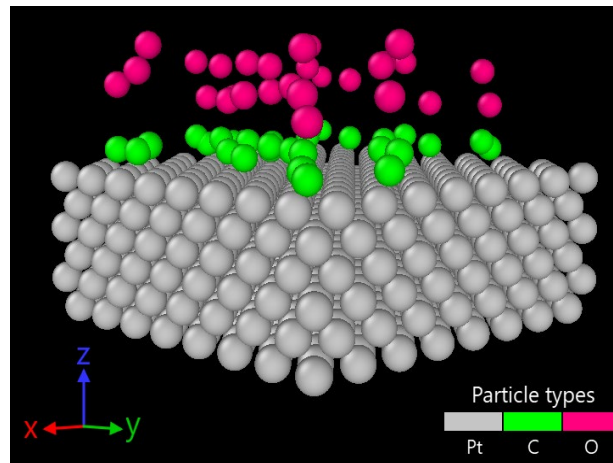


Figure 13. A snapshot of initial (time $t=0$) configuration of carbon atoms (green spheres) lying at the surface of Pt slab (shown by light grey spheres), and oxygen atoms placed close to the surface. The temperature was chosen to be 380 K.

The presence of both the carbon and oxygen atoms at and near the Pt surface leads to the formation of CO and CO₂ molecules. This is shown more clearly in Fig. 14. The snapshot of the system consisting of carbon and oxygen atoms at the surface of the Pt slab is evident. Furthermore, ejection of CO bonded molecules is predicted. This emission becomes more apparent in Figure 15. The number of carbon and oxygen atoms remaining at the Pt surface as a function of time is shown in Fig. 15 at different operating temperatures. The number of remaining atoms at the surface after applying a temperature ramp from 300 K to 1350 K. A steady decrease in number of oxygen atoms remaining at the Pt surface is predicted after a ~ 400 K temperature.

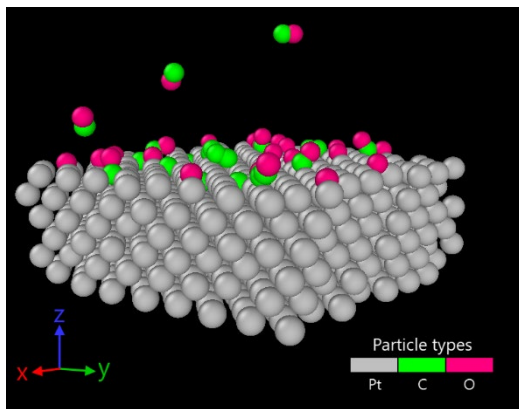


Figure 14. A snapshot of the system consisting of carbon and oxygen atoms at the surface of the Pt slab. Ejection of CO bonded molecules is predicted.

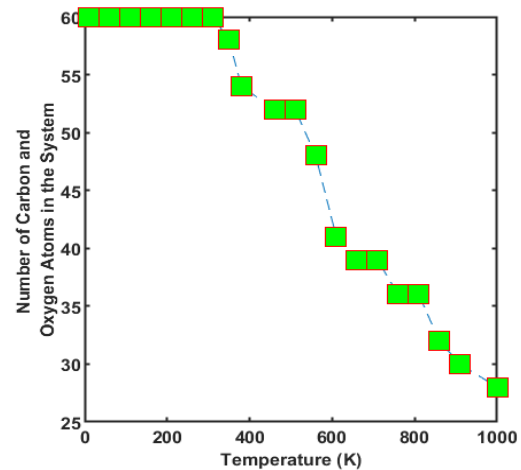


Figure 15. Number of carbon and oxygen atoms remaining at the Pt surface upon running MD simulations for a temperature ramp from 300 K to 1350 K.

Thus, the above results indicate that it would be possible to free the Pt surface of carbon adsorbates via a two-step process. First, the carbon could be oxidized, and then surface heating would lead to the emission of CO or CO₂ molecules. The process of such ejection would effectively clean the Pt surface.

(D) Herding of Impurities and Contaminants to Surface By Quasi-Isentropic Compression

The central idea behind Quasi-Isentropic Compression (QIC) is to apply a strong pressure ramp from one end of an anode sample, say the back surface. This squeezes the lattice material. The lattice atoms are strung together and mutually connected via bonds. However, the impurities, dissolved gases, and other atoms absorbed in the lattice material are not attached or linked by a network of bonds. As a result, it should be possible in theory to move adsorbates and infused gas atoms by applying an external pressure. Though the lattice would deform with built-in strain, the basic structure and geometry would be retained. For the foreign atoms and adsorbates, on the other hand, the pressure would nudge and push them upwards and finally place them at positions of internal energy minima towards the top surface. In other words, the pressure ramp would drive and herd the gas/impurities to the anode surface. Two benefits could then result:

(i) A high density of gas atoms would get lined up at or near the front face from where they could be removed by surface treatment such as a laser raster scan. Thus, a material clean up would occur.

(ii) The compression at the opposite face might work to "seal" that open surface. As a result, the anode sample might remain resistant to further intake of gaseous absorption from the top face, and the dense surface layer could make outgassing harder as gas atoms would have to squeeze out of a denser matrix.

The simulation results obtained are presented and discussed next. A pressure ramp was applied to the bottom face of a rectangular copper slab (blue spheres) representing an anode containing hydrogen atoms (red spheres) randomly distributed within the copper as shown in Fig. 16. The pressure magnitude was increased from 0 Pascals to 2 Giga-Pascals over 100 picoseconds. The resulting structure and atomic configuration of the system at 48 ps after pressure application is shown in Figure 16. Around 45% of the hydrogen atoms are predicted to be located at or near the surface. With increasing time and applied pressure the hydrogen atoms were seen to move even further towards the upper surface. A 100 ps snapshot of the structure and atomic configuration is given in Figure 17. At this time, about 68% of the hydrogen atoms are predicted to be near the top surface.

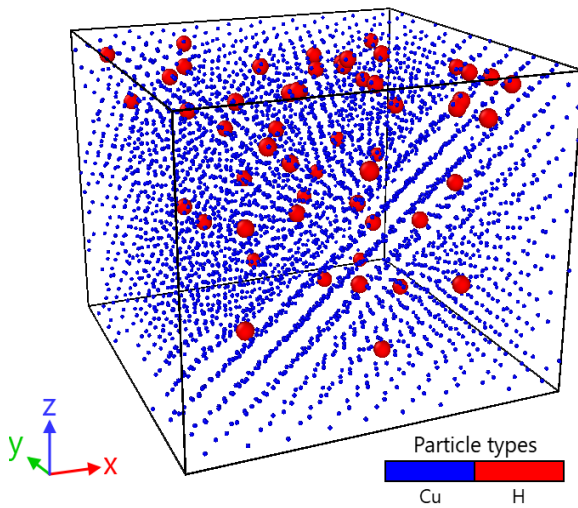


Figure 16. A 48 ps snapshot of the system shown in Figure 1 upon application of the 200 Giga-Pascal pressure ramp. Many of the hydrogen atoms are seen to now lie at or near the top surface of the copper slab.

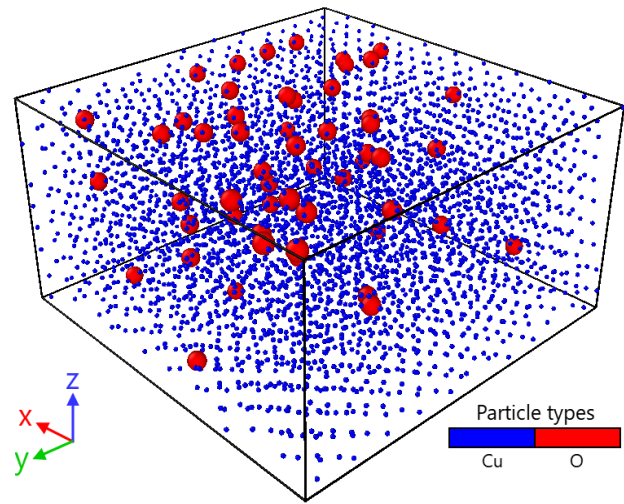


Figure 17. A 100 ps snapshot of the system upon application of the 200 Giga-Pascal pressure ramp over a 100 picosecond duration. At this time, about 68% of the hydrogen atoms are predicted to be near the top surface.

Figure 18 shows the time dependent evolution of the hydrogen population in the region near the top surface. A region two monolayers thick was chosen starting from the top surface for counting the hydrogen atoms. About 43 of the 60 hydrogen atoms are predicted to be near this top region and denotes about 70% of the hydrogen population.

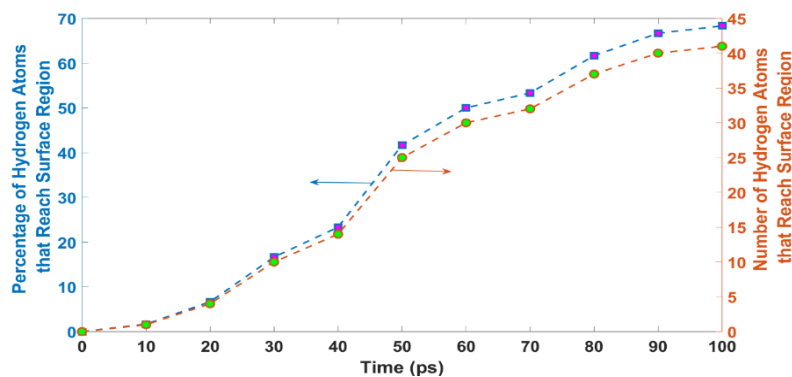


Figure 18. Time dependent evolution of the hydrogen population in the region near the top surface. A region two monolayers thick was chosen starting from the top surface for counting the hydrogen atoms. About 43 of the 60 hydrogen atoms are predicted to be near this top region and denotes about 70% of the hydrogen population.

The above figure satisfactorily demonstrates the possibility of gathering and herding the hydrogen atoms at the top surface for potential laser ablation or other surface cleaning treatments, based on the isentropic compression.

For completeness, the strain based on dimensional changes obtained from the MD simulations was also calculated. At the 100 ps instant, the height of the starting copper cube was seen to be compressed ($= \Delta L$) by 14.8325 Å along the z -direction. This represents a strain ($= \epsilon = \Delta L/L$) of 0.4319.

(E) Attachment of Adsorbate Atoms in Compressed Versus Uncompressed Cu and Pt

The simulation results discussed in this section can be summarized as give below.

(i) Our simulation results reveal that both *compressed* copper and *compressed* Pt can reduce the attachment of oxygen from the ambient onto the surface.

(ii) In comparison to a copper anode, the attachment of oxygen onto the surface is much lower for Pt as compared to Cu material, for both the uncompressed and *compressed* cases.

The actual results obtained from our simulations are discussed next. The attachment of oxygen to the surface of an anode sample from the ambient was probed for copper and platinum materials. For both cases, a regular lattice was first assumed without any compression. This provided baseline results against which subsequent results involving attachment over compressed materials could be compared. Details of the Molecular Dynamics (MD) simulations, dimensions of the simulation volume, number of atoms used etc. are ignored, as these were provided in previous monthly reports. The simulations were performed at 300K.

For simulations with compression, the Molecular Dynamics (MD) simulations were carried out starting from an ideal copper (Cu) lattice slab as above, with ideal, defect-free material containing no gas atoms or impurities. *A pressure ramp was applied to the bottom face, with pressure magnitude increasing from 0 Pascals to 200 Giga-Pascals over 100 picoseconds. At the end of the 100 ps simulation run, a compressed sample was thus created.* Applying the same strategy and technique to the Pt slab, a compressed Pt anode was similarly obtained. These two compressed slabs were then tested through numerical MD simulations for oxygen adsorption at the surface from the ambient.

Results for the oxygen adsorption or drive-in for both the uncompressed and compressed Cu and Pt materials are shown in Figure 19. Time dependent evolution of the oxygen atoms population that either attached or penetrated into the Cu or Pt metal slabs were tracked. In Fig. 19, about 31 of the 100 oxygen atoms are predicted to be at or near the top surface for compressed platinum. By comparison, the number of oxygen atoms in the case of compressed Pt is predicted to be much higher at 95. The numbers of attached oxygen for copper, on the other hand, were predicted to be 38 and 100 for compressed and uncompressed Cu, respectively.

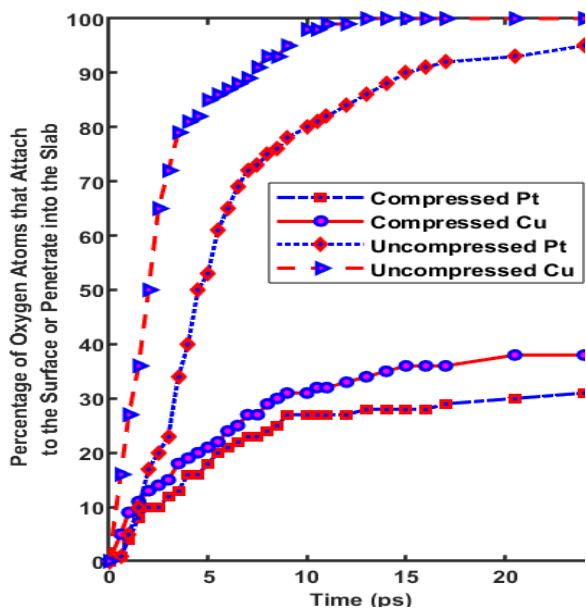


Figure 19. Time dependent evolution of the oxygen population that either attaches or penetrates into the Cu or Pt metal slabs. in the region near the top surface.

Two points are immediately obvious from the results of Fig. 19: (i) First, for both materials, the attachment of ambient oxygen to the surface is dramatically lowered by quasi-isentropic compression (QIC). (ii) In comparing Pt to Cu, the former is predicted to have lower oxygen attachments in both the compressed and uncompressed states.

The above makes a strong case for QIC and supports the use of Pt, a noble metal, over copper. While other potential anode metals have not been tested, previous results obtained over the span of the past 6-months seem to confirm the continued benefit in using Pt. However, since it is an expensive material, a more likely scenario would be the use of a Pt coating over a traditional anode metal.

As a next step, details of the attachment of oxygen from the ambient onto an *uncompressed* platinum surface, *as a function of time*, were probed through MD simulations. Figure 20 shows the initial set up for the 300K case. The platinum lattice slab is shown by the green spheres, while 100 oxygen atoms (red spheres) were randomly placed in the vacuum above the Pt slab. The system setup and atomic configuration after running the MD simulations for 8 ps is shown in Figure 21. As evident from the figure, many of the oxygen atoms (about 70%) are predicted to be at the surface of the platinum and attached.

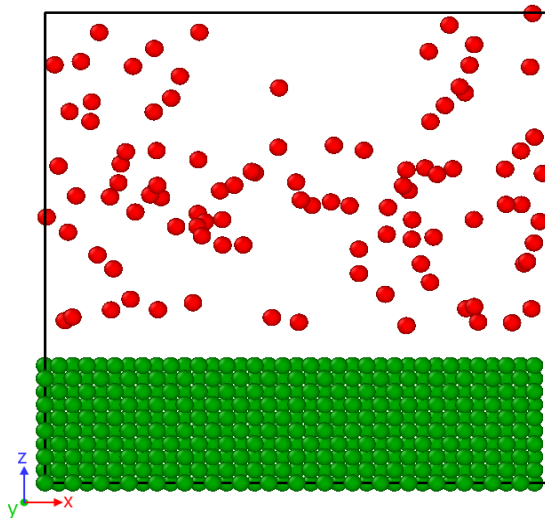


Figure 20. Initial starting setup with randomly placed oxygen atoms (red spheres) in the vacuum region over an ideal, defect-free uncompressed platinum lattice slab at 300K. The Pt atoms are shown in green and oxygen in red.

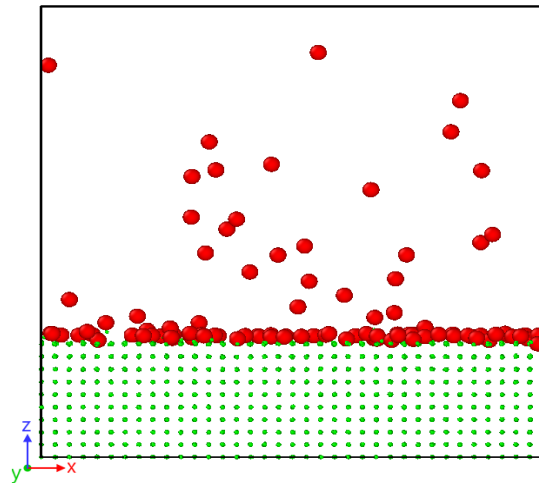


Figure 21. A 8 ps snapshot of the system after running MD simulations at 300K. Many of the oxygen atoms (about 70%) are predicted to be at the uncompressed platinum surface.

For comparisons, a similar calculation as the one just shown and discussed above, was carried out for *compressed* Pt. Figure 22 shows the initial set up for the compressed Pt slab simulated 300K case. The platinum lattice slab is shown by the black spheres, while 100 oxygen atoms (red spheres) were randomly placed in the vacuum above the Pt slab. The system setup and atomic configuration after running the MD simulations for 8 ps is given in Fig. 23.

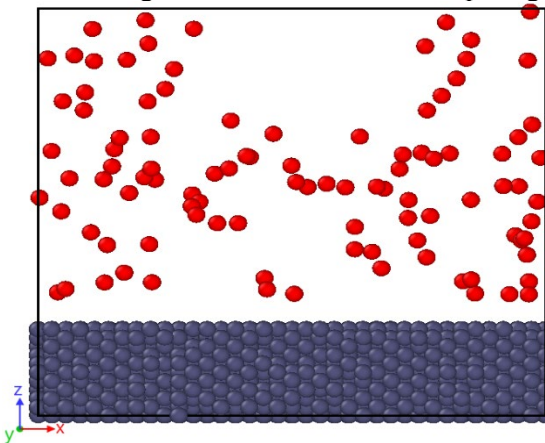


Figure 22. Initial starting setup with randomly placed oxygen atoms (red spheres) in the vacuum region over an ideal, defect-free *compressed* platinum lattice slab at 300K. The Pt atoms are shown in black and oxygen in red.

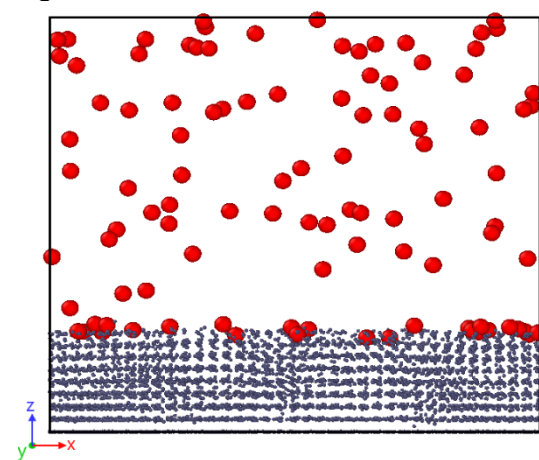


Figure 23. A 8 ps snapshot of the system after running MD simulations of the *compressed* Pt slab at 300K. Most of the oxygen atoms (about 75%) are predicted to remain in the vacuum region **above** the *compressed* platinum.

In this case, most of the oxygen atoms (about 75%) are predicted to remain in the vacuum region above the *compressed* platinum. This is in strong contrast to the situation predicted in Fig. 21 where a majority of the oxygen were at the Pt surface.

Similar time-dependent calculations as discussed above, were performed for the uncompressed Cu-O and compressed Cu-O systems. Figure 24 shows the initial set up for uncompressed Cu at 300K case. The copper lattice slab is shown by magenta spheres, while 100 oxygen atoms (red spheres) were randomly placed in the vacuum above the Cu slab. The system setup and atomic configuration after running the MD simulations for 8 ps is shown in Figure 25. As evident from the figure, many of the oxygen atoms (about 95%) are predicted to be at the surface of the uncompressed copper and attached.

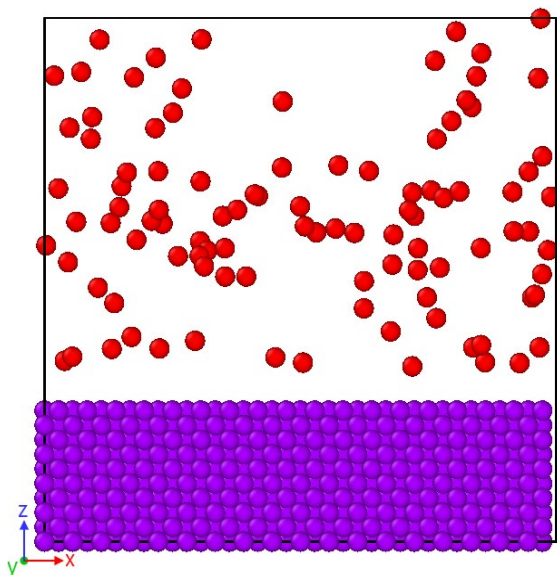


Figure 24. Initial starting setup with randomly placed oxygen atoms (red spheres) in the vacuum region over an ideal, defect-free uncompressed copper lattice slab at 300K. The Cu atoms are shown in magenta and oxygen in red.

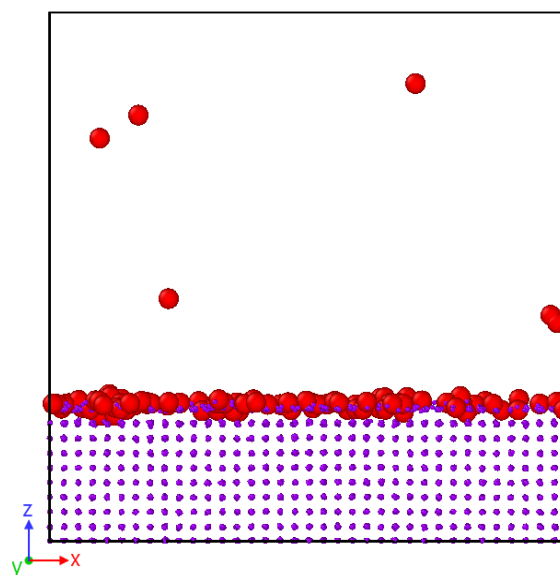


Figure 25. A 8 ps snapshot of the system after running MD simulations at 300K. Many of the oxygen atoms (about 95%) are predicted to be at the uncompressed copper surface.

Finally, similar calculations as presented above were undertaken for *compressed* copper as a comparison. Figure 26 shows the initial set up for the compressed Cu slab simulated 300K case. The copper lattice slab is shown by the blue spheres, while 100 oxygen atoms (red spheres) were randomly placed in the vacuum above the Cu slab. The system setup and atomic configuration after running the MD simulations for 8 ps is given in Fig. 27.

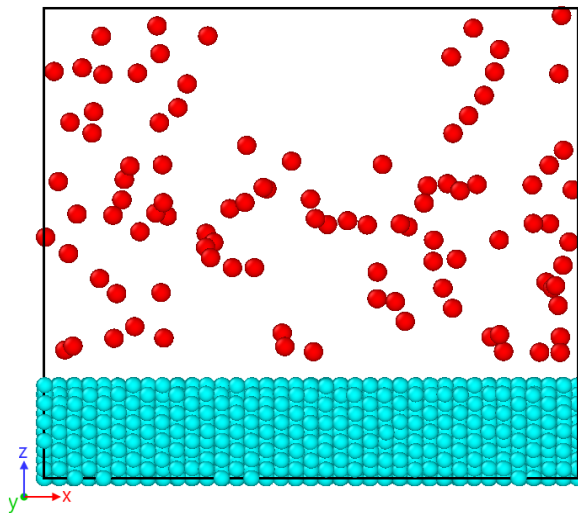


Figure 26. Initial starting setup with randomly placed oxygen atoms (red spheres) in the vacuum region over an ideal, defect-free *compressed* copper lattice slab at 300K. The Cu atoms are shown in blue and oxygen in red.

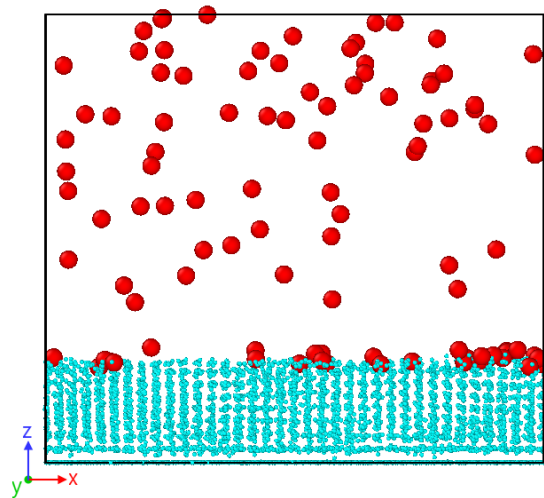


Figure 27. A 8 ps snapshot of the system after running MD simulations of the *compressed* Cu slab at 300K. Most of the oxygen atoms (about 30%) are predicted to be at the surface of the *compressed* copper.

In this case, about 30% of the oxygen atoms are predicted to be at the surface, with almost no penetration into the anode material. This is a far lower percentage of adsorption as compared to the uncompressed case shown in Fig. 25. Also, though much smaller, the oxygen attachment in Fig. 27 for compressed Cu is slightly higher than that for compressed Pt in Fig. 23.

3. Findings and Conclusions

(i) Our simulations have shown that isentropic compression applied at one surface can help compact and densify the top layer at the opposite surface. This has two advantages: (i) the outgassing at the surface is reduced as the gas atoms would have to squeeze through and flow past a denser layer, and (ii) it was also shown that adsorption at the denser surface was more difficult. Hence, surface adsorption would be curtailed as well.

(ii) Our Molecular Dynamics simulations predict that surface laser treatment could raise the surface temperature to blow off deleterious gases and clean the material of surface adsorbates. Thus, such pre-emptive treatments prior to use of the anodes in HPM systems could reduce deleterious outgassing.

(iii) Use of coatings such as Platinum which is an unreactive inert material on anodes has been shown by our group through simulations to mitigate surface adsorption. With reduced surface adsorbates, the outgassing would be less. It was also shown that the coating could act as a physical barrier to block the outflow of dissolved gases from the anode bulk. The only issue might be the stability, mechanical adherence and lifetime of such coatings.

4. Plans and Upcoming Events

(i) Our simulations have shown that isentropic compression applied at one surface can help compact and densify the top layer at the opposite surface. This was shown to reduce outgassing.

We thus feel that other techniques that could similarly the material should also be evaluated. One possibility is “material quenching”, which could involve surface heating by an external laser, for example, followed by rapid cooling. This is an aspect that we plan to investigate in the future.

(ii) Collaborations with Dr. Portillo to carefully compare surface laser-irradiation as a technique to mitigate outgassing. Such comparisons could probe temperature thresholds for getting rid of different surface contaminants (e.g., carbon, oxygen, CO, CO₂, etc.). A better quantitative understanding of both the laser energy and pulse duration would be another aspect that would emerge through such comparisons between modeling and experimental data.

(iii) Extend concepts of isentropic compression and material quenching to anode material with coatings such as Platinum which is an unreactive inert material. We have already shown that such material can help mitigate surface adsorption.

5. Transitions and Impacts

None.

6. Recommendations for Future Work

See section 4, Plans and Upcoming Events.

7. Personnel

<u>Principal Investigator</u>			
Full Name	Approximate Level of Effort – LOE - (Hours This FY)	Country of Residence	National Academy Member? (Y/N)
Ravi Joshi	160 hours	USA	No
<u>Co-Investigator(s) or Co-PI(s)</u>			
Full Name	Approximate Level of Effort – LOE - (Hours This FY)	Country of Residence	National Academy Member? (Y/N)
Mahdi Sanati	160 hours	USA	N
<u>Performer Business Contact(s)</u> N/A			
<u>Additional (Non-Student) Team Members</u> N/A			
<u>Subcontractors</u> N/A			

8. Collaborations

Full Name	Organization	Collaboration Summary
Dr. Salvador Portillo	Electrical Engineering Department, University of New Mexico	Discussions on outgassing mitigation, with analyses and comparisons with experiments (either planned or carried out at University of New Mexico) pertaining to surface adsorbates.
Dr. Mahdi Sanati	Physics Department, Texas Tech University	Discussion and calculations of energies and binding of adsorbates or defects/dislocations based on Density Function Theory.

9. Students

<u>Doctoral Student(s)</u>			
Full Name	University	Graduated?	Graduation Year
Yagnya Pokhrel	Texas Tech University	No	05/15/2025

10. Technology Transfer

None.

11. Products, Publications, Patents, License Agreements, etc.**Archival Publications**

#	Citation	Acknowledged ONR Support Received? (Y/N)	Peer Reviewed? (Y/N)
1	Y. M. Pokhrel, S. Portillo, and R. P. Joshi, "Outgassing Reductions via Quasi-Isentropic Ramp Compression: A Molecular Dynamics Study in a Copper Anode," submitted for publication, June 2024 -- Under Review.	Y	Y
2	Y. M. Pokhrel, S. C. Shrestha, Y. Iqbal, S. Portillo, and R. P. Joshi, "Calculations for Preemptive Surface Adsorbate Drive Off to Minimize Plasma Formation During Operation of High Power Microwave Sources," <i>Journ. Appl. Phys.</i> 136 , 043303 (2024).	Y	Y

3	Y. M. Pokhrel, Y. Iqbal, S. C. Shrestha, M. Sanati, and R. P. Joshi, "Coupled Monte Carlo Density Functional Theory Calculations of Cold and Laser Assisted Electron Field Emission from a Graphene Coated Copper Cathode," <i>Journ. Appl. Phys.</i> 135, 223301 (2024).	Y	Y
---	---	---	---

Conference Papers No information to report.

Books No information to report.

Book Chapter No information to report.

Theses

#	Citation	Acknowledged ONR Support Received? (Y/N)	Peer Reviewed? (Y/N)
1	Yagnya M. Pokhrel, MS completed May 2024, "Molecular Dynamics Analysis of Outgassing With Self-Consistent Temperature Calculations for High Power Devices".	Y	Y

Websites No information to report.

Patents No information to report.

Other Products: No information to report.

12. Point of Contact in the Navy

None

Enhanced Free Recovery for Kilohertz Operation of Spark Gaps

Grant No. N00014-23-1-2801

Annual Report for Fiscal Year 2024

Period of Performance: October 1, 2023 to September 30, 2024

Prepared by:

Professor Jane Lehr,
University of New Mexico
jmlehr@unm.edu,



This work was sponsored by the Office of Naval Research (ONR), under grant/contract number N00014-23-1-2801. The views and conclusions contained herein are those of the authors only and should not be interpreted as representing those of ONR, the U.S. Navy or the U.S. Government.

Section I: Project Summary

1. Overview of Project

Executive Summary:

High power radiofrequency (HPRF) systems with high pulse repetition rate (PRR) capability create operational advantages by delivering an increased energy to the target even with moving platforms. Modulators based on Tesla transformers are of interest because of their compact size and the potential of using folded energy lines for further reductions in size and weight. The potential of these modulators is not yet realized because of the limitations imposed on the PRR by the spark gaps. The traditional method to increase the PRR uses a mechanical gas flow to sweep the arc byproducts from the channel volume and the system's PRR is determined by the mass flow rate in the gap. This approach manifests as a significant increase in system size, weight, power and complexity. This effort seeks solutions to increase the PRR capability in spark gaps operated under static pressure conditions by investigating parameters to decrease the time between pulses needed to regain the voltage holdoff. Under static pressure, this property is known as free dielectric recovery.

A testbed has been constructed which can operate at PRR of 1kHz at peak voltages of 50 kVDC. The testbed has the capability to perform both dielectric recovery measurements (determining the time between successive pulses to recover the withstand voltage) and demonstrate full repetitive operation. While the conventional wisdom holds that the insulating gas properties determine the PRR capability, UNM has tested three conventional switch geometries and observed deviations in performance with the same insulating gas. All three switches have been shown to operate in the range of 400-500 Hz. An alternative approach has also been tried which alters the electrode profile and has shown enhancements in the PRR operation. A major accomplishment is demonstrating that the switches physical geometry affects the dielectric recovery so that PRR capability can be designed into the switch.

Objective:

This effort aims to increase the pulse repetition rate (PRR) of spark gaps. Spark gaps operate over an astonishingly wide operating range and are the sole candidate for very high voltages. Of particular interest is spark gaps suitable for operation in a high-performance, Tesla transformer-based modulator for pulsed high power RF generation. Static pressure (sans gas flow) is essential for reducing the requirements from a "balance of system" perspective. The goal is to operate spark gaps, the only option for the Telsa transformer's secondary switch, at a PRR of 1 kilohertz.

Naval Relevance:

The Navy is interested in repetitive pulsed power because it allows more energy on target and a deep magazine. Compact and repetitive modulators are needed to drive the plethora of directed energy sources. The chosen circuit architecture has a high potential for a size and weight reduction by a factor of two to four when subsystems are included. The project underway is the essential enabling component for very high peak power repetitive systems.

Introduction/Background:

While it is known that high pressures and short gaps enhance the dielectric recovery, additional benefits can be achieved by modifying the electrode profile to adjust the characteristics of the

switch operation with voltage. To fully investigate the potential for repetitive HPRF modulators, the physics of recovery under long bursts will be studied to identify the role that heat plays by comparing it to the so-called “double pulse” experiments. Double pulse experiments are the conventional methodology for exploring repetitive operation where two separate pulsers are devised and applied to the test gap with a time gap. The time between pulses is measured to record the dielectric recovery which is, in turn, a measure of the repetition rate. The double pulse experiments, associated with the atomic recombination characteristics of the gas, are problematic because of deviations between two separate devices. This will be done with at least two energies to investigate early, astonishing reports that spark gap recovery is independent of the energy switched. These tests can be done using a Tesla transformer for the double pulse and burst tests. While hydrogen will be used as a baseline, the focus will be on gases of current interest such as air, nitrogen and carbon dioxide with the goal of eliminating the need for complicated high flow rate mass transfer in the system, known as free dielectric recovery. The use of hydrogen may yield high repetition rate spark gaps but introduces other complications for deployment.

If the hypothesis that heat deposition in the channel is truly the culprit limiting the PRR, targeted solutions can be conceived. One solution could include introducing turbulent flow via plasma jets to homogenize the temperature in the channel. Another is the investigation of a Supercritical Fluid (SCF), an intermediate state between gas and liquid, as insulating switch media. Supercritical fluids for high repetition rate modulators have the attractive properties of exceptional dielectric strength, high heat transfer capability, and low viscosity. Electrical breakdown strengths of 2700 kV/cm at a gap length of 100 microns have been demonstrated under uniform field conditions. Although widely used for chemical and industrial purposes, research on utilizing SCFs as an insulator is nascent and its application in high repetition rate applications, novel.

2. Activities and Accomplishments

Testbed: A switch testbed, shown in Figure 1, was constructed to discharge a bank of capacitors into a resistive load R_L through the spark gap under test. The testbed is charged with the 50kV ALE constant current power supply. The capacitance is deliberately kept small so that the full repetitive capability of the switch-under-test can be operated at rates up to 1 kHz. Initial tests showed voltage standoff of ~ 40 kV in atmospheric air before corona initiates. A Northstar voltage probe measures the voltage at either the charged side or the load side and a current viewing resistor (CVR) measures the current through the resistive load.

Repetitive pulsed power applications typically use specially designed, constant current power supplies to rapidly charge the capacitors in the primary energy storage stage. Conventional power supplies are constant voltage and take a time of at least $5RC$ to charge. Constant current supplies, on the other hand, quickly charge the capacitive load with a resulting linear voltage *ramp and hold* waveform, shown in Figure 2. It is controlled by an external control waveform, the inhibit signal, where the power supply is off when the signal is high and charges when the signal is low. The

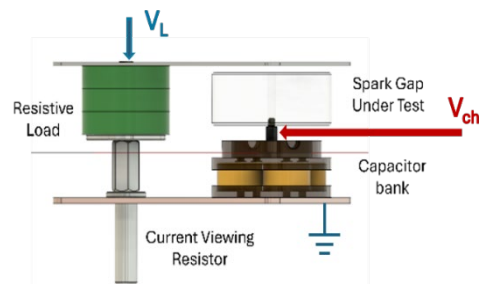


Figure 31 The single switch test bed is capable of 50kV and pulse repetition rates (PRR) up to 1 kHz.

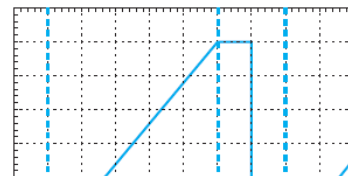


Figure 32 The charging waveform from a constant current power supply is controlled by an external TTL signal (the inhibit) which determines the PRR.

charge time is determined by the duration when the inhibit signal is off. The voltage is then held at that voltage level until switched when the spark gap fires. The PRR is the inverse of the period determined by the control signal.

Typically, switch characterization is done with a linear voltage ramp and recording when the spark gap switches. By varying the pressure and recording the voltage, the V - p curve is generated. This curve is an excellent indicator of the intrinsic switch quality. The TDK ALE supplies operate differently where it is “charge and hold” with the duration controlled by an inhibit signal. Voltage monitoring on the capacitor side of the switch shows that the voltage stays high past the charge duration, indicating the switch has not closed. This gives us a measure of the switch delay time for the untriggered switch. However, this is resulting in our rethinking the operational curve.

Initial testing was performed with a L3/Maxwell three electrode switch, shown in Figure 3a, in the untriggered mode. The testbed was characterized by discharging the switch to ground and measuring the current as shown in Figure 3b. This determines the stray reactance and resistance values for the circuit simulation model. Comparing Figure 3a and 3c, an assessment of the electrode indicates suboptimal switch operation because of the arc damage on the outer edge. The switch is being characterized by first doing a V - p curve with a conventional power supply, such as a Glassman voltage supply with a multi-second ramp. This provides a basis to judge the switch performance. We do this because the ALE operation has a ramp and hold for the capacitor charging so that time is another variable in determining operation. Experimentally, we saw that given enough time, breakdown would occur. This eliminates the full utility of the V - p curve but it does give an indication of the state-of-health of the spark gap.

The L3 spark gap is shown below after cleaning. It has two planar electrodes (of arbitrary profile) with a plane (for triggering, unused) between them. Looking at the arc damage after numerous discharges, it appears that many breakdowns occur at the edges, due to field enhancements at the edges, indicating the electrodes are not profiled.

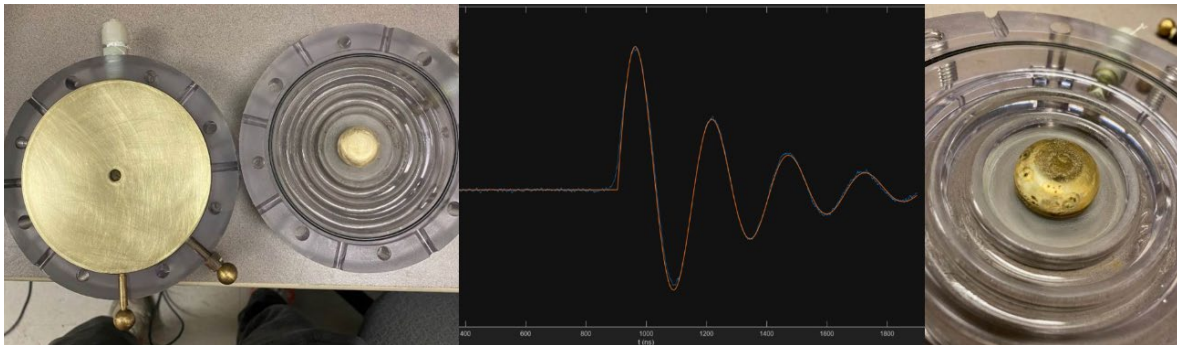


Figure 33 Initial testing was conducted with an L3 spark gap. (a) The refurbished switch showing the trigger plane and the spark gap electrode. (b) The testbed was characterized by measuring the short circuit current to determine the intrinsic R and L values of the realized fixture. (c) The arc damage pattern on the electrode indicates a field enhancement on the edge leading to unpredictable performance.

Since the 50kV test bed is set, a fit for its equivalent RLC circuit parameters was performed for a LT Spice model. The parameter extraction is done in MATLAB using a fit to the analytical circuit solution. The values are $R = 1.11\Omega$, $L = 198.15\text{nH}$ and $C = 8.16\text{nF}$. The capacitance is reduced from its nominal value by the addition of stray capacitance. These values are modified with the ASR spark gap due to accommodation in the size and attachment hardware with resultant parameters of $R = 0.76\Omega$, $L = 176\text{ nH}$ and $C = 8.6\text{ nF}$. The L3 gap proved to be problematic and

was replaced by a similar spark gap, shown below in Figure 4, made by Montena. It is also a three-electrode spark gap with a planar trigger plate operated in self-break mode. Spark gaps made by ASR, shown in Figure 4b, are also used. The ASR switch has a much higher operating pressure capability.

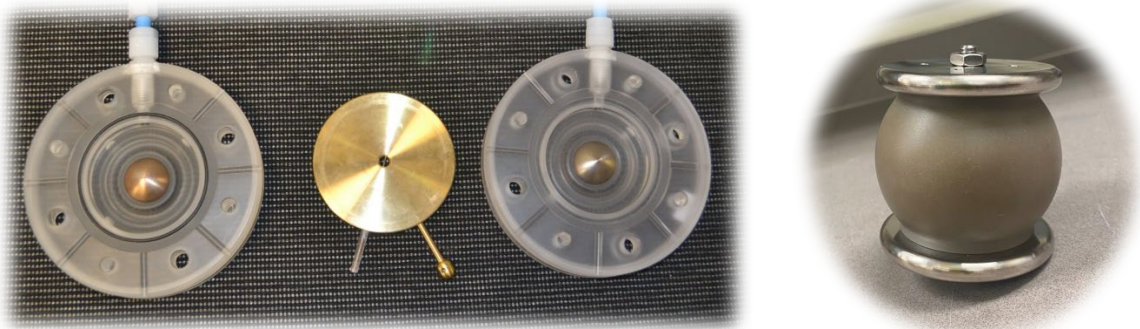


Figure 34 Multiple spark gaps were tested including (a) a Montena three electrode spark gap and (b) The ASR switch.

The vast majority of dielectric recovery experiments use a “double pulse” technique where pulses are applied from two separate generators with a variable time delay (interpulse) between them. This time is then adjusted until the pulse gains its full amplitude which is then termed the time to full recovery. Here, a true repetitive operation was demonstrated. Initially, it was assumed the power supply’s *inhibit* signal would be used as the dielectric recovery time. In Figure 5, the correlation between the inhibit signal and the voltage charging waveform are shown. The inhibit signal (shown in orange) controls the time the voltage is charging the capacitor. When the spark gap switches, the voltage returns to zero. When a voltage divider is placed on the resistive load, the true repetitive operation can be observed using the Fast Frame mode on the digitizer. Typical data from the Montena switch is shown in Figure 6 showing five pulses in a 5000 pulse burst at the beginning, middle and end. This data indicates full recovery.

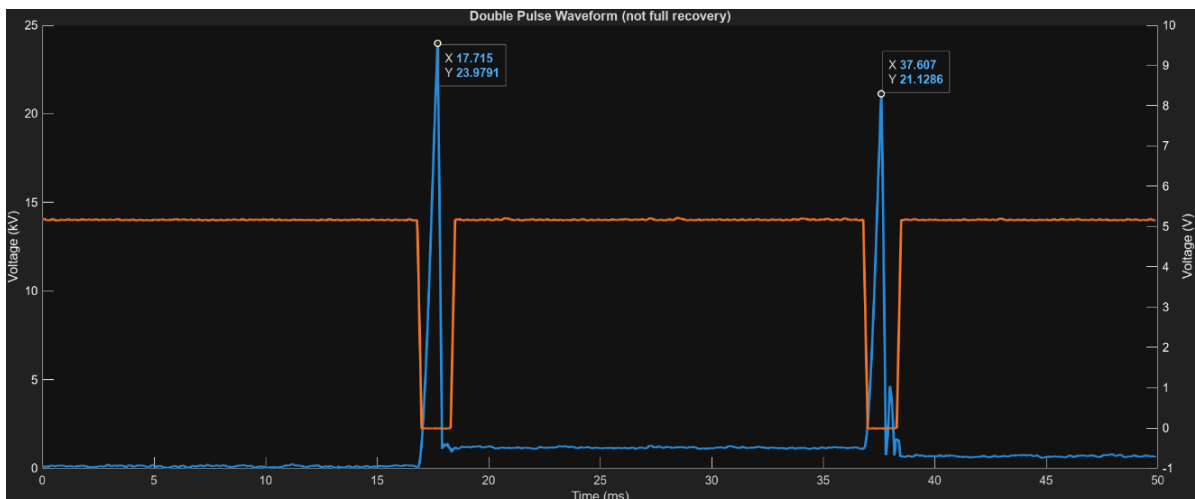


Figure 5 The charging waveform must be carefully set so that the switch doesn’t run long. This presents as non- recovery when it is truly a charge side issue.

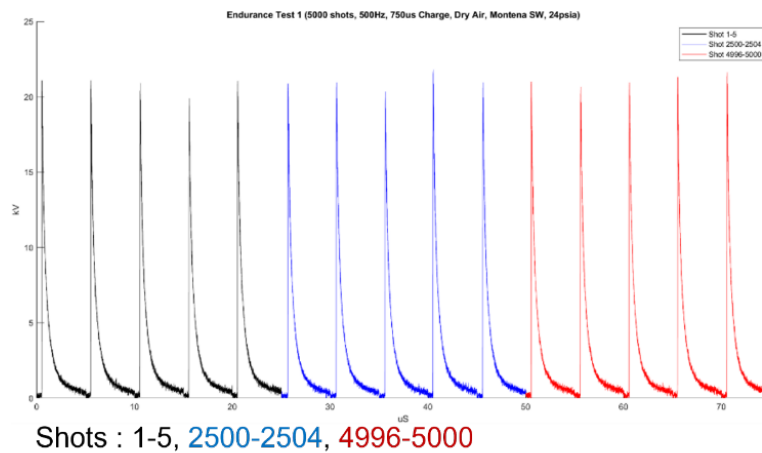


Figure 6 A 5000 shot burst with the Montena switch shows 500 Hz operation. This long burst test captured 5 pulses in the beginning, middle and end of the run to look for degradation.

An issue with the operation was quickly identified and shown in Figure 7. When the high side voltage is measured, if the inhibit signal is not optimized, the first pulse has a long delay time before switching and the voltage stays high for several milliseconds. The second pulse arrives 10ms (corresponding to 100 Hz) after the start of the first pulse but breaks early because the time between the last breakdown and the second pulse arrival (the quantity relevant to the dielectric recovery time) is too short. This is an unusual way to monitor switch operation but provides valuable information on switch operation. Moreover, it appears that the first shot often has a significantly longer delay time than subsequent shots. By monitoring the high side of the spark gap, we see that not only that this is not viable but that it casts doubt on the double pulse experiments where this is not seen.

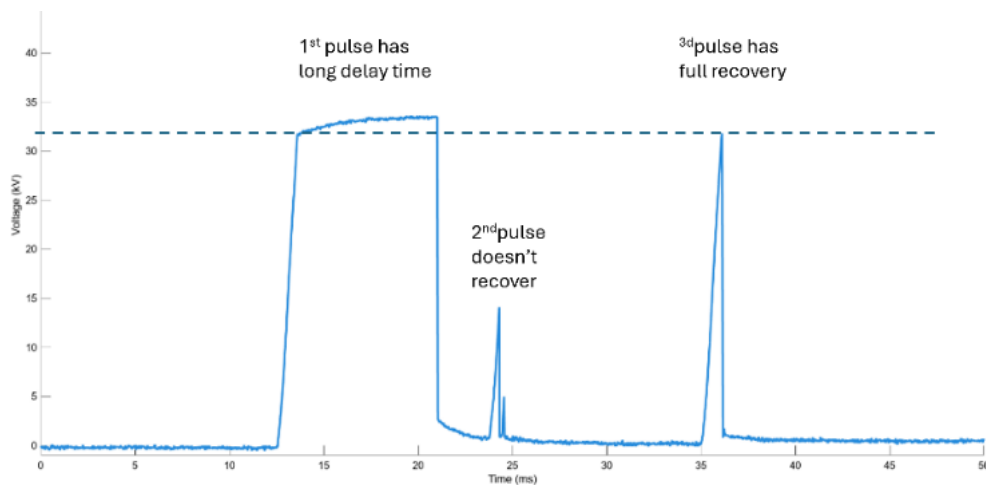


Figure 7 The charging waveform and breakdown (blue) overlaid with the control signal (orange). The charge side voltage measurements contain information on the delay time to breakdown even with a DC charge.

System Miscontrol: In many instances, it is deceptively convenient to think of repetitive systems as being identical to single pulse ones. Therefore, it is particularly important to identify

the circumstances where repetitive systems are different. We have identified one such scenario where the charging waveform and its control are not set properly and the current in the load appears to be inconsistent. This presents as though the switch is not recovering when, in fact, the charging side parameters are improperly set. To illustrate, in Figure 8, the top is the pulse train of “inconsistent” load current. The bottom figure is the voltage waveforms on the charging side of the switch, along with the non optimal control (inhibit) signal which is at the heart of the problem.

The first two pulses switch as expected but the third pulse has a very long time to breakdown (delay time) after charge is complete and is said to “run long”. This results in an excessive time between the second and third pulses and also affects the fourth pulse. The duration between the third breakdown and the start of the charging cycle for the fourth pulse is insufficient for the gas to recover its dielectric strength to hold off the voltage, and it breaks at a much lower voltage. However, the control signal is a fixed duration and continues to charge the capacitor so that at the end of the cycle, a voltage remains on the switch, causing the fifth pulse to breakdown early in its cycle and at a lower voltage. This early run time consequently leaves a voltage on the switch again leading to further reduced recovery. Of course, it is customary to monitor the load current to verify PRR operation. However, the load indicates sporadic currents and one could easily conclude the switch was not recovering when in fact, the switch is not properly controlled.

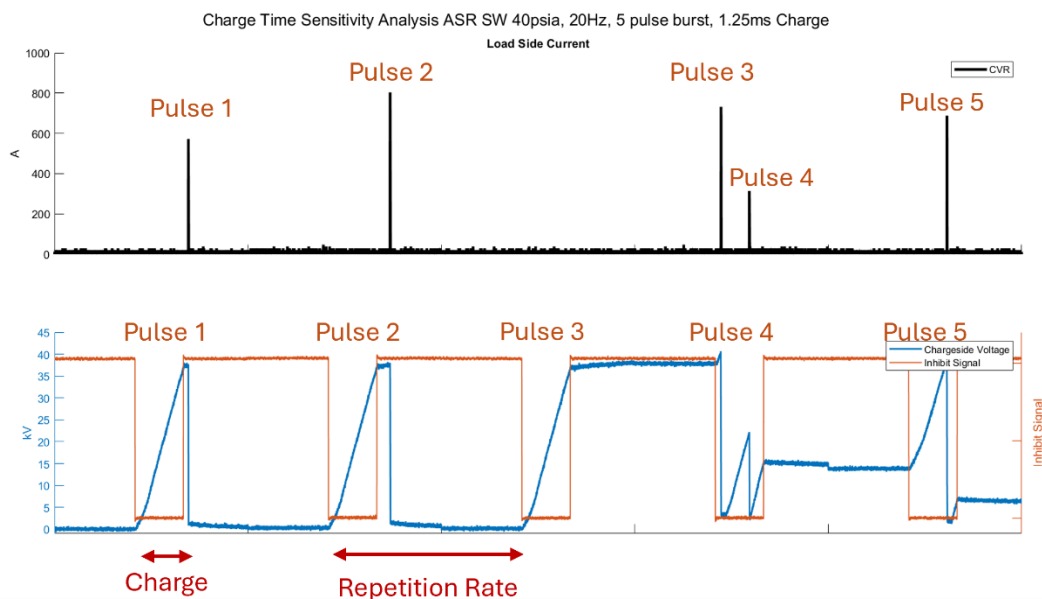
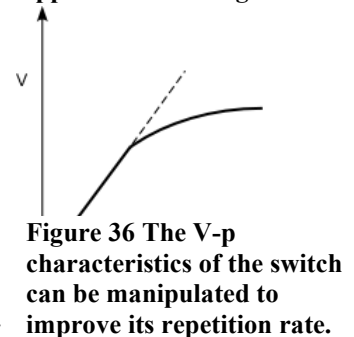


Figure 35 The load current and the charging waveforms show that what appears to be irregular switching (expected from a gap not recovering) is actually the gap not properly set.

Altered Profile Switch The possibility to passively increase the PRR is very attractive from a system perspective. It is thought that residual heat left in the spark channel alters the local pressure and that full dielectric recovery occurs only when the so-called similarity parameter pd , is regained. The similarity parameter is the well-established scaling parameter for collisional physics. This opens the possibility that tailoring the operating characteristics (V- pd curve) can lead to enhanced recovery.



Specifically, deviations from the linear relationship would produce similar operating voltages across some range of pressures. Dielectric recovery occurs with the return to neutral density in the spark channel. Nonuniform geometries may be used to alter the V - p curve so that at relative low pressures the rate of change of the breakdown voltage is decreased. Thus, by minimizing $\partial V / \partial p$, a switching gas will recover its insulating properties more quickly because it is less dependent on the deviation from the neutral density. This was anticipated to improve voltage recovery and PRR with only average density recovery.

A suitable switch was designed and fabricated to test the concept. The switch, referred to as “The Donald” after its designer, can be used in either the baseline plane-to-plane (“flat”) configuration or with a specialized electrode with an altered electrode profile (the “baby belly button”). The Donald had a design pressure of 1000psi and was pressure tested to failure (o-ring) at 600 psi. Thus, operation to 200 psi is permissible. We suspect that the operation of the specialized electrode invokes the phenomena of corona stabilization. Corona stabilization is a process that occurs in strongly electronegative gases which involves the charge dynamics of ions and electrons within the gas. The approach is to exploit these dynamics to extend the PRR capability. If the operational principle is corona stabilization, only PRR improvement when a negative voltage was applied to the nonuniform electrode is expected. Moreover, it is unclear if air is sufficiently electronegative to have a pronounced effect.



Figure 37 The Donald was made in house for testing flat and “belly button” electrode profiles.

The first test of The Donald was to look at the V - p curve, with no discernable effect from the altered electrode. It was also assessed for PRR performance. The “belly button” is not very pronounced and will be increased in the next iteration. PRR testing, however, shown in Figure 11, had marked improvement. Figure 11 below shows operation at 200 Hz showing that the flat-flat configuration does not recover – which is interesting – and the addition of the belly button shows full recovery.

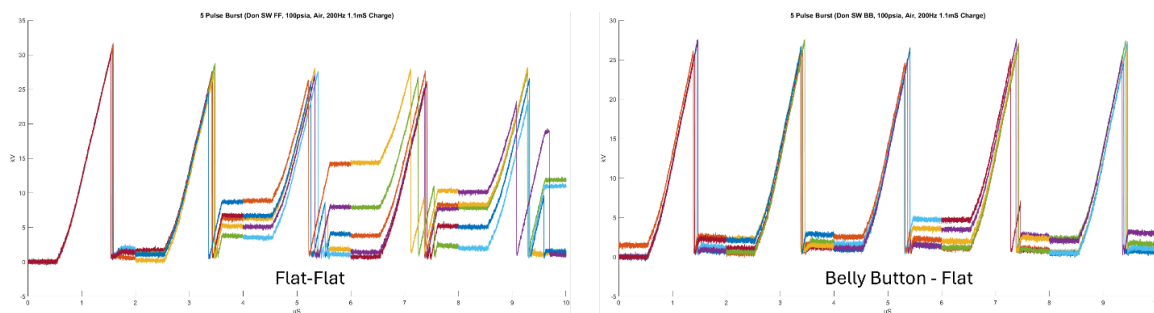


Figure 38 The Donald switch with the flat-flat electrode profiles do not recover at 200 Hz but when one electrode is a 0.5mm belly button, recovery was significantly improved even without observable change in the V - p curve.

The most significant finding of this test is the contrast to that of the ASR and Montena switches because it shows that the physical implementation of the switch influences the PRR performance even with the same gas. This implies that PRR can be engineered, at least to some extent, and is not solely dependent on the gas species.

A major concern is the voltage range over which the switch will operate. Since our objective is the secondary switch on a Tesla transformer, the voltage threshold is essentially the DC value. This may mean that the pressure may get very high to hold off the voltage.

Free Dielectric Recovery and Switched Energy: In devices where electrical breakdown is operative, the pulse repetition rate is dependent on the time it takes for the insulating gas to regain its voltage holdoff – a property known as dielectric recovery. This is primarily of interest for gases because solids are damaged during the breakdown process and the molecules in liquids tend to align in the electric field without mechanical agitation. Because of the difficulty in performing research on repetitive operation, gases were screened using the methodology of free dielectric recovery, with “free” referring to static pressure conditions.

Starting in the 1980s through the mid-90s, a significant research effort into repetitive spark gap switches was performed at NSWC-Dahlgren. Testing was performed with various pulses and confirmed the trends still in use today: small gap lengths, high gas pressures and high electric fields aid in recovery. Moreover, extensive testing showed the role of the gas species in the recovery process and identified hydrogen as having superior properties. Additionally, the broad study found the startling conclusion that the free dielectric recovery of spark gaps is (mostly) independent of the switched energy. In a summary paper, Grothaus (1993) cites earlier work with stored energy ranging from 5 J to 12.5 kJ as yielding the same dielectric recovery times. While hydrogen became the gas-of-choice for extremely high voltage, short pulse repetitive systems, it was found that flowing gas through the spark gap improved the pulse repetition rate to the ~ 200 Hz range. This, however, leads to larger and more complicated HPRF systems.

In practice, realized systems appear to achieve much more modest pulse repetition rates. An examination of that experimental series shows the data was taken with vastly different test setups and with limited data sets. However, those results are consistent with some more studies with confined parameters. Korytchenko (2021) studied the influence of spark length on the discharge parameters and the distribution of thermodynamic parameters of the gas during its development. A linear relationship between the gap length and the deposited energy was found for total energy >10 J after a threshold. This appears consistent with Churchill (1971), Reddy (2016) and Diswas (1998) who found recovery to be nearly independent of gap length but highly dependent on electrode area.

This forms the basis for a theoretical investigation into how this seemingly incongruous observation could be true. First, if the recovery is independent of switched energy, then the process cannot be very lossy. First, we consider the discharge process is deconvolved into three phases: charging, the resistive fall and the fully formed arc. The first phase is when the voltage charges the capacitance of the spark gap, and the effective switch impedance is high. With no current flow, the energy lost to the switch is negligible. The last phase is the fully formed arc, where the circuit model is a gap length dependent inductance with a small series resistor to account for finite conductivity. The resistor has a value of ~ 100 mΩ. These values are slightly length dependent, but difficult to discern because the length scales do not change too much. Because the major parts are energy storing reactive elements, loss in the post-breakdown phase is only from the small series resistance.

The resistive fall phase is more complicated as breakdown is developing. A small amount of energy is expended in collisions and ionization, a larger expenditure occurs in expanding the streamer channel (~100μm radius) to accept the circuit limited current. This energy is absorbed by the gas for expansion of the spark channel and can be considered a positive $L\dot{}$ term which is a loss. This is consistent with the UNM circuit model for the high-pressure spark gap where the Vlasov model captures the resistive phase initially developed for exploding wires. Initially, the switch has a sufficiently high impedance that power cannot flow into the load. As the discharge evolves, the

switch impedance collapses so that as the switch impedance approaches the load impedance, power may be delivered to the load. This occurs during a portion of the switch risetime when the channel is being established.

If the energy absorbed in the gas W_{loss} for a peak power $P_{peak} = I_p V_p$, the normalized quantity can be calculated with units of time and is shown in Figure 12. In the expression, the energy loss for a given gap length is controlled by the parameter ζ which has a functional dependence on the pressure and the electrical breakdown field in the form $\zeta = \sqrt{p} \times E_{BD}^{-1.3}$. The pressure term is the work done in moving the gas in channel expansion so that high pressures require more work and is counterbalanced by driving the channel expansion harder. The electric field can be increased by either pulse charging the gap and/or by increasing the pressure.

The immediate study is for a dual resonant Tesla transformer. On one side is a DC charged switch to feed the energy from the primary energy store into the transformer. The other switch controls the secondary stage with timescales \sim microseconds. This means that for the purpose of estimating electrical breakdown fields, the DC values may be used without significant loss of accuracy. This is fortunate because a very good estimate of the DC breakdown of air exists and captures the functional dependence with pressure and gap distance and is shown below.

This plot of the normalized energy loss in Figure 12 shows that with increasing pressure, the energy loss drops drastically for pressures < 10 atm and decreases more slowly after that. It is also notable that at low pressure, the gap distance has an effect. At elevated pressure, the difference with gap size is indistinguishable.

This is consistent with reported observations:

- the PRR dependence on gap length is minimal.
- increasing pressure decreases recovery time/increases PRR.
- for pressures $p > 5$ atm, the energy loss per switch will at least appear to be largely independent of transferred energy.

A similar analysis as that presented for air is not possible since there is not a good estimate for the variation of DC breakdown with pressure for hydrogen. The pressure factor is actually gas density normalized to that of air at NPT. In looking at the factor $\sqrt{\frac{\rho}{\rho_0}}$ with pressure, it is clear that hydrogen will have significantly less energy loss than air at a given pressure. Tests to validate these predictions are planned for the next year and will likely take the form of measuring the rise in temperature of the electrode surface.

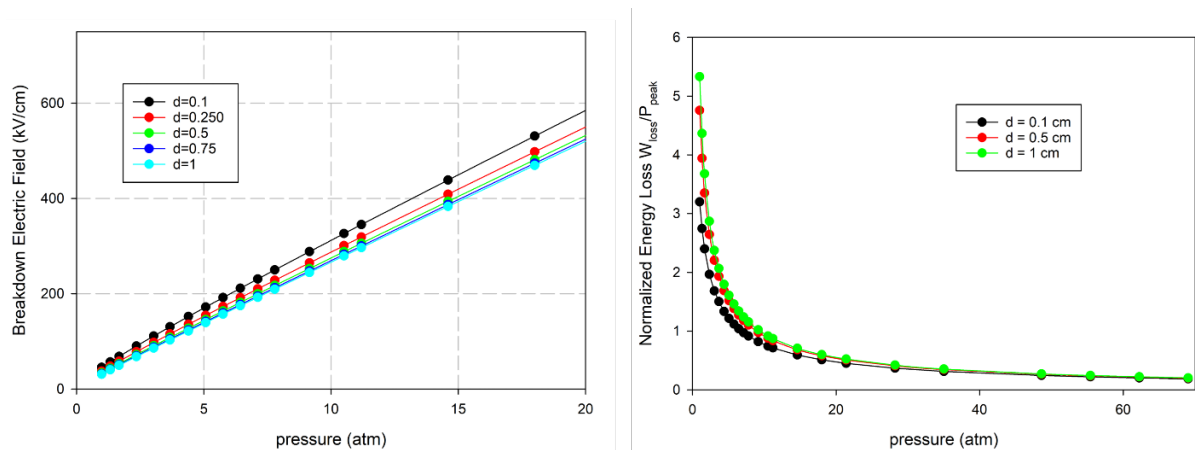


Figure 39 (a) The electrical breakdown field as a function of pressure, parameterized by gap distance (a) is used to estimate the normalized energy loss with gas pressure for a Thevenin equivalent 50Ω load.

References:

- [1] Turnbull, S. M., S. J. MacGregor, F. A. Tuema, and J. Harrower. "The repetitive operation of a spark gap column." In *Digest of Technical Papers. 11th IEEE International Pulsed Power Conference*, vol. 2, p. 899, 1997.
- [2] X. Cai, L. Wang, X. Zou, X. Wang and W. Jiang, "Overvolted breakdown and recovery of gas spark gap," *2010 IEEE International Power Modulator and High Voltage Conference*, Atlanta, GA, USA, 2010, pp. 541-544, doi: 10.1109/IPMHVC.2010.5958414.
- [3] MacGregor, Scott J., Steven M. Turnbull, Fadhil A. Tuema, and Owen Farish. "Enhanced spark gap switch recovery using nonlinear V/p curves." *IEEE Transactions on Plasma science* 23, no. 4 (1995): 798-804.
- [4] Korytchenko, K. V., I. S. Varshamova, O. V. Shypul, D. Samoilenko, A. Lisniak, S. V. Harbuz, and K. M. Ostapov. "Numerical simulation of gap length influence on energy deposition in spark discharge." *Электротехника и электромеханика 1 (eng)* (2021): 35-43.

3. Findings and Conclusions

A key finding is the observation that PRR is not solely determined by the properties of the gaseous insulator. We have demonstrated significant variations in dielectric recovery times with conventional spark gaps with different geometries with UZ Air as the insulator. Testing with 4 different conventional spark gaps shows different levels of recovery even with the same gaseous insulator. This implies that repetitive capability can be engineered into switches!

The best recovery happens with a three-electrode spark gap. We hypothesize the large third electrode acts as a heat sink.

Novel theoretical analysis of the breakdown process has determined that energy is lost to the spark channel formation almost exclusively during the resistive fall. This provides a quantitative predictive tool that also explains the qualitative observations.

By monitoring the charge side of the switch, we identified a performance anomaly where the switch appears to fail the PRR but the switch is actually running long. This is easily fixed by careful

calibration of the operating curve. This may explain the seeming failure of the secondary switch on a tesla transformer.

Experiments observing the PRR over an order of magnitude range of currents at the same switching voltage show that PRR is independent of current.

Preliminary results with the “belly button” switch show improved PRR performance relative to flat electrodes even with no discernable change in the V - p characteristics. More pronounced belly button electrodes are being fabricated.

4. Plans and Upcoming Events

Our investigation to date has indicated that a key element of the dielectric recovery to increase the PRR of generic spark gaps is the removal of the heat deposited by the previous spark from the channel. This can be conceptually related to the Paschen curve where the temperature decreases the local pressure, resulting in a lower breakdown voltage. This related dielectric recovery to the return of the neutral density. To investigate the role of heat generation in the spark gap, a rugged fiber optic-based thermal monitor has been identified to measure the temperature rise in an electrode. A spark gap will be constructed where the support will either be a heat sink or an insulator. The temperature rise can be investigated and related to the theoretical estimate completed this year. This will be supported through Multiphysics simulations with COMSOL to generate designs for a thermal balance.

The “belly button” electrode has shown encouraging results to passively increase PRR in spark gaps. The theory of operation involves dynamic charge redistribution under static voltage excitation in electronegative gases. Demonstrations with a variety of gases will be performed to validate the hypothesis. Larger protrusions have been fabricated to investigate their effect. Because of the dependence on separation of the ion and electron densities within the gas, it is unclear as to whether the attributes of the belly button will scale to higher voltages. A demonstration with a switch appropriate to a secondary side of the tesla transformer would be beneficial but predictions will also be developed.

A full demonstration of the Tesla transformer is planned for the next year. This past year’s results used a mockup of the primary side of a Tesla transformer and the theoretical work implies the recovery should be identical on the secondary side. An explicit test is warranted because it is not possible to operate a spark gap at different voltages under identical gap d and pressure p conditions.

5. Transitions and Impacts

In past efforts to increase PRR, the focus has been on the properties of gases and trends with operational parameters. This has led to the widespread use of high-pressure hydrogen for repetitively operated spark gaps. While hydrogen has some outstanding properties, there are many circumstances where it is undesirable so that a lower pressure alternative is enabling or at least very attractive.

Our direct transition partners in this effort are Semsol (Isaac Blesner) and NSWC DD (Cameron Pouncey) who have Tesla transformer-based modulators currently in development. Those efforts are large and complex systems that will use hydrogen to achieve the PRR. Both are aware of our efforts and the focus on the root cause and design centric solutions that can be retrofitted or

incorporated into next generation modulators. Other entities have shown interest including APELC (Jon Mayes) and Raytheon (Eric Berry).

6. Recommendations for Future Work:

Future work could expand the effort to look at mitigation techniques for overvolted recovery. In this effort, the dielectric recovery is primarily limited to the DC range because of the specific application to the secondary side of a Tesla transformer. The resonant condition requires a long charge time of a few microseconds in highly coupled systems which corresponds to the DC value for pulsed power purposes.

The Tesla transformer-based modulators are very attractive for high PRR systems. Of particular interest is the SINUS series from Russia where techniques have been developed to reduce the overall size of the modulator by incorporating such innovations as spiral, double and triple forming lines for pulse forming.

7. Personnel

Principal Investigator			
Full Name	Approximate Level of Effort – LOE - (Hours This FY)	Country of Residence	National Academy Member? (Y/N)
Jane Lehr	350 hours	USA	N
Co-Investigator(s) or Co-PI(s)			
Full Name	Approximate Level of Effort – LOE - (Hours This FY)	Country of Residence	National Academy Member? (Y/N)
N/A			
Performer Business Contact(s)			
Full Name	Role	Country of Residence	
Sandra Griffenberg	N/A	USA	N
Additional (Non-Student) Team Members			
Full Name	Approximate Level of Effort – LOE - (Hours This FY)	Country of Residence	National Academy Member? (Y/N)
N/A			
Subcontractors			
Full Name and Organization	Approximate Level of Effort – LOE - (Hours This FY)	Country of Residence	National Academy Member? (Y/N)
N/A			

8. Collaborations

Full Name	Organization	Collaboration Summary

Isaac Blesner	SemSol	Semsol is building a tesla transformer based system so that we share progress/insights/history
---------------	--------	--

9. Students

<u>Doctoral Students</u>			
Full Name	University	Graduated?	Graduation Year
Donald Mercer	University of New Mexico	N	05/15/2027
Torin Sammeth	University of New Mexico	N	12/15/2026
<u>Masters Students</u>			
Full Name	University	Graduated?	Graduation Year
Alex McDonald	University of New Mexico	N	12/15/2025
<u>Undergraduate Students</u>			
Full Name	University	Graduated?	Graduation Year
Quentin Bean	University of New Mexico	N	05/15/2025
Max Starceski	University of New Mexico	N	05/15/2025
Trinity Watson	University of New Mexico	N	05/15/2025

10. Technology Transfer

Because the potential parameter space is very large and the navy has the specific application in mind, we have restricted our research focus to the spark gaps in a tesla transformer driven HPM system. We regularly speak with Dr. Pouncey as well as Dr. Isaac Blesner and Dr. Peter Duselis of SemSol who are both building Tesla transformer-based systems as the transition is direct. The Directed Energy program at Raytheon saw the student presentations at DEPS and inquired as to our progress. I have spoken to Dr. Eric Berry and Dr. Walters on a few occasions. Dr. Huhlman is looking at higher voltage spark gaps for an upgrade of Mercury. This effort can help in some critical aspects of that effort such as prefire rate.

11. Products, Publications, Patents, License Agreements, etc.

Publications resulting from this project for the reporting period:

Archival Publications

No Information to Report

Conference Papers

#	Citation	Acknowledged ONR Support Received? (Y/N)	Peer Reviewed? (Y/N)
1	A. McDonald, T. Sammeth and J.M. Lehr, "Enhanced Free Dielectric Recovery for kHz Operation of Spark Gaps," Directed Energy Professional Society Science and Technology Symposium, 2024.	Y	N
2	T. Sammeth, A. McDonald and J.M. Lehr, "Spark Gap Recovery for High Repetition Rate Tesla Transformer Pulser," Directed Energy Professional Society Science and Technology Symposium, 2024.	Y	N

Books

No Information to Report

Book Chapter

No Information to Report

Theses

No Information to Report

Websites

No Information to Report

Patents

No Information to Report

Other Products:

No Information to Report

12. Point of Contact in U.S. Navy / Marine Corps

Full Name	Organization	Date of Last Contact
J. Cameron Pouncey	NSWCDD	09/15/2024
Jack Chen	NSWCDD	10/1/2024
Matthew McQuage	JDETO	8/15/2024
Brett Huhlman	NRL	9/25/2024

Distributed Coordination of Aerial Swarms for High-Gain Wireless Transmission

Grant No. N00014-20-1-2389

Annual Report for Fiscal Year 2024

Period of Performance: October 1, 2023 to September 30, 2024

Prepared by:

Dr. Jeffrey Nanzer, Principal Investigator
Associate Professor, Electrical and Computer Engineering
Michigan State University
428 S Shaw Lane, Room 2120 Engineering
East Lansing, MI 48824
Tel: (517) 432-8089
Email: nanzer@msu.edu



MICHIGAN STATE
UNIVERSITY



This work was sponsored by the Office of Naval Research (ONR), under grant number N00014-20-1-2389. The views and conclusions contained herein are those of the authors only and should not be interpreted as representing those of ONR, the U.S. Navy or the U.S. Government.

Section I: Project Summary

1. Overview of Project

Executive Summary:

This report provides a summary of progress made towards distributed synchronization of separate wireless systems for distributed beamforming operations. Distributed beamforming requires accurate synchronization of the electrical states of the nodes in a distributed array to ensure that transmitted signals arrive sufficiently aligned at the intended destination so that the signals add constructively, yielding significant increases in signal power at the destination. In this report, we summarize the objectives of this effort and report on advancements made in the areas of decentralized electrical state coordination, distributed localization, and experimental implementations of the concepts developed in this effort.

Objective:

In this effort, we will develop novel decentralized coordination techniques for high-gain transmission from swarms of hundreds of nodes and evaluate the possibilities of achieving high-gain signal transmission using existing commercial off-the-shelf (COTS) microwave technologies. In particular, we will investigate new techniques for the coordination of large arrays using decentralized consensus algorithms based on physical-layer coordination of array element location, frequency, phase, and time. We will assess the feasibility of achieving high-power transmission under realistic system-level constraints, such as coordination errors, noise, array motion, amplifier efficiencies, and beam steering errors, among others. The results of this effort will inform future high-gain microwave transmission concepts and identify any technology areas for future development to achieve greater capabilities than COTS technologies can provide. The proposed research directions are two-fold:

- Develop a distributed approach enabling the coherent coordination of the spatio-electrical states of arrays consisting of hundreds of nodes, investigate the possibilities of using distributed optimization for high-gain microwave signal transmission, and demonstrate distributed signal transmission in a scaled testbed.
- Develop system design rules for achieving specified high-gain signal requirements, determine bounds on achieving high levels of coherent gain given system specifications, provide notional designs based on COTS technologies, and identify areas for future technology development.

Naval Relevance:

Achieving large signal gains in wireless systems has traditionally been approached through a platform-centric model, relying on improving the power-handling capabilities and efficiencies of transmitter technologies. We propose a novel alternative approach that achieves increases signal gain through the coherent aggregation of the signals emitted by a large network of small wireless systems. Since such a distributed array is easily scalable by adding additional low-cost nodes, it will enable future Navy applications to achieve greater operational range, higher power delivered to a destination, and increased robustness to interference and failures without the need to develop new hardware technologies.

Introduction/Background:

Current and future wireless applications, including sensing, communications, and high-power transmission, have driven the need for continual increases in transmitted signal gain. However, the ability to achieve high-gain wireless transmission of microwave signals is restricted by the traditional platform-centric model used to develop wireless systems, where single, large platforms are limited by aperture size, device power handling and efficiency, and heat dissipation, among other factors. Achieving increases in signal gain under the current platform-centric model requires redesigns of devices, apertures, or entire systems, an approach that is not only costly but time-consuming. To overcome these platform-centric challenges, we propose a novel approach to high-gain microwave signal transmission using distributed, scalable arrays of small, low-cost platforms, each with individually low-power transmitters. In particular, coordinating separate wireless systems to create a coherent distributed phased array can yield dramatic system-level gains that cannot feasibly be achieved with a single platform, or even with non-coherent signal coordination on multiple platforms. These benefits include transmit power gains proportional to the number of platforms squared, significant spatial diversity affording robustness to interference and failures, and the ability to directly scale capabilities by simply adding or removing nodes in the array. The ultimate level of flexibility is achieved in an open-loop array, where the nodes self-align without using feedback from the target location. Whereas closed-loop distributed arrays are possible with signal inputs from the target, such approaches are limited in that the array can only direct signals back to the point of the emanating signal. In contrast, open-loop distributed phased arrays can arbitrarily steer beams to any desired angle.

Achieving coherent transmission in distributed arrays requires coordination of the spatio-electrical states of the elements in the array; our group has pioneered efforts in developing technologies for high-accuracy coordination for distributed beamforming in small arrays of 2-4 platforms. Our group has extensive experience developing open-loop distributed phased arrays through our prior efforts developing and demonstrating critical technologies enabling fully open-loop coherent distributed transmission, which have demonstrated the feasibility of achieving and maintaining sufficient phase stability between separate platforms. In prior efforts, a high-accuracy microwave ranging technique using a novel spectrally sparse waveform achieved sub-mm range accuracy and was used to experimentally demonstrate the first open-loop coherent distributed transmission. Other efforts developed a novel one-way wireless frequency locking approach, which was used to demonstrate the first fully wireless open-loop distributed phased array. Current efforts are focused on building cognitive-enabled adaptive coordination algorithms that are robust to changing environmental conditions. The outcome of these efforts is that the basic coordination technology to achieve distributed phase coherence with small array sizes has been largely proven. The challenge for high-gain microwave applications is in creating a framework amenable to coordinating hundreds of nodes or more. The proposed effort is, to our knowledge, the first to investigate approaches to implementing distributed coordination in large-scale arrays of tens to hundreds of nodes, and to explore the implications of array scalability.

2. Activities and Accomplishments

In this reporting period, we made significant progress in the development of technologies and techniques for wireless decentralized localization of distributed phased array elements, distributed transmission and reception, and multiobjective distributed beamforming. Specifically, in this reporting period we:

- Implemented a distributed localization algorithm based on our decentralized time synchronization algorithm developed in earlier years on this effort;
- Demonstrated distributed transmission and distributed reception of signals using wireless coordination;
- Demonstrated multiobjective distributed beamforming from a three-node distributed phased array system.

Our results on these topics are described in the following.

a. Distributed Localization of Array Elements¹⁴

One of the fundamental challenges for beamforming from a distributed array is that the transmitted signals must be tightly aligned in phase. In order to achieve 90% probability of high coherent gain (a common metric for beamforming), the ranging RMSE must be less than $\lambda/15$, where λ is the wavelength of the carrier frequency. After estimating the internode ranges, the relative locations of the elements can be computed. SDR clocks are first coarsely aligned with a single pulse from the PPS output of a reference SDR. Then, using a two-way time alignment method in combination with time-division multiplexing for scheduling, bias offsets between the local clocks of nodes N_i and N_j , denoted by Δ_{ij} , are computed. These are added to local clocks through an implementation of an average consensus method with a Metropolis-Hastings mixing matrix to achieve clock synchronization. Channels are assumed to be quasi-static (symmetric and reciprocal) over the synchronization epoch. In order to minimize digitization errors, the received matched filter output is refined using quadratic least squares (QLS) peak interpolation. The delay τ_{ij} of a transmitted signal for a quasi-static channel is given by

$$\tau_{ij} = \frac{(t_{RXi} - t_{TXj}) + (t_{RXj} - t_{TXi})}{2}$$

where t_{TXi} , t_{RXi} , t_{TXj} , and t_{RXj} are the transmit and receive timestamps at nodes N_i and N_j , respectively. In general, this delay can be expressed as the sum of system hardware delays τ_{proc} and the real propagation delay, so that the distance estimate d_{ij} is given by

$$\hat{d}_{ij} = (\tau_{ij} - \tau_{proc})c$$

where c is the speed of light in free space.

For many applications, it is desirable to localize distributed topologies of large arrays of N elements. Metric multidimensional scaling (mMDS) takes as an input the Euclidean distance matrix (EDM) \mathbf{D} for a point set, which is an $n \times n$ symmetric and positive semidefinite matrix; and the dimension r of the output coordinate space. For each i and j , the entry $[\mathbf{D}]_{ij}$ represents the squared distance estimates between nodes i and j . We then obtain the double-centered Gram matrix \mathbf{G} of \mathbf{D} . Using eigenvalue decomposition, we then exploit the rank-deficiency of \mathbf{G} to produce an

¹⁴ Dula, Matthew J., Naim Shandi, and Jeffrey A. Nanzer. "Decentralized Localization of Distributed Phased Array Elements Using High-Accuracy Ranging and Multidimensional Scaling." 2024 IEEE Wireless and Microwave Technology Conference (WAMICON). IEEE, 2024.

$n \times r$ matrix, \mathbf{X} . The columns of \mathbf{X} are the eigenvectors corresponding to the r largest eigenvalues of \mathbf{G} , and the i^{th} row of \mathbf{X} represents the coordinates of node N_i .

The aim of the mMDS algorithm is to minimize the following stress function:

$$S(\mathbf{X}) = \sum_{i < j \leq N} [\hat{d}_{ij} - d_{ij}(\mathbf{X})]^2$$

where \hat{d}_{ij} is the input distance estimate between nodes i and j , and $d_{ij}(\mathbf{X})$ represents the distance between nodes i and j of the recovered points \mathbf{X} . Because the mMDS algorithm minimizes the stress function, it will return the desired coordinates if the internode distance estimates contain no error and the EDM represents a set of points constrained to the r -dimensional subspace to be recovered. We demonstrate that the approach will successfully recover point approximations even in the case of noisy distance estimates.

In order to demonstrate the efficacy of the proposed algorithm for localization, an experiment was conducted in an indoor lab environment using six Ettus Research X310 SDRs, each equipped with a UBX-160 daughterboard and a Pulse Electronics SPDA24700/2700 dipole antenna, designed to operate in a central frequency range of 1.7 to 2.1 GHz (See Figs 1 and 2). Dipole antennas were chosen since their azimuth radiation pattern is appropriate for generally unknown node locations. Frequency alignment was achieved by designating node 0 as the reference frequency and locking nodes 1 through 5 to node 0 in series. (Wireless frequency alignment may be achieved in various ways as demonstrated in our previous report) The SDRs were controlled by a desktop PC running GNURadio. In order to establish baseline locations for the nodes, the experimental space was fitted with six OptiTrack Flex 13 cameras, connected to another desktop PC running OptiTrack Motive motion capture software. Each antenna was fitted with optical reflectors to be monitored by the cameras, and the OptiTrack Motive calibration indicated sub-millimeter mean localization errors.

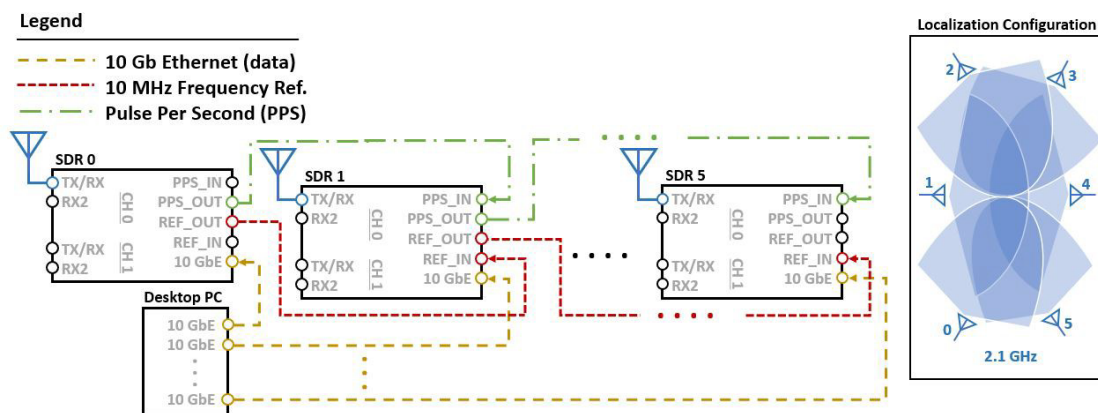


Figure 1. Schematic diagram where SDR 0 is node 0, SDR 1 is node 1, etc. The 10 Gb Ethernet is used to control the SDRs via GNU Radio. 10 MHz frequency reference is generated internally from SDR 0 and daisy chained as an external reference for nodes 1 through 5. The Time transfer and delay estimation is performed with a two-tone waveform at a 2.1 GHz carrier frequency; the experimentally configuration of antennas is shown approximately (right).

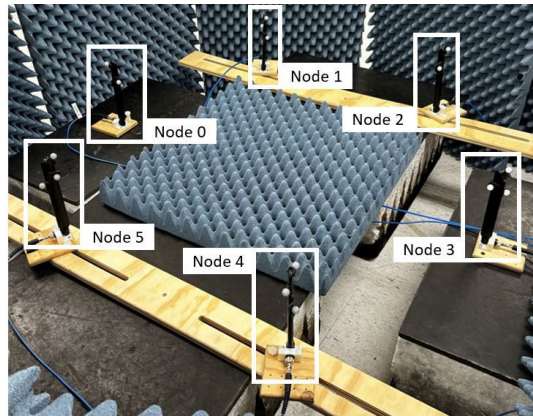


Figure 2. Experimental configuration of the distributed localization system. Node 0 is at the upper left, followed in clockwise order. The system is surrounded by RF absorber in order to reduce the effects of multipath for the indoor environment. Adjacent nodes are spaced at least 50 cm apart.

First, the locations corresponding to the OptiTrack measurement were computed to serve as the basis for error comparison. Then, the distance estimates were compiled for each time-synchronized iteration and input to the mMDS algorithm to generate a set of location estimations, Fig. 3. The first 50 samples of each trial were discarded to ensure the system clocks had reached consensus. The discrepancy between each node’s location estimate and its true location was calculated to create an array of error vector magnitudes (EVMs). This was repeated for each iteration, resulting in an array of location estimations at each transmit power value. Fig. 4 shows the mean and standard deviation of the average nodal EVM. We were able to achieve a mean EVM of 1.9 cm with the implementation of mMDS, supporting distributed beamforming at frequencies of more than 1 GHz.

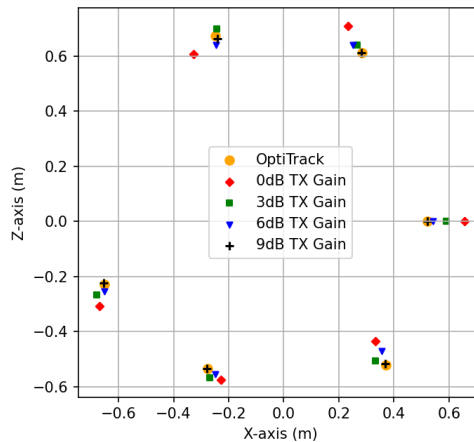


Figure 3. Recovered node locations after mMDS application, averaging the 10 most recent internode distance estimates. Node 0 estimates lie on positive x-axis, continuing toward node 1 in counter-clockwise direction. Note that OptiTrack locations represent true locations, and others represent estimated locations as a function of transmit gain.

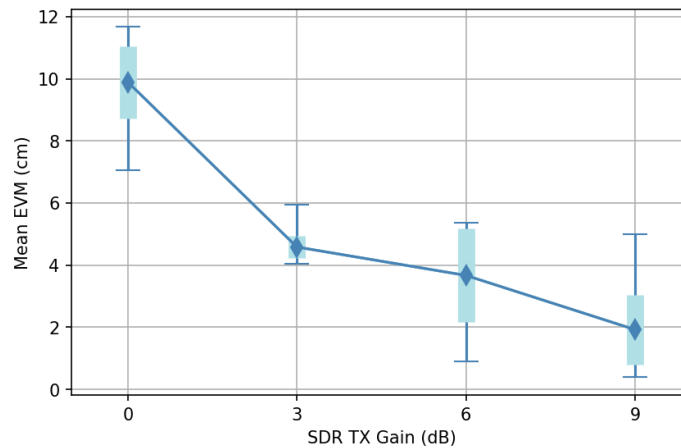


Figure 4. Mean coordinate location error vector magnitude (EVM); the standard deviation is given by powder blue bars, and the minimum and maximum EVM are shown by the vertical lines.

b. Distributed Transmission and Reception¹⁵

Based on the coordination techniques developed earlier in this effort, we implemented a two-node distributed phased array to demonstrate distributed transmission and reception. The experimental system configuration consisted of a three- node distributed phased array which was coordinated fully wirelessly in time, frequency, and phase. A system schematic is shown in Fig. 5 and the experimental setup is shown in Fig. 6. Four Ettus Research X310 Universal Software Radio Peripherals were used in this experiment to perform the time and phase coordination, and beamforming operations. Each SDR was run with a base clock rate of 200 MHz and a digital sampling rate of 200 MSa/s and utilized two UBX-160 daughterboards, supporting 160 MHz of instantaneous analog bandwidth. The system operated in a centralized topology with node 0 as the primary node. One SDR on each node was used for time synchronization and ranging on channel 0 and beam-forming on channel 1, and node 0 used a second SDR for an auxiliary triggering signal implemented to trigger the receiver. The receiver was a Keysight DSOS8404A oscilloscope which sampled at a rate of 20 GSa/s; channel 1 was used to receive the beamforming waveforms while channel 3 was used for the triggering control and used a high Q factor filter to mitigate unwanted ambient RF signals from triggering the oscilloscope. The beamforming antennas used on the nodes and receiver were 10-dBi L-Com HG72710LP-NF log-periodic antennas and the triggering antennas used were 8-dBi L-Com HG2458-08LP-NF log-periodic antennas.

The primary node was used as the frequency, time, and positional reference. This node contained a Keysight PSG E8267D vector signal generator used as the primary reference frequency which disciplined the LOs of the SDRs on node 0 directly, and the LOs of the secondary nodes via wireless frequency transfer. The reference port of the signal generator was connected to the reference input of SDR 0 to provide the required 10 MHz frequency reference and its RF port was connected

¹⁵ J. M. Merlo, N. Shandi, M. Dula, A. Bhattacharyya and J. A. Nanzer, "Fully Wireless Collaborative Beamforming Using A Three-Element Coherent Distributed Phased Array," IEEE Phased Array Systems and Technology, 2024

to a power combiner to be sent from the joint time-frequency-ranging antennas. From the RF port, the signal generator transmitted a continuous two-tone signal with a tone separation of 10 MHz at a carrier frequency of 4.3 GHz. Two self-mixing frequency locking circuits are connected to the reference input ports on SDRs 2 and 3 to provide the 10 MHz frequency references. The joint time-frequency-ranging antennas used on the secondary nodes were L-Com HG2458-08LP-NF 8-dBi log-periodic antennas; the primary node used a commodity omni-directional dipole antenna.

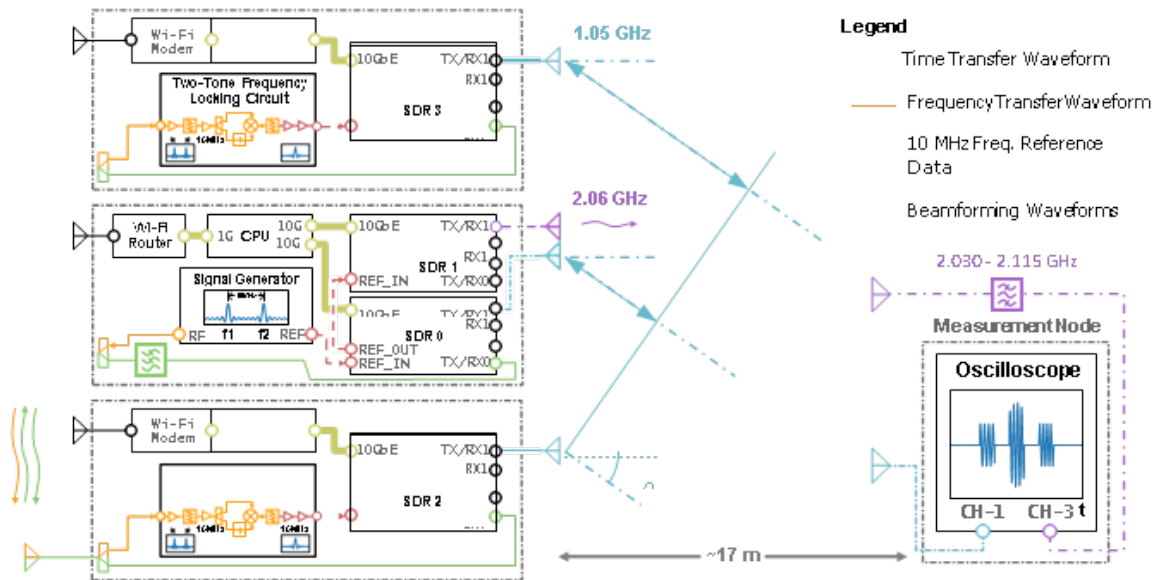


Figure 5. Distributed array system schematic. Three mobile carts were used to construct the distributed array nodes. Each node contained its own computer and Wi-Fi interface; the primary node hosted a Wi-Fi router while the other nodes used Wi-Fi modems to communicate coordination information with the rest of the array. The primary node also hosted the signal generator which was used as the primary frequency reference; the SDRs on node 0 were disciplined directly by its reference output while the other nodes used two-tone frequency locking circuits to demodulate the two-tone waveform transmitted from the RF port. Time and frequency coordination utilized shared antennas. Beamforming antennas were connected to a separate RF channel on the SDRs. An oscilloscope placed in the far-field was used as a receiver and an auxiliary triggering antenna was used between node 0 and the oscilloscope. A narrow-band filter was placed on the triggering receiver to remove unwanted RF to trigger the oscilloscope only on pulses transmitted from the array, independent of beamforming performance.



Figure 6. Photograph of the distributed phased array. Antenna masts are placed along the far edge of the carts.

The system utilized a distributed computing model such that parts of the computation process were performed across separate host computers, one on each node. Nodes 0 and 1 used desktops with Intel i7-8700's while Node 2 used an Intel i7-9700; all three hosts contained 16 GB of DDR4 memory and ran Ubuntu 22.04. The SDRs were connected to the host computers through 10 Gigabit Ethernet (GbE) cables and were controlled using GNU Radio software with custom controller and signal processing blocks written in C++ and Python. To enable network communication of the electrical states and ranging coordination, the primary node host was connected to a Wi-Fi router via 1 GbE while the other two nodes were connected to Wi-Fi modems. The time and phase synchronization (inter-node ranging) were achieved using the two-way time transfer method described in Section II-B and used a pulsed two-tone waveform with pulse duration of 5 μ s and a carrier frequency of 2.1 GHz. The initial clock alignment process was performed over the network via TCP/IP to an accuracy of 10 ms. After the coarse network timing synchronization, the iterative refinement high accuracy synchronization process started at a sample rate of 5 MSa/s, tone separation of 2 MHz, and with a time-domain multiplexing (TDM) window separation of 10 ms; the TDM window separation was then iteratively refined down in geometrically decreasing steps to 5 μ s. Once the TDM window is below 1 ms, the sample rate is increased to 200 MSa/s and the tone separation is increased to 40 MHz to reach a fine level of synchronization. Utilizing this technique, we eliminate the need for external time references such as GNSS-derived PPS entirely.

The three nodes were positioned in a straight line to simplify localization of the nodes to only the inter-node range estimation and each element was separated by 525 mm. The receiver was placed at 17 m, approximately at broadside to the array, and beamforming was performed at 1.05 GHz.

To estimate the coherent gain G_c —the ratio of received signal power to the ideal signal power received at the target if all electrical states were perfectly synchronized—an amplitude modulated pulse train was transmitted, shown in Fig. 7. In this pulse train, the time was divided into seven slots—the first three slots were allocated to each node individually, the following three slots were combinations of two nodes, and the final slot was all three nodes transmitting simultaneously. If all nodes are transmitting coherently, the final pulse magnitude should equal the summation of the magnitude of the first three pulses scaled by the array pattern at the given beam steering angle. The peak amplitudes were estimated by downconverting the waveforms to baseband by digitally mixing them with the carrier frequency of 1.05 GHz, then matched filtering against the pulse duration of 770 ns. A sample of the coherent gain pulse measurements with the beam steered to broadside is shown in Fig. 8.

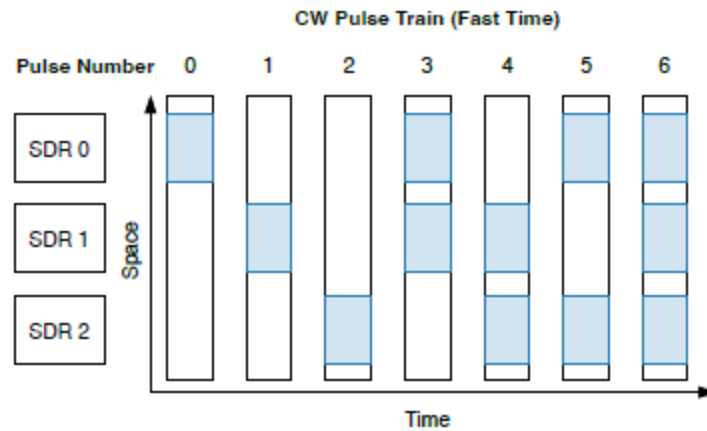


Figure 7. Coherent gain evaluation modulation pattern. All combinations of SDRs are evaluated. If the time and phase delays are appropriately aligned, the coherent gain of the last pulse (summation of all nodes) will equal that of the first three pulses (each node transmitting individually), scaled by the array pattern for the beam steering angle.

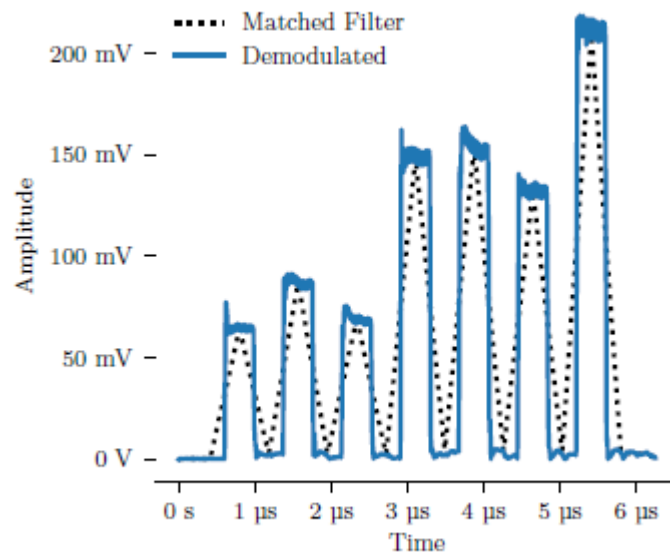


Figure 8. Measured coherent gain evaluation pulse train. The solid line indicates the filtered and demodulated waveform peak magnitude while the dotted line indicates the matched filter for the pulses. This illustrates the summations of the space-time modulated waveform shown in Fig. 7.

c. Multiobjective Distributed Beamforming¹⁶

Based on our localization and coordination work, we implemented a three-node distributed phased array system to demonstrate multiobjective beamforming in the array nearfield. In the near-field multi-objective beamforming experiments, three SDRs, SDR 0, SDR 1 and SDR 2 represents the three separate nodes of the distributed array (See Fig. 9).

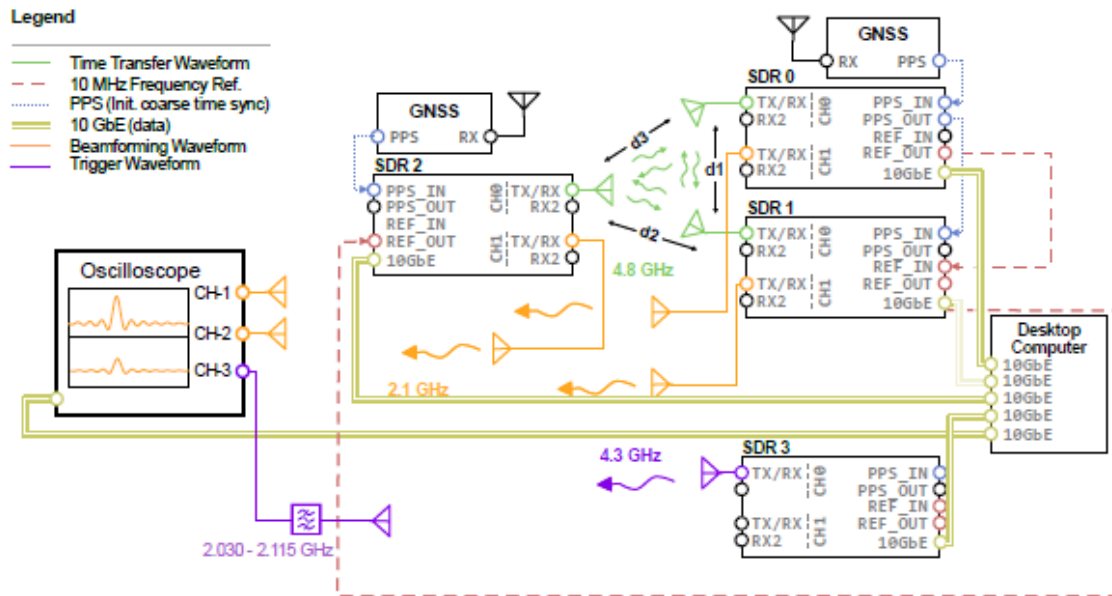


Figure 9. Wireless time transfer, cabled frequency transfer near-field multi-objective beamforming system schematic. The experiment configuration shows SDRs forming the three nodes of the distributed array. SDR 0 acts as the primary SDR and the frequency syntonization is done using the internal 10 MHz reference from SDR 0, distributed using coaxial cables. A pulse-per-second (PPS) is used to initialize the time synchronization epoch window using GNSS antenna on SDR 0 and SDR 2. The same is done via a coaxial cable connecting SDR 0 and SDR 1. The oscilloscope is utilized to sample and digitize the beamforming waveforms, enabling the determination of beamforming accuracy during the execution of wireless localization. SDR 3 is used as an auxiliary node to trigger the oscilloscope. A narrow-band filter was employed on the triggering receiver to eliminate undesired RF signals, ensuring that the oscilloscope would exclusively capture pulses transmitted from the array. This operation remained independent of the beamforming performance. The 10 Gb Ethernet cables are employed to control the nodes and the oscilloscope through GNU Radio software.

¹⁶ Bhattacharyya, Ahona, and Jeffrey A. Nanzer. "Multiobjective Distributed Beamforming Using High-Accuracy Synchronization and Localization." *IEEE Transactions on Microwave Theory and Techniques*, 2024.

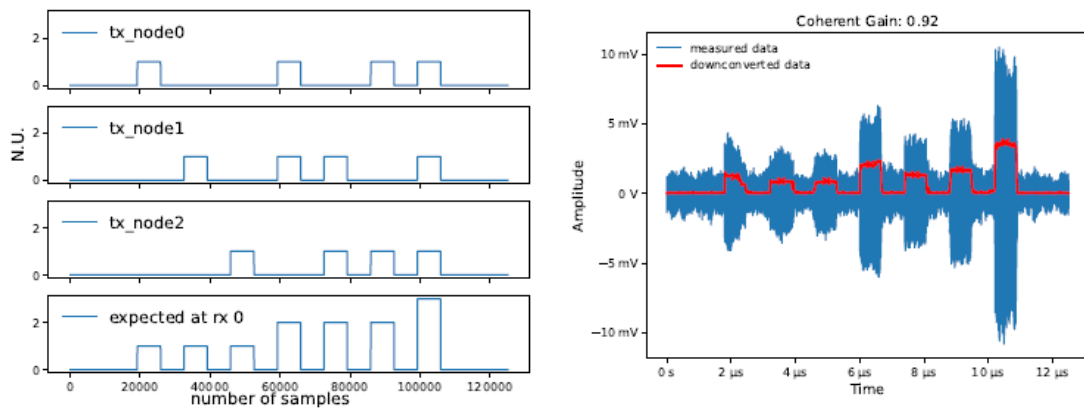


Figure 10. (Left) Simulation of the envelopes of the transmitted waveforms. Each node transmits a sequence of pulses in a pattern that yields reception at the focal location of the three transmitters individually, followed by each pair of transmitters, followed by the summation of all three. This pattern allows a quantitative evaluation of the relative beamforming gain. (Right) Example of average received waveform at the receiver RX 0. The coherent gain in this example was 92 %.

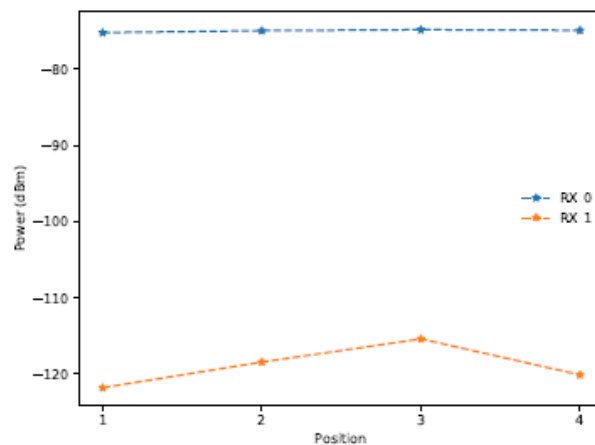


Figure 11. Average received power at the focus RX 0 and null RX 1 while Node 2 was moved to the four different positions, demonstrating the ability to maintain simultaneous focusing and nulling.

The left plot in Fig. 10 shows the simulated response of a distributed transmission from the three-node system, with the individual transmitted waveforms and the summed waveforms. This sequence of pulses allows an evaluation of the pairwise performance as well as the full coherent gain. The right plot shows a measured result of the summed waveform at a receiver, clearly matching the expected superposition of the waveforms. In Fig. 11 the average power at RX 0 and RX 1 are plotted for all the four different locations of Node 2, showing clearly that the distributed beamforming system maintains a focus and a null with appreciable null depth.

3. Findings and Conclusions

The results of this reporting period provide critical pieces of the foundation of a distributed approach to phase coherent transmission of microwave signals, and demonstrate the feasibility of

distributed coherent beamforming from separate wireless systems. Our ongoing work will focus on implementing transmission from larger sets of nodes using the techniques shown in this report.

4. Plans and Upcoming Events

In the final months of this effort we will work towards a distributed beamforming setup with up to 6 node using a fully decentralized coordination architecture, and we will identify next-step challenges in distributed phased array development.

5. Transitions and Impacts

N/A.

6. Recommendations for Future Work:

Future work may build on the results in this effort to explore arrays with larger numbers of nodes and with greater bandwidth and frequency capability.

7. Personnel

Principal Investigator			
Full Name	Approximate Level of Effort – LOE - (Hours This FY)	Country of Residence	National Academy Member? (Y/N)
Jeffrey Nanzer	1 person month	USA	N

8. Collaborations

Full Name	Organization	Collaboration Summary
John Lancaster	LLNL	Collaborated on distributed time synchronization for a two-node high-power transmitter.

9. Students

Doctoral Student(s)			
Full Name	University	Graduated?	Graduation Year
Ahona Bhattacharyya	Michigan State University	N	
Jason Merlo	Michigan State University	N	
Naim Shandi	Michigan State University	N	
Matthew Dula	Michigan State University	N	
Masters Student(s)			

Full Name	University	Graduated?	Graduation Year
William Torres	Michigan State University	N	

10. Technology Transfer

N/A.

11. Products, Publications, Patents, License Agreements, etc.

Publications resulting from this project for the reporting period:

Archival Publications

#	Citation	Acknowledged ONR Support Received? (Y/N)	Peer Reviewed? (Y/N)
1	A. Bhattacharyya and J. A. Nanzer, "Multi-Objective Distributed Beamforming Using High-Accuracy Synchronization and Localization," IEEE Transactions on Microwave Theory and Techniques, accepted	Y	Y
2	N. Shandi, J. M. Merlo, and J. A. Nanzer, "Decentralized Picosecond Synchronization for Distributed Wireless Systems," IEEE Transactions on Communications, accepted	Y	Y
3	J. M. Merlo, S. Wagner, J. Lancaster, and J. A. Nanzer, "Fully Wireless Coherent Distributed Phased Array System for Networked Radar Applications," IEEE Microwave and Wireless Technology Letters, vol. 34, no. 6, 2024	Y	Y

Conference Papers

#	Citation	Acknowledged ONR Support Received? (Y/N)	Peer Reviewed? (Y/N)
1	J. M. Merlo, N. Shandi, M. Dula, A. Bhattacharyya and J. A. Nanzer, "Fully Wireless Collaborative Beamforming Using A Three-Element Coherent Distributed Phased Array," IEEE Phased Array Systems and Technology, 2024, 2nd Place Student Paper Competition	Y	Y
2	N. Shandi, J. M. Merlo, and J. A. Nanzer, "High Accuracy Decentralized Time Synchronization Using SNR Based Weighting," IEEE International	Y	Y

	Symposium on Antennas and Propagation and USNC-URSI Radio Science Meeting, 2024		
3	J. M. Merlo, S. Wagner, J. Lancaster, and J. A. Nanzer, "Fully Wireless Coherent Distributed Phased Array System for Networked Radar Applications," IEEE International Microwave Symposium, 2024, Finalist, Student Paper Competition	Y	Y
4	M. Dula, N, Shandi, and J. A. Nanzer, "Decentralized Localization of Distributed Phased Array Elements Using High-Accuracy Ranging and Multidimensional Scaling," WAMICON, 2024, Finalist, Student Paper Competition	Y	Y

Books

No information to report

Book Chapter

No information to report

Theses

No information to report

Websites

No information to report

Patents

No information to report

Other Products:

No information to report

12. Point of Contact in U.S. Navy / Marine Corps

N/A.

An Accessible Platform for Simultaneous Macro, Meso and Microscopic Measurements of Polymeric Materials at High Loading Rates and Temperatures

Grant No. N00014-22-1-2490

Annual Report for Fiscal Year 2024

Period of Performance: October 1, 2023 to September 30, 2024

Prepared by:

Research Professor Sal Portillo, Principal Investigator
Department of Electrical and Computer Engineering
University of New Mexico
Albuquerque, NM 87131-0001
Tel. 505-417-9822
Email: sportil@unm.edu



This work was sponsored by the Office of Naval Research (ONR), under grant/contract number N00014-22-1-2490. The views and conclusions contained herein are those of the authors only and should not be interpreted as representing those of ONR, the U.S. Navy or the U.S. Government.

Section I: Project Summary

1. Overview of Project

The overall arching goal of the electrode materials modification is to develop the underlying technologies to design and build a high frequency, long pulse, high repetition rate HPM (High Power Microwave) source that can effectively be used by US Naval forces against enemy combatant electronics. We are accomplishing this through the use laser modification of surfaces to reduce the neutrals adsorbed but more importantly to cap the surface so these neutrals do not return and can then be pumped out of the system. The electrode desorbed neutrals lead to ions which ultimately lead to a large reduction on EM (Electromagnetic) energy production and much lower pulse repetition and short energy pulses. Our efforts include the use of single frequency laser energy deposition as well as broadband laser energy on various conductors suitable for use as electrode materials on HPM sources. Additionally, we are utilizing advanced surface characterization tools such as XPS (X-ray Photo Electron Spectroscopy) and SEM (Scanning Electron Microscopy) to characterize the residual neutrals after laser irradiation and subsequent exposure to ambient air to measure the effectiveness of the energy deposition. We are also carrying out in situ firing of irradiated electrodes on our LTD (Linear Transformer Driver) accelerator that is a very close surrogate for an HPM source to measure the resultant ionization levels after bombarding with high energy electrons much like in an HPM source. The research carried out under this award is part of multipronged effort with our partner university, Texas Tech, who are carrying out atomic and molecular density numerical simulations as part of this effort.

The success of our research will lead to the actual development of HPM sources that can give Naval operations asymmetric and effective capabilities to neutralize enemy combatant electronic assets

Executive Summary:

The document section of this report focuses on the efforts and success of the basic research of these laser irradiations and surface characterizations as well as in situ measurements to ultimately develop an effective HPM source for the period of October 1, 2023 to September 30, 2024 supported by ONR award N00014-22-1-2490.

Objective:

The overarching objective is to develop laser irradiation methodologies to reduce outgassing via surface morphological changes that will lead to an effective long pulse high repetition HPM source that can effectively be made into system and be put into the hands of the Naval warfighter to interdict and effectively neutralize electronic enemy combatant assets of interest

Naval Relevance:

Developing an effective HPM source that is high energy, long pulse and high repetition capable will provide the Naval warfighter an asymmetric capability that will aid in continued dominance of the electronic battlefield.

Introduction/Background:

Given the highly dynamic and novel way that unmanned battlefield devices are being utilized in high conflict zones such as Syria, Eastern Europe and even Myanmar as well as the often complete dominance of unprepared combatants in littoral as well as blue waters in the Black Sea by similar devices it is clear that an effective electromagnetic combat system coupled to kinetic munitions is

what is needed to give the US Navy the means to continue to dominate these battlefields. Various DOD laboratories as well as UNM and other USA universities as well as large American corporations are actively working to develop these systems. Our work here can form the lynchpin of such a family of systems.

There is of course strong interest from possible enemy adversaries in this field with concomitant funding streams to develop similar technologies.

2. Activities and Accomplishments

Our laser test bed, shown in figure 1 below, is comprised of a light tight enclosure that allows us to expose the sample to various laser wavelengths and energies as well as different set of narrow and broadband energies. During this reporting period we have utilized single longitudinal mode (SLM or very narrow band) 488 nm laser energy, 563 SLM 900 nm broadband. The areal energy deposited is varied by either power control of laser or by broadening the beam optically via an expander telescope.

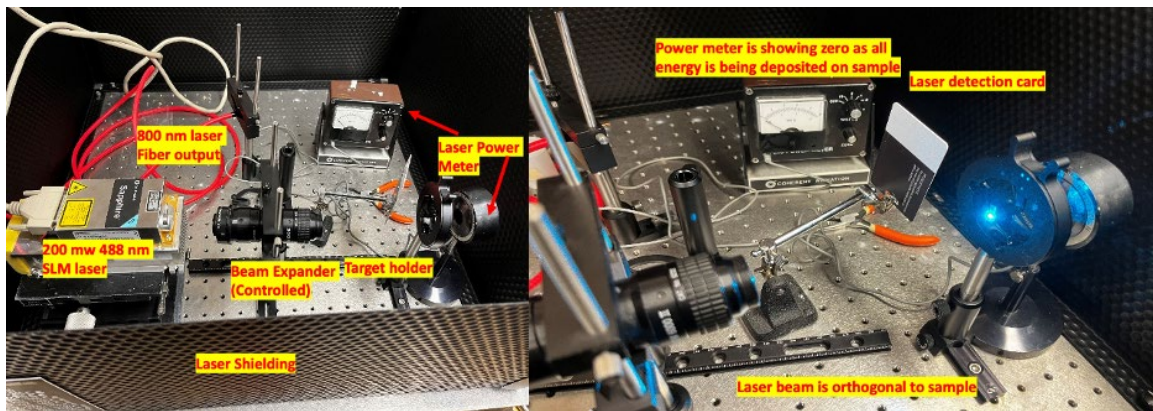


Figure 1. Photo, on left, shows the laser irradiation set up with a 488 nm SLM laser power with a beam expander followed by target holder and laser power meter. The last two are mutually exclusive and thus are not fielded simultaneously. Right image is a close up of set up with laser beam on showing of course the blue light of a 488 nm continuous wave laser.

The laser energy deposition alters the surface by breaking bonds and thus making the path for outgoing as well as adsorption more tortuous. We have been attempting to measure these morphological changes via SEM measurements and one of these results is shown in figure 2. There is a large parameter space comprised of material, laser energy, laser wavelength and laser bandwidth that requires a large set of measurements. The SEM resolution may not be enough for us to correlate surface changes versus effectiveness of electrode energy deposition and we may have to try different techniques such as Atomic Force Microscopy (AFM).

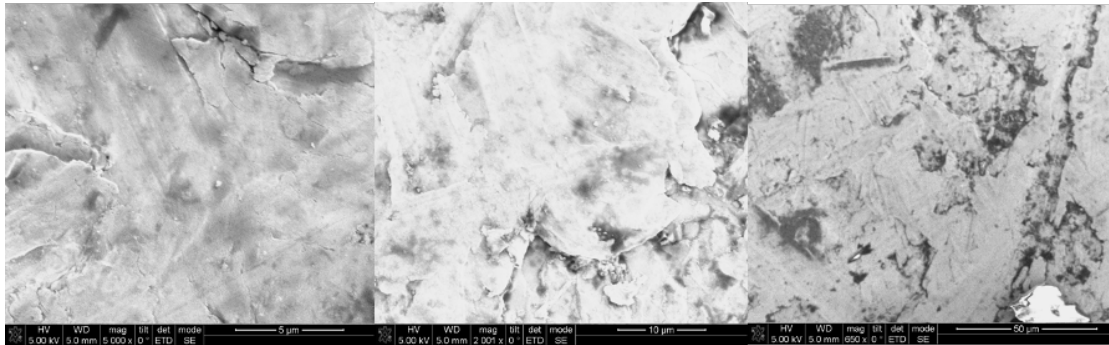


Figure 2. Composite image of SEM frames for unexposed material at 5, 10 and 50 micron resolution. There are plateaus as to be expected throughout the surface and these transition from each other via jagged peaks. The SEM will only reach so far and so eventually we will have to use AFM to see atomic structure. However, the present images serve for showing the effects of irradiation.

These laser irradiations were preceded by technical cleaning of the surface using various ethanol/acetone washes. These produce a heavy hydrocarbon load upon evaporation and thus we chose to maintain their use as a way to test the surface photon treatment. The resultant samples of course could not span the entire parameter space and thus were chosen principally due to their relative ease of accessibility and also because some HPM sources are actually built using some of these materials. The samples were then examined via Scanning Electron Microscopy to measure surface morphology changes such as spall, cavitation effects and of course gross changes indicative of an effect from the laser that could indicate a more tortuous path for adsorbates. Figures 2 and 3, preceding and immediately following this paragraph shows some of these studies.

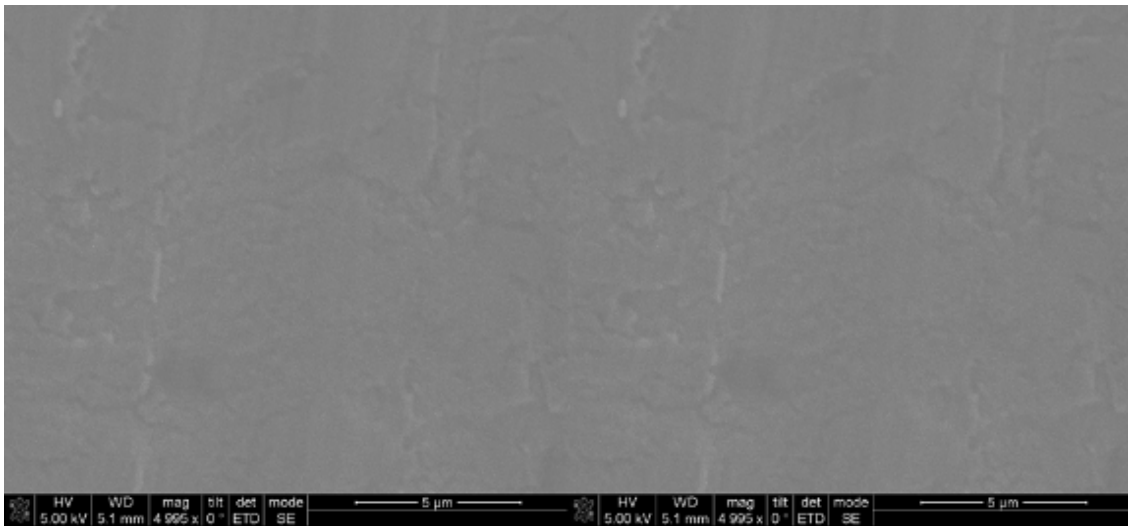


Figure 3. Exposure of sample at 50 mw and 100 mw respectively both imaged at 5 micron resolution. We can see that some of the edges are beginning to soften compared to our control sample.

These experiments were followed by additional irradiations on different anodes and then investigated using the XPS system. The goal was to show that laser irradiation not only reduces the adsorbate load but also the reabsorption of neutrals once the material has been irradiated.

Table 1 shows the results of the treated and untreated Al samples. With figure 1 shows a noticeable reduction in overall background load and carbon contaminants. Figure 4 shows the overall spectrum with some of these peaks identified. I think the important part is those hydrocarbons that are readily present in the system and still need to be identified. These relatively large atoms with many protons will be removed at different rate than the hydrocarbons and travel as well as affect the incident beam much differently.

Table 1. Initial list of adsorbates in treated and untreated Al with 488 nm photons.

Sample Identifier	Al 2p %	C 1s %	Ca 2p %	Cl 2p %	F 1s %	O 1s %
untreated Al	15.39	54.69	1.08	1.02	1.39	26.42
treated Al	17.78	49.64	1.40	0.57	1.25	29.36

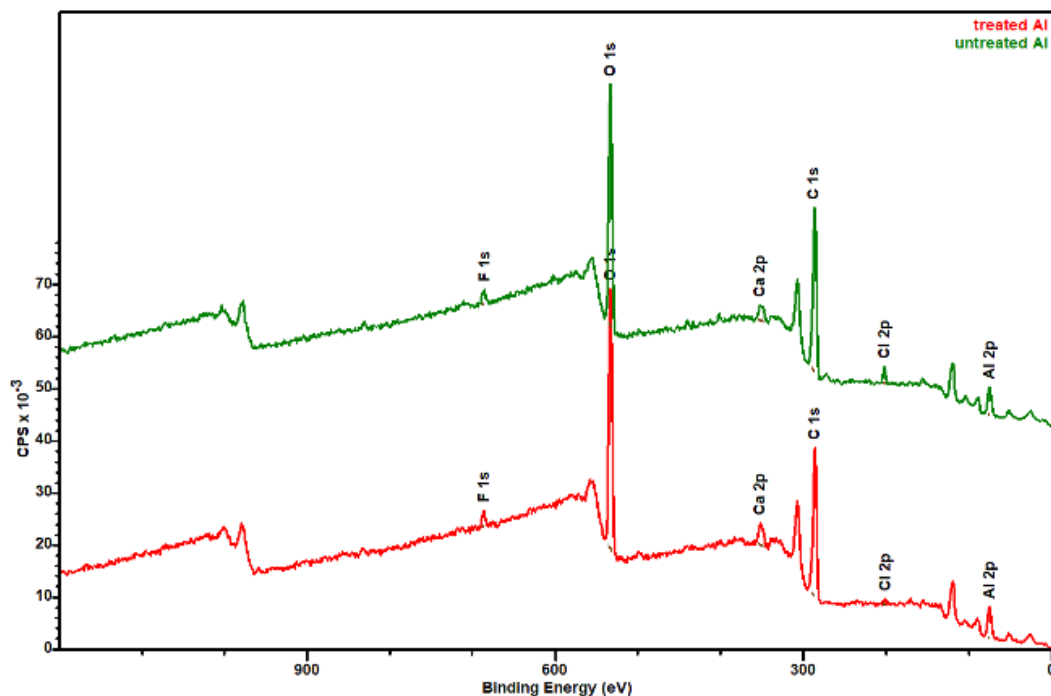


Figure 4. Spectra from laser irradiation of Al with 488 nm photons.

Similar analysis and results were acquired for other materials with table 2 and figure 5 showing these results for Cu.

Table 2. Adsorbates– not inclusive of hydrocarbons– of laser irradiated and non-exposed Cu.

Sample Identifier	C 1s %	Ca 2p %	Cl 2p %	Cu 2p %	N 1s %	Na 1s %	O 1s %
untreated Cu	66.16	0.31	1.37	2.82	2.05	1.06	26.23
treated Cu	70.66	0.42	1.06	1.83	2.28	0.65	23.10

Again, the irradiation removed some percentage of the adsorbates – but not all, for example the OIs content was reduced by 3%. Again, it is very important to note that it is not simply heating of the material that removes the adsorbates but also the photoelectric effect of the incident photons on the physi and chemisorbed bonds which likely calls for a Monte Carlo treatment of these incident particles in order to model the effect.

Figure 5 gives the spectral plot of these exposures on Cu. The plot may look odd to the eye as the energy is going down from the zero abscissa point but that is typical convention where the highest energy is located on the left most abscissa location.

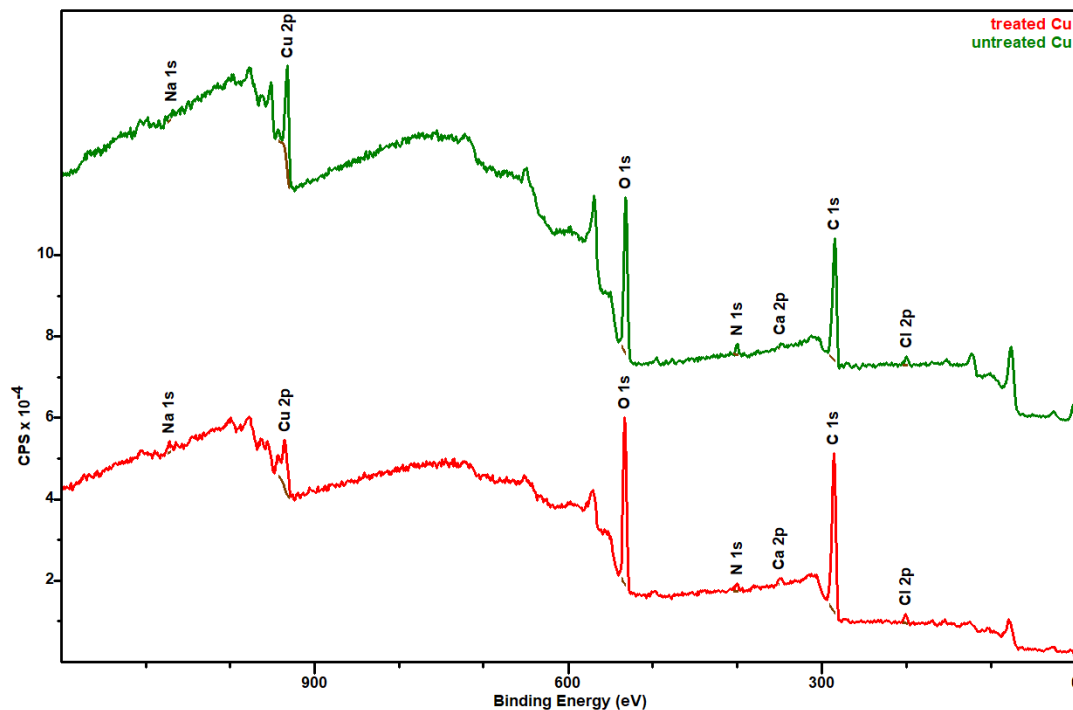


Figure 5. Composition of adsorbates on laser irradiated and unirradiated Cu.

In the Cu there was still the Cl, C, N and Ca to be found but no iron and of course no Al. And of course, we are still working on understanding the hydro-carbon load. The above data can now be used then in the numerical simulations for validation.

Our In Situ spectroscopy experiments were taken with laser irradiation of 900 nm as this laser provided higher energy which was needed to expand the beam to 5 cm diameter. These experiments were carried out on our LTD accelerator using our standard set up with an array of fibers interrogating the resultant plasma- The LTD spectroscopic configuration is well established producing very good spectra and is shown in figure 6. This configuration is akin to that seen by relativistic HPM sources and serves as an excellent surrogate to characterize materials in situ. The LTD will also serve as a driver for an upcoming HPM high frequency source design to be built in house at UNM. Our goal is to irradiate the innards of the new source to show effective laser treatment by having lower outgassing.

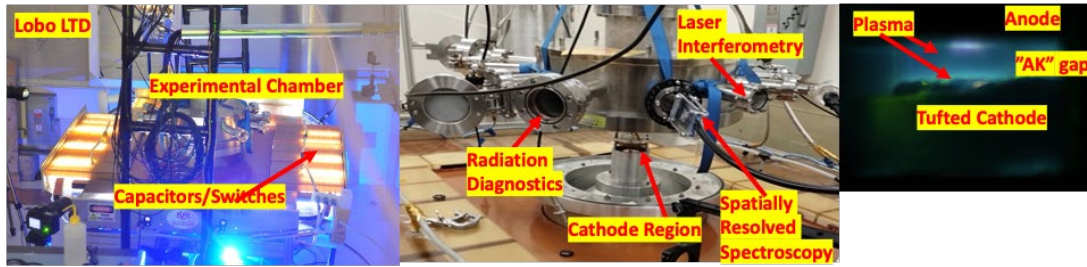


Figure 6. Composite image of the LTD firing, the experimental chamber and a typical shot electrode experiment. The latter clearly shows plasmas from both the anode and the cathode.

Figure 7 shows some of these results for the control and irradiated sample. There is a change in the spectra due to a low energy irradiation. Figure 8 shows a line profile from one of the fibers of this exposure.

Sample Vs. Irradiated Anode spectroscopy images

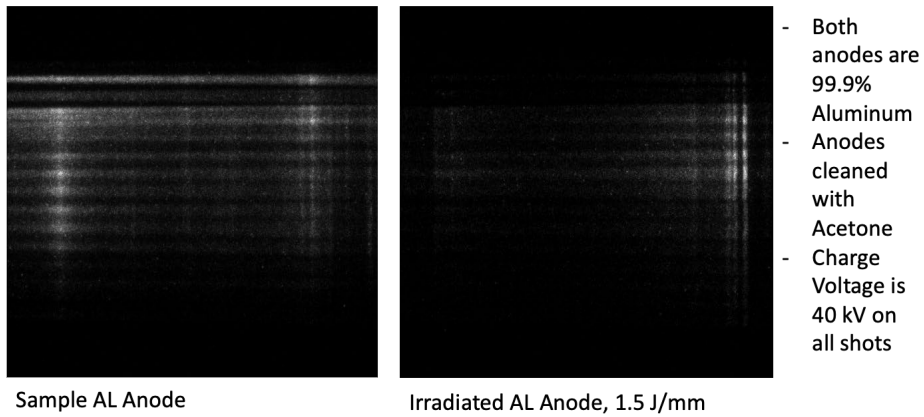
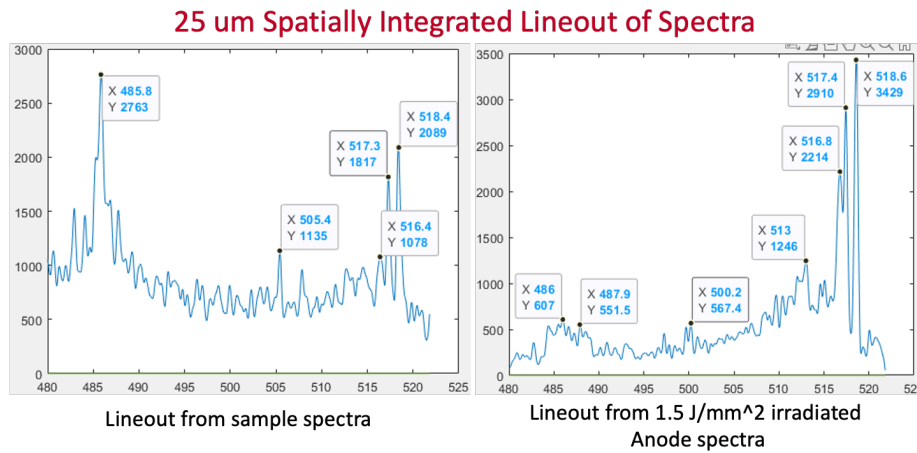


Figure 7. Spectroscopy images from CCD camera from our 500 mm spectrometer. Left side image is control showing more peaks and right side image shows same material after laser exposure.



Note: Y-axis is given in photon count, X axis is in nanometers

Figure 8. Line out of CCD images shown in figure 7.

Our spectra results are being iteratively fed back to our TTU partner Dr. Ravi Joshi for use in his numerical simulation development.

3. Findings and Conclusions

Initial findings are showing some promise and this is with a large parameter space still yet to be covered. The XPS measurements specifically as well as the In Situ spectroscopic measurements are showing measurable reduction in adsorbate content and ionization load. Even after the sample has been purposely exposed to ambient environment as well as preloaded with hydrocarbons via ethanol cleaning. The exposure to ambient environment was suggested via prior work from one of the crossed field device (very similar to HPM sources) manufacturers that stated materials were readily exposed for days to ambient environment prior to build of source. The reduction in neutrals is principally in the hydrocarbon content.

This reduction in neutral load is the key to making a long pulse high repetition rate, high energy HPM weapon that will benefit the Naval and Marine warfighter as they will be able to interdict electronic threats much more readily.

4. Plans and Upcoming Events

Our near future plans are to complete these laser irradiation experiments and design a high frequency source via Particle in Cell simulations and build that source with the fruits of our experiments. That is our models will incorporate reduced gas loads on certain key regions and show a concomitant reduction in neutral outgassing and show a longer higher energy pulse. We plan on showing the fundamental basic science experimental results at two upcoming conferences- IVEC and ICOPS 2025. We have the capability to not only design this source but also build it in house and would like to move forward in the future with such a build.

5. Transitions and Impacts

Once we have established the laser irradiation methodology that serves the source the best our goal is to build and to transfer this to our collaborators at a naval laboratory. We would like to engage Mr. John Shannon, a lead in HPM source effects as well as Jack Chen- Both at NSWC Dahlgren Division to show the effectiveness of this technology. Additionally, we expect to engage both small companies here in the Albuquerque area as well as show our work to large aerospace companies (Lockheed Martin) as well as pursue SBIR funding to bring this technology and source development to a program of record.

Our laboratory has recently brought on board 4 new USA citizens as students to focus on aspects related to this work, from numerical modeling to HPM source build, to laser experiments and to pulse power. One of our key tenets is that our laboratory will focus exclusively in developing the talents of our New Mexico students and provide them the skill sets needed to work in areas and laboratories in the national interest. These 5 students encompass the breadth of our American experience and include a first nation (Navajo) Electrical Engineer, A woman physicist, a Hispanic mechanical engineer and a non-traditional older student who came into the university after working in the trades and a Physicist student from Alaska. We have graduated a USA citizen with a master's degree under this award who is now pursuing a Ph.D. at University of California San Diego in plasma physics. All of these students will graduate from our lab and are supported in some way via this award and are destined to be of high impact in developing technologies in the national interest.

This spring of 2025 we are also bringing on board 6-7 USA citizens still in high school to ensure that they continue on a STEM path. These high school students hold the promise to develop into strong scientist and engineers and our aim is to immerse them in advanced research and encourage them to stay in these fields.

6. Recommendations for Future Work:

In a related ONR project we have shown that internal geometric changes to HPM sources can lead to a reduction in the outgassing of neutrals from electrodes. Further reduction via laser treatment will increase the pulse length and repetition work as such we strongly recommend that the path to building a source that incorporates all new design, geometric changes as well as laser irradiation, be implemented in the build of a test HPM source that can serve as the seed for target irradiation and electronic effects as well as the commercial development and ultimately program of record for the naval warfighter.

7. Personnel

Principal Investigator			
Full Name	Approximate Level of Effort – LOE - (Hours This FY)	Country of Residence	National Academy Member? (Y/N)
Salvador Portillo	360	USA	N
Co-Investigator(s) or Co-PI(s)			

Full Name	Approximate Level of Effort – LOE - (Hours This FY)	Country of Residence	National Academy Member? (Y/N)
N/A	N/A	N/A	N/A
Performer Business Contact(s)			
Full Name	Role	Country of Residence	
N/A	N/A	N/A	N/A
Additional (Non-Student) Team Members N/A			
Full Name	Approximate Level of Effort – LOE - (Hours This FY)	Country of Residence	National Academy Member? (Y/N)
N/A	N/A	N/A	N/A
Subcontractors N/A			
Full Name and Organization	Approximate Level of Effort – LOE - (Hours This FY)	Country of Residence	National Academy Member? (Y/N)
N/A	N/A	N/A	N/A

8. Collaborations

Full Name	Organization	Collaboration Summary
Dr. Ravi Joshi	TTU	Density Functional Theory Simulations
Dr. Steve Fairchild	AFRL/RX	Carbon Fiber Materials
Dr. Yitzhak Maron	Weizmann Institute of Science	Spectroscopic Science
Dr. Kost Ilyenko	Ukraine National Academy of Science	High Frequency Magnetron sources

9. Students

Doctoral Student(s)			
Full Name	University	Graduated?	Graduation Year
Tyler Rocha	UNM	No	12/15/2028
Masters Student(s)			
Full Name	University	Graduated?	Graduation Year
Robert Beattie-Rossberg	UNM	Yes	05/15/2024
Undergraduate Student(s)			
Full Name	University	Graduated?	Graduation Year
Christopher Evans	UNM	No	05/15/2025
Wade Warner	UNM	No	05/15/2025
Maximo	UNM	No	05/15/2026
Sasha Palko	UNM	No	05/15/2026
Sebiyam Werdinn-Kenicott	UNM	No	05/15/2027

10. Technology Transfer

Have submitted 1 patent application on neutral atom desorption reduction via compression. The patent application is still in early stages of review, with Dr. Portillo as sole applicant. Beginning process to seek SBIR funding to move forward with commercialization efforts – the company name is Ars Fisica based in Albuquerque with Dr. Portillo is owner. Additionally, we are carrying out continuing experiments on carbon fiber electrodes with AFRL/RX.

11. Products, Publications, Patents, License Agreements, etc.

Publications resulting from this project for the reporting period:

Archival Publications

#	Citation	Acknowledged ONR Support Received? (Y/N)	Peer Reviewed? (Y/N)
1	No Information to Report		

Conference Papers

#	Citation	Acknowledged ONR Support Received? (Y/N)	Peer Reviewed? (Y/N)
1	No Information to Report		

Books

#	Citation	Acknowledged ONR Support Received? (Y/N)	Peer Reviewed? (Y/N)
1	No Information to Report		

Book Chapter

#	Citation	Acknowledged ONR Support Received? (Y/N)	Peer Reviewed? (Y/N)
1	No Information to Report		

Theses

#	Citation	Acknowledged ONR Support Received? (Y/N)	Peer Reviewed? (Y/N)
1	Development of Interferometric Diagnostics for Anode Neutral Desorption	Y	Y

Websites

#	Citation	Acknowledged ONR Support Received?	Peer Reviewed? (Y/N)
---	----------	--	----------------------------

		(Y/N)	
1	www.unm.edu/~sportil	Y	N

Patents

#	Citation	Acknowledged ONR Support Received? (Y/N)	Peer Reviewed? (Y/N)
1	Reduction of neutral adsorbates via isentropic compression	Y	Y

Other Products:

#	Product Description	Acknowledged ONR Support Received? (Y/N)	Peer Reviewed? (Y/N)
1	No Information to Report		

12. Point of Contact in U.S. Navy / Marine Corps

<u>Navy Point(s) of Contact Student(s)</u>			
Full Name	Organization	Email	Date of Last Contact
Dr. Jack Chen	HPM Technology Development Branch E52, NSWC DD	Y	12/16/2024

High Power Electromagnetic Sources from X-Band to Ka-Band

Grant No. N00014-23-1-2072

Annual Report for Fiscal Year 2024

Period of Performance: October 1, 2023 to September 30, 2024

Prepared by:

Distinguished Professor Edl Schamiloglu, Principal Investigator
Department of Electrical and Computer Engineering
University of New Mexico
Albuquerque, NM 87131-0001
Tel: 505-269-3525
Email: edls@unm.edu

Co-Principal Investigator(s):

Salvador Portillo,
University of New Mexico
sportil@unm.edu,



This work was sponsored by the Office of Naval Research (ONR), under grant (or contract) number N00014-23-1-2072. The views and conclusions contained herein are those of the authors only and should not be interpreted as representing those of ONR, the U.S. Navy or the U.S. Government.

Section I: Project Summary

1. Overview of Project

This project seeks to advance the state-of-the-art in high power sources of RF (HPRF) from X-band to Ka-band. This is accomplished through a combination of simulation (particle-in-cell simulations – PIC simulations), analytical theory, and experiment. The comprehensive literature survey is continuing. Experimental work commenced in Year 2 on the X-band backward wave oscillator (BWO). In addition, previous work on the Magnetically Insulated Line Oscillator (MILO) is being pushed to much higher frequencies than previous designs in simulation space. This includes development of novel high-power microwave (HPM) geometries to deliver higher energy electromagnetic (EM) pulses to give the naval warfighter an asymmetric capability to interdict electronic devices.

In terms of Navy relevance, our goal is to address, via focused and translational HPM research, some of the critical challenges facing Naval operations due to asymmetric threats, such as those faced by the US Navy in the Red Sea in the Fall of 2023, which caused the Navy over \$1B in operations and munitions! HPRF sources in the X-band to Ka-band range are critical to this objective. Developing an effective MILO HPRF source that is high energy and capable of operating at multiple high frequency points, will provide the Naval warfighter an asymmetric capability that will aid in continued dominance of the electronic battlefield.

Executive Summary:

This annual report summarizes activity on the FY2023 awarded ONR grant “High Power Electromagnetic Sources from X-Band to Ka-Band” covering the period December 01, 2023 – September 30, 2024.

Objective:

The objective of this effort is to i) first perform a comprehensive literature review of HPRF sources from X-band to Ka-band in Year 1, ii) select a source concept and frequency range to design and implement an experiment that can be performed using the facilities at UNM in Year 2, and iii) continue with experiments in Year 3. In addition, PIC simulations are being performed to advance the MILO to higher frequency with a secondary objective to understand and overcome the limitations imposed by the smaller separation distances within this class of high frequency cross-field device in all three years.

Naval Relevance:

In terms of Navy relevance, our goal is to address, via focused and translational HPM research, some of the critical challenges facing Naval operations due to asymmetric threats, such as those faced by the US Navy in the Red Sea in the Fall of 2023, which caused the Navy over \$1B in operations and munitions! HPRF sources in the X-band to Ka-band range are critical to this objective. Developing an effective MILO HPRF source that is high energy and capable of operating at multiple high frequency points, will provide the Naval warfighter an asymmetric capability that will aid in continued dominance of the electronic battlefield.

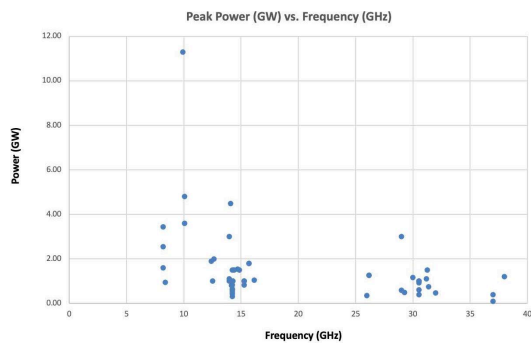
Introduction/Background:

The UNM group excels in designing novel HPRF source concepts of relevance to the Navy using PIC simulations and then validating the source designs in experiment. Whereas most of our work since 2000 has been in L-band and S-band, we are now advancing the capabilities of such sources to higher frequency, specifically from X-band to Ka-band, including advancing the MILO to higher frequency. This is to fill the gap in sources and avoid any technical surprise since our near peer adversaries have been very active in this space.

2. Activities and Accomplishments

Survey of Sources from X-Band to Ka-Band

In our literature review we focused mostly on publications over the last 20 years. The publications reviewed were in the frequency bands of 8.2-15.0 GHz, 12.4-18.0 GHz, 18.0-26.5 GHz, 26.5-40 GHz with a minimum of 100 MW output power. (For context, Table 1 summarizes the band designations.) We gathered most of our publications in Year 1 but we identified about a half dozen in Year 2. A single plot summarizing our findings is shown in Fig. 1. A key finding was the unavailability of sources in the vicinity of 20 GHz.



Common Frequency Band Ranges & Applications

NAME	FREQUENCY RANGE	NAME ORIGIN
X Band	8 to 12 GHz	X for "crosshair" (used in WW2 for fire control radar)
Ku Band	12 to 18 GHz	Kurtz Under
K Band	18 to 26.5 GHz	Kurtz (German for short)
Ka Band	26.5 to 40 GHz	Kurtz Above

Table 1. Designation of bands of interest (from <https://www.megaind.com/microwave-frequency-bands/>.)

Figure 1. Summary of findings from the literature survey.

X-Band BWO Experiments

The campaign on X-band BWOs was motivated by a recent Russian publication.¹⁷ Our campaign has three components to it: i) calculation of the dispersion characteristics of the device, ii) virtual prototyping (PIC simulations) of the device, and iii) experiments.

Dispersion Characteristics

Figure 2 presents the CAD drawing of the slow wave structure (SWS) that we designed. It is characterized by nine ($N=9$) azimuthally symmetric, uniform, sinusoidally varying in the axial direction corrugations formed on the inner wall of a smooth cylindrical waveguide with radius 15.52 mm. Corrugations are specified by their average radius, $r=17.40$ mm, period, $p=12.95$ mm, and amplitude, $h=3.76$ mm; minimum radius of corrugations, 15.52 mm = 17.40 mm $- 0.5 \cdot 3.76$ mm, is defined by their average radius, r , and half of their amplitude, h . The SWS (Fig. 1) is extended from its left and right sides in the axial direction by a smooth cylindrical waveguide with the same inner radius 15.52 mm.

The “cold” dispersion diagram of the SWS (Fig. 3) is calculated using the 2D SuperFish code. In summary, the azimuthally symmetric open 3D corrugated cavity (Fig. 3) is closed from its left and right sides, orthogonal to the z -axis in 2D cylindrical coordinates (r,z) (Fig. 4), with either Perfect Electric Conductor (PEC) or Perfect Magnetic Conductor (PMC) boundary conditions (BC) and modeled in the frequency domain.

SuperFish searches for all possible TM_{0nl} modes of the closed 2D corrugated cavity (Fig. 4), calculates its characteristic frequencies, and plots the electric field patterns of each TM_{0nl} mode possible to exist inside the cavity. The electric field patterns show how many wavelengths, λ , of electric field variations fits within the cavity for each TM_{0nl} mode in axial and radial directions of 2D SuperFish simulation space.

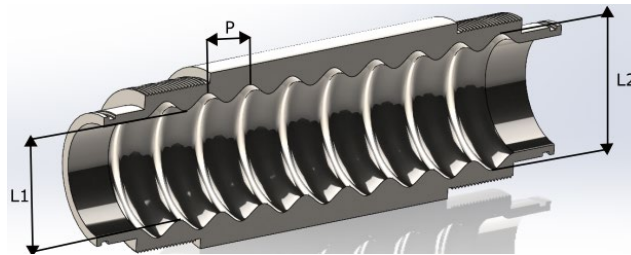


Figure 2. CAD drawing of the slow wave structure (SWS).

Characteristic TM_{0nl} modes with different radial n and axial l indexes are visually identified by analyzing their electric field patterns individually, one by one, and arranged in subsequent sets of electromagnetic TM_{0n} modes with the same radial index $n=1,2,3,\dots$; the total number of characteristic TM_{0nl} modes within each set of electromagnetic TM_{0n} modes is $2N+1$. Characteristic TM_{0nl} modes within each set of electromagnetic TM_{0n} modes are distinguished from one another

¹⁷ V.V. Kladukhin et al., “Relativistic backward-wave oscillator with longitudinal-slotted diffraction output,” *Tech. Phys. Lett.* 50, 190–193 (2024).

by the number of axial variations, l , of the electric field pattern along the z -axis of the cavity. It is also important to note that all characteristic TM_{0nl} modes are the standing wave modes.

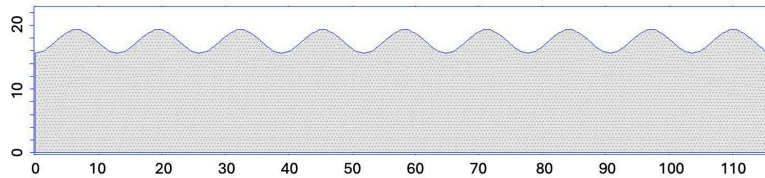


Figure 3. 2D SuperFish model of an X-band SWS (Fig. 2) in a cylindrical (r,z) coordinate system (dimensions are in [mm]).

The resulting dispersion diagram for the closed 2D SWS (Fig. 4) plots the characteristic frequencies of all identified longitudinal TM_{0nl} modes against the axial index l ranging from 0 to $2N$, and $n=1,2$.

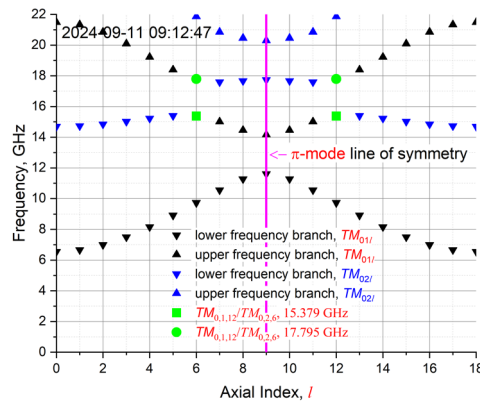


Figure 4. “Cold” dispersion diagram of a “closed” X-band SWS (Fig. 2) constructed from identified discrete TM_{01} and TM_{02} modes.

Virtual Prototyping

PIC simulations are performed using the CST-PS code with a simplified model of the BWO, consisting of two components of its electrodynamic structure, from left to right in Fig. 5: (i) a resonant reflector (RR) redirecting the backward-traveling wave (BTW) generated in the SWS toward an output port of the SWS, and (ii) axially symmetric SWS formed by nine sinusoidal corrugations of a smooth-walled cylindrical waveguide, $\varnothing_w=1.222''$. The input port of the VP/BWO is a metal plate up-stream of the RR, from which an annular electron beam, $\varnothing_e=1''$, is injected. Electrons travel downstream of the SWS in a uniform axial magnetic field, B_z , while within the RR/SWS. However, the guide magnetic field diverges to the wall near the collector after the SWS (Fig. 5). This prevents the electron beam to flow into the output port of the BWO, near which the output microwave power and the frequency of microwave oscillations, f_1 , are measured.

Results of PIC simulations of the simplified BWO (Fig. 5) model with input parameters $U_z=460$ kV and $I_e=4$ kA show that the tube starts to operate at a clearly-defined single frequency ~ 10.384 GHz (Fig. 6(b)) after ~ 10 ns of simulations time with average output microwave power ~ 700 MW (Fig. 6(a)), which results in electronic efficiency of BWO operation $\sim 38\%$.

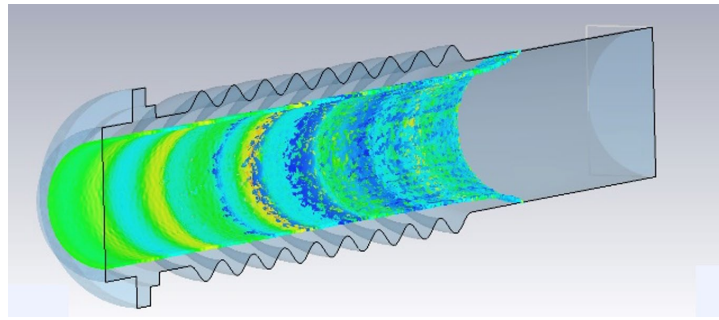


Figure 5. Simplified computer model of the BWO with the electron beam injected upstream of the resonant reflector and diverging radially following the SWS. The color coding represents electron energies, on a scale ranging from blue (25 keV) to red (750 keV).

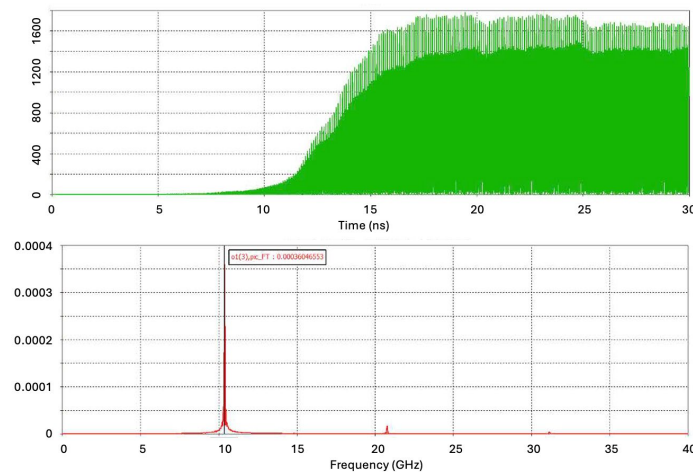


Figure 6. Results of PIC simulations of the simplified X-band BWO model (Fig. 2): a) output microwave power, and b) output microwave frequency.

The next step of this effort is to integrate the magnetically insulated coaxial diode (MICD) with $\varnothing_c=1''$, $\varnothing_a=2''$, and the RR/SWS (Fig. 2) together into the virtual environment using the CST-PS code, perform PIC simulations at different cathode voltages, V_c , the result of which will be with the I_e-V_c characteristic obtained in PIC simulations, along with f_1 (Fig. 6(b)) and P_1 (Fig. 6(a)) dependences on V_c , and compare all the calculated parameters with the related experimental measurements to be described next.

Experiments

The electrodynamic structure consists of (i) a cylindrical graphite cathode, $\varnothing=1''$, at the inlet to the SWS, which is a source of the cylindrical electron beam of the same diameter, (ii) a magnetic field producing system creating a uniform longitudinal magnetic field that provides electron beam transport through the SWS, and (iii) a smooth-walled cylindrical waveguide at the outlet to the SWS – an electron collector, where the diverging magnetic field redirects the beam electrons onto the collector's inner surface.

Pulses of the cathode voltage and the discharge current, primarily the electron-beam current, are monitored by (i) a voltage divider and (ii) a Rogowski coil, respectively. The cathode voltage of the SINUS-6 accelerator is controlled by the self-breakdown gas switch, whose pressure varies from 150 psi to 250 psi (Fig. 7). Measured pulses of the cathode voltage and the discharge current are arranged in 3D-oscillograms (Figs. 8 and 9), analysis of which allows to construct the current-voltage characteristic of the BWO (Fig. 7). The latter characteristic shows that a cathode voltage of 500 kV, for example, results in a discharge current ~ 5 kA.

The electric field oscillations in front of the output antenna of the BWO are monitored by a section of WR-90 waveguide; the results of the measurements are also arranged in 3D-oscillogram, an FFT analysis of which allows to construct 3D-plot of frequency spectra (Fig. 10) linked to 3D-oscillograms of the cathode voltage (Fig. 8) and the discharge current (Fig. 9). The obtained 3D-frequency spectra (Fig. 10) shows that the BWO predominantly oscillates at frequency ~ 10.3 - 10.4 GHz within the given range of cathode voltages, 300-500 kV (Figs. 7 and 8), which correlates with the dispersion diagram of the BWO structure (Fig. 11).

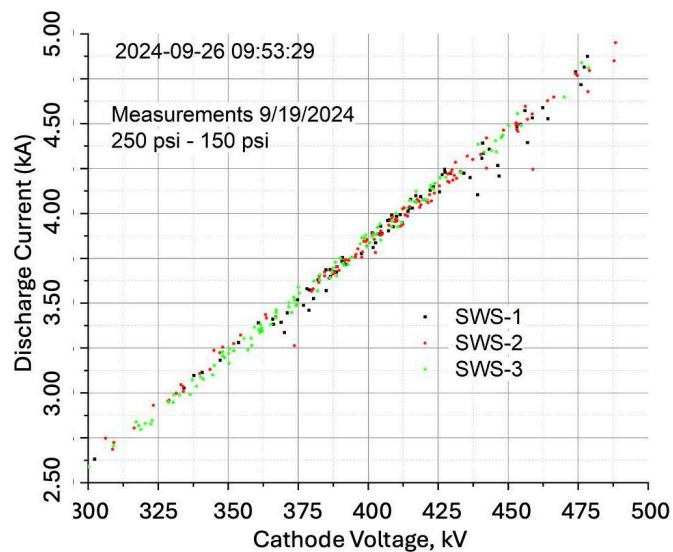


Figure 7. Current-voltage characteristic of the X-band BWO driven by the SINUS-6 accelerator.

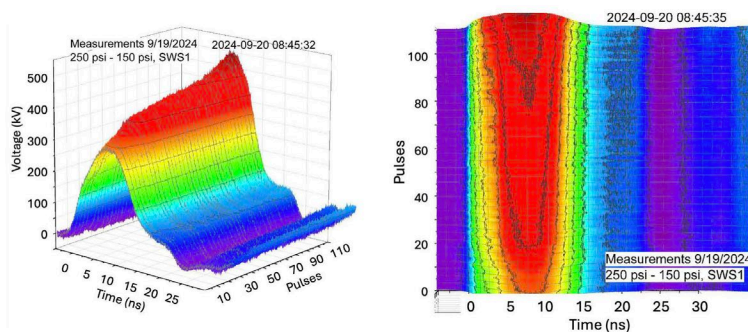


Figure 8. Experimentally measured 3D oscillogram of the cathode voltage.

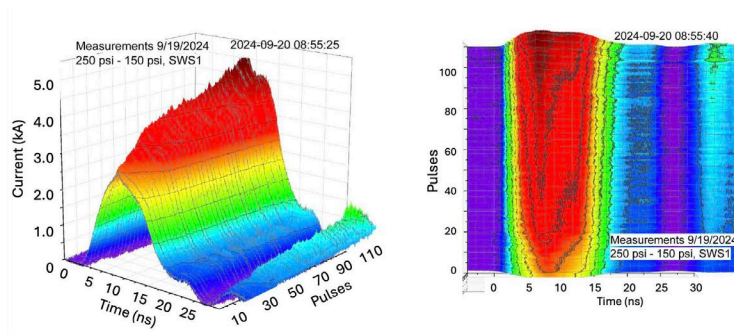


Figure 9. Experimentally measured 3D oscillogram of the discharge (primarily electron-beam) current.

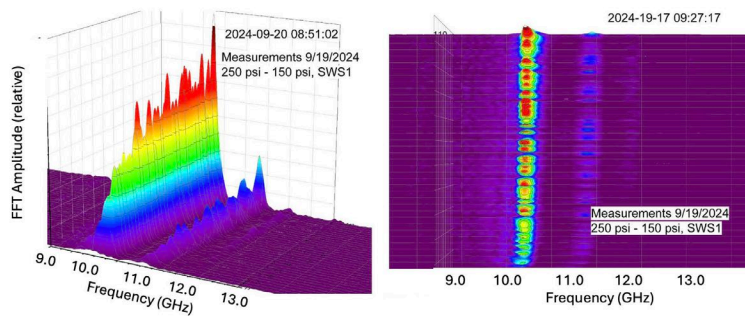


Figure 10. Experimentally measured 3D plot of the frequency spectra.

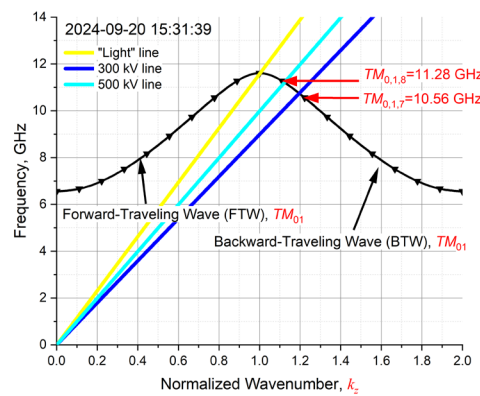


Figure 11. “Cold” dispersion diagram of an X-band SWS overlaid with 300 keV and 500 keV “electron beam” lines.

The experimentally measured 3D-oscillograms of the cathode voltage (Fig. 8), the discharge current (Fig. 9), and 3D-plot of the frequency spectra (Fig. 10) characterize the BWO operation. Microwave power in front of the output antenna of the BWO is not measured because the commonly used method to do this – vertical/horizontal scans of a local microwave power by a section of WR-90 waveguide and a crystal detector with the following integration of the measured results – is not reliable when the BWO is driven by the SINUS-6 accelerator because of large variations of the cathode voltage amplitude from one pulse to the next.

The only reasonable way to estimate the output microwave power is to perform PIC simulations of BWO operation, where the cathode voltage of the simulated BWO gives, as a result of PIC simulations, the discharge current, the frequency of oscillations, and the output microwave power. If the first two output parameters obtained in PIC simulations correlate with the experimentally measured ones (Figs. 9 and 10), then it is reasonable to conclude that the PIC-calculated microwave power is about the same as that actually generated in experiments.

This three-pronged campaign will continue in Year 3.

Collaboration with Technion

Our collaboration with Krasik and Leopold at the Technion is continuing. HPM generation by a solid cathode-fed MDO was studied in experiment for different values of charging voltage ($V_{ch} = \pm(30-38)$ kV) and magnetic fields ($B_z = 0.4 - 1.0$ T). In these experiments, the results were almost the same for carbon and stainless steel cathodes of the same diameter. The cathode length (15 or 21 mm) also made little difference. Typical waveforms of the voltage, total current, the microwave electric field and its time-frequency analysis are shown in Fig. 11. These waveforms were obtained for a 9-mm diameter stainless steel cathode, a 20-mm diameter downstream reflector, a 40-mm diameter upstream reflector placed at a distance $d_{AR} = 52$ mm from the anode edge, $B_z = 0.55$ T and $V_{ch} = \pm 34$ kV. The microwave electric field was measured using a D-dot probe placed at 40 degrees at a distance of 40 cm from the output window.

The beginning of the current in Fig. 11(a) is delayed by ~ 10 ns from the beginning of the voltage. This is the result of the ≥ 100 kV/cm electric field threshold necessary for explosive plasma formation. Microwave generation starts after ~ 35 ns when the voltage reaches its maximal amplitude of ~ 200 kV, and the total current is ~ 0.5 kA. The microwave electric field reaches ~ 75 kV/m along ~ 10 ns, followed by a decay over a few tens of ns. Microwave generation terminates when the voltage becomes ≤ 150 kV and when the total current reaches ~ 1.8 kA while still rising. Thus, the total duration of the microwave pulse is ~ 50 ns. The microwave frequency is $f = 8.6$ GHz [Fig. 11(b)] over ~ 15 ns at peak amplitude and then gradually decreases to 8.2 GHz. In other experiments with different cathode diameters, values of B_z and V_{ch} , the frequency dependence was similar.

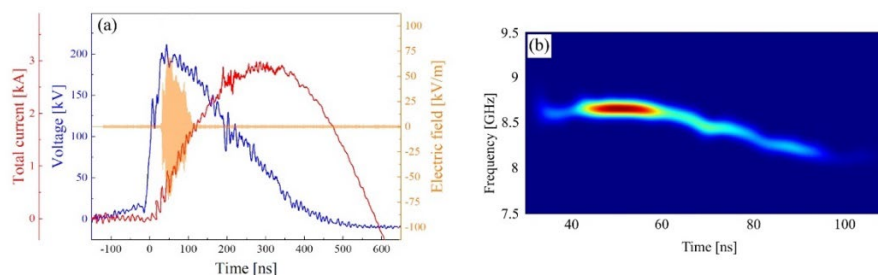


Figure 11. (a) Typical waveforms of the voltage (blue), total diode current (red), and microwave electric field (gold) and (b) the power distribution of the time-dependent frequency of the electric field. The color map of the frequency distribution is normalized to the maximal power ranging from 1 (deep red) to zero (deep blue).

It is disappointing that we are observing pulse shortening even though we are using a split cathode, an unexpected result. Simulations show that this relativistic magnetron does not operate in the ideal π -mode and that mode competition is present as well. Pulse shortening for the split cathode

could not be the result of plasma expansion but could be related to the instability observed in simulations. This work shows that a relativistic magnetron based on the KF MDO is a feasible X-band microwave source, but much more work is needed to reach an optimal design. Work is in progress on optimizing this MDO. This work was recently published in IEEE Trans. Plasma Sci.

Extending the MILO to Higher Frequency

We have been investigating the scaling of our low-frequency MILO work to X-band and higher. Using our PIC code to model variations, we changed the shape of the cathode and shortened the dump beam as well as increased the number of cavities and modified the input cathode stack. It was unsurprising that our internal changes of increasing cavity numbers affected the spectral output as well as change the oscillation behavior. Figure 12 shows our semi canonical MILO design with an added ring around the beam end as well as a shortened beam dump and perhaps more importantly additional cavities.

These changes opened up a multitude of possibilities, increasing the ‘experimental’ phase space by a large margin. Among the multitude of possibilities are – to shorten the beam dump even more, increase the ring diameter, increase the separation between the last cavity and the beam dump. To this end we are carrying out this work – not all successful but some quite – and only show some key results in Fig. 13.

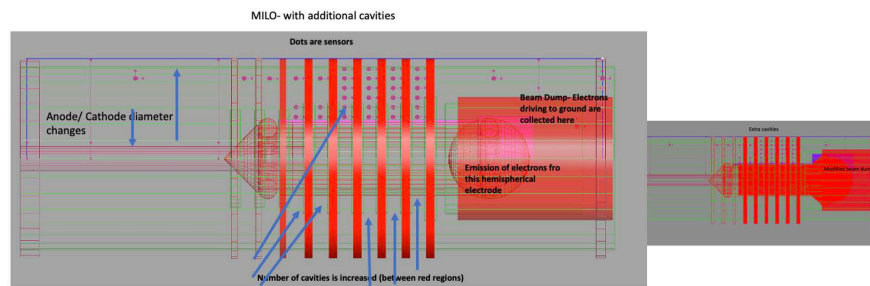


Figure 12. Cross-section of our modified MILO showing global changes in the anode end structure. Clearly visible is the extra cavities which were accommodated by lengthening the cathode stalk and shortening the beam dump. Inset image shows one of our modified hemisphere regions with shortened beam dump and extra cavities.

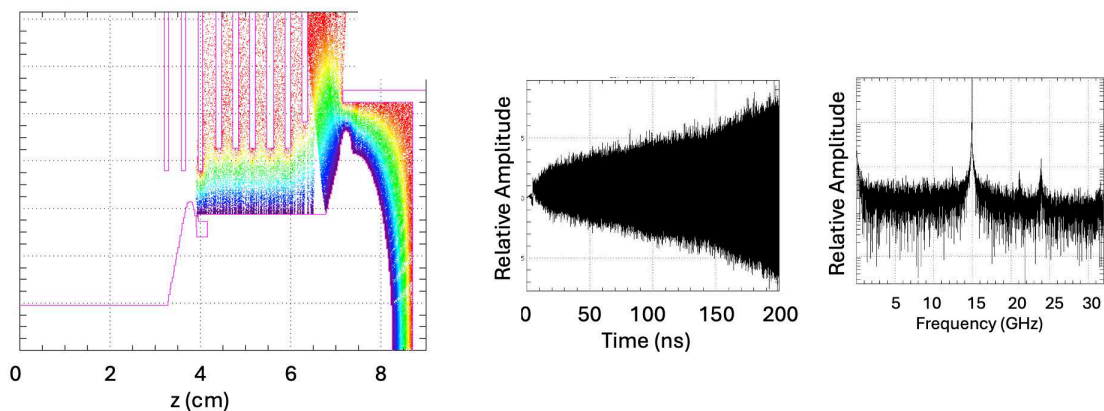


Figure 14. Left: PIC output of the modified MILO geometry showing shortened beam dump and modified end hemisphere, as well as extra cavities. The color code refers to the kinetic energy of the electrons. There are apparent discrete emission regions on the cathode due to numerical choices made in the run. Right: Pulsewidth and frequency output from one of our series of modified MILOs. Two things to notice. First is that there is coupling to the cavities leading to synchronicity. Second is that the principal frequency has increased from 12.3 GHz to around 15 GHz.

3. Findings and Conclusions

The literature review is continuing to give us a good picture as to what the state-of-the-art is in HPRF sources ranging from X-band to Ka-band. We have identified a lack of sources in the 20 GHz range. We have commenced experiments with an X-band BWO. Experimental results to-date have been consistent with PIC simulations and calculations of the dispersion curves. Our collaboration with Technion researchers is pushing the MDO to X-band.

For the MILO, our work has shown that the standard geometry of a scaled down MILO from 1 GHz to 12.5 GHz is also capable of operating at >15 GHz. This is critical as, in order to achieve high fields, we need high voltages and large AK gaps and so by not reducing the AK gap to go to higher frequencies we can still achieve these higher frequencies. The key is changing the load area structure and increasing the number of cavities.

In terms of Navy relevance of the project, our goal is to address, via focused and translational HPM research, some of the critical challenges facing Naval operations due to asymmetric threats, such as those faced by the US Navy in the Red Sea in the Fall of 2023, which caused the Navy over \$1B in operations and munitions! HPRF sources in the X-band to Ka-band range are critical to this objective.

In conclusion, our progress-to-date has been consistent with our stated objectives.

4. Plans and Upcoming Events

Our progress-to-date has been consistent with our stated objectives. As we transition to Year 3 we hope to be on target with our proposed goals. We were successful with a DURIP proposal to acquire a long pulse pulser. This should open new opportunities for us to explore different devices in experiment.

5. Transitions and Impacts

The Air Force declassified the fact the UNM MDO (magnetron with diffraction output) is the HPRF source used in the AFRL THOR system.¹⁸ The MDO was developed over the years through support by ONR and partial support by AFOSR. This is an important transition of this effort from 6.1 research to the field.

¹⁸ B. Hoff and J. Luginsland, "Applications of Vacuum Electron Devices to Base Defense Challenges," *Proc. IVEC 2024* (Monterey, CA, April 22-26, 2024).

6. Recommendations for Future Work

Our recommendations for immediate term future work are to continue with the objectives as originally proposed for this effort. With the availability of a new longer-pulse electron beam accelerator we will have an opportunity to research a wider variety of potential HPRF sources from X-band to Ka-band. This would be part of a proposed follow-on effort.

7. Personnel

Principal Investigator			
Full Name	Approximate Level of Effort – LOE - (Hours This FY)	Country of Residence	National Academy Member? (Y/N)
Edl Schamiloglu	160 Hours	USA	No
Co-Investigator(s) or Co-PI(s)			
Full Name	Approximate Level of Effort – LOE - (Hours This FY)	Country of Residence	National Academy Member? (Y/N)
Salvador Portillo	640	USA	No
Performer Business Contact(s)			
Full Name	Role	Country of Residence	
Office of Sponsored Projects (osp@unm.edu)	N/A	USA	N/A
Additional (Non-Student) Team Members			
Full Name	Approximate Level of Effort – LOE - (Hours This FY)	Country of Residence	National Academy Member? (Y/N)
Ahmed Elfrgani	480	USA	No
Subcontractors			
Full Name and Organization	Approximate Level of Effort – LOE - (Hours This FY)	Country of Residence	National Academy Member? (Y/N)
None			

8. Collaborations

Agency/Org	Performer	Project Name	Purpose of Research/ Collaboration
NSWCDD	John Kreger, Jack Chen, and Jon Cameron Pouncey	HPM collaboration	We discussed proceeding with MDO and transparent cathode testing at NSWC
AFRL/RD	Brad Hoff	HPM cathode and switch collaboration	We are discussing collaborative research on HPM cathodes and pulsed power switches/CsI coatings
Technion, Haifa, Israel	Yakov Krasik and John Leopold	Comparison of magnetic mirror vs. cathode rod and reflector	Optimize suppression of magnetron leakage current via an electron beam in a squeezed state – now in X-band
Weizmann Institute of Science	Yitzhak Maron	Diagnostics	Time-resolved spectroscopic diagnostics in high power, cross-field devices
Drexel University	Genevieve Dion	Cathodes	Large area cathode assembly
DexMat	Dmitri Tsentalovich	Cathodes	Providing base material for sewn cathodes
Verus Research	Sameer Hemmady	MILO	High impact outcomes
Stanford University	Ken Hara	Cathodes, MILO, MDO	Spectroscopy
Texas Tech University	Ravi Joshi	Cathodes, MILO, MDO	Effects of outgassing
Sem-Sol	Peter Duselis, Sterling Beeson	MILO, cathodes	X-band and higher frequency
Collins Clark Technologies	Collins Clark	Pulser	Acquisition of a longer pulse pulser

9. Students

Doctoral Student(s)			
Full Name	University	Graduated?	Graduation Year
None			
Masters Student(s)			
Full Name	University	Graduated?	Graduation Year
None			

Undergraduate Student(s)			
Full Name	University	Graduated?	Graduation Year
Christopher M. Rodriquez	University of New Mexico	No	
Edwin Falcon Guzman	University of New Mexico	No	
Eduardo Hernandez	University of New Mexico	No	
Johnny I. Montoya	University of New Mexico	No	

10. Technology Transfer

The MILO work is in collaboration with Kost Ilyenko, Institute for Radiophysics and Electronics, National Academy of Sciences of Ukraine and the results of this collaboration will be shared with NSWCCD.

UNM is continuing its collaboration with scientists at the Technion on a high frequency relativistic magnetron with split cathode and this design will be shared with NSWCCD.

Other technology transfers are pending.

11. Products, Publications, Patents, License Agreements, etc.

Publications resulting from this project for the reporting period:

Archival Publications

#	Citation	Acknowledged ONR Support Received? (Y/N)	Peer Reviewed? (Y/N)
1	G. Liziakin, O. Belozerov, J.G. Leopold, Yu. Bliokh, Y. Hadas, Ya.E. Krasik, and E. Schamiloglu, "Experimental Research on a Split-Cathode-Fed Magnetron Driven by Long High-Voltage Pulses," IEEE Trans. Electron Dev., vol. 71, 2099-2104 (2024).	Yes	Yes
2	M. Liu, E. Schamiloglu, Z. Kan, C.L. Liu, W. Jiang, C. Wang, Q. Wu, and Z. Liu, "PIC Simulations of a Novel Sub-1-GHz Compact Relativistic Cherenkov Oscillator Using Spiral Metamaterials with High Output Power," IEEE Trans. Plasma Sci., vol. 52, 666-671 (2024).	Yes	Yes
3	G. Liziakin, O. Belozerov, J.G. Leopold, Yu. Bliokh, Y. Hadas, Ya.E. Krasik, and E. Schamiloglu, "Experimental Research on a Split-Cathode-Fed	Yes	Yes

	Magnetron Driven by Long High-Voltage Pulses,” IEEE Trans. Electron Dev., vol. 71, 2099-2104 (2024).		
4	O. Belozarov, G.D. Liziakin, J.G. Leopold, A.D. Andreev, Y. Hadas, E. Magid, E. Schamiloglu, and Y. Krasik, “Experimental Research on an X-Band Magnetron Fed by Solid and Split Cathodes,” IEEE Trans. Plasma Sci., vol. 52, 2749-2759 (2024).	Yes	Yes
5	K. Ilyenko, T. Yatsenko, V. Vekslerchik, A. Opanasenko, and S. Portillo, “Upper-Hybrid Oscillations of High Current Relativistic Electron Beam Under Conditions of Magnetic Self-Insulation,” Phys. Plasmas, vol. 31, 072303 (2024).	Yes	Yes

Conference Papers

#	Citation	Acknowledged ONR Support Received? (Y/N)	Peer Reviewed? (Y/N)
1	E. Schamiloglu and C. Christodoulou, “Recent High Power Electromagnetics Research at the University of New Mexico,” Proc. ICEAA 2023 (Venice, Italy, October 9-13, 2023), p. 565.	Yes	Yes
2	A.D. Andreev, E.F. Guzman, C. Rodriguez, and E. Schamiloglu, “Experimental Measurements of Magnetically-Insulated Coaxial Diode’s Space-Charge-Limited Electron-Beam Current, a.k.a. Fedosov Current, on the SINUS-6 High-Current Electron-Beam Accelerator at the University of New Mexico,” Proc. IVEC 2024 (Monterey, CA, April 22-26, 2024), paper 11.5.	Yes	Yes
3	E. Schamiloglu and J.M. Lehr, “High Power RF (HPRF) Through the Lens of the SUMMA Foundation,” Proc. NATO Radio-Frequency Directed Energy Weapons – Status and Perspectives (Keynote Address) (Copenhagen, Denmark, May 16-17, 2024), paper KN-5.	Yes	Yes
4	E. Schamiloglu, B. Petit, R. Hoad, and W. Radasky, “Summary of Recent HPEM Standards Activities of IEC SC 77C,” Proc. GlobalEM 2024 (Austin, TX, July 14-19, 2024).	Yes	Yes
5	A.D. Andreev and E. Schamiloglu, “Experiments with 6-Cavity S-Band (A6) Relativistic Magnetron,” Proc. GlobalEM 2024 (Austin, TX, July 14-19, 2024).	Yes	Yes

6	A.D. Andreev and E. Schamiloglu, "Simulations of 8-Cavity X-Band Relativistic Magnetron," Proc. GlobalEM 2024 (Austin, TX, July 14-19, 2024).	Yes	Yes
7	E. Schamiloglu and C. Christodoulou, "Advancing High Power Microwave Sources and Antennas to Higher Frequencies," Proc. ICEAA 2024 (Lisbon, Portugal, September 2-6, 2024), p. 209.	Yes	Yes

Books

Nothing to report

Book Chapter

Nothing to report

Theses

Nothing to report

Websites

Nothing to report

Patents

Nothing to report

Other Products:

#	Product Description	Acknowledged ONR Support Received? (Y/N)	Peer Reviewed? (Y/N)
1	E. Schamiloglu, "High Power Microwave Sources – The Quest for Higher Frequencies," DEPS UK/US Directed Energy Workshop (Shrivenham, UK, July 22-26, 2024).	Yes	Yes
2	E. Schamiloglu, "Status and Development of New Sources for Producing HPEM Fields (Invited Tutorial)," GlobalEM 2024 (Austin, TX, July 14-19, 2024).	Yes	Yes
3	G. Liziakin, O. Belozorov, J.G. Leopold, Y.E. Krasik, A.D. Andreev, and E. Schamiloglu, "An X-Band High Power Magnetron," Proc. EAPPC-BEAMS-Megagauss 2024 (Amsterdam, Netherlands, September 22-26, 2024), paper P3-28.	Yes	Yes

4	E. Schamiloglu, "Evolution of the Relativistic Magnetron (Invited)," Proc. EAPPC-BEAMS-Megagauss 2024 (Amsterdam, Netherlands, September 22-26, 2024), paper O20-1.	Yes	Yes
---	---	-----	-----

12. Point of Contact in U.S. Navy / Marine Corps

Full Name	Organization	Date of Last Contact
Dr. Jon Cameron Pouncey	HPM Technology Development Branch E52, NSWC DD	09/20/2024
Dr. Jack Chen	HPM Technology Development Branch E52, NSWC DD	12/16/2024

Novel HPM source topologies for high power microwave and millimeter wave generation

Grant No. N00014-23-1-2305

Annual Report for Fiscal Year 2024

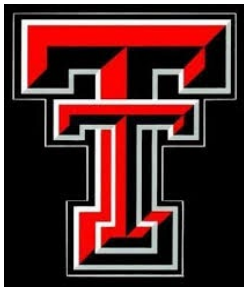
Period of Performance: October 1, 2023 to September 30, 2024

Prepared by:

Professor Jacob Stephens, Principal Investigator
Texas Tech University
jacob.c.stephens@ttu.edu,

Co-Principle Investigator(s):

John Mankowski, john.mankowski@ttu.edu, Texas Tech University
James Dickens, james.dickens@ttu.edu, Texas Tech University
Andreas Neuber, andreas.neuber@ttu.edu, Texas Tech University



This work was sponsored by the Office of Naval Research (ONR), under grant/contract number N00014-23-1-2305. The views and conclusions contained herein are those of the authors only and should not be interpreted as representing those of ONR, the U.S. Navy or the U.S. Government.

Section I: Project Summary

1. Overview of Project

Executive Summary:

This effort is an experimental study to understand the power and frequency scaling limits of a split-cavity oscillator (SCO) high power microwave (HPM) sources. SCOs are a comparatively simple HPM source topology, requiring little to no guiding magnetic field, and featuring lower demand from the pulsed power system. However, the frequency scaling characteristics of this topology to X-band and higher frequencies are not well understood. Over the full duration of the project, various X-band to K-band SCO sources are to be designed, built, and experimentally characterized (quantifying power, frequency, lifetime, etc.), and a comprehensive summary of our findings will be reported.

Objective:

The objective of this work is to conduct an experimental study of various SCO designs, in various geometries (coaxial, planar, radial) at X-band to K-band frequencies. In addition, we will explore various grid materials, including pyrolytic graphite, which has been successfully demonstrated to endure relativistic \sim kA electron beam loading in a vircator. We seek to improve the understanding of the power-frequency-lifetime scaling characteristics of SCO HPM sources to inform future decisions regarding their further study and application.

Naval Relevance:

HPM sources are needed at X-band and higher frequencies for applications such as *in-band* counter-electronics. However, HPM sources tend to follow a power-frequency squared scaling law (e.g. a 10x increase in frequency is associated with a 100x decrease in power). In addition, the physical dimensions of HPM sources are proportional to wavelength. Thus, the needed HPM sources with higher frequency capabilities will feature smaller dimensions (higher fields, power density, and beam current density). Though some HPM sources have been successfully demonstrated at these higher frequencies, they are often accompanied by technological challenges (e.g. high magnetic requirements, need for extreme current and/voltage with extreme precision). The SCOs explored in this effort are a highly simplified HPM source topology. While in some ways inferior to these more advanced sources, SCOs may offer somewhat comparable performance at a fraction of the system demand. This study seeks to quantify the performance metrics of SCOs such that the trade-off between complexity and performance in SCOs may be better understood.

Introduction/Background:

There is a wealth of HPM source topologies that have been and could be explored to meet the objective of realizing X-band and higher frequency HPM platforms. Though there have been a number of notable successes in developing HPM systems at these higher frequencies, they often feature a number of technological challenges, especially when considering field readiness.

For X-band and higher frequencies, HPM interaction structures become physically small, resulting in much higher fields, power densities, and current densities. These small dimensions and higher fields are associated with increased breakdown susceptibility, heating, and electron beam-induced

degradation. Further, the smaller dimensions and increased electron beam current density are also associated with a higher magnetic field requirement to keep the electron beam confined on axis.

Historically, vircators and magnetically insulated line oscillators (MILOs) have been considered as technologically simplified HPM sources, not requiring an external guiding magnetic field, and generally featuring lower demand on the required pulsed power driver. However, previous efforts in literature to scale vircators and MILOs to higher than X-band frequencies have highlighted a number of challenges and limitations. Another possible simplified source technology is the SCO.

SCOs were explored in previous decades, but have not been explored in more recent years owing to lifetime issues associated with the destruction of their grid, which is exposed to a relativistic kA electron beam. In recent previous studies, we achieved long-lifetime operation of a vircator ($\sim 1\text{E}6$ shots) by employing pyrolytic graphite as the grid material. Pyrolytic graphite features modest electrical conductivity, high thermal conductivity, and notably, will not melt (the nearest phase change is sublimation, which occurs at much higher temperature). We postulate that the lifetime of SCO HPM sources may be extended by employing pyrolytic graphite (or similar material) grids, which would enable a new simplified HPM source technology to be explored as a candidate for realizing a simplified HPM platform at X-band and higher frequencies.

2. Activities and Accomplishments

Our first task was to develop the experimental capability to conduct the experimental SCO characterization effort. This began with the development of a Marx generator with integrated pulse forming network (PFN) stages. With a threshold objective of 500 MW of HPM and a target objective of 1 GW, assuming $\sim 10\text{-}20\%$ efficiency, an electron beam power of ~ 5 GW was required. Considering the trade-offs in challenges between current and voltage, we selected a target voltage and current of 500 kV and 10 kA. Assuming a ~ 50 kV initial charging voltage, taking into account the voltage-halving due to matching the erected PFNs to the device, ~ 20 stages are required. Finally, this also requires a very low PFN impedance per stage on the order of 2-3 Ohms. Multiple PFN topologies were tested, but ultimately, a high-order Rayleigh PFN proved to be approximately on par with the type C and type E Guillemin networks that were tested. The final PFN and measured voltage waveform are shown in the below figure 1. This design used 15, 2.6 nF FHV-9AN ceramic capacitors, connected by a large bus bar, which was optimized to give a ~ 2 Ohm impedance.

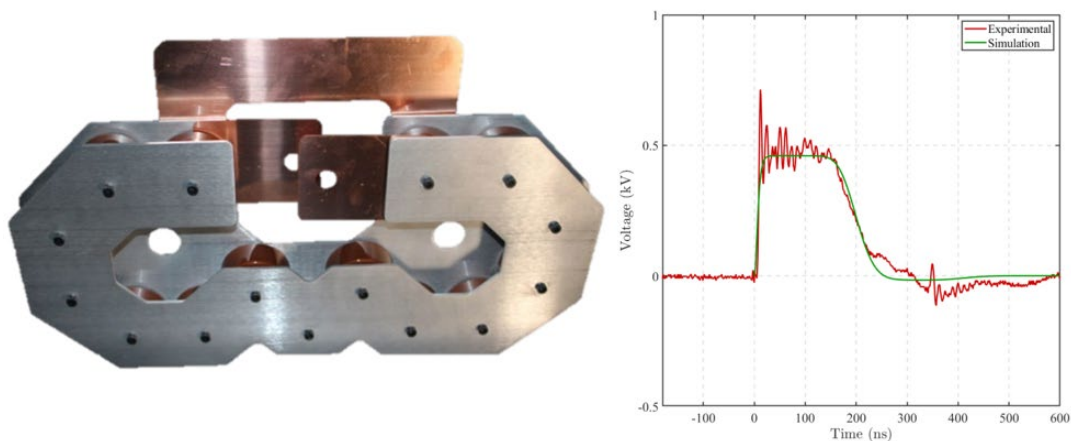


Figure 1: (left) Image of the physically constructed, 15-stage Rayleigh PFN. (right) Comparison of measured and simulated load voltage for a 1 kV initial charge and 2 Ohm load.

This system was tested in a scaled configuration, as shown in the below figure 2. A 7-stage Marx generator was fabricated based on this PFN design. In the first tests, poor voltage flat top was achieved, owing to excess stray inductance in the Marx generator assembly. We found that by adjusting the current flow in the Marx to follow a zig-zag pattern, partial nulling of the magnetic field between stages resulted in lower stray inductance and better pulse characteristics.

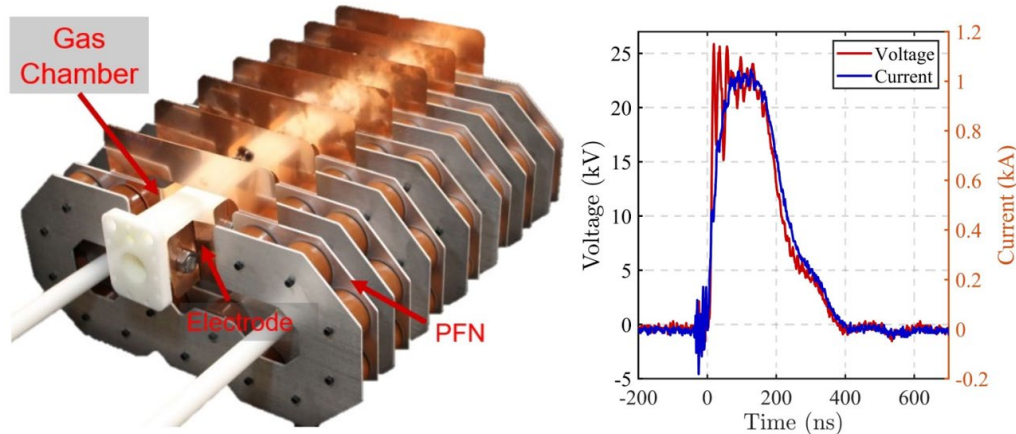


Figure 2: (left) Physically constructed 7-stage PFN-Marx. (right) Experimentally measured PFN-Marx output voltage and current (10 Ohm load, ~4 kV charging voltage). Measurements performed in open air.

With these results, the full 19-stage PFN Marx design was completed and assembled (see below figure 3). In the initial tests, some breakdowns were observed and mitigated with additional insulation and ad-hoc modifications. Additionally, the material selected for the spark gap assembly (acetal copolymer, i.e. Delrin) was found to have seams in the bulk material that resulted in air leaking and bubbling in the oil assembly. Nonetheless, the device has been successfully operated for hundreds of shots.



Figure 3: Top-down view of the 19-stage PFN Marx generator hanging from the suspension rack into the oil tank for experimental testing.

Notably, the voltage and current waveforms are increasingly distorted with the addition of more stages in the Marx assembly, owing to the increased stray inductance. Overall, the pulse quality is acceptable for this research effort but could be improved.

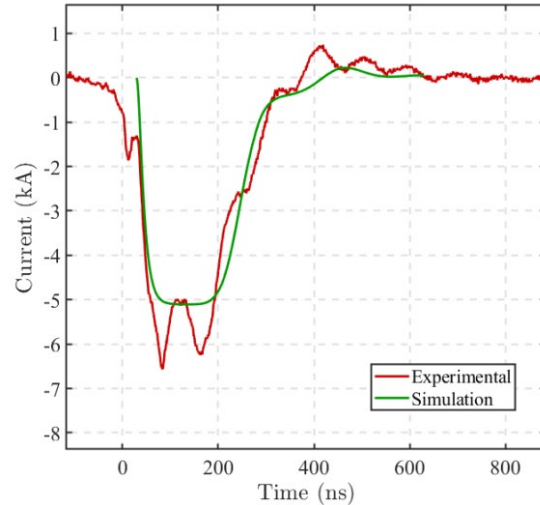


Figure 4: Comparison of experimentally measured and simulated PFN-Marx output current for ~ 45 kV charge voltage and a 90 Ohm load (approximately 500 kV load voltage).

With the successful build of the Marx generator, the next item was getting the high voltage into the vacuum assembly. A custom high voltage feedthrough (figure 5) was designed and optimized through electrostatic simulation. This system was based on an off-the-shelf ceramic insulator, and field grading rings were added to the insulator interior and exterior to shield the field at the cathode triple junctions in both the oil and vacuum side. In testing, this device did not hold vacuum due to a failed weld joint. In order to get to test as soon as possible, Torr-seal was applied, and moderate vacuum, to below $1E-6$ Torr has been achieved. A revised design, with simplified welding requirements has been developed, and fabrication is in progress.



Figure 5: Assembled high voltage feedthrough (electro-mechanical interface between the oil and vacuum sections).

In parallel to the above efforts, a second student has been developing various designs of SCO HPM sources, employing particle-in-cell (PIC) simulations using CST Particle Studio. The main two geometries that have been simulated are a coaxial split-cavity oscillator (CSCO) with an annular cathode and a rectangular split-cavity oscillator (RSCO) with a rectangular cathode. Both utilize pyrolytic graphite sheets as the front, split, and back of the cavity. The most successful design of the CSCO with a TEM to TM mode converter, along with the annular cathode design, can be seen in the below two figures 6 and 7. The second design features insertable cavity stubs, which have been shown in simulation to help select lower-order modes.

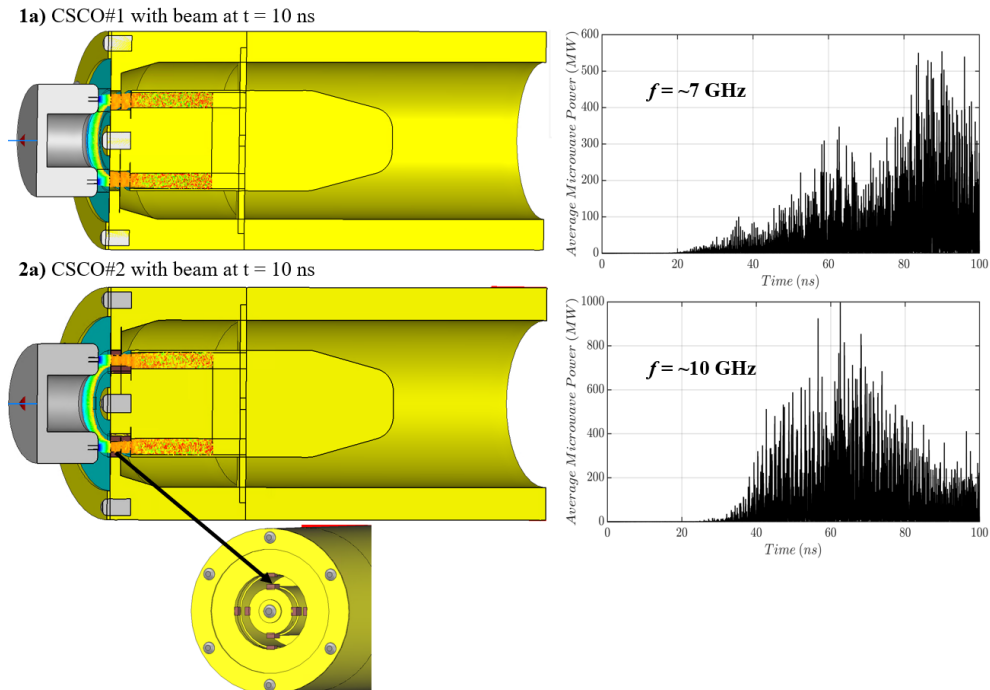


Figure 6 (top) CSCO design 1 with no cavity stubs and associated average microwave power vs. time plot. (bottom) CSCO design 2 featuring cavity stubs with 90-degree spacing within the cavity interaction region and associated average microwave power vs. time plot.

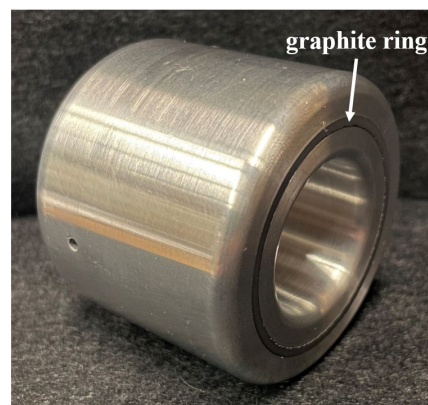


Figure 7: Cathode with a press-fit POCO Angstrom-fine graphite ring inserted into the aluminum guiding shell.

To test the electron beam generation, a beam dump (see figure 8) was placed in the vacuum chamber where the front resembles the front of the CSCO. A nylon witness plate was also placed behind the pyrolytic graphite sheet to confirm if electrons were propagating through the graphite sheet. The alignment of the assembly without the graphite sheet or witness plate and the before and after pictures of the parts from testing can be seen in the below figure. The beam dump assembly was subjected to 8 shots, with the Marx generator being charged to -30 kV. The ring-like damage on the front of the graphite sheet and the yellowing of the nylon witness plate represent signs of an annular beam propagating from cathode to anode.

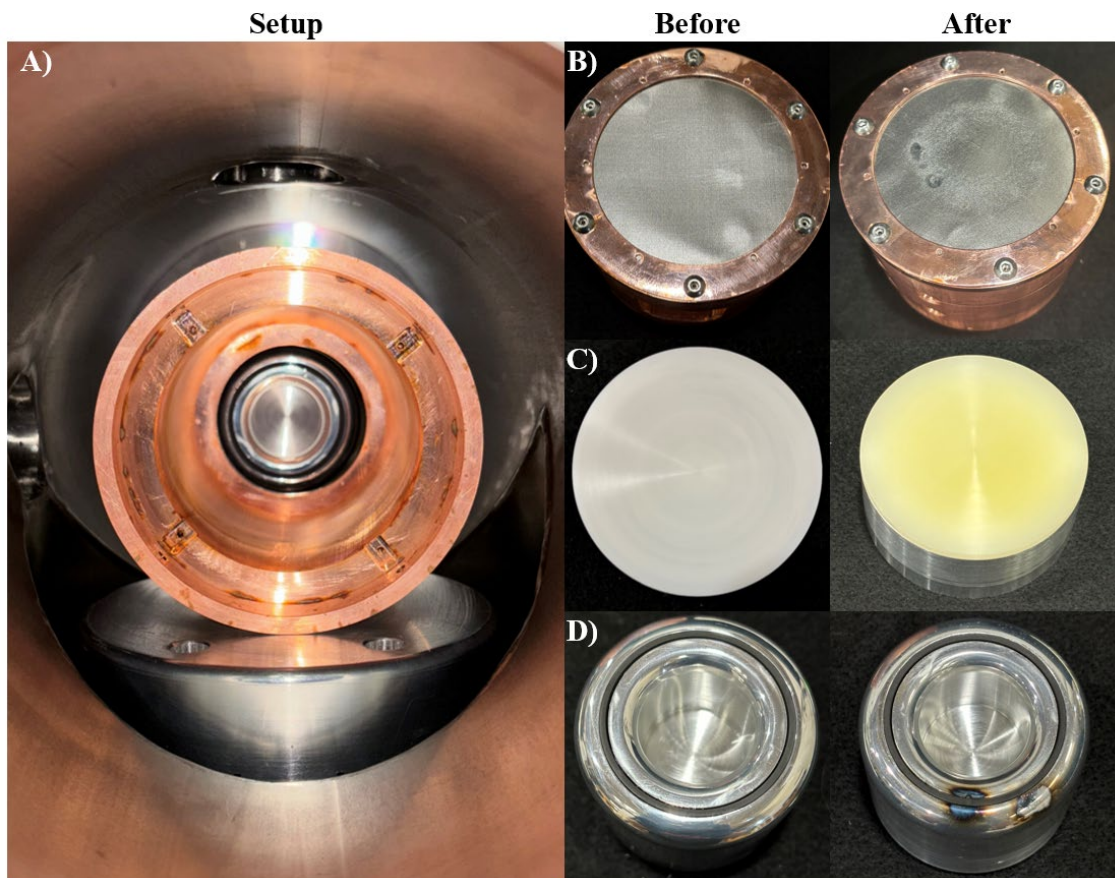


Figure 8: A) A back view of the beam dump assembly without the nylon witness plate and front pyrolytic graphite sheet to show alignment between the cathode and beam dump. B) Before and after photos of the front of the beam dump assembly showing the ring pattern and breakdown locations caused by the electron beam. C) Before and after photos of the nylon witness showing yellowing after the shots due to electron impact. D) Before and after photos of the cathode showing the breakdown locations on the cathode's aluminum casing surrounding the graphite emission ring.

After testing beam generation with the beam dump, a preliminary test of a CSCO was performed. In this first test, no baking was performed, which resulted in premature AK gap closure in many shots and ultimately led to premature failure of the CSCO. Still, a total of 23 shots were taken on

the CSCO, with Marx charging voltages ranging from -35 kV to -50 kV. There was no transmitting antenna on the output of the vacuum chamber, so any microwaves produced would simply radiate through the glass window. Two receiving double ridge guide horn antennas were placed downrange of the output of the glass window. Detector diodes were used to observe the microwave profile, and direct measurement of microwaves was achieved via a fast, 12 GHz, 40 GSa/s oscilloscope. Waveforms of the Marx voltage and current and the signals from the two horn antennas, as seen on the oscilloscope, for a -50 kV charging shot can be seen in the below figure 9. Initially, the cathode is not emitting, leading to an early peak in the applied voltage. Once the cathode turns on, current flow begins, inducing the expected voltage decrease resulting from the finite impedance of the PFN Marx pulsed power driver. The diode detectors showed evidence of microwaves and direct measurements showed a ~ 1 GHz signal, which is far below the anticipated ~ 7 -10 GHz. This discrepancy is currently being investigated. Pictures of the post-test CSCO components are given in the below figure, showing extensive damage due to arcing in the AK gap.

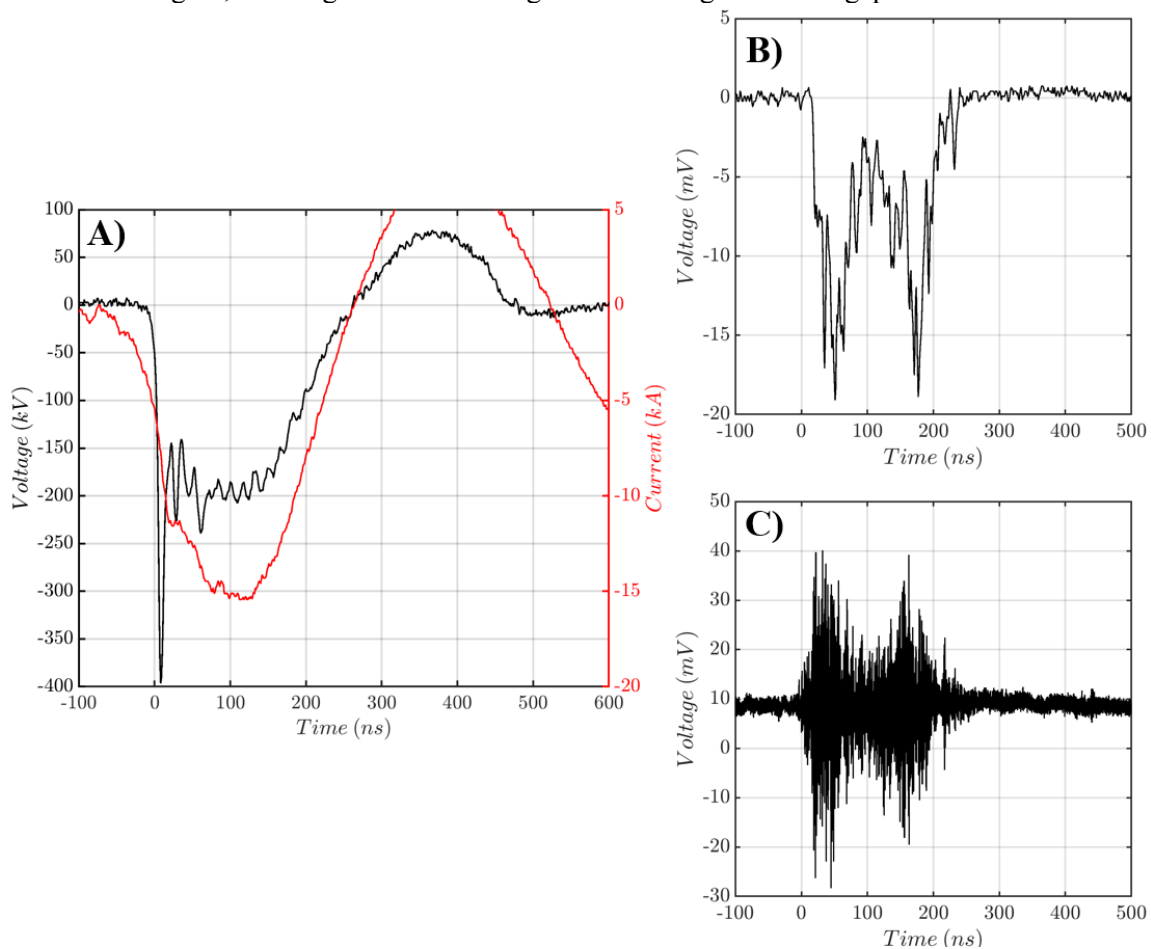


Figure 9: A) Voltage and current data seen on the CVD and CVR (CVR on the current return of the HPM source) for a -50 kV charging shot. B) Microwave profile seen at the oscilloscope from a receiving antenna with a detector diode. C) Signal received at the oscilloscope from the second receiving antenna with no detector diode (~ 1 GHz). Note that all waveforms are from the same shot and likely after extensive damage to the CSCO was done.

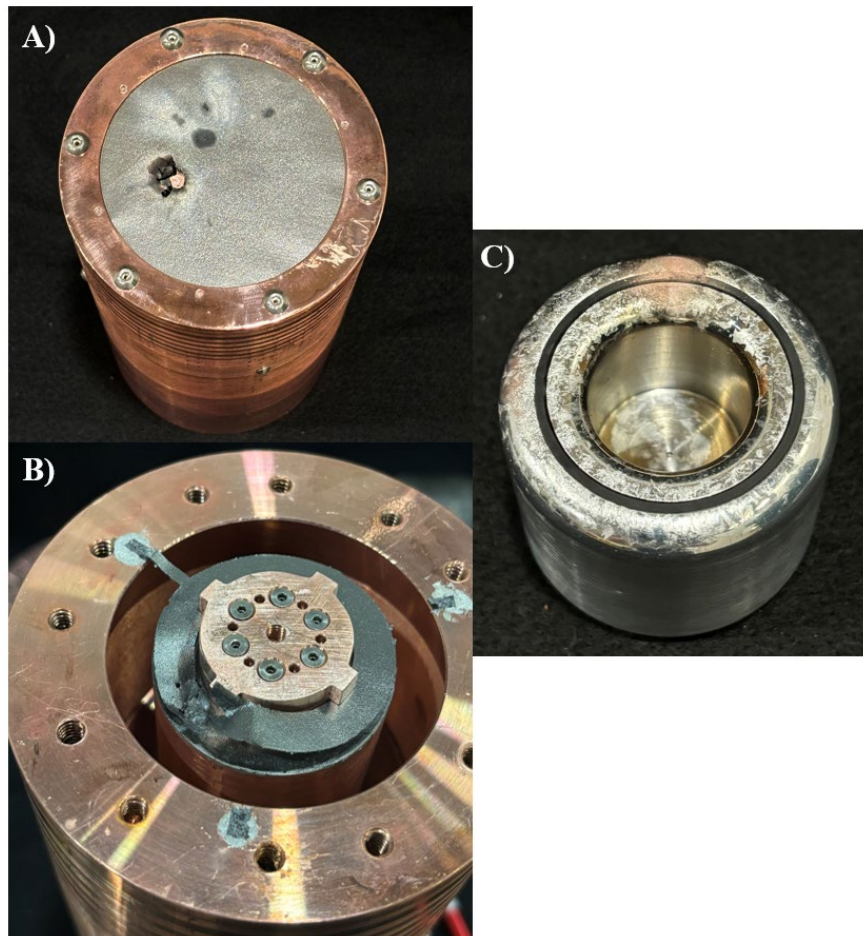


Figure 10: A) The front (entrance) to the CSCO after 23 shots. B) The middle “split” graphite sheet within the CSCO after 23 shots. C) The cathode after 23 shots.

Additional Figures / Photos:

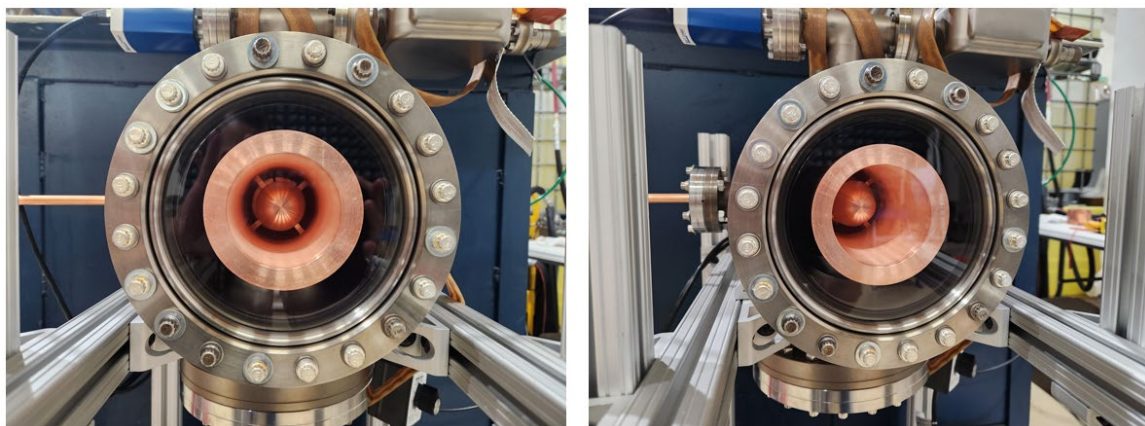


Figure 11: (left) Down-bore look at the mode converter and SCO. (right) Off-axis, down-bore look at the mode converter and SCO.

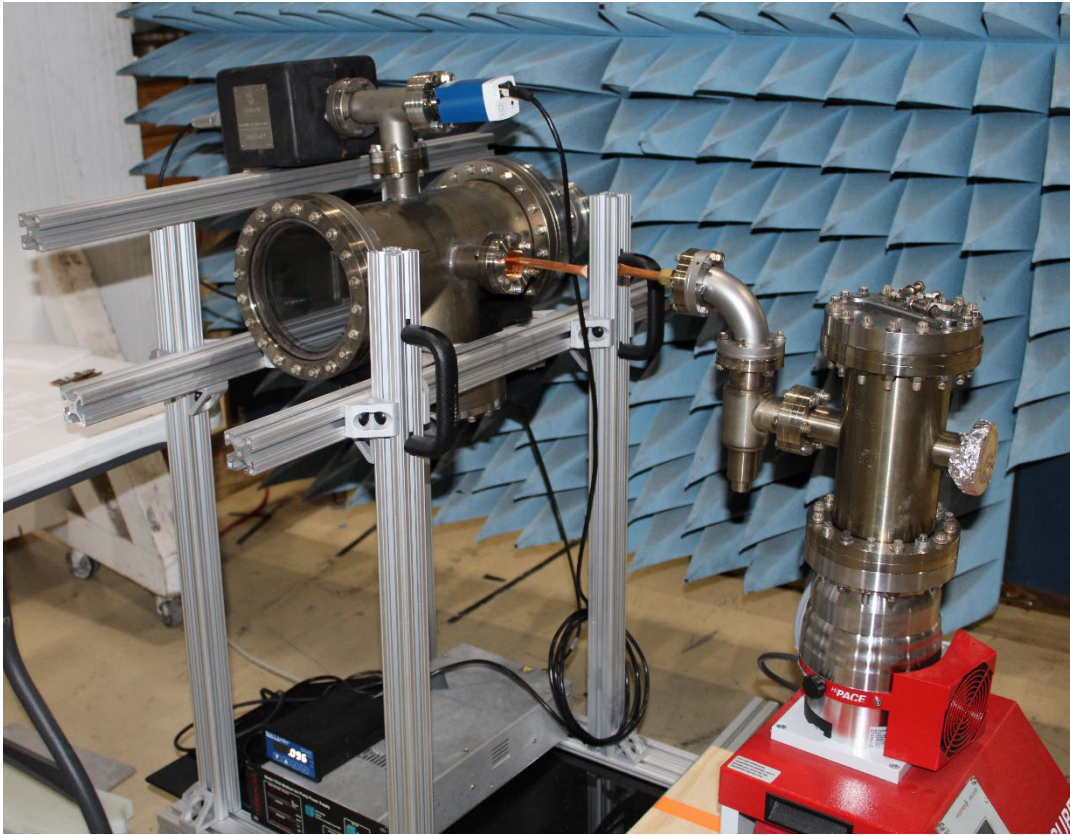


Figure 12: Picture of the vacuum system, disconnected from the Marx tank, in front of the anechoic wall.

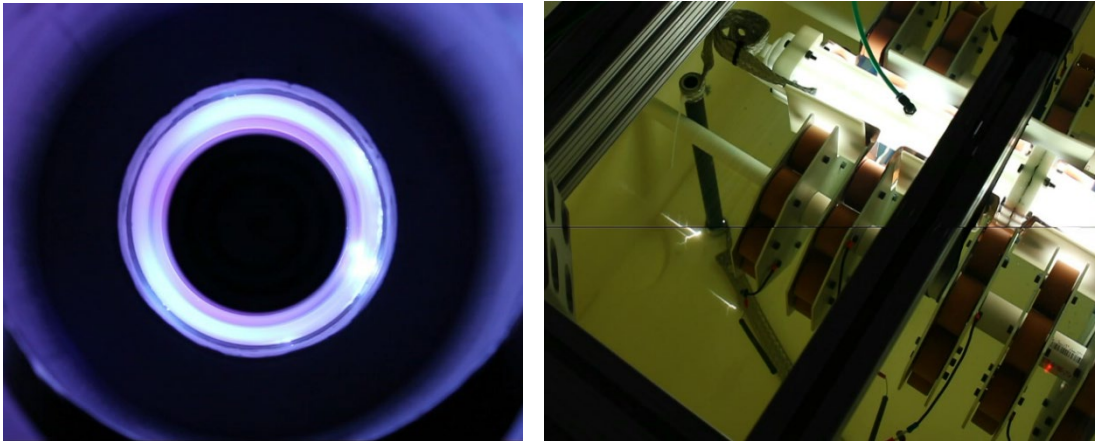


Figure 13: (left) Open shutter image of vacuum surface flashover on the high voltage feedthrough. (right) Open shutter image of breakdown on the PFN-Marx in the oil-tank.

3. Findings and Conclusions

At the close of FY24, we are approximately 1.5 years into a 3 year effort. We have succeeded in developing our experimental platform and are in the very early stages of device testing. We anticipate first microwave results in the next 1-2 quarters. As we progress, we anticipate producing results that will inform decisions about the suitability of SCO devices for future HPM platforms.

4. Plans and Upcoming Events

With our experimental test bed operational, we plan to continue testing our HPM sources in FY25 and into FY26, and we are hopeful for first HPM results in the first or second quarter of FY25. Additional SCO designs will be fabricated and tested as part of this experimental campaign.

In 2025, we plan to present results at a Directed Energy Professional Society (DEPS) meeting, and the Pulsed Power and Plasma Science Meeting. With successful tests of SCO devices, we also plan to publish our findings in peer reviewed journals.

5. Transitions and Impacts

No information to report

6. Recommendations for Future Work:

No information to report

7. Personnel

Principal Investigator			
Full Name	Approximate Level of Effort – LOE - (Hours This FY)	Country of Residence	National Academy Member? (Y/N)
Jacob Stephens	500 (approx.)	USA	[N]
Co-Investigator(s) or Co-PI(s)			
Full Name	Approximate Level of Effort – LOE - (Hours This FY)	Country of Residence	National Academy Member? (Y/N)
John Mankowski	60 (approx.)	USA	N
Andreas Neuber	15 (approx.)	USA	N
James Dickens	15 (approx.)	USA	N
Performer Business Contact(s)			
Full Name	Role	Country of Residence	
Additional (Non-Student) Team Members			
Full Name	Approximate Level of Effort – LOE - (Hours This FY)	Country of Residence	National Academy Member? (Y/N)
Subcontractors			

Full Name and Organization	Approximate Level of Effort – LOE - (Hours This FY)	Country of Residence	National Academy Member? (Y/N)

8. Collaborations

No information to report

9. Students

<u>Doctoral Student(s)</u>			
Full Name	University	Graduated?	Graduation Year
Michael Mounho	Texas Tech U.	N	May 2026
<u>Masters Student(s)</u>			
Full Name	University	Graduated?	Graduation Year
Braden Baird	Texas Tech U	N	May 2025
Anna Slovak	Texas Tech U.	N	Dec. 2025
Taewhan Ko	Texas Tech U.	N	Dec 2024
<u>Undergraduate Student(s)</u>			
Full Name	University	Graduated?	Graduation Year

10. Technology Transfer

No information to report

11. Products, Publications, Patents, License Agreements, etc.

Publications resulting from this project for the reporting period:

Archival Publications

No information to report

Conference Papers

No information to report

Books

No information to report

Book Chapter

No information to report

Theses

#	Citation	Acknowledged ONR Support Received? (Y/N)	Peer Reviewed? (Y/N)
1	Taewhan Ko “Development and Test of Pulse-Forming Network Marx Generator for High-Power Microwave Applications” MS Thesis, Texas Tech University 2024.	Y	N

Websites

No information to report

Patents

No information to report

Other Products:

No information to report

12. Point of Contact in U.S. Navy / Marine Corps

<u>Navy Point(s) of Contact Student(s)</u>			
Full Name	Organization	Email	Date of Last Contact
Yeong-Jer Chen	NSWCDD	Y	11/21/2024

Elucidating Plasma Formation Near Dielectric Interfaces in High Power Microwave Systems

Grant No. N00014-23-1-2306

Annual Report for Fiscal Year 2024

Period of Performance: October 1, 2023 to September 30, 2024

Prepared by:

Professor Thomas C. Underwood, Principal Investigator
The University of Texas at Austin
Email: thomas.underwood@utexas.edu



This work was sponsored by the Office of Naval Research (ONR), under grant/contract number N00014-23-1-2306. The views and conclusions contained herein are those of the authors only and should not be interpreted as representing those of ONR, the U.S. Navy or the U.S. Government.

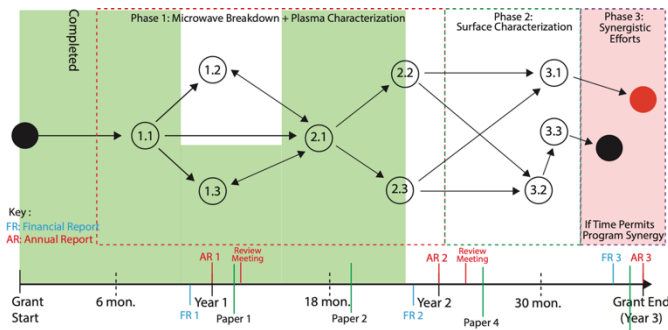


Figure 2. Project flowchart depicting deliverables and a breakdown of tasks. Efforts over the past month have focused on developing and validating plasma diagnostics related to THz spectroscopy as well as the design and setup of the microwave cavity as we are awaiting delivery of our microwave amplifier.

a fundamental tradeoff that influences the time resolution and plasma properties that can be inferred with THz spectroscopy. We have demonstrated how to configure this diagnostic to achieve a desired resolution in measuring the concentration of gaseous molecules (i.e., absorption) or plasma density (i.e., phase shift) by exploiting independent control over the chirped width and bandwidth of a probe pulse. Numerical simulations of chirped pulse and supercontinuum-extracted THz pulses were conducted to validate and elucidate the characteristics of experimentally measured chirped pulse and supercontinuum THz pulses at 1.5-2 ps probe pulse widths. The results demonstrate a favorable correlation between theoretical and experimental data for chirped pulses, along with a strong agreement between delay line and supercontinuum-extracted THz signals. This gives further confidence over our resolution and ability to probe plasma during fast breakdown transients. Highlights of our progress over the last year include:

- We developed a generalized theory for quantitative single-shot THz spectroscopy in terms of reducing signal distortion, improving spectral bandwidth while maintaining good spectral resolution.
- We demonstrated quantitative agreement between the dispersive effects of plasmas and our single-shot THz diagnostic. These measurements correspond to plasma densities in the range 10^{17} - 10^{19} m^{-3} , conditions of interest for breakdown in cavities.
- We demonstrated chirped pulse widths and bandwidths of probe pulses that are necessary to measure gaseous concentrations of molecules near dielectric surfaces.
- We generated supercontinuum and detected a temporal distortion in single-shot THz time-domain signals due to plasmas at various powers.
- We have setup our microwave cavity and microwave amplifier. We have begun characterization of the cavity for determining forward and reflected power. We are adding dielectric resonators to cause breakdown near surfaces.

Objective: The goal of this project is to understand the mechanism that governs plasma formation near dielectric surfaces in HPM systems (Fig. 3). This includes quantifying the (1) threshold for plasma production, (2) dielectric response of plasmas, (3) interfacial coupling and boundary effects, and (4) the interaction with microwave transmission. Insights into the synergy between dielectric interfaces (e.g., charge distributions, ablation, temperature, etc.), plasma, and microwaves will be developed, *for the first time*, while capturing the time and spatial scales over which it evolves. Collectively, these innovations will aid in improving the predictability of HPM systems and evaluate the feasibility of extrapolating to new regimes of operating power, frequency, and pulse

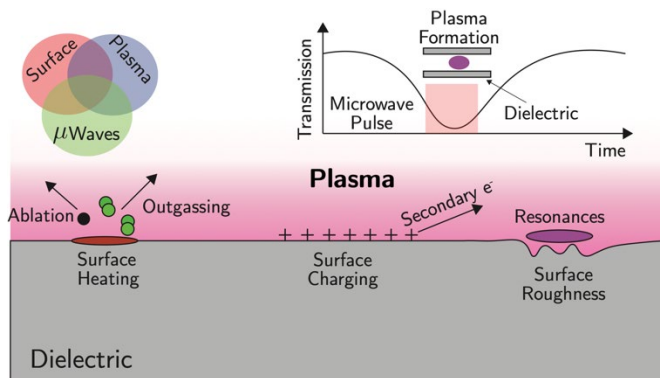


Figure 3. This project focuses on developing mechanistic insight about plasma formation near dielectric interfaces as they are exposed to microwaves. Objectives focus on identifying the role of interfacial chemistry (i.e., charging, heating, outgassing) in establishing the threshold and pathway to microwave breakdown. Diagnostics will probe the dielectric properties of plasmas and how they influence microwave transmission.

duration. To aid in developing this understanding, we will design and assemble a unique resonant cavity to create localized plasmas near interfaces of interest. Advances in dielectric resonance will enable control over localized field strengths and conditions that lead to microwave breakdown. This control will enable the integration of state-of-the-art optical diagnostics (including single-shot THz spectroscopy, absorption/emission spectroscopy, and laser polarimetry) at targeted locations to probe plasma, surface, and gas properties simultaneously as microwave breakdown occurs. Specific objectives during the project include:

- 1) *Predict* and detect the generation of local plasmas in HPM conditions using diagnostics that are independent of microwave propagation.
- 2) *Identify* the mechanism of microwave breakdown near dielectric surfaces.
- 3) *Understand* the role of interfacial chemistry, surface charging, and dielectric properties on plasma formation in HPM systems.
- 4) *Quantify* the dielectric properties of plasmas and identify their influence on microwave transmission during simulated HPM pulses.

Naval Relevance: Mechanistic control over where, when, and how plasma forms in HPM systems will enable new classes of HPM and DEW technologies, systems, and techniques. This study will develop a set of design strategies, diagnostics, predictive mechanisms, and a modular validation reactor to mitigate plasma formation near boundaries. Together, these research initiatives will improve the predictability of HPM technologies, capability to probe performance (i.e., diagnostics to infer plasma formation), and establish a set of evaluation criteria for design strategies of novel HPM sources. Other programmatic impacts of this work include insight into dielectric breakdown and surface flashover in pulsed power applications. Diagnostics and mechanistic insights in this study can be used to infer similar synergies between the state of gas, surface, and plasmas that lead to surface flashover in pulsed power applications (in collaboration with others in the HPM and DEW portfolio). The state-of-the-art diagnostics described in this study also enable time and spatially resolved characterization of gas, surface, and plasma properties leading to microwave breakdown, including the validation of numerical simulations (i.e., density functional theory and molecular dynamics models) (in collaboration with other researchers within the HPM portfolio).

Introduction/Background: High power microwave systems lack the diagnostic access to probe the coupling between microwave breakdown, dielectric surfaces, and microwave propagation. This limits the development of mechanistic insight into conditions that lead to the formation of plasmas and hinders the development of predictive solutions that can push HPM technologies to new frontiers of performance. Existing studies lack the capability to (1) probe mechanisms of microwave breakdown across different geometries, (2) identify the synergistic role of interfacial

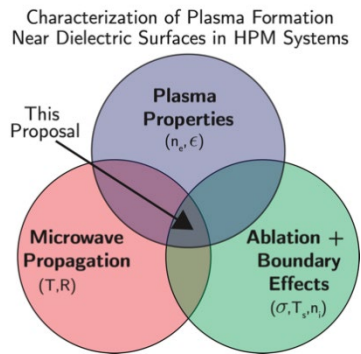


Figure 4. This project characterizes the mechanism that governs plasma formation near dielectrics in HPM systems. This includes operando characterization of plasma properties, microwave waveform properties, and surface properties of interfaces as breakdown occurs.

- 1) In-situ characterization;
- 2) Quantitative spatiotemporal measurements of plasma properties (i.e., dielectric response) and the interfacial properties of dielectrics during breakdown (i.e., surface charge, etc.);
- 3) Sufficient spatial resolution to assess the non-equilibrium state of plasmas below the diffraction limit of HPMs;
- 4) Sufficient temporal resolution to resolve HPM pulses;
- 5) Sufficient acquisition rates to visualize evolutions in performance between HPM pulses.

Opportunities for Innovation. Mechanistic insight into microwave breakdown near surfaces, including how, where, and why plasmas form, will enable new performance thresholds, reliability, and reproducibility in HPM systems. However, the complexity and optical accessibility in these systems limit the ability to probe microwave breakdown while capturing the time and spatial scales over which it evolves. *Instead, opportunities exist to design a modular resonant cavity that can mimic HPM conditions over localized scales. This approach focuses on generating conditions that lead to breakdown at an interface between gas, dielectrics, and vacuum that is accessible and amenable to characterization during HPM pulses.* More than just inferring mechanisms, a modular resonant cavity creates a test bed for evaluating strategies to mitigate the generation of plasma. Resonant cavities zoom into the interface where plasma is formed instead of recreating the complexities of entire microwave systems. This enables rapid testing of strategies that have shown promise in mitigating plasmas ranging from patterned surfaces to applied magnetic fields (Fig. 5). The modularity of resonant cavities enables probing at dielectric interfaces that are being exposed to microwaves with comparable field strengths, frequency bandwidths, and pulse durations to HPM conditions. Innovations in design,

properties and boundary effects, and (3) quantify the interaction of localized plasmas with microwave propagation. More than just accessibility, advances in the design and understanding of microwave breakdown requires diagnostics that can quantify properties spanning the plasma, gas, and solid phases. These requirements include the ability to measure free electron densities, collision frequencies, populations of ablated species, rovibrational temperatures, and surface charging of dielectrics while HPMs are propagating. The intersection of these measurements is a new frontier in HPM research (Fig. 4) and requires the integration of advances in reactive air chemistry, plasma physics, and materials science. Specific capabilities of diagnostics that are needed to characterize plasmas in HPM systems include:

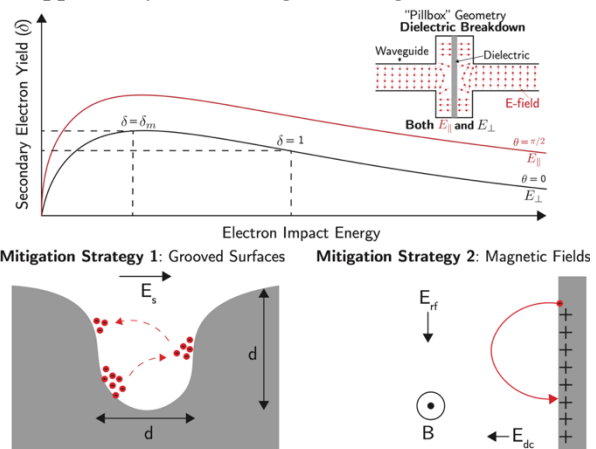


Figure 5. Design strategies to limit microwave breakdown near dielectrics. Breakdown thresholds depend on the geometry of windows and polarization of the driving microwave waveform. Strategies including the use of grooved structures and resonant magnetic fields have been shown to impede breakdown.

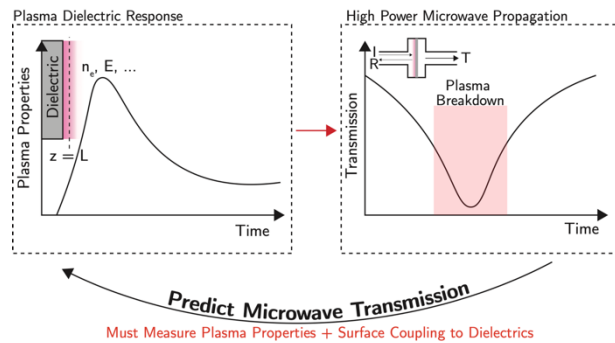


Figure 6. Improving the predictability and performance of HPM systems require advances in diagnostics and optical access to (1) quantify plasma production and its dielectric response, (2) identify where, why, and how it forms, and (3) infer the change in microwave propagation.

The microwave test reactor (Fig. 7) is built around a WR284 waveguide which is designed to operate over 2.60 – 3.95 GHz, which will be the operating range for the reactor. The setup is built around the central test section which is encapsulated by a custom stainless steel vacuum chamber. The chamber has two bulkheads on either side that adapt the CF800 flanges to WR284 waveguide adapters, allowing the waveguides to interface with the chamber while maintaining a vacuum seal. All flanges have copper or Viton gaskets to hold the pressure. The chamber has electrical feedthroughs, a vacuum line, and multiple viewports to see the interior of the chamber. On the transmitting side, the microwave amplifier signals propagate through a circulator into the test chamber and is absorbed by the dummy load on the receiving side. Any signal that is reflected gets redirected through the circulator to the measurement side and terminated at a dummy load once again (Fig. 8). This design choice was made to prevent damage to the measurement equipment and signal generator in the event of total signal reflection back at the antenna when breakdown occurs.

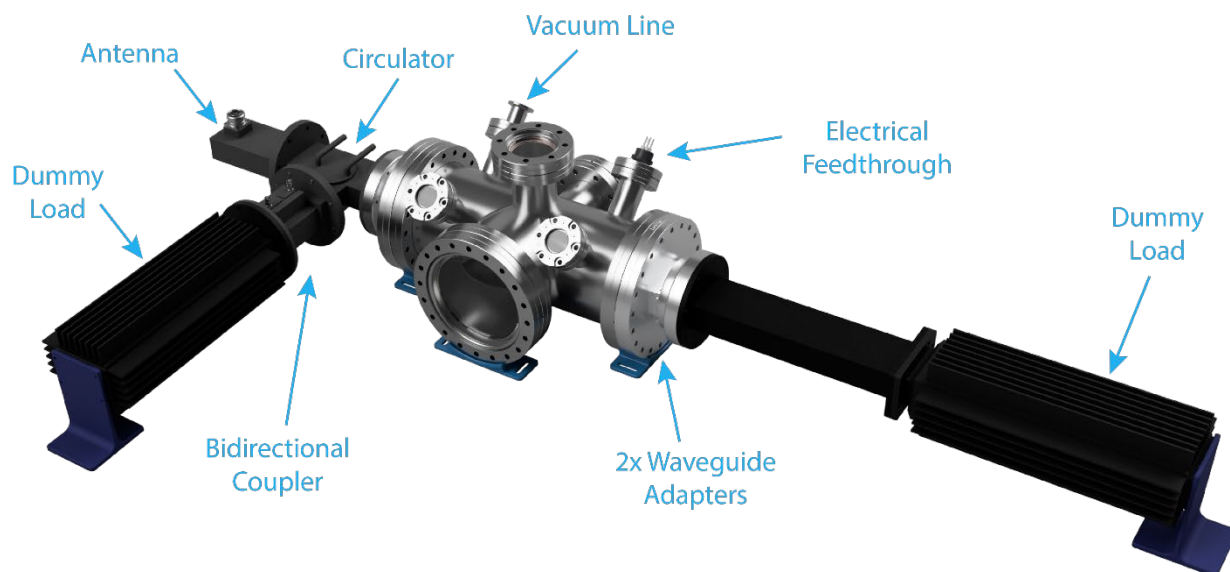


Figure 7. CAD diagram of overall setup. Shows the four key regions of the setup: Transmitting, Test Section, Receiving, and Measuring. The selected WR284 waveguide series sets the operating range of the setup at 2.60 – 3.95 GHz and components can sustain up to 2000 W of power with adequate cooling.

probing volume, and diagnostic capability will develop new insights into plasma production in HPM systems. *These innovations will enable predictive insight into the coupling between plasma formation and microwave transmission in HPM systems (Fig. 6).*

2. Activities and Accomplishments

a) Microwave Test Reactor: Our microwave reactor has been setup and installed. The microwave amplifier has been received after months of delays.

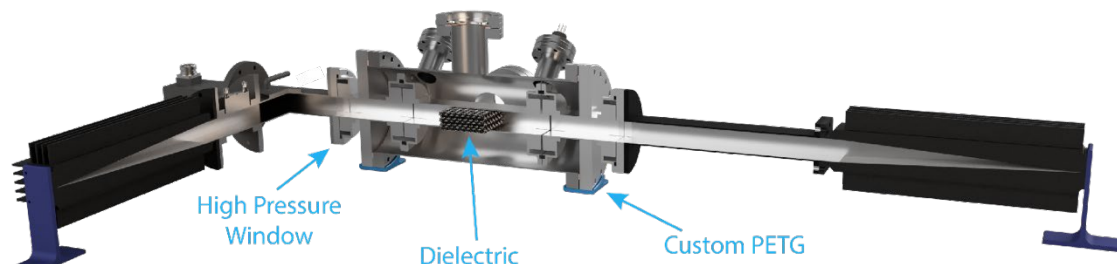


Figure 8. Cutaway of CAD model depicting internal geometry of test chamber highlighting dielectric resonator. The resonator is placed inside of the straight section and is held with non-invasive RF-transparent pins.

A dielectric resonator ($Q \geq 1000$) is placed in the test section to generate plasmas close to dielectric surfaces. Plasma generation in this region will be monitored using the THz spectroscopy diagnostic (see later sections of report), absorption spectroscopy, and the forward and reflected microwave power. The setup (Fig. 9) uses a microwave signal generator (Keysight E8257D) that outputs directly to a 2.5 kW RF Amplifier (EmpowerRF (Model 2229-001)). The amplifier is capable of 2.5 kW peak output between 2.9 and 3.5 GHz as a total amplification of 64 dB. On the measurement end, a bidirectional coupler is able to pickup incident and reflected power with a -30 dB coupling which is then connected to an analog Schottky Power Detector from RF Lambda (RPDT0012GA) which converts the power reading to a mV output which is logged and processed by the Tektronix TBX 2000B Oscilloscope. All parts and links to relevant datasheets can be found below in Table 1.

Component	Manufacturer	Model	Region	Datasheet
Vacuum Chamber	LDS Vacuum	156223	Test Section	N/A

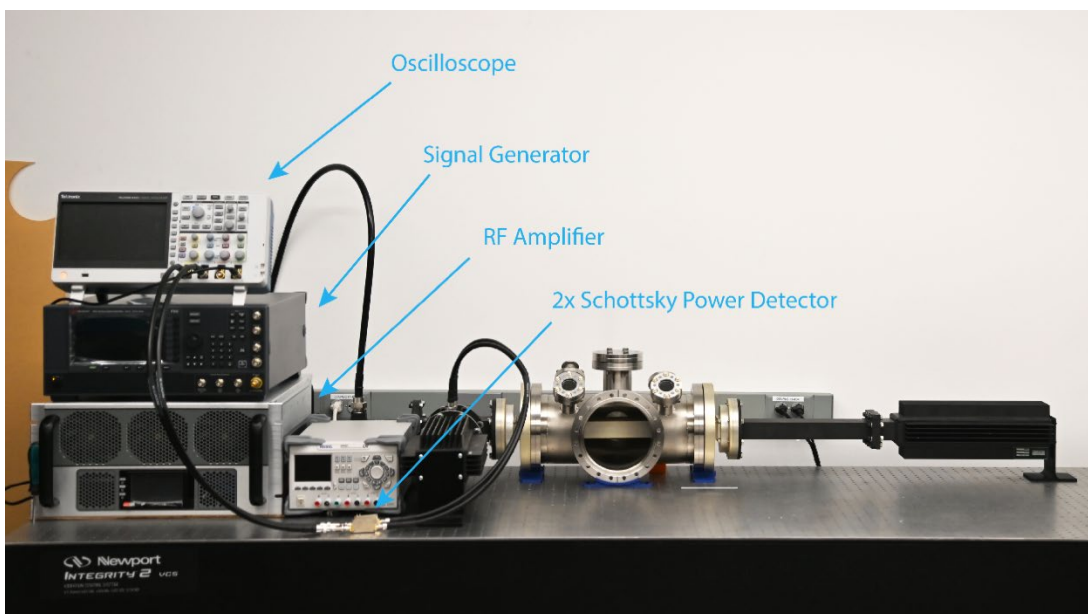


Figure 9. Picture of actual setup and data collection equipment.

CF800 to WR284 Bulkheads	Microtech	WR284-BLKHD	Test Section	N/A
Pressure Window	Microtech	WRPW284HAI	Test Section	Link
Test Section	Microtech	MRHC284HHA10A	Test Section	N/A
Vacuum Fitting	LDS Vacuum	275xSWG-25	Test Section	N/A
Electrical Feedthrough	Kurt J Lesker CO	EFT0265063	Test Section	Link
Signal Generator	Keysight	E8257D-1EU	Transmitting	Link
RF Amplifier	EmpowerRF	2229-001	Transmitting	Link
Antenna	CT Microwave	CM571.0015-2	Transmitting	Available upon request
Circulator	CT Microwave	CM506.7001	Transmitting	Available upon request
Dummy Load	CT Microwave	S707-CPR	Receiving	Available upon request
Bidirectional Coupler	CT Microwave	CM571.0011-2	Measuring	Available upon request
Power Meter	RFLambda	RPDT0012GA	Measuring	Link
Oscilloscope	Textronix	TBX 2000B	Measuring	Link
Cables	Pasternack	LMR-400	Measuring	Link

Table 1. Parts List for major components

b) Single-Shot Supercontinuum-Enhanced THz Spectroscopy: A supercontinuum THz time-domain spectroscopy (THz-TDS) optical setup was developed. The optical setup consisted of a THz generation module using optical rectification, probe modulation via electro-optic effect, and a flexible modular design for THz detection. The design supported a transition between three experimental setups: a traditional delay-line-based THz-TDS, single-shot acquisition with a chirped pulse of finite bandwidth, and single-shot acquisition with a chirped supercontinuum pulse. Each setup was used to compare the THz transmission through gaseous media in a test section.

Amplified Femtosecond Laser System: A Spectra-Physics Spirit 1030-70 ytterbium femtosecond laser (pulse energy > 70 μ J) was used to pump a Spectra-Physics NOPA VISIR optical parametric amplifier. The amplified signal (1532 nm, 80 fs) served as the pump beam to generate THz, while the idler (780 nm, 350 fs) was used as the probe beam to detect THz in both a delay line and single-shot configuration. Both the pump and probe beams were vertically polarized, with pulse energies of \sim 1 μ J and repetition rates up to 2 MHz.

THz Generation: THz radiation was generated through optical rectification in a 500 μ m-thick (E)-4-((4-nitrobenzylidene)amino)-N-phenylaniline (PNPA) crystal (THz Innovations), phase-matched for 1250-2100 nm with an optimal phase-matching wavelength of 1550 nm. The polarization of the pump beam was aligned with the c-axis of the crystal, which is orthogonal to the direction of beam propagation. A stepping motor-controlled delay line (VXM-1, Velmex) was

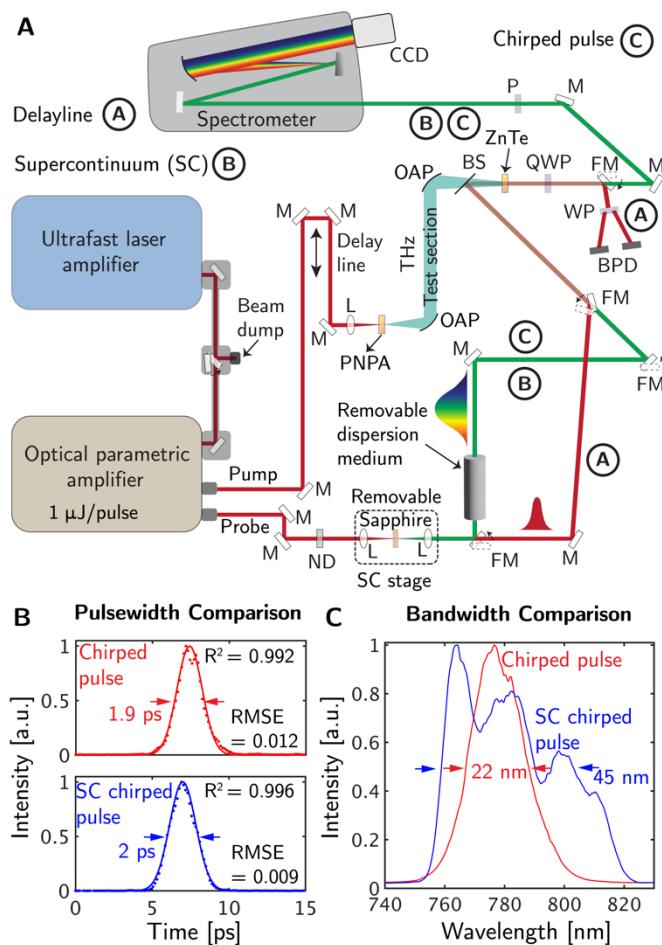


Figure 10. Single-shot THz detection schemes and a solution to chirp penalty using supercontinuum. (A) A schematic illustrating three THz detection schemes: the conventional delay line technique, which raster scans the THz time-domain signal using multiple probe pulses to extract different points sequentially; the single-shot approach using a chirped pulse with limited bandwidth; and the single-shot method using supercontinuum, which achieves expanded bandwidth via a sapphire crystal. Key components in the setup include OAP: off-axis parabolic mirror, M: mirror, L: lens, FM: flip mount, BS: beam splitter, P: polarizer, ND: neutral density filter, QWP: quarter-wave plate, WP: Wollaston prism, and BPD: balanced photodetectors. (B) The supercontinuum pulse is chirped to 2 ps using a 5 cm SF11 rod, in contrast to the original probe beam, which requires a 10 cm SF11 rod to achieve a similar chirp duration. (C) This difference arises from the ~ 2 -fold higher bandwidth of the supercontinuum pulse.

with a 12 dB/octave roll-off, 30 ms time constant, and 10 dB gain. The resulting signal was acquired using a multi-channel digital oscilloscope (MSO44, Tektronix), and the mean value was extracted at each delay line step using custom software. The motorized delay line (VXM-1, Velmex) was stepping at 133 fs/step.

used to scan the THz pulse over 3-100 ps with 2.5 $\mu\text{m}/\text{step}$ increments. Low pump pulse energy of $\sim 1 \mu\text{J}$ and an organic crystal (PNPA) were utilized to generate THz electric field amplitudes of $> 1 \text{ MV}/\text{cm}$, corresponding to a THz generation efficiency exceeding 4%.

Electro-Optic Modulation: A 2 mm thick ZnTe crystal (ZnTe-2000H, Eksma Optics) with $\langle 110 \rangle$ orientation was used for probe modulation using electro-optic effect. This crystal offers optimal phase-matching conditions within the desired THz bandwidth (100 GHz-2 THz). Both the THz and probe beams were polarized along the z-axis (001) of the ZnTe crystal. This modulation technique was used for both conventional delay-line-based and single-shot detection modes.

Delay Line THz Detection (Balanced Photodetection): A polymer zero-order quarter-wave plate at 780 nm (05RP34-780, Newport) and a Wollaston prism (Calcite crystal, 10WLP08AR.16, Newport) were used to implement balanced photodetection. The elliptically polarized modulated probe beam was split into two orthogonally polarized components, which were then analyzed by a balanced photodetector (PDB210A, Thorlabs). The balanced photodetector had a bandwidth of 1 MHz within a wavelength range of 320 – 1060 nm with a fixed common mode gain of 500 kV/A. To further enhance signal-to-noise ratio, a lock-in amplifier (Moku-go, Liquid Instruments) was employed

Single-Shot THz Detection (Spectral Modulation): In this module, the frequency components of the chirped probe pulse were phase-modulated at the electro-optic crystal in proportion to the local THz electric field. Since phase changes cannot be directly detected by photosensors, this phase modulation was converted into intensity modulation using the cross-polarizers. The spectrometer then analyzed the intensity-modulated chirped probe beam to extract the THz signal. (Procedure detailed in the section ‘Data Acquisition and Post-Processing’). A crossed-polarizer configuration (LPNIRB100, Thorlabs) was integrated with a 0.5 m spectrometer (iHR550, Horiba Scientific) and an EMCCD camera (Synapse) for spectral modulation. An 1800 grooves/mm grating (with a blaze wavelength of 500 nm) was used in the spectrometer, with a slit width of 1000 μm and no EM gain. The wide slit width enhanced the signal-to-noise ratio (SNR) for both unmodulated and modulated probe pulses. Additionally, the crossed-polarizers improved the extinction ratio of the probe pulse, as detected by the spectrometer, further optimizing the SNR.

Supercontinuum Generation: A 6 mm thick sapphire crystal, AR-coated for 780 nm, was used as the bulk medium for supercontinuum generation. Supercontinuum was produced by focusing an uncompressed, negatively-chirped probe beam (350 fs) onto this crystal. A pair of AR-coated plano-convex lenses ($f = 1$ cm, $f/D = 1.67$, Thorlabs LA4280-B) were used to focus the 2.5 mm wide ($1/e^2$) laser beam through the crystal and recollimate it afterward. A peak probe power of 4 MW was used (greater than the required threshold of 3 MW for supercontinuum generation).

Pulse Chirping: Probe pulses were chirped to the desired pulse widths using a highly dispersive SF11 glass (SCHOTT, dispersion coefficient: -603.91 ps/(nm-km) at 780 nm) in both single-shot schemes. A 5 cm long SF11 rod was used for dispersing/chirping the supercontinuum beam to 2 ps, while a 10 cm long rod was employed for chirping the probe pulse with limited bandwidth to 1.9 ps to accommodate their differing bandwidths.

c) THz Spectroscopy - Dispersion/Chirp penalty: We have deployed our THz-TDS diagnostic and used it to measure gaseous and plasma properties. The spectral encoding technique for terahertz (THz) measurements relies on using a chirped probe pulse to extract time-domain information in the spectral domain via a spectrometer. This allows the measurement of plasma properties over timescales that are necessary to resolve breakdown processes. This method, however, introduces a chirp penalty, which manifests as signal distortion in the time domain and a trade-off between bandwidth and spectral resolution in the frequency domain. In particular, the longer the chirped pulse (T_c), the more significant the distortion, reducing the spectral resolution. While shortening the pulse width (T_c) reduces this distortion, it sacrifices spectral resolution. To overcome this, reducing the transform-limited pulse width (T_0) for a given T_c helps lower distortion and increase spectral bandwidth without compromising resolution.

In our experimental setup, we compare three methods for measuring THz radiation: the delay line method, the regular chirped pulse single-shot method, and the chirped supercontinuum single-shot method. The delay line method offers high accuracy but is too slow for capturing transient plasma phenomena due to its mechanical scanning process. The regular chirped pulse method, though faster, is limited by the time-bandwidth trade-off and can suffer from significant signal distortion, such as multi-cyclic waveforms and spurious spectral peaks, which degrade accuracy. The chirped supercontinuum single-shot method overcomes this limitation by generating a broader supercontinuum pulse, allowing for higher time resolution and reduced spectral artifacts. This approach maintains the advantages of spectral resolution while extending the usable bandwidth and

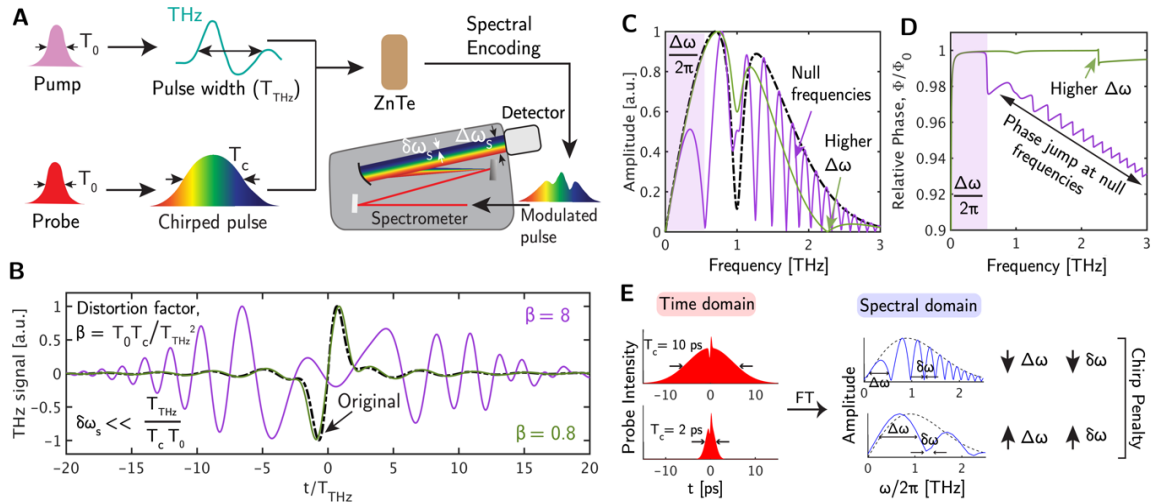


Figure 11. The spectral encoding technique uses (A) a chirped probe pulse to extract the THz time domain information in spectral domain using a spectrometer, which results in chimp penalty. (B) In the time domain, this chimp penalty manifests as signal distortion, and in the frequency domain, it manifests as a trade-off between bandwidth and spectral resolution in both (C) amplitude and (D) phase spectra. Reducing chirped pulse width (T_c) to reduce the distortion factor results in poorer spectral resolution (chimp penalty). Reducing the transform-limited pulse width (T_0) for a given T_c , however, overcomes this penalty by lowering the distortion factor, increasing the spectral bandwidth while maintaining spectral resolution.

minimizing the distortions seen with regular chirped pulses, demonstrating a more efficient method for capturing THz radiation with higher fidelity.

d) Pulse Characterization: The laser pulse and supercontinuum pulses were chirped using SF11 crystals of varying lengths (5 cm and 10 cm). Temporal and spatial characterization was performed using a streak camera and a spectrometer. Supercontinuum generation was achieved by propagating the 250-fs probe pulse through a 6 mm thick sapphire window in a single pass. Previous experiments with a 4 mm thick sapphire window yielded a slightly broader bandwidth but were less efficient. Our sapphire window approach offers a compact, efficient, and robust method for generating broadband light sources from ultrafast laser pulses.

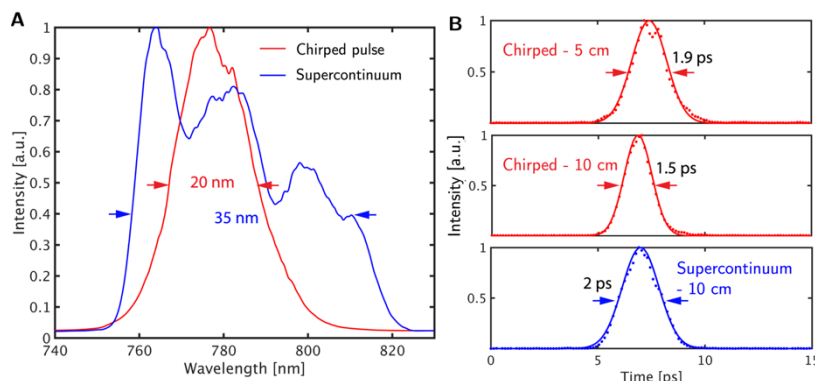


Figure 12. Characterization of the ultrafast pulses used in our experimental pulses including chirped laser pulse and chirped supercontinuum pulse. (A) The chirped supercontinuum pulse shows ~1.5-2 times higher bandwidth than the chirped pulse along with (B) a 2 ps temporal pulse width after propagating through a 5 cm long SF11 dispersion rod compared to 1.9 ps long chirped pulse with a 10 cm long SF11 rod.

A minimum laser peak power of 3 MW was required for this process, which our probe pulse (peak power of 4 MW) readily met. Experimental measurements revealed a spectral bandwidth of approximately 30-40 nm for the supercontinuum (at its widest point), compared to the ~20 nm bandwidth of the original probe pulse (Fig 12). After passing through a 5

cm long SF11 rod, the supercontinuum was chirped to 2 ps due to the strong material dispersion of SF11. The regular laser pulse was chirped to 1.5 ps and 1.9 ps using 5 cm and 10 cm SF11 rods, respectively, reflecting its narrower bandwidth. Additional passes through SF11 could further increase the pulse width and broaden the supercontinuum to desired levels.

e) Single Shot Cutoff Characterization: Increasing the bandwidth of the probe beam, or equivalently reducing the transform-limited pulse width (T_0), mitigates the distortion factor in the time domain. As shown in Fig. 8, using a regular chirped pulse results in a distortion factor (β) of 1.22, which can be improved by transitioning to a supercontinuum pulse, reducing β to 0.64. This reduction in distortion directly impacts the spectral characteristics, leading to an increase in usable bandwidth ($\Delta\omega$) while maintaining a fixed spectral resolution. This is demonstrated in both the amplitude and phase spectra, showcasing how the supercontinuum pulse enhances the overall spectral fidelity. Furthermore, the bandwidth can be tuned based on the requirement by adjusting T_0 with respect to the chirped pulse width (T_c), allowing for precise control over the spectral characteristic in single shot approaches.

f) Generalizing THz-TDS Amplitude Measurements: Accurate THz measurements rely heavily on optimizing both the experimental setup and the measurement conditions, particularly when extracting physical properties like the line-averaged number density (\tilde{n}). We used a purge box in order to isolate the THz beam path from the surroundings and control the water vapor content. The

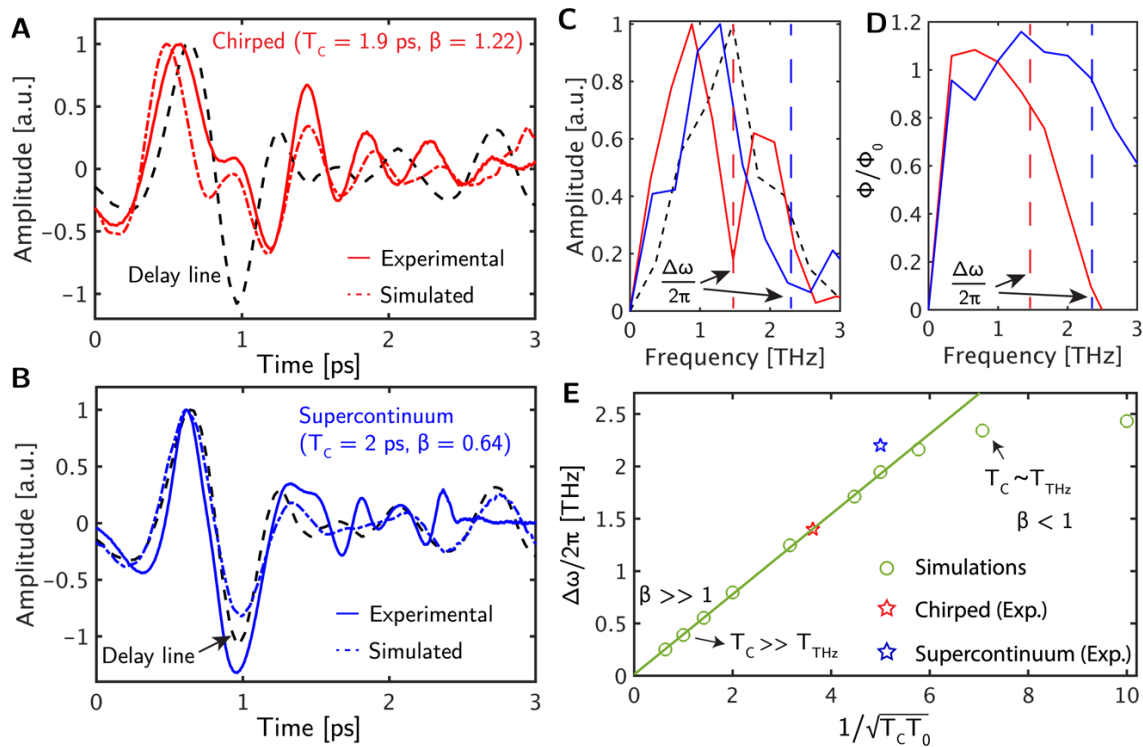


Figure 13. Increasing the bandwidth of the probe beam (or reducing T_0) reduces the distortion factor in time domain from (A) $\beta = 1.22$ with chirped pulse to (B) $\beta = 0.64$ with supercontinuum pulse. This manifests as increased bandwidth, $\Delta\omega$, for a fixed spectral resolution in both (C) amplitude spectrum and (D) phase spectrum (represented as a ratio with respect to the delay line phase, ϕ_0). (E) This bandwidth can be set to a desired level by tuning T_0 with respect to T_c . When T_c approaches T_{THz} , the results deviate from the ideal straight line obtained by fitting the data points with $T_c \gg T_{THz}$.

reliability of THz measurements is also influenced by the duration of the measurement window (Fig. 14C). Shorter measurement windows, such as the 2 ps window used in our experimental setup (Fig. 14B-C), can lead to inaccurate fits when analyzing the experimental signals from chirped or supercontinuum pulses. With these shorter windows, the signal data is insufficient to capture the full spectral characteristics, leading to unreliable results. As the measurement window is extended, more information is captured, allowing for a better fit and more precise extraction of \tilde{n} .

While increasing T_c allows for capturing more information and bring the measured \tilde{n} closer to the actual \tilde{n} , the reliability of the fit is dependent on T_0 (Fig. 14D). Higher T_0 results in more null frequencies (Inset in Fig. 14C) that can interact with the peaks of interest in the absorbance spectrum. This results in higher uncertainty with the extraction of \tilde{n} . A lower T_0 , however, addresses this issue and minimizes the number of null frequencies for a better reliability of the fit.

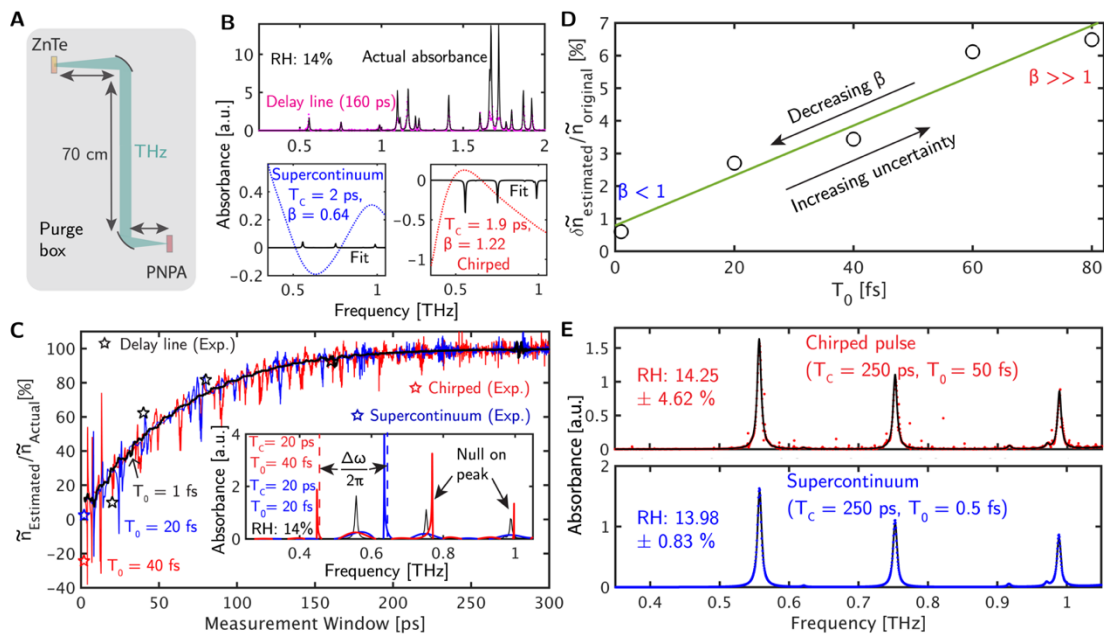


Figure 14. (A) The purge box used to control water vapor content in the THz beam path. (B) Plots showing fits for experimental delay line, chirped and supercontinuum signals with unreliable fits for supercontinuum and chirped pulse due to a short measurement window of 2 ps. (C) Increasing the measurement window allows for increasing accuracy of the fits to extract the line averaged number density ($\tilde{n} = \frac{1}{L} \int_0^L \int n dL$, where n is number density and L is path length), however, (D) the uncertainty in the estimation of \tilde{n} increases with increasing T_0 (i.e., decreasing probe bandwidth). (E) The best fit is achieved when the measurement window (i.e., T_c in the case of single-shot measurements) is longer and T_0 is shorter. The uncertainties in RH were taken from part D.

g) Single Shot Plasma Characterization: Terahertz time domain signals can be distorted due to changes in the refractive index caused by reacting flows or plasmas. In this study, we employed a 27.17 MHz inductively coupled plasma at 200 mTorr, operating at various power levels from 150 W to 500 W (Fig. 15). The level of distortion increased proportionally with the input power (Fig. 10C). The distortion is related to the complex refractive index of the plasma, which is a function of plasma frequency and collision frequency. Consequently, time domain distortion can serve as a valuable diagnostic tool for measuring plasma frequency and collision frequency.

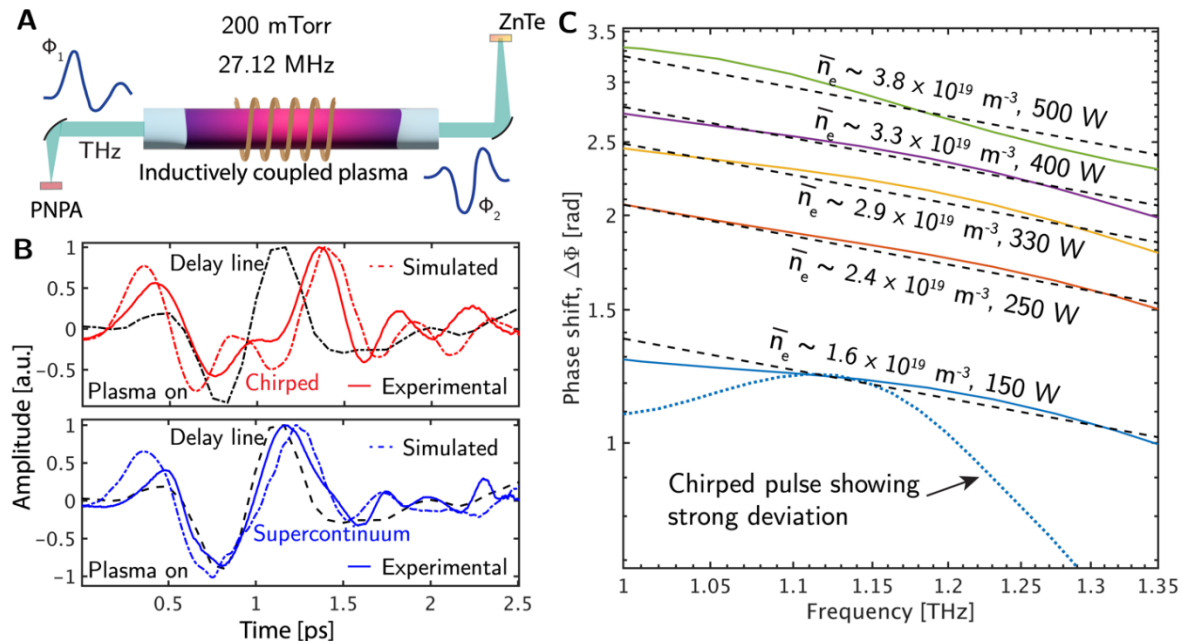


Figure 15. (A) The schematic of the inductively coupled plasma (ICP) flow reactor used to obtain the phase shifts with different RF powers at a fixed pressure of 200 mTorr at 27.12 MHz. (B) The time domain THz signals with ICP at 150 W showing that supercontinuum offers a better fit compared to delay line method. (C) Phase shift as a function of frequency to show a systematic variation in plasma density with plasma power by fitting the data with Drude’s model.

3. Findings and Conclusions

We have made progress in developing a modular resonant cavity and ultrafast diagnostic to probe the mechanism responsible for dielectric breakdown in high power microwave conditions. Specific innovations include:

- We developed a novel diagnostic called “Quantitative Single-Shot Supercontinuum-Enhanced Terahertz Spectroscopy” that can measure plasma properties near surfaces with ps measurement time, ~ 100 MHz sampling rates, and spatial resolution down to $\sim 100 \mu\text{m}$. The diagnostic is more sensitive than traditional microwave cutoff behavior with densities down to 10^{16}m^{-3} .
- We have shown the integration of a supercontinuum probe pulse eliminates pulse distortion in chirped ultrafast diagnostics.
- We demonstrated quantitative agreement between the dispersive effects of plasmas and our single-shot THz diagnostic. These measurements correspond to plasma densities in the range 10^{17} - 10^{19}m^{-3} , conditions of interest for breakdown in cavities.
- We demonstrated chirped pulse widths and bandwidths of probe pulses that are necessary to measure gaseous concentrations of molecules near dielectric surfaces.
- We generated supercontinuum and detected a temporal distortion in single-shot THz time-domain signals due to plasmas at various powers.
- We have setup our microwave cavity and microwave amplifier.

4. Plans and Upcoming Events

The next phase of our project will integrate novel ultrafast diagnostics to study microwave breakdown. We are excited to study these processes with unprecedented scales of space and time to uncover key physics. Other upcoming events will explore how these diagnostics can be leveraged in other facilities within the HPM portfolio at ONR.

- We have submitted a manuscript entitled “Quantitative Single-Shot Supercontinuum-Enhanced Terahertz Spectroscopy (SETS)” to the journal Light. This is a high impact journal for the photonics community.
- We will begin testing of microwave resonant cavity to generate plasmas close to dielectric surfaces.
- We will then deploy a suite of diagnostics, including SETS, to study the dynamics of the breakdown process.

5. Transitions and Impacts

We have leveraged our microwave signal generator and diagnostic capabilities for synergistic projects to the Department of Defense. This includes a hypersonics project through the University Consortium for Applied Hypersonics (UCAH) that is exploring how conjugately matched metamaterials can allow microwaves from 1-10 GHz to transmit through plasmas without attenuation. Our plan is to demonstrate this in reentry conditions. If the solution works, this could be integrated within HPM systems.

6. Recommendations for Future Work

Future work of this project could branch in a number of directions. We are having ongoing discussions with a number of other groups that have collaborative expertise or facilities within the HPM portfolio. Ideas include:

1. Incorporate novel ultrafast diagnostics to probe HPM sources at collaborative facilities.
2. Validate secondary electron or atomistic surface emission from collaborative facilities.

Other directions could reimagine plasmas as, not being a design problem, but as a tool to control the propagation of microwaves. We have shown that the dispersion properties of plasmas can be engineered to control the propagation of microwaves. This, along with conjugately matched metamaterials, could be an emerging approach to extend the scalability of HPM systems.

7. Personnel

<u>Principal Investigator</u>			
Full Name	Approximate Level of Effort – LOE - (Hours This FY)	Country of Residence	National Academy Member? (Y/N)
Thomas C. Underwood	200	United States of America	N
<u>Performer Business Contact(s)</u>			
Full Name	Role	Country of Residence	
Yasmin Deosaran	20	United States of America	N

8. Collaborations

Full Name	Organization	Collaboration Summary
------------------	---------------------	------------------------------

Ken Hara	Stanford University	Mutual verification and validation of numerical models using experiments.
Ravi Joshi	Texas Tech University	Mutual verification and validation of numerical models using experiments.
Jacob Stephens	Texas Tech University	Diagnosis of HPM source.
William Fahrenheitt	Missouri University of Science and Technology	Hypersonic metamaterials for RF transparency (using select DURIP equipment)

9. Students

Doctoral Student(s): 2			
Full Name	University	Graduated?	Graduation Year
Charan R. Nallapareddy	The University of Texas at Austin	N	05/01/2025 (Expected)
Arnav Mohapatra	The University of Texas at Austin	N	05/01/2030
Undergraduate Student(s): 1			
Full Name	University	Graduated?	Graduation Year
Joaquin Vives	The University of Texas at Austin	N	05/01/2026

10. Technology Transfer

Microwave amplifiers are being leveraged for a University Consortium for Applied Hypersonics (UCAH) project that explores how engineered material can mitigate radiofrequency blackout.

11. Products, Publications, Patents, License Agreements, etc.

Publications resulting from this project for the reporting period:

Archival Publications:

#	Citation	Acknowledged ONR Support Received? (Y/N)	Peer Reviewed? (Y/N)
1	Nallapareddy, Charan, and Thomas C. Underwood. "Quantitative Single-Shot Supercontinuum-Enhanced Terahertz Spectroscopy." <i>Light</i> , Submitted (2024).	Y	Y

Conference Papers:

#	Citation	Acknowledged ONR Support Received? (Y/N)	Peer Reviewed? (Y/N)
1	Nallapareddy, Charan, and Thomas C. Underwood. "High-Resolution Single-Shot Terahertz Spectroscopy Using Probe Multiplexing for Plasmas." <i>Bulletin of the American Physical Society</i> (2024). * Student Excellence Award	Y	N

2	Nallapareddy, Charan R., and Thomas C. Underwood. "Chirped Terahertz Time-Domain Spectroscopy for Reactive Plasma Flows." <i>AIAA SCITECH 2024 Forum</i> . 2024. * Best Paper	Y	N
3	Nallapareddy, Charan, et al. "Single-Shot Terahertz Time-Domain Spectroscopy for Reactive Plasma Flows." <i>APS Annual Gaseous Electronics Meeting Abstracts</i> . 2023.	Y	N

Books: No information to report

Book Chapter: No information to report

Theses: No information to report

Websites: No information to report

Patents: No information to report

Other Products: No information to report

12. Point of Contact in U.S. Navy / Marine Corps

Full Name	Organization	Date of Last Contact
Suchitra Ramani, PhD	Office of Naval Research	10/15/2024

Pulsed Dielectric Breakdown of Solid Dielectric Insulation Materials

Grant No. N00174-20-1-0025 and N00174-22-1-0023

Annual Report for Fiscal Year 2024

Period of Performance: October 1, 2023 to 30, September, 2024

Prepared by:

Professor David Wetz, Principal Investigator
Associate Professor Electrical Engineering Department
University of Texas at Arlington
Department of Electrical and Computer Engineering
416 Yates Street, Rm. 537
Arlington, TX 76019
Tel: (512) 788-0848
Email: wetz@uta.edu



Acknowledgement/Disclaimer: This work was sponsored by the Office of Naval Research (ONR), under grant/contract number N00174-22-1-0023 & N00174-20-1-0025. The views and conclusions contained herein are those of the authors only and should not be interpreted as representing those of ONR, the U.S. Navy or the U.S. Government.

Section I: Project Summary

1. Overview of Project

Liquids and gases are often used as insulating materials in high voltage pulsed power systems and dielectric breakdown is always a concern. Gasses and liquids are conforming and self-healing, but they introduce significant engineering challenges and restrictions when it comes to sealing and/or pressurizing them. Liquid dielectrics are heavy so they may reduce a system's power and energy density, and their dielectric properties are unable to be functionally graded which can lead to boundary conditions that create high electric-field enhancements. Solid dielectrics could be more attractive from a maintenance, power density, and energy density perspective, but they are not self-healing and can be difficult to manufacture, especially around complex geometries. Epoxies have been studied but much more work is needed to fully understand their future uses. The rapid rise of additive manufacturing has also opened new avenues that need to be better explored. Epoxy, thermoset plastics, and additively manufactured materials can be functionally graded using nanoparticle additives, potentially minimizing electric field enhancements. In the work presented here, raw and dielectrically altered solid dielectric materials have been modeled using finite element techniques and experimentally studied under pulsed experimental conditions to evaluate their dielectric strength. Additional work was performed this year to study materials with extremely high permittivities, specifically how their frequency-dependent permittivity varies up to 12 GHz.

Executive Summary:

This reporting period was focused on fabricating epoxy samples that are loaded with varying nanoparticle fill percentages. EPON 815C epoxy is loaded with Copper Calcium Titanate, Calcium Titanate, Alumina, and Barium Titanate fillers. Pulsed breakdown data was collected from a minimum of five samples at each loading percentage. Additional work has been focused on measuring the permittivity and permeability of the loaded dielectrics at frequencies up to 12 GHz.

Objective:

The objective of this effort is to identify and study solid dielectric materials that can be employed to replace gas and liquid insulators in high voltage pulsed power systems. The team is using modeling and simulation (M&S) and experimental techniques to characterize the dielectric properties and pulsed dielectric strength of raw and altered solid dielectric materials. An additional SoW is performed to identify dielectric materials that have extremely high relative permittivity values and measure how the permittivity value changes as a function of frequency up to 12 GHz.

Naval Relevance:

Directed energy weapon (DEW) systems introduce significant tactical advantage on the battlefield. Many DEW systems employ high voltage pulsed power supplies. Typically, gas and liquid dielectrics are used to insulate high voltage systems, however, these pose many challenges when it comes to sealing, maintaining, and storing them for extended periods of time. Solid dielectrics solve many of these issues but face many of their own challenges. The significance of finding suitable solid dielectric materials pertains to reduction in size, weight, and maintenance of fielded high voltage pulsed power systems; solid dielectrics require no maintenance under normal storage or operational conditions and can lead to reductions in size and weight of fielded systems. A primary concern comes with a solid dielectric's inability to self-heal, as a single dielectric breakdown can cause electrical and mechanical failure that results in the need for replacement of the entire system. It is imperative that the insulator is well understood and properly designed to ensure reliability under high electric fields. Identifying methods to tune dielectric properties of insulator materials

enables functionally graded dielectrics to be employed, which aims to reduce electric field enhancements along with the size of the system. The experimental and M&S work being performed here is aimed at advancing our understanding of solid dielectrics and their use in DEW systems.

Introduction/Background:

This project serves to investigate the feasibility of using solid dielectric materials as replacements for conventional liquid or gas dielectrics in high voltage pulsed power applications, including high power microwave (HPMs) systems. The solid dielectrics of interest include epoxies and plastic materials. Epoxies are of especially high interest due to their ability to pot complex geometries, since they are formulated and cast in a liquid state that hardens as a solid. Composite solid dielectric materials, which are produced by introducing particulate filler materials into a base material of interest during its formulation, are also being investigated. The motivation for investigating composites is to determine how the dielectric properties of solids can be tuned to achieve specific desired dielectric characteristics that may reduce high electric field enhancements in complex geometries. This effort focuses on using experimental as well as M&S techniques to characterize the dielectric properties and pulsed dielectric strength of raw and altered epoxy materials. Over the course of the four-year project period of performance, several tasks have been executed, listed below, and those performed in this reporting period will be described in detail later.

Task 1: Technology, Raw Epoxy Material, and Dielectric Additives Literature Survey

A review of previously performed research investigating dielectric breakdown of epoxies and plastics has been performed in year 1 and materials to be studied have been chosen. In FY23/24, an extensive literature review was performed in collaboration with Purdue Univ. identifying materials with extremely high permittivity (UTA) and permeability (Purdue).

Task 2. Testbed Design and Fabrication

A testbed was designed and fabricated in FY21/22 to apply pulsed electric fields to epoxy and plastic samples manufactured in house. A 30 stage, 600 J/pulse Marx generator is employed as the pulsed power source. In FY24 (February), a failure of the Marx's epoxy liner occurred that set back progress considerably. The team worked with the manufacturer, APELC, to redesign the Marx and get it operational again. The redesigned Marx was delivered in November 2024.

Task 3. Existing Pulsed Power System Survey

UTA worked with NSWC-DD to identify a Marx topology that has been employed in HPM studies and M&S tools were used in FY23 to evaluate how solid dielectrics could be employed and functionally graded to reduce field enhancements in the system.

Task 4. M&S and Pulsed Dielectric Breakdown of Raw and Additively Manufactured Dielectrics

EPON 815C base epoxy material has been studied. Over 200 pulsed dielectric breakdown experiments have been performed between FY22 and FY24 to characterize each sample's pulsed dielectric strength in raw and dielectrically altered forms. Novel M&S techniques have been developed to quickly study the electric fields present when employing the materials being studied.

Task 5: Permittivity Measurements

A VNA and test fixture were procured in FY23 to study the freq. dependent permittivity of Task 1 materials.

Task 6: Permeability Measurements

Purdue Univ. setup experiments to measure the freq. dependent permeability of Task 1 materials.

Task 7: Reporting

Reporting has been completed monthly to satisfy the ONR and NEEC requirements.

Background:

Many research papers were found in which epoxy dielectrics have been studied in their natural form or with dielectric modification. The results of all these previously published works suggest that it is feasible to alter the dielectric properties of epoxy resins by using many different types of micro and nano sized particles. Most of the previously documented work is focused on studying only low-voltage dielectric properties of altered materials, not on studying their dielectric strength. The work here is focused on not only studying how material properties are altered when they are dielectrically altered, but also what impact the alteration has on the dielectric strength. When coupled with the M&S approaches being taken, a wholistic approach to studying solid insulator materials is being taken. Epoxy materials are being altered and cast in-house using careful techniques to minimize the presence of air bubbles. The work with thermoset plastics is limited to date but techniques have been developed and verified for creating dielectrically altered samples.

2. Activities and Accomplishments

FY24 was a bit of a mess technically at UTA due to problems with the high voltage Marx, but some good progress was made. This year's goals were to complete the fabrication of a test matrix of dielectrically altered epoxy samples, perform pulsed high voltage dielectric testing on them, and use those results to understand how the inclusions impact the dielectric strength of the base epoxy. In this report, the experimental setup will be revisited, the progress made this FY will be discussed, and the plans for wrapping up will be discussed as well.

Material Literature Survey & Characterization

Funds were awarded from the Joint Directed Energy Transition Office (JDETO) in late FY22 to investigate materials with high permittivity or permeability at high frequencies (up to 12GHz) for NLTL applications. The findings from this literature survey are far too long to report on here but they are available upon request. The survey was performed collaboratively between UTA who focused on ferroelectrics, their fabrication methods, and applications in DE systems Purdue focused on ferrite-based composites, the synthesis & manufacturing method of relevant ferrites, their application space, and look at the state of the field. Somnath Sengupta at Powerhouse Consulting was also engaged to provide sintered materials.

In support of the dielectric breakdown effort, UTA procured a coaxial airline dielectric fixture, seen in Figure 1, from MuEpsIn and a 20GHz Anritsu Shockline VNA is used with it. Samples are loaded into the airline that have an outer diameter of 7 mm, inner diameter of 3 mm, and length of up to 5 cm. A mold fixture, shown in last year's report, was designed to fabricate those samples and the permittivity of all the materials tested under pulsed load were also characterized using this fixture up to 12 GHz. The samples are mixed the same way as the dielectric breakdown samples, with the only difference being the mold used. The selection of materials fabricated was driven by their demonstrated performance in a range of frequencies and from the exhaustive literature survey. These identified materials can be used to modify solid dielectrics and make them more suitable for use in high frequency NLTL applications.

This FY, EPON 815C samples were fabricated with varying loading, by mass percentage of Alumina (Al_2O_3), Barium Strontium (BST), Calcium Titanate



Figure 1. MuEpsIn coaxial airline dielectric test fixture (top-left). Test fixture assembled with sample showing a good fit between inner and outer conductor (top-right). Bottom half of test fixture with permittivity sample and inner conductor in place (bottom).

(CTO), Copper Calcium Titanate (CCTO), Barium Titanate (BT), Titanium Oxide (TO), and Strontium (ST). The real permittivity measured for each material, except ST due to space limits, at each mass % are shown in Figure 2. As shown in the data, the permittivity is quite frequency dependent, dropping sharply as frequency increases beyond a few hundred kHz and then dropping more slowly between 500 kHz and 12 GHz.

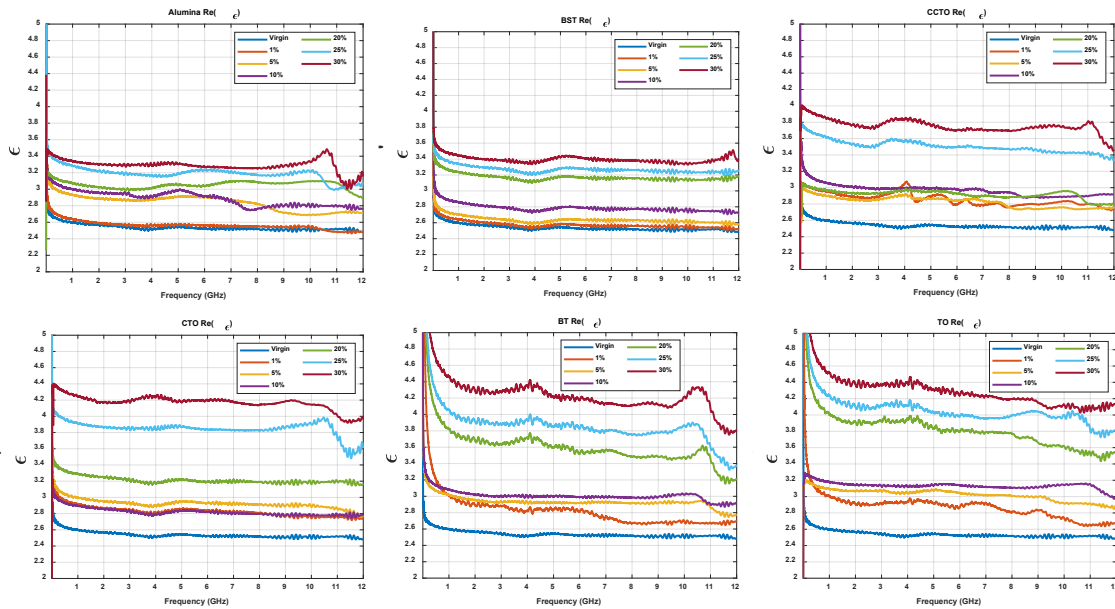


Figure 2. Real permittivity measurements from 1MHz to 12GHz of dielectrically filled samples up to 25% by mass.

Purdue Measurements and Nonlinear Pulse Forming Lines

In FY24, Purdue focused on characterizing the magnetization curves for various materials used as inclusions and multiferroic materials incorporating these inclusions, followed by developing tapered nonlinear pulse forming lines comprised of these materials. They used a Dynacool quantum design vibrating sample magnetometer (VSM) to measure the BH curves for all composites for temperatures from 100 K to 400 K. The samples were mounted on a glass rod with Teflon tape and placed between a sensing coil. An axial field was applied to the sample and then vibrated at 50 Hz in a longitudinal magnetic field ranging from 0 to 4 T. Figure 3 shows the magnetization curves for nickel zinc ferrite (NZF), cobalt ferrite (CoFe), and yttrium iron garnet YIG. The saturation magnetization values were taken at the point of convergence between the lower and upper bounds of the hysteresis curves. The saturation magnetization for all the samples decreases with increasing temperature because excess thermal energy disrupts the alignment of the material's magnetic moments by increasing thermal vibration. CoFe had the highest saturation magnetization (57.96 emu/g), followed by NZF (42.4 emu/g) and YIG (11.26 emu/g) with saturation occurring at applied magnetic fields of 4.31, 1.29, and 0.87 kOe, respectively. The hysteresis loss of CoFe increased with decreasing temperature. NZF and YIG had low coercivity with narrow magnetization curves.

The low saturation field of YIG will most rapidly saturate the nonlinear pulse forming (NPFL), reducing the current bias required to align the magnetic moments and concomitantly decreasing the overall system size. YIG also has low hysteresis loss. NZF offers high saturation magnetization but requires a stronger magnetic field to achieve saturation. NZF also has high resistivity and low eddy

current losses. However, both YIG and NZF exhibit large swings in saturation magnetization over the temperature range studied here, while CoFe offers a large saturation magnetization and more stable saturation magnetization from 100 K to 300 K. This comes at the cost of increased hysteresis loss at lower temperature as the curve broadens and its coercivity increases.

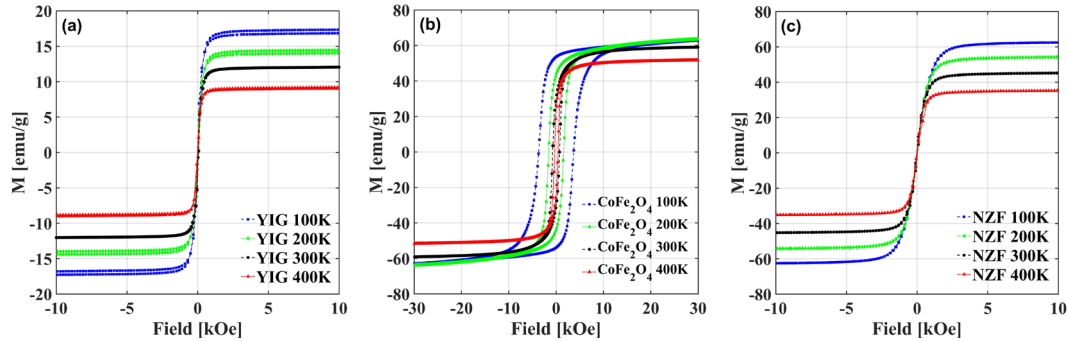


Figure 3. Magnetization curves for (a) YIG, (b) CoFe, and (c) NZF from 100 to 400 K. YIG and NZF show very little coercivity and retentivity. The coercivity of CoFe increases with decreasing temperature.

Next, they manufactured multiferroic materials by adding BST to YIG, CoFe, and magnesium ferrites. Figure 4 shows the hysteresis curves for YIG $\text{Ba}_{0.3}\text{Sr}_{0.7}\text{TiO}_3$, YIG $\text{Ba}_{0.5}\text{Sr}_{0.5}\text{TiO}_3$, CoFe_2O_4 $\text{Ba}_{0.55}\text{Sr}_{0.45}\text{TiO}_3$, and MgFeO_4 $\text{Ba}_{0.55}\text{Sr}_{0.45}\text{TiO}_3$. Adding BST to YIG reduced the saturation magnetization from 11.26 emu/g to 6.01 and 5.72 emu/g for the YIG $\text{Ba}_{0.3}\text{Sr}_{0.7}\text{TiO}_3$ and YIG $\text{Ba}_{0.5}\text{Sr}_{0.5}\text{TiO}_3$ samples, respectively. The coercivity of YIG increased with increasing temperature. The saturation magnetization of CoFe_2O_4 $\text{Ba}_{0.55}\text{Sr}_{0.45}\text{TiO}_3$ was 74.03 emu/g at room temperature, compared to 57.91 emu/g for cobalt ferrite.

The size and shape of the ferrite inclusions can significantly alter a material's magnetic properties. For nanoparticles and nanoclusters, the temperature dependence of saturation magnetization and coercivity are given by Bloch's and Kneller's laws, respectively [1], [2]. Bloch's law for the saturation magnetization $M_s(T)$ of nanoparticles as a function of temperature T is given by

$$M_s(T) = M(0) \left[1 - \left(\frac{T}{T_0} \right)^\alpha \right], \quad (1)$$

where $M(0)$ is the saturation magnetization at 0 K and T_0 is the temperature at which $M_s(T_0) = 0$, or the Curie temperature [2]. Generally, Bloch's exponent $\alpha = 3/2$ is used for bulk ferrite and was derived by considering the magnon excitations of spin-waves at low temperature [2] and agreed well with our data. Kneller's law, given by

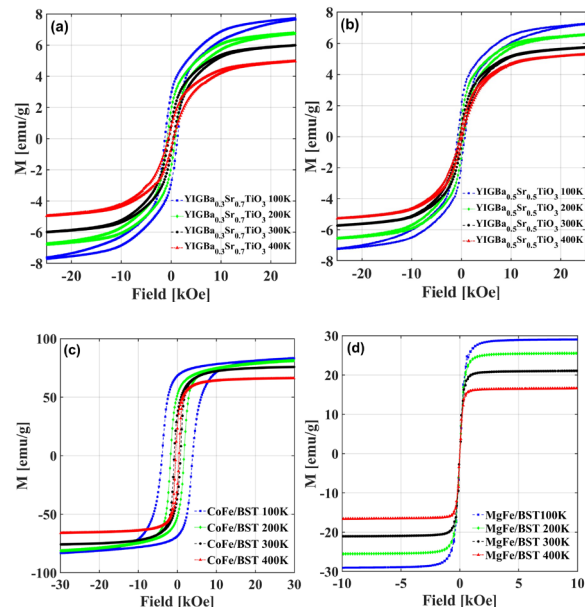


Figure 4. Hysteresis curves of multiferroics comprised of ferrimagnetic powders mixed with various weight percentages and stoichiometric ratios of barium strontium titanate (BST):P (a) YIG $\text{Ba}_{0.3}\text{Sr}_{0.7}\text{TiO}_3$; (b) YIG $\text{Ba}_{0.5}\text{Sr}_{0.5}\text{TiO}_3$; (c) CoFe_2O_4 $\text{Ba}_{0.55}\text{Sr}_{0.45}\text{TiO}_3$; (d) MgFeO_4 $\text{Ba}_{0.55}\text{Sr}_{0.45}\text{TiO}_3$.

$$H_c(T) = H_0 \left[1 - \left(\frac{T}{T_B} \right)^{\alpha_k} \right], \quad (2)$$

where T_B is the superparamagnetic blocking temperature, H_0 is the coercivity at 0 K [1], $\alpha_k = 1/2$, and H_0 and T_B are used as the fitting parameters, gives the temperature dependent coercivity $H_c(T)$. The coercive field data is obtained by averaging the positive and negative field values on the hysteresis loops.

For all samples, the saturation magnetization decreases with the increase in temperature as $T^{3/2}$ with some deviation observed for the 100 K NZF measurement. Measurements are in reasonable agreement with Kneller's law, although there is deviation from Kneller's law for the CoFe samples, which have R^2 of 0.92 and 0.86 for the CoFe/BST and CoFe samples, respectively. Such deviation may be attributed to inter-particle interactions and particle size distribution, which may influence the temperature dependent coercivity.

Recent experiments at Purdue have implemented the NLTL simultaneously as the RF source and the pulse forming line (PFL) to reduce system size. The impedance of this system plays a significant role in the RF formation of the NLTL, with lower impedances producing oscillations at lower charging voltages than their higher impedance counterparts. The elimination of the biasing field in these systems further contributes to the reduced size, although the mechanisms responsible remain incompletely understood. They reference this combined NLTL/PFL topology as a nonlinear PFL (NPFL).

To use standard connections, the manufactured NPFL starts with a 50 Ω impedance and tapers exponentially to 25 Ω over a 200 mm section when using the saturation permeability, which is 1.421. The impedance remains constant for 600 mm before tapering back up to 50 Ω over another 200 mm section to achieve the desired impedance

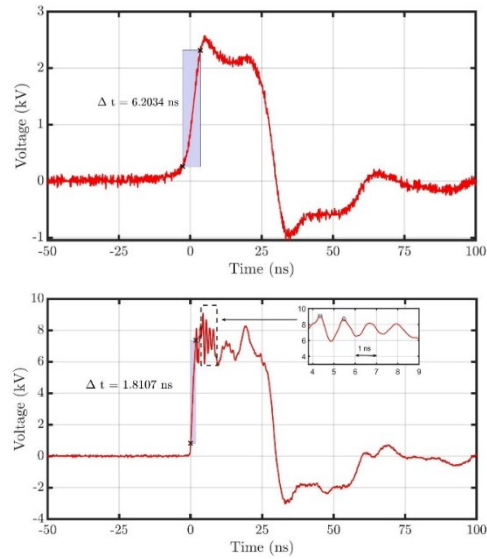


Figure 5. Unbiased NPFL at (left) 5 kV and (right) 10 kV charging voltages. The rise-time (10%-90% of the peak voltage) is 6.2034 ns for 5 kV and 1.8107 ns for 15 kV.

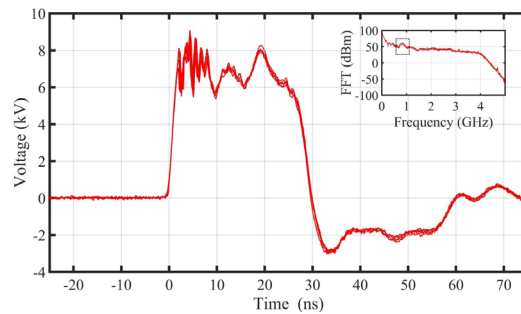


Figure 6. Voltage waveforms for five consecutive shots of an unbiased NPFL at 15 kV charging voltage overlaid on top of one another. The pulse period of the oscillations after the initial rise is 1.18 ns and the FFT in the inset indicates they have a central frequency of ~850 MHz.

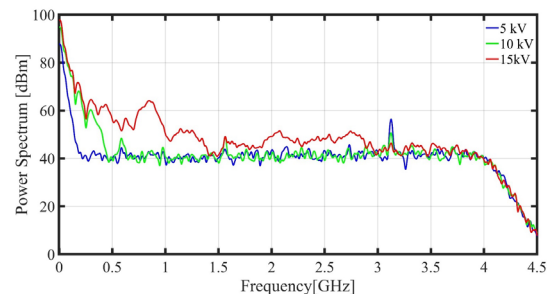


Figure 7. Frequency domain analysis for the unbiased NPFL setup for single pulses.

profile. For a smooth and continuous taper, the ferrite core was constructed from a 60% volume fraction of impregnated NZF encased in polydimethylsiloxane (PDMS). Unlike traditional SF₆ or oil insulators, our ferrite core was encased in a shell consisting of 5% BST in PDMS to give a fully solid-state line.

Several 3D printed molds were made using a FormLabs Form 3 3D printer set to 25 μm resolution. The line was manufactured in sections to facilitate manufacturing. The same material manufacturing protocols presented previously were used [6-8]. The molds could be slid over the NPFL center conductor, which allowed us to manufacture the core without a discontinuity. End caps were also slid over the center conductor to fix it in place. After filling the molds, the material was outgassed for 30 min to eliminate any air bubbles. After curing a section for 80% of its pot life, the next mold could be fitted. Dimensions were $a = 1.55$ mm, $c = 9$ mm, $\mu_{r1} = 1.4$, $\epsilon_{r1} = 21$, $\mu_{r2} = 1$, and $\epsilon_{r2} = 3.5$, where a and c are the radii of the center and outer conductor, respectively; ϵ_1 and μ_1 are the ferrite core permittivity and permeability, respectively; and ϵ_2 and μ_2 are the insulator permittivity and permeability, respectively.

The NPFL was charged to 5, 10, and 15 kV with the internal pressure of the spark gap switches set to 0, 20, and 40 psi, respectively. The load for terminating the pulses consisted of four branches of four 50 Ω HVR resistors in series to create a 50 Ω load at the pulse output. A substantial reduction of pulse rise-time was achieved (10%-90% of the peak voltage) from 6.2 ns at 5 kV and 0 psi to 1.81 ns at 15 kV and 40 psi, as shown in Figure 5.

Figure 6 shows five consecutive shots of the 15 kV charge overlaid, demonstrating the repeatability of these unbiased results. The period of the oscillations is 1.18 ns, as shown by the FFT in the inset, indicating a central frequency of ~ 850 MHz, which the FFTs for the single pulses in Figure 7 confirm.

The implications of incorporating a bias was assessed, which should shift both the frequency and modulation. In general, an increase in the bias field strength increases depth modulation and decreases frequency. This phenomenon is bounded when the magnetic bias becomes so strong that the transient field strength is insufficient to perturb the moments and they become stuck in place, leading to no precession.

For the 15 kV biasing charge, the NPFL was discharged into a load under biasing magnetic fields of 15 to 35 kA/m in increments of 10 kA/m and at the highest magnetic field that the current supply could reach of 60 kA/m. Figure 8 shows the results in the time domain. Figure 9 shows the measured depth modulations of 29.86%, 31.01%, and 17.035% for bias fields of 15, 25, and 35 kA/m, respectively. At a biasing field of 60 kA/m, the oscillations disappear, and the waveform resembles

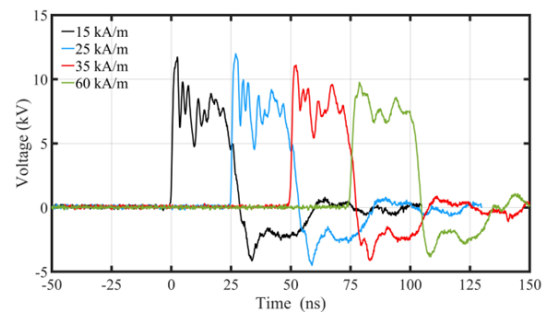


Figure 8. Output waveforms for the biased NPFL at 15, 25, 35, and 60 kA/m offset in time for comparison.

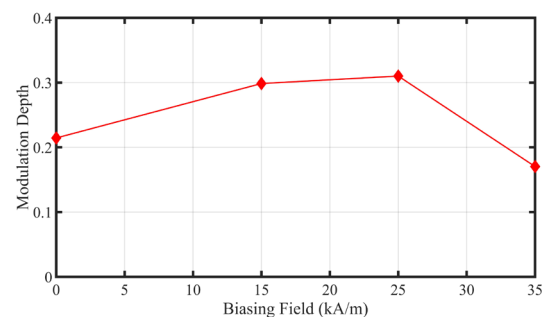


Figure 9. Modulation depth of the NLTL under bias. The line provides an aid to understand the variation of modulation depth.

the results previously observed for an unbiased 10 kV charging voltage. The distortion of the top of the waveform most likely does not result from the gyromagnetic precession in the unbiased case. However, nonlinearity due to the varying radial field of the transient may also introduce some distortion of the pulse flat top if the ferrite core is not fully saturated.

Pulsed Dielectric Breakdown Measurements (UT Arlington)

ONR DURIP funding was obtained in FY21, to procure a Marx generator and a load fixture from Applied Physical Electronics (APELC) in Austin, Texas, seen in Figure 10. The Marx is a 30-stage, 600kV supply with a 100 ns rise time and 500 ns pulse width. The load is a 38 Ω electrical load in which samples can be installed and pulsed with the Marx output. A planetary mixer is used to ensure that the epoxy and additives are well mixed with homogeneous dispersion. Breakdown samples are loaded into the testbed such that when the Marx is fired, current will flow through the

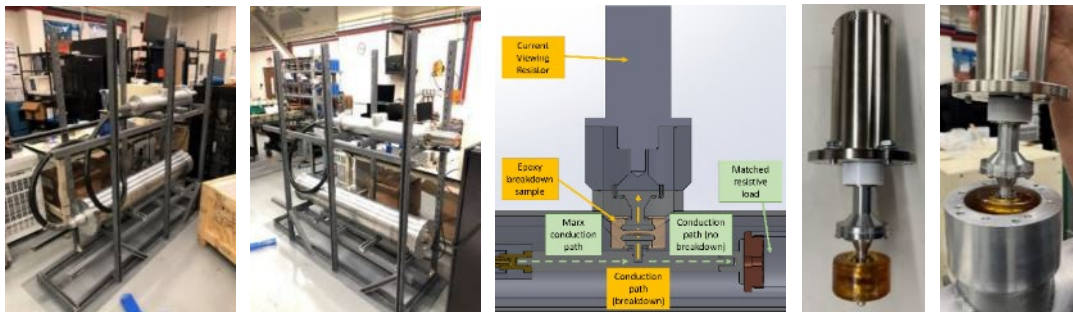


Figure 10. Marx and test fixture (left, second left), rendering of the dielectric sample holder and CVR, (third left), fabricated assembly (second right), sample assembly being loaded into testbed (right).

matched load or through the sample if the electric field is great enough to cause a breakdown event to occur. CVRs (current viewing resistors) are used on the load side as well as the sample side of the load to detect breakdown and measure the voltage. The Marx, test fixture, and sample CVR assembly are shown in Figure 10. The epoxy samples are manufactured in house using a custom mold assembly, seen in Figure 11.

The mold casts epoxy around two parallel electrodes at a fixed separation distance that is set by the thickness of the middle section of the mold. The epoxy is mixed in the planetary mixer and then injected into the mold from the bottom using a large syringe. There is a disposable reservoir installed above for ensuring the mold is filled and degassed in a vacuum chamber. EPON 815C epoxy samples with a 0.025" and 0.015" electrode spacing were made to reliably cause breakdown events. Bruce profile electrodes have been used to apply a near uniform electric field across the sample. Figure 12 shows breakdown voltage and current measured during an experiment. The sudden rise in the orange current trace indicates a breakdown has occurred.

This year several pulsed dielectric breakdown experiments were performed, in which EPON 815C epoxy is used as the host material, with varying fill percentages of the nanoparticles shown in Figure 2. The plan was to complete a test matrix of multiple samples of each material at a few different fill percentages ranging from 1%

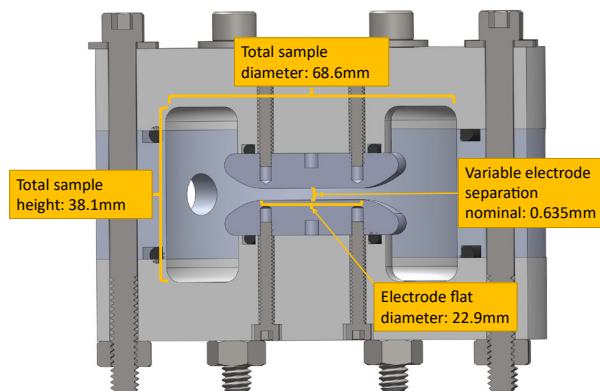


Figure 11. Rendering of epoxy sample mould assembly.

to 25%. This was occurring fine until February when the epoxy liner inside the APELC Marx generator failed, causing the power supply to be unusable. It took several months to repair and a fully refurbished, and improved Marx, was delivered in October 2024. Therefore, through FY24, the number of experiments performed was much less than planned. The most data was collected from samples loaded with Alumina nanoparticles, seen in Figure 13. The data shows a sharply decreasing breakdown strength as a function of increasing field strength. These results will be discussed briefly in the findings section.

3. Findings and Conclusions

UTA's Work: The DC published permittivities of the additives are significantly higher than what is measured as the frequency increases from DC. The permittivity measurements made here start in the few hundred kHz range and the results show how the permittivity of the dielectrically altered epoxies studied strongly decreases as the frequency increases. It remains relatively stable after the very sharp drop but most still have a decreasing trend between a few hundred kHz and 12 GHz. This is less than desirable given the need to operate NLTL and similar sources in the GHz range. Though it may not be possible, additional work to identify higher permittivity materials at higher frequencies is always desirable. With respect to the dielectric breakdown data collected, the variation is a little bit higher than expected but dielectric breakdown is probabilistic. The only way to possibly reduce that variation is to collect more data and hope that it gets tighter. Preliminarily, the theory is that the dielectric inclusions are creating field enhancements within the material due to the dielectric mismatch and that is causing the breakdown voltage to decrease. That said, one could argue that the more inclusions there are in a sample, the more uniform the field should be within the sample, and they should have less impact. These are theories that need to be explored using M&S tools in FY25. Preliminary CST simulation results with Alumina particle fill is shown in Figure 14. The result show field enhancements around the inclusions and those of course increase as the fill percentage increases. More work is needed to correlate these results with those seen experimentally but that will be done in FY25.

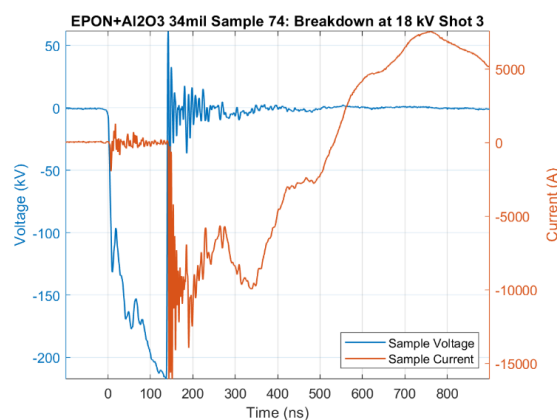


Figure 12. Breakdown voltage and current waveform through the sample (right).

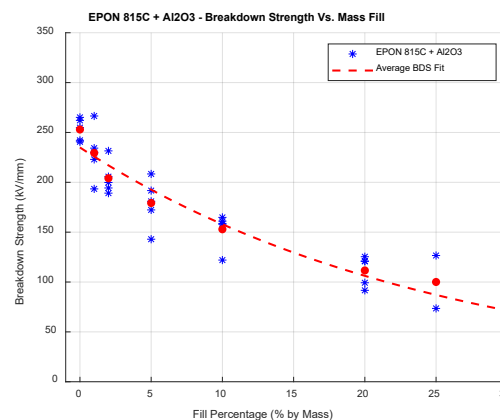


Figure 13. Dielectric breakdown strength of EPON 815C with varying mass fill percentages of Alumina

Purdue's Work: Characterizing temperature dependent behavior in ferroic and multiferroic materials is important for designing NPFLs for practical applications. In particular, understanding the behavior of the magnetization saturation and coercivity of the material under temperature change is necessary to ensure proper operation [12], [13]. The magnetization of both ferroic and

the multiferroic samples agreed well with Bloch's law, demonstrating that the temperature dependence of the saturation magnetization of a multiferroic material does not differ significantly from its single ferroic counterpart.

Additionally, measured coercivity agreed well with Kneller's law with $\alpha = 1/2$, except for CoFe samples. In general, saturation magnetization decreases with increasing temperature due to randomization induced by thermal vibration [14]. Cobalt/BST samples demonstrated the highest saturation magnetization of 80 emu/g. A fully solid-state NPFL based on an NTL topology was introduced.

Such systems reduce device footprint because they do not require a traditional pulsed power driver, which also eliminates the need to electrically match to the PFL. An exponentially tapered ferrite core was used to facilitate easy mating between subsystems. This taper increased bandwidth compared to previous studies. The results reinforced previous observations that this topology can generate oscillations without a biasing field, which further reduces device footprint. We also demonstrated that biasing the lines with a magnetic field ranging from 15 kA/m to 60 kA/m increased depth modulation and decreased the output frequency. Thus, the system developed could provide a flexible means to control output by changing the material properties of the composites that make up the NPFL, while also providing flexibility in size by eliminating the need for a separate pulsed power line and permitting operation without a biasing field. This could provide flexibility for smaller systems that could be easily portable (e.g., a cart or on a jeep) by eliminating these additional systems, which would further reduce the need for additional power requirements. Moreover, we could obtain frequencies up to 1 GHz. For optimum materials, higher frequencies (e.g., S or C band) should be reasonable. These are higher than most lumped element NTLs.

4. Plans and Upcoming Events

Purdue has completed their work and there is no additional work planned under this grant. This report only covers FY24 and as of that time, the Marx had not been repaired and many samples still needed to be tested. Since that time, the Marx has been repaired and all test samples have been dielectrically tested early in FY25, seen in Figure 14. That being the case, the only remaining task as of December 2024 is to analyze the data and provide scientifically backed reasoning for why the data is the way it is and what the take aways and advice going forward should be for using epoxy dielectrics that are loaded with nanoparticles in high voltage pulsed power systems. That work will be completed by the end of Q2 FY25.

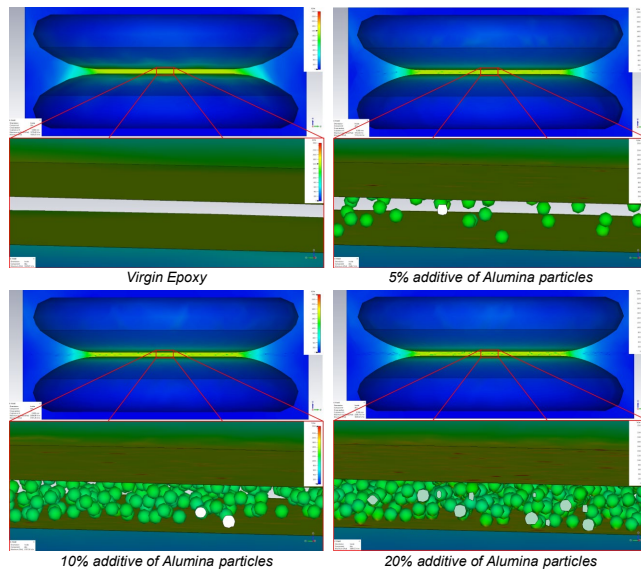


Figure 14. M&S results obtained from modeling Alumina particles of f varying fill percentage in EPON 815C epoxy.



Figure 15. Newly refurbished APELC Marx.

5. Transitions and Impacts

There are many ways to transition this work. The first would be to expand upon the work that was already performed evaluating existing Marx topologies and how their size and weight would be impacted if their oil dielectrics were replaced with a solid epoxy dielectric. Preliminary work was performed here to evaluate how dielectric field enhancements could be reduced by using a more closely matched dielectric and the results were promising. Following this through with a full design, fabrication, and testing effort would be great. If there are already power modulator, transformer, or other similar high voltage projects that are ongoing and suffer from high electric field enhancement spots, they would be prime candidates for putting this work to the test in a real application.

6. Recommendations for Future Work:

A proposal was submitted in FY24 to the Joint Directed Energy Transition Office (JDETO) proposing additional work studying potted dielectrics as coatings on antenna surfaces. That work was recently funded and will be begin soon. There is significantly more work to do studying raw and altered thermoset plastics that should also be explored based on the methods and preliminary results obtained through this effort. More data would always help to understand the results that are being seen how the decreasing electric field as a function of increasing nanoparticle filler mass can be reduced. Efforts like the ones discussed in the transition discussion where a full M&S, design, fabrication, and testing would be an amazing follow on effort to put the work performed here to the full test would be beneficial and fun to work on.

7. Personnel

Principal Investigator			
Full Name	Approximate Level of Effort – LOE - (Hours This FY)	Country of Residence	National Academy Member? (Y/N)
David Alan Wetz Jr.	100	USA	N
Co-Investigator(s) or Co-PI(s)			
Full Name	Approximate Level of Effort – LOE - (Hours This FY)	Country of Residence	National Academy Member? (Y/N)
Performer Business Contact(s)			
Full Name	Role	Country of Residence	
Sarah Panepinto	Director of G&CS	USA	N
Additional (Non-Student) Team Members			
Full Name	Approximate Level of Effort – LOE - (Hours This FY)	Country of Residence	National Academy Member? (Y/N)
Hayden Atchison	1040	USA	N
Subcontractors			
Full Name and Organization	Approximate Level of Effort – LOE - (Hours This FY)	Country of Residence	National Academy Member? (Y/N)

Allen Garner – Purdue University	100	USA	N
-------------------------------------	-----	-----	---

8. Collaborations

Full Name	Organization	Collaboration Summary
Somnath Sengupta	The Sengupta Group	Discussion of results and guidance of research direction

9. Students

Doctoral Student(s)			
Full Name	University	Graduated?	Graduation Year
Shawn Tyler Scoggin	UTA	Y	05/2024
Travis Crawford	Purdue	Y	08/2024
Masters Student(s)			
Full Name	University	Graduated?	Graduation Year
Jordan Lloyd	UTA	N	N/A
Undergraduate Student(s)			
Full Name	University	Graduated?	Graduation Year
N/A			

10. Technology Transfer

No technology transfer other than reporting to the sponsor and community in reporting.

11. Products, Publications, Patents, License Agreements, etc.

Publications resulting from this project for the reporting period:

Archival Publications

#	Citation	Acknowledged ONR Support Received? (Y/N)	Peer Reviewed? (Y/N)
1	S.T. Scoggin, H.L. Atchison, N.E. Jennings, and D.A. Wetz, 'Pulsed Dielectric Breakdown of Solid Composite Epoxy Insulators', <i>IEEE Transactions on Plasma Science Special Issue Journal</i> , Vol. 52, No. 9, September 2024, pp. 4235 – 4241.	Y	Y
2	S.T. Scoggin, N.E. Jennings, H.L. Atchison, D.A. Wetz, and A.J. Fairbanks, 'Dielectric Property Alteration and Measurement Techniques of Composite Solid Insulators,' <i>IEEE Transactions on Plasma Science Special Issue Journal</i> , Vol. 52, No. 9, September 2024, pp. 4294 – 4303.	Y	Y

Conference Papers

#	Citation	Acknowledged ONR Support Received? (Y/N)	Peer Reviewed? (Y/N)
1	S.T. Scoggin, H.L. Atchison, N.E. Jennings, and D.A. Wetz, 'Pulsed Dielectric Breakdown of Dielectrically Altered Solid Insulators,' 2024 IEEE International High Voltage and Power Modulator Symposium, May 28 – June 1, 2024, Indianapolis, Indiana.	Y	N

Books

#	Citation	Acknowledged ONR Support Received? (Y/N)	Peer Reviewed? (Y/N)
1	No Information to Report		

Book Chapter

#	Citation	Acknowledged ONR Support Received? (Y/N)	Peer Reviewed? (Y/N)
1	No Information to Report		

Theses

#	Citation	Acknowledged ONR Support Received? (Y/N)	Peer Reviewed? (Y/N)
1	Shawn Tyler, Scoggin, 'Dielectric Breakdown and Permittivity Characterization of Solid Composite,' May 2024, UTA	Y	Y (committee)
2	Travis Crawford, 'Design Considerations for Composite Based Nonlinear Pulsed Forming Line Systems,' August 2024, Purdue	Y	Y (committee)

Websites

#	Citation	Acknowledged ONR Support Received? (Y/N)	Peer Reviewed? (Y/N)
1	No Information to Report		

Patents

#	Citation	Acknowledged ONR Support Received? (Y/N)	Peer Reviewed? (Y/N)
1			

Other Products:

#	Product Description	Acknowledged ONR Support Received? (Y/N)	Peer Reviewed? (Y/N)
1	No Information to Report		

12. Point of Contact in U.S. Navy / Marine Corps

Full Name	Organization	Date of Last Contact
Andrew Fairbanks	NSWC-DD	12/14/2024
Jordan Chaparro	NSWC-DD	9/12/2024
Matthew McQuage	JDETO	12/10/2024

ONR Young Investigator Program (YIP) Reports

Direct Generation of Electromagnetic Radiation with a Compact, Air-Stable, Optically Modulated Electron Emitter

Grant No. N00014-21-1-2634

Annual Report for Fiscal Year 2024

Period of Performance: October 1, 2023 – September 30, 2024

Prepared by:

Prof. Rehan Kapadia, Principal Investigator
University of Southern California
Dept. of Electrical and Computer Engineering
3737 Watt Way, PHE 626
Los Angeles, CA, 90089-0271
Tel: (213) 821-0845
Fax: (213) 740-8677
Email: rkapadia@usc.edu



Acknowledgement/Disclaimer: This work was sponsored by the Office of Naval Research (ONR), under grant/contract number N00014-21-1-2634. The views and conclusions contained herein are those of the authors only and should not be interpreted as representing those of ONR, the U.S. Navy or the U.S. Government.

Section I: Project Summary

1. Overview of Project

Executive Summary:

In this report, we will cover the objectives, background, accomplishments, and future plans for the grant titled “Direct Generation of Electromagnetic Radiation with a Compact, Air-Stable, Optically Modulated Electron Emitter”. Through this grant we aim to demonstrate a new type of electron source that enables rapid modulation of emitted electron density but allows the use of established telecommunications photon sources to excite the electron source. In this way, an optical signal imprinted on the incident photon source can be converted into an electron density modulation. Using this density modulated electron beam, we then aim to design a vacuum electron device that can convert the density modulated electron beam into a high-power RF signal.

Objective:

The first goal of this proposal is to continue to develop and demonstrate a simple *planar* silicon-insulator-graphene structure to create an air-stable, *electrically tunable*, negative electron affinity surface by applying a bias between the graphene and silicon, termed Hot Electron Light Assisted Cathode (HELAC). A continuous or pulsed photon source may then be used to excite electrons in the silicon, which will then be emitted into vacuum when a small (4-10 V) bias is applied across the device. This electron source can be compact, environmentally robust, and use low energy photons in the near-IR to visible range. Based on initial simulations, modulation frequencies of >250 GHz and 1 A/cm² emission currents should be achievable through device optimization. Initial experimental prototypes have already demonstrated 1 mA/cm², despite a relatively unoptimized structure.

Using this electron source, we will then design and build a device similar to an Inductive Output Tube (IOT), where an electron beam is density modulated by incident light, then accelerated to a desired voltage, and finally RF power is extracted from the beam using an output cavity. We refer to this device as a Light Modulated IOT (LM-IOT). Unlike IOTs, which have frequency and total current limitations due to the grid-cathode spacing and uniformity, this approach is expected to overcome those issues by eliminating the need for a grid and input cavity. We will build a prototype LM-IOT, where the beam generation, confinement, and collector segments are fixed, and the output frequency will be determined by swapping the output cavity. Specifically, we will carry out simulations to establish basic operation principles, design the overall device, and then fabricate and assemble the device. This will be used to establish the proof of principle operation for LM-IOTs as well as make projections about device parameters.

Finally, we aim to explore multi-frequency devices, where we simultaneously excite the electron emitter with multiple modulation frequencies, creating an electron beam with multiple frequencies, and then use multiple output cavities to extract and emit those frequencies separately. In this task, the goal is to understand the interaction between multifrequency beams and multiple cavities, the

limitations in power distribution between frequencies, and any non-linear effects due to the electron source itself that could take two input frequencies and generate different output frequencies. These limits would be driven by a combination of the physics of the electron source and the beam-cavity interactions

Naval Relevance:

The proposed Light Modulated Inductive Output Tube (LM-IOT) technology offers potential for high-power, high-frequency electromagnetic (EM) radiation sources. These compact and air-stable devices enable the direct generation of modulated electron beams, which can be converted to RF energy with minimal physical constraints compared to traditional grid-based systems. This capability is particularly critical for: high-power microwave (HPM) systems, which may be used for a variety of purposes, including counter-drone systems and jamming. The ability to modify these devices so that they can exhibit frequency agile and multi-frequency operation are important for operating in contested electromagnetic environments.

Introduction/Background:

The modern day congested and contested electromagnetic spectrum has placed stringent demands on electronic systems. A single electromagnetic (EM) source that can change transmission bands, multiple frequencies, or even frequency bands, and be able to quickly switch frequencies when the desired communication channels become contested is of value in a contested environment. Additionally, directed EM sources which can temporarily or permanently deny communications are of significant value. One approach to this may be the direct generation of EM radiation from a modulated electron source. This approach could enable compact, high-frequency, high-power HPM sources which could serve the needs of directed energy systems. An Inductive Output Tubes (IOT) is a source which utilizes a directly modulated, where a continuous beam of electrons is modulated by a grid, and an output cavity converts the high frequency component in the beam to electromagnetic radiation. IOTs, however, use a high voltage grid which couples to an input RF signal, this limits the frequency of operation due to electron transit time between the grid and cathode, and also limits scaling of the cathode due to grid spacing uniformity requirements. Here, we propose utilizing an optically modulated cathode technology to directly create a density modulated electron beam, and then extract the high frequency content from the beam using an output cavity. By eliminating the use of a grid to modulate the electron density, this approach would enable (i) higher frequency operation, (ii) larger cathodes for increased drive current, (iii) higher beam voltages, (iv) a reduction in size and weight, and (v) multi-frequency operation from a single device.

Electron emission cathodes are used in a wide variety of applications, including but not limited to, electron microscopes, electron beam lithography, space propulsion, high power microwave (HPM) devices, free electron lasers, and displays. HPM sources for millimeter-wave and terahertz radiation are of great interest for military and defense applications such as radar, electronic counter measures, and communications. While photo-assisted field emission devices have been explored in the past, as promising high frequency emitter, these are generally studied utilizing free-space optics to directly focus a laser on a tip or tip array, and use p-type silicon to enable photogating of field emission. Recently, simulation and experimental results have shown that optically driven emitters could play a valuable role in cathodes for high power microwave and vacuum electron devices in general.

2. Activities and Accomplishments

We have carried out activities focused on (i) HELAC development, (ii) Vacuum HELAC development, (iii) LM-IOT simulation and development, (iv) Diamond Amplifier development, and (v) Other cold cathode development for comparison purpose

1) HELAC Device Development

This strategy focuses on optimizing existing HELAC designs by reducing device capacitance and resistance. Our previous studies have identified two primary contributors to the high device resistance observed in HELACs. First is the lateral resistance introduced by the graphene electrode and second is the bulk resistance of the absorber layer. In silicon-based absorbers, the active region is confined to the depletion width and the absorption depth corresponding to the incident wavelength. The remaining portion of the moderately doped absorber layer primarily lowers the effective voltage drop across the active regions, leading to increased losses and reduced photocurrent. This limitation becomes more pronounced under high-intensity illumination, where the demand for electron flow escalates. Elevated resistance restricts the dynamic range of the photocathode by limiting the detection of low-intensity signals and causing saturation at high intensities, thereby reducing its efficacy in applications requiring a broad dynamic range. Furthermore, high series resistance can result in significant Joule heating due to current flow through the photocathode. This heating not only degrades performance by introducing thermal noise but also poses a risk of material degradation over time, potentially shortening the photocathode's operational lifespan. So, addressing these challenges is important for advancing the development of well-performing photocathodes suitable for high-frequency applications.

We have been working on developing HELACs with epitaxially grown moderately doped p-layer on top of p⁺⁺ Si substrate. Due to the low bulk resistivity of the substrate, this device is capable of operating at comparatively lower voltages and also able to respond linearly to the optical power.

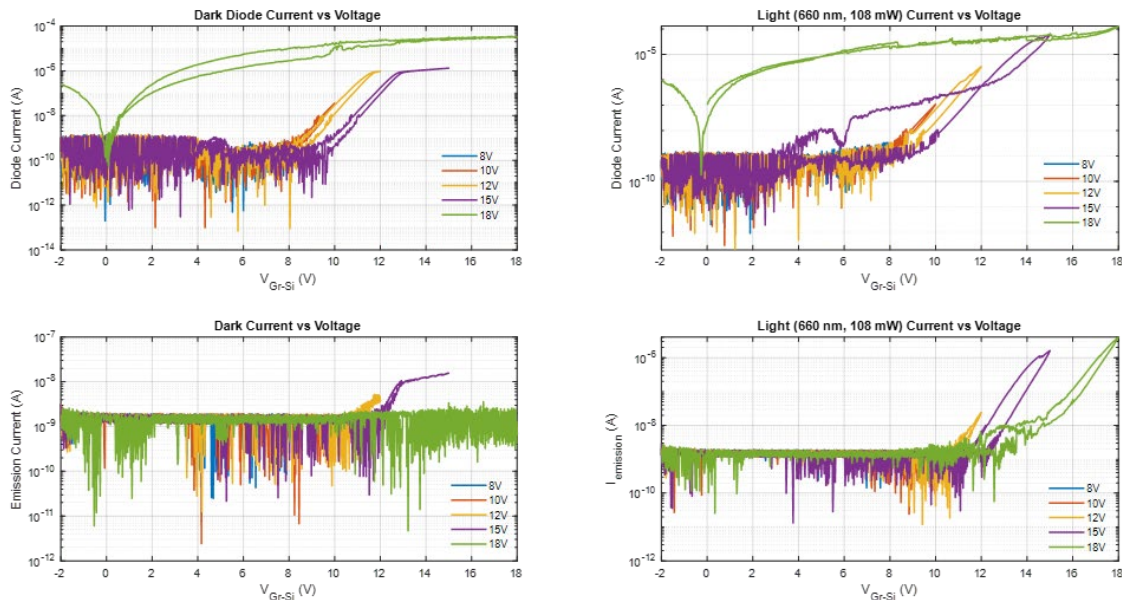


Figure 1: I-V characteristics of HELAC with p++Si substrate containing epi p-Si/Al₂O₃ (Tunnel Oxide)/Graphene active layers. Diode I-V plot at dark (top left). Diode I-V plot with light excitation (top right). Emission I-V plot at dark (bottom left). Emission I-V plot with light excitation (bottom right).

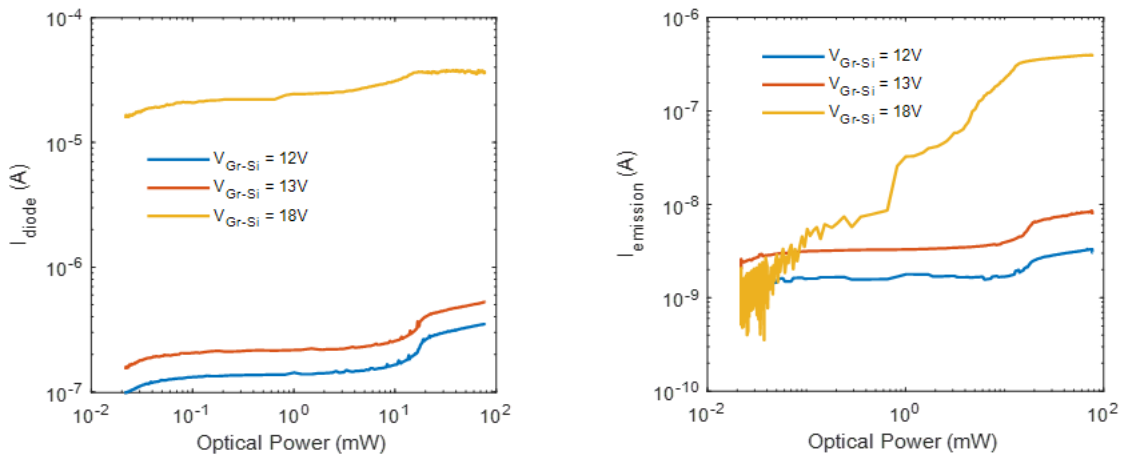


Figure 2: Device characteristics at various optical power levels. Diode Current (left) and Emission Current (right) observed under varying optical power conditions

Figure 1 shows the I-V characteristics of both diode and emission currents for these new HELAC devices with overall low resistance, and the optical power-dependent response is shown in Figure 2. It clearly shows that the device responds very linearly to the imposed optical signal with certain operating conditions offering a better dynamic range of operations. We are also working on

fabricating devices with smaller active areas to achieve low device capacitance. These devices with low RC delay are supposed to achieve high frequency e-beam modulation capability.

2) VHELAC Device Development

We designed and fabricated alternative approaches to the VHELAC cathode. We have previously shown that this approach requires that the mesa edges be rounded to prevent strong field emission and that the mesa be several orders of magnitude thicker than the vacuum gap thickness to prevent emission from the silicon chip edges. Therefore, we fabricated two structures, oxide offset VHELACs and micropillar on mesa VHELACs, in addition to our previous mesa VHELAC structure as depicted in figure 3.



Figure 3: a) Oxide Offset VHELAC cathode. b) Micropillar on mesa VHELAC cathode. c) Mesa VHELAC cathode

Our initial results indicate that the oxide offset VHELAC cannot directly replace the mesa VHELAC structure due to the anode used currently. A schematic displaying the top down view as well as IV measurements for 350 nm offset with 100 nm thin oxide are shown in figure 4. The current measured for these devices is likely not emission as it progressively increased with succeeding measurements. Instead, the oxide under the active area appears to be progressively breaking down. This was later confirmed as we saw damage on the anode far away from the active area. Therefore, the anode is the primary point of failure for these devices.

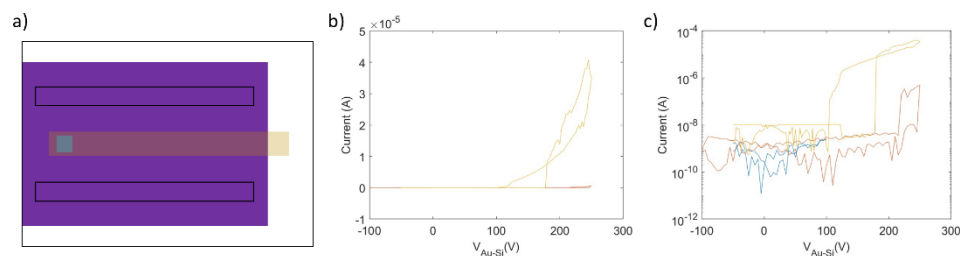


Figure 4: a) Schematic of the top down view of assembled oxide offset VHELAC. A semi-transparent metal anode on glass is held up by the oxide. Offsets are indicated by rectangular traces on the substrate. IV measurements in b) linear and c) log scale.

Figure 5(a) illustrates the tunneling current density of VHELAC at different optical intensities. At constant optical power, the tunneling current increases with the vacuum field. However, most of the generated electrons get emitted at some point, leading to saturation. Increasing the optical

intensity generates greater electron density in the depletion region, which helps achieve higher current density. However, regardless of the applied light intensity, the maximum current is ultimately Fowler-Nordheim (FN) tunneling limited since the FN equation is formulated for a metal junction, which is an infinite reservoir of electrons. The bandwidth of the VHELAC is mostly dictated by vacuum resistance and capacitance since the semiconductor resistance and depletion region capacitance become less dominant at higher optical intensities. We differentiated the FN J-E characteristic of the silicon/vacuum junction to get the vacuum field limited conductance and calculated the maximum frequency at a given vacuum field (Figure 5(b)).

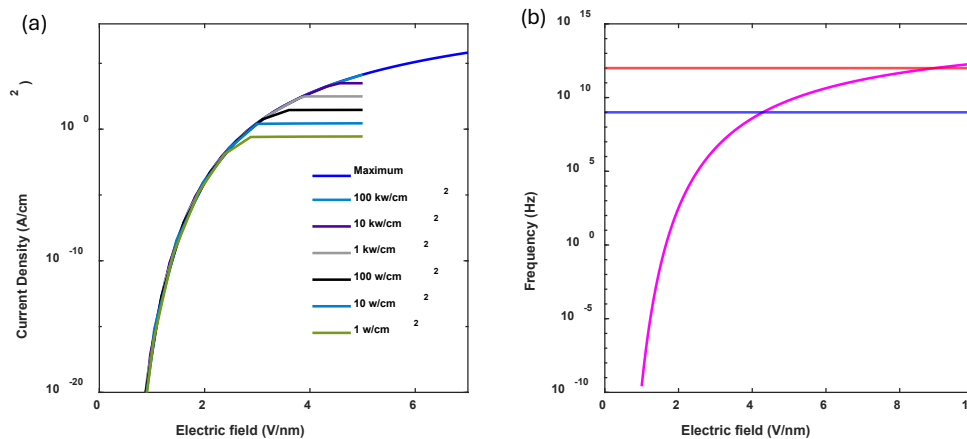


Figure 5: a) Fowler-Nordheim tunneling current density at Silicon/Vacuum junction vs Vacuum electric field at different optical powers, b) The maximum attainable bandwidth for Silicon/Vacuum devices vs vacuum electric fields.

For achieving 1 GHz bandwidth, at least ~ 4 V/nm field is required, whereas to achieve 1 THz bandwidth, the vacuum field needs to be greater than 9 V/nm. Moreover, we may not even reach the tunneling current required for such bandwidths at smaller optical intensities. For instance, to achieve 1 GHz, ~ 10 kW/sq-cm light power is required. Therefore, both light intensity and vacuum electric field dictate the response time of the device.

One of the ways to surpass the maximum frequency at a given vacuum field is by utilizing high energy photon flux, which helps faster tunneling as these photons can excite hot electrons that will face smaller tunnel barriers. Electrons with more energy than the semiconductor's electron affinity may see no barrier at all and show ballistic transport with minimum resistance. These electrons should be able to respond much faster, resulting in improved bandwidth. In that case, the bandwidth will only be limited to the minimum drift time in the semiconductor.

3) LM-IOT Development

As a preliminary investigation, experiments were carried out utilizing an electron gun setup that was not optimized for the current study. This electron gun had been initially fabricated to be used in another experimental setup. Still, it helped to evaluate and compare the performance

characteristics of the new setup with the previous cases without any electron gun. From the results, it was clearly evident that with much less field applied for extracting the electrons as well as for enabling the tunneling we can get ~ 0.3 mA/cm² level of emission current densities. Notably, these emission current levels were previously only attainable by employing significantly higher field for both cases of carrier heating and extraction. The experimental setup, as well as the data supporting these findings, are presented in Figures 6 and 7, respectively.

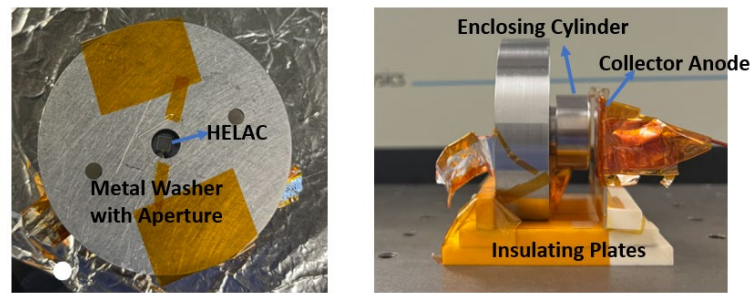


Figure 6: Electron Gun with HELAC setup for experiments

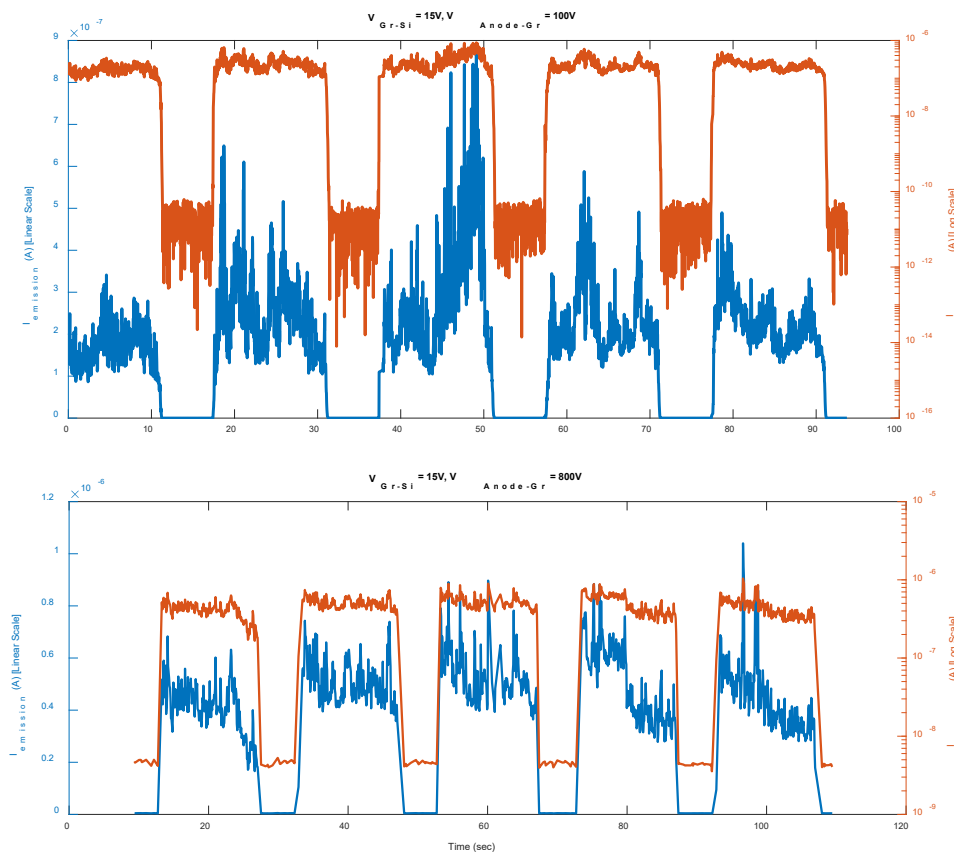


Figure 7: Emitted electron collection at the collector anode terminal without gun (top) at $1\text{V}/\mu\text{m}$ extraction field applied and with gun setup (bottom) at $0.08\text{V}/\mu\text{m}$ extraction field applied.

As part of our beam-cavity coupling optimization, we have conducted simulations in which the beam frequency and cavity length are swept. Additionally, a coaxial output has been integrated with a coupling loop to investigate the cavity-output coupling and to characterize maximum output power; however, this component has not been optimized for the given beam and cavity. For this simulation a 31 keV beam is coupled to a 1 GHz cavity with a 50 Ω coaxial output. The beam source area, resonant cavity, and output can be seen in figure 8. The beam wavelength is defined simply by

$$\lambda_{\text{beam}} = u_{\text{beam}} / f_{\text{beam}}$$

where u_{beam} is the beam velocity and f_{beam} is the beam frequency. Figure 9 shows the RMS output power measured at the coax port at various beam frequencies and cavity lengths. As expected, optimal power coupling to the cavity occurs when the beam frequency matches the cavity frequency. The 100 MHz frequency offset for the 900 MHz and 1100 MHz beam frequency cases leads to a 100 MHz beat wave forming within the cavity.

In addition to sweeping the beam frequency, the cavity length was also swept to lengths proportional to the beam wavelength. Figure 10 showcases the wave-particle power transfer where negative values indicate power transferred from beam to cavity and positive values indication power transfer in the opposite direction. Figure 10 also shows the RMS power measured at the coaxial output port. In both cases, it can be seen that a steady state is reached quickly for the case when the cavity length is $0.75\lambda_{\text{beam}}$. It can also be noted that for the case of $0.25\lambda_{\text{beam}}$ and $0.5\lambda_{\text{beam}}$ the power transfer from beam to cavity increases over time. This result indicates that a longer simulation time is required to fully characterize the beam-cavity coupling with this approach. In this timeframe, the maximum efficiency is 0.9% given the beam power of 136.4 kW. In order to continue optimizing the efficiency of this cavity and develop a model for beam-cavity coupling optimization, longer simulations and output coupling optimization is required.

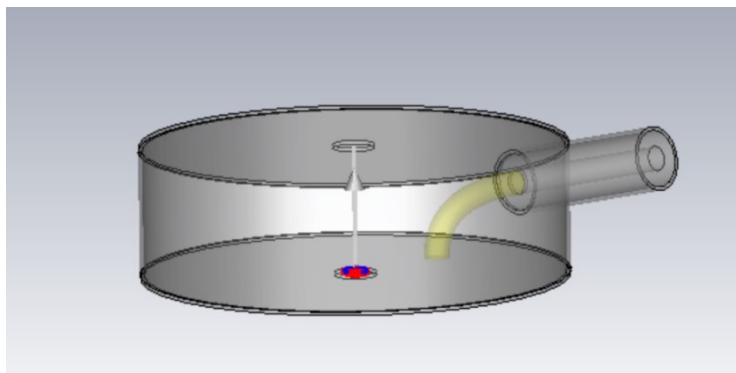


Figure 8: Resonant cavity implemented in CST showcasing the coaxial output, coupling loop in yellow, electron beam source in red and blue. The gray arrow indicates the path along which voltage is measured.

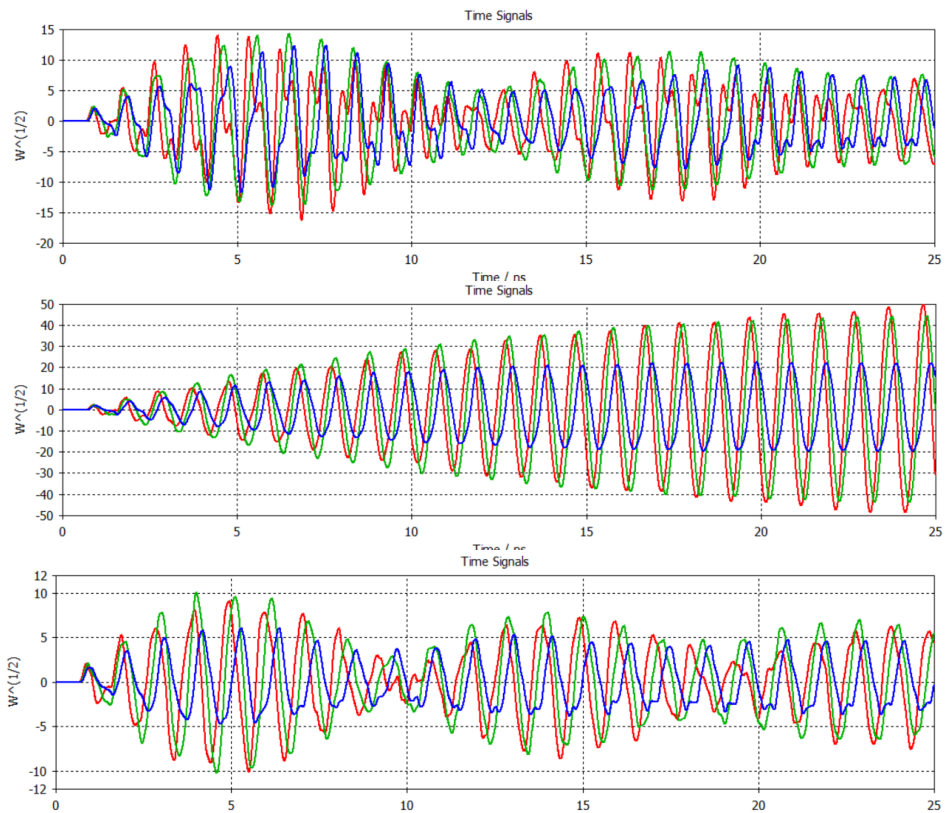


Figure 9: RMS power measured at the coaxial output for 0.9 GHz (top), 1 GHz (middle), and 1.1 GHz (bottom) beam frequencies. The red, green, and blue curves pertain to cavity lengths of 0.25, 0.5, and 0.75 times the beam wavelength.

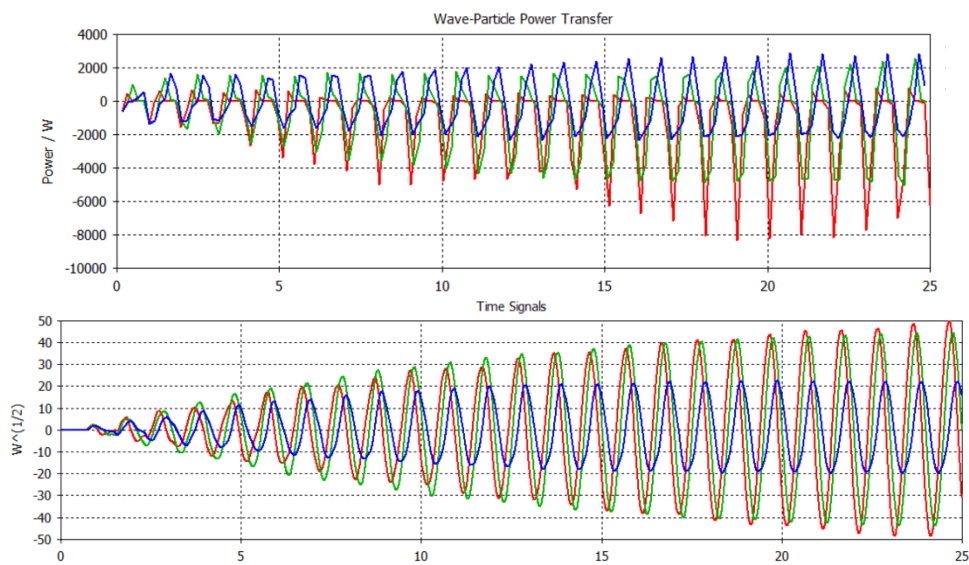


Figure 10: Instantaneous wave-particle power transfer and RMS output power for cavity lengths of $0.25\lambda_{beam}$ (red), $0.5\lambda_{beam}$ (green), $0.75\lambda_{beam}$ (blue)

4) Diamond Amplifier

In our quest of developing high quantum efficiency, high brightness, and fast photoemitters, the integration of diamond with a robust photoemission device is essential to achieve the desired performance metrics. Here diamond can serve as an electron amplifier, significantly increasing

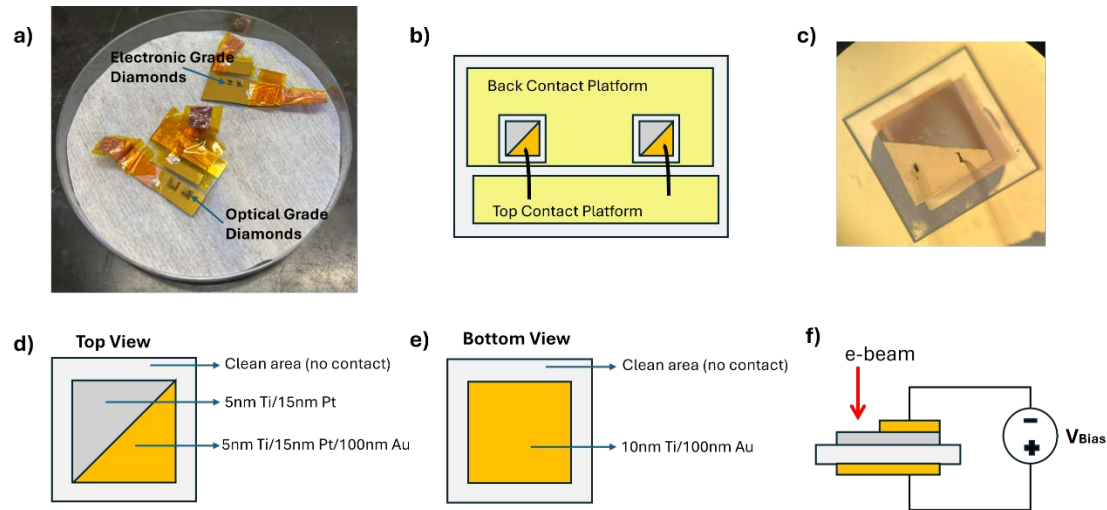


Figure 11: a) Experimental setups made with two different diamond grades; b) Diagram of samples mounted on Ti/Au-deposited glass using wirebonding; c) Microscope view of a mounted sample; d) Top contact structure; e) Bottom contact structure of the sample; f) Diagram of electrical connections, showing e-beam injection on thin contact areas to minimize scattering and maximize amplification. Here thicker pads ensured proper wirebonding and connections.

the electron output by several orders of magnitude compared to the initially injected electron input. We conducted transmission mode experiments on diamond to quantify the achievable levels of electron amplification. For these experiments, we used two distinct grades of single-crystal diamonds: one was electronic grade, characterized by defect densities below 1 part per billion (ppb), and the other was optical grade, with substantially higher defect densities, ranging from 50 to 100 parts per million (ppm). The samples were placed inside a scanning electron microscope (SEM) chamber, where energetic electrons at varying energy levels (5–30 keV) were injected into one side of the samples, and the transmitted electrons were collected from the opposite side.

Upon the interaction of the high-energy primary electron beam with the diamond, the depth of penetration of the primary e-beam should be dependent upon the beam's energy. During this process, the beam loses energy through electron scattering, and as it thermalizes, it excites valence electrons into the conduction band, generating electron-hole pairs. Prior studies have indicated that for every 13.3 eV of energy, one electron-hole pair is produced. To facilitate the drift-based transport of these newly generated secondary electrons, an internal electric field was established across the samples via an external source using contacts deposited on both sides. As a result, we

observed significant amplification, ranging from approximately 350x to 4500x, depending on the energy and current levels of the injected electron beam.

A key observation from these experiments was that amplification was only evident in the electronic grade diamond. In contrast, the optical grade samples exhibited no amplification and displayed very poor electron transmission. To optimize the transport efficiency of secondary electrons, maintaining high crystal quality with minimal defects is crucial. This minimizes

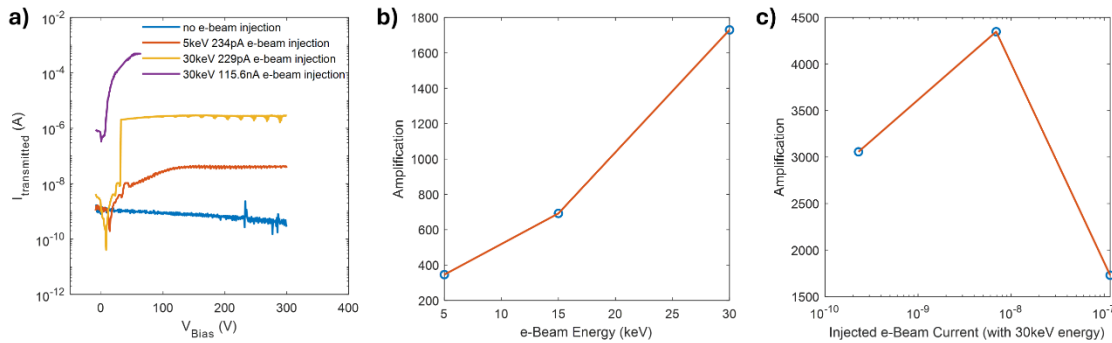


Figure 12: a) *I-V characteristics of electronic grade diamond showing Transmitted current vs Applied bias across the sample for different e-beam injection conditions. b) Amplification achieved with 115.6nA e-beam injected with various energy levels c) Amplification achieved with 30keV e-beam injected with various current levels. For both b and c experiments, 300V bias was applied across the samples.*

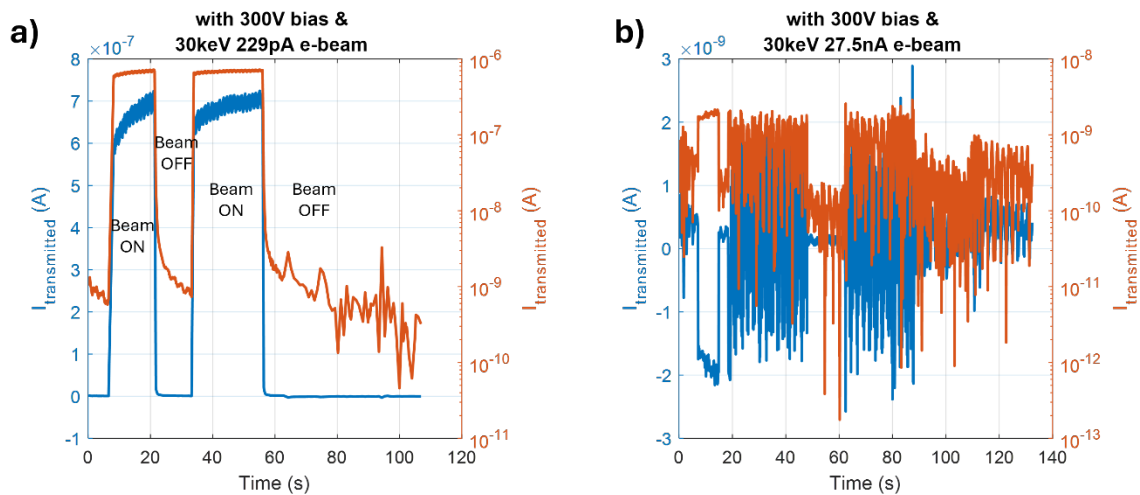


Figure 13: a) *Transmitted current vs Time characteristics of Electronic grade diamond showing adequate amplification of ~3000x when 30keV 229pA e-beam was injected. b) Transmitted current vs Time characteristics of Optical grade diamond showing inconsistent and little to no transmission when 30keV 27.5nA e-beam was injected. Larger current level is used for this sample to get above the noise level of the measuring instrument. For both cases 300V bias was applied across the*

samples scattering and trapping at defects and grain boundaries, while ensuring sufficient field strength to promote efficient electron transport to the emitting surface.

Figure 11 illustrates the experimental setup, while Figure 12 presents the I-V characteristics and the amplification levels achieved under different e-beam injection conditions for the electronic grade diamond samples. Figure 13 compares the performance of electronic and optical grade diamond samples when the e-beam was sequentially switched on and off. It is evident that only the higher quality electronic grade diamond demonstrated significant current amplification, whereas the optical grade, with higher defect density, exhibited poor electron transmission and no amplification. Given that both samples were subjected to identical experimental conditions, these findings corroborate our hypothesis that consistent electron amplification is achievable in low-defect, high-quality diamond, and that thermalized secondary electrons can be effectively collected under sufficient biasing conditions.

Our next goal was to create a Negative Electron Affinity (NEA) surface on diamond to enable the emission of the amplified and thermalized electron beam from the NEA surface. One approach to achieving the NEA effect is through hydrogen termination of the diamond surface, which forms a dipole layer that effectively reduces the work function. This dipole lowers the vacuum energy level below the conduction band minimum of the diamond, allowing electrons to be emitted directly into the vacuum without requiring extra energy to overcome a potential barrier. To accomplish this termination, we are conducting thermal annealing in a hydrogen atmosphere. A high-purity single-crystal diamond substrate is heated under a continuous flow of H₂ gas at up to 850°C for several hours, then cooled in a controlled manner. This process should result in a hydrogen-terminated NEA diamond surface. We have performed conductivity tests on both diamond grades and compared the results between hydrogen-terminated and untreated samples, as shown in Figure 14.

When NEA is achieved, electrons leave the diamond surface and bind to adsorbed impurities, creating holes in the valence band near the surface. This leads to the formation of a 2D hole accumulation layer, effectively inducing p-type doping at the surface allowing these holes to move freely and making the diamond surface conductive. Exposure to air further enhances this effect due to the adsorption of water and other atmospheric molecules.

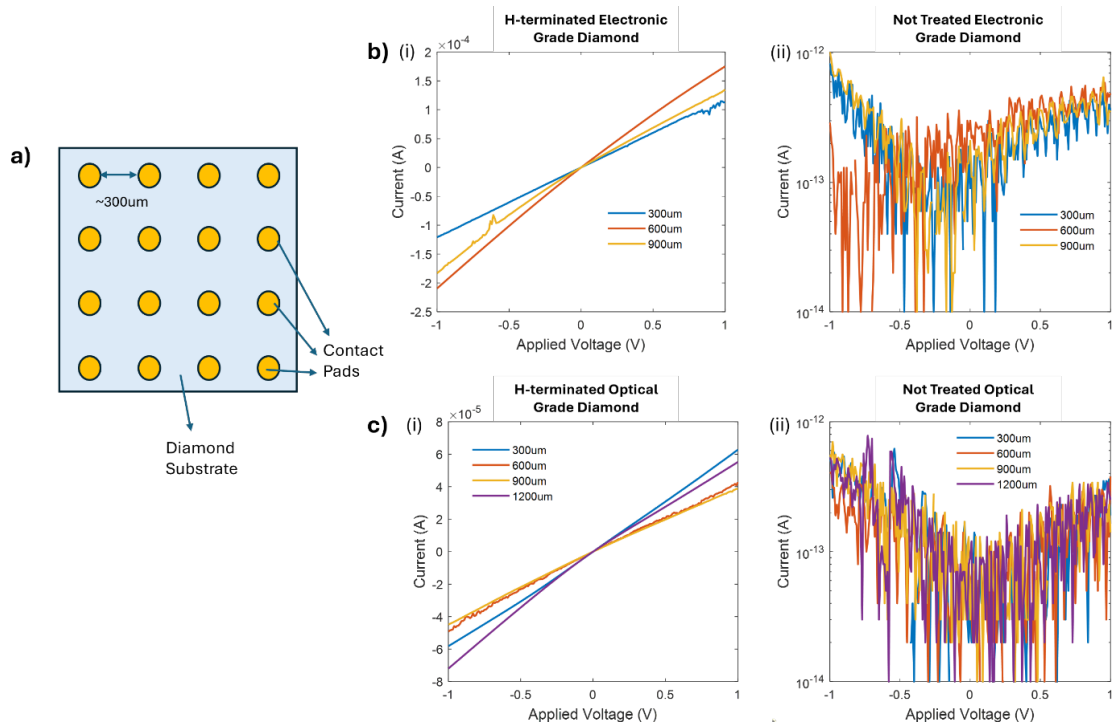


Figure 14: a) Structure used for Conductivity test of diamond, b) I-V characteristics for electronic grade (i) Treated (H-terminated and (ii) Untreated diamonds, c) I-V characteristics for optical grade (i) Treated (H-terminated) and (ii) Untreated diamonds. In both cases H-terminated diamonds are quite more conductive compared to untreated samples.

After achieving the intended surface termination, the samples were mounted on glass platforms using sapphire spacers and Kapton tape, creating a gap of approximately 700 μm between the terminated diamond surface and the collector contact. According to our calculations, at least 11.14% of the total biasing voltage should be dropped across the diamond substrate to create the internal electric field for facilitating electron transport. The rest should be dropped across the vacuum gap. Figure 15 shows the experimental setup, while Figure 16 presents the time-dependent behavior of the samples under different electron beam injection energies for both AlO-terminated and H-terminated electronic-grade diamonds. The results reveal that, contrary to expectations, no amplification was observed; in fact, transmission worsened with higher energy beam injection. Although the samples still responded when the electron beam was switched on and off, it is likely that the NEA (Negative Electron Affinity) state was not achieved. The currents observed are likely due to backscattered electrons from the sample, as lower energy beams produced higher currents.

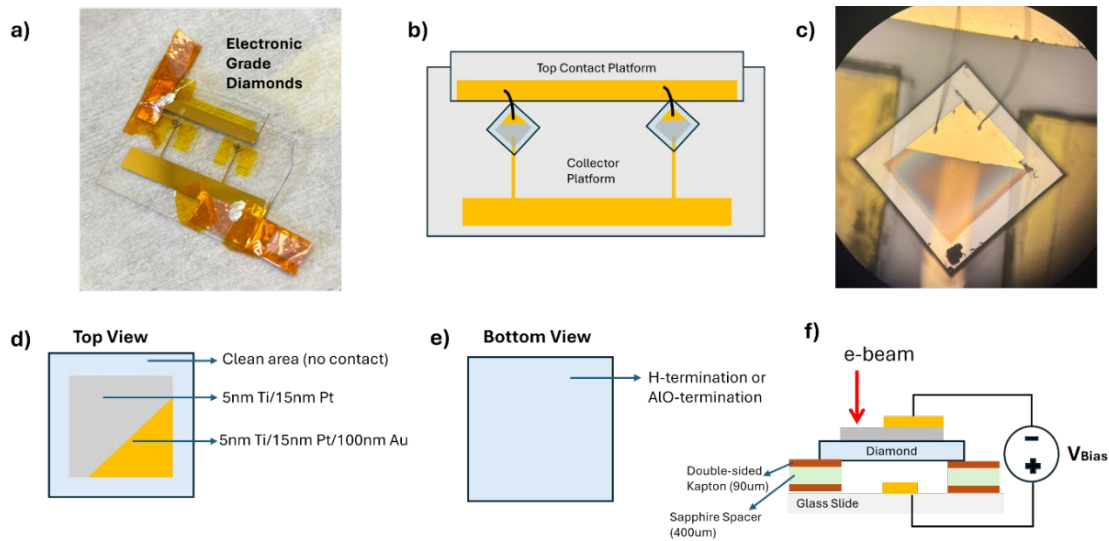


Figure 15: a) Experimental setups made with two electronic grade diamonds (one with H-termination and one with AlO-termination); b) Diagram of samples mounted on Ti/Au-deposited glass using wire-bonding; c) Microscope view of a mounted sample; d) Top contact structure; e) Bottom structure of the sample; f) Diagram of electrical connections, showing e-beam injection on thin contact areas to minimize scattering and maximize amplification. Here thicker pads ensured proper wirebonding and connections.

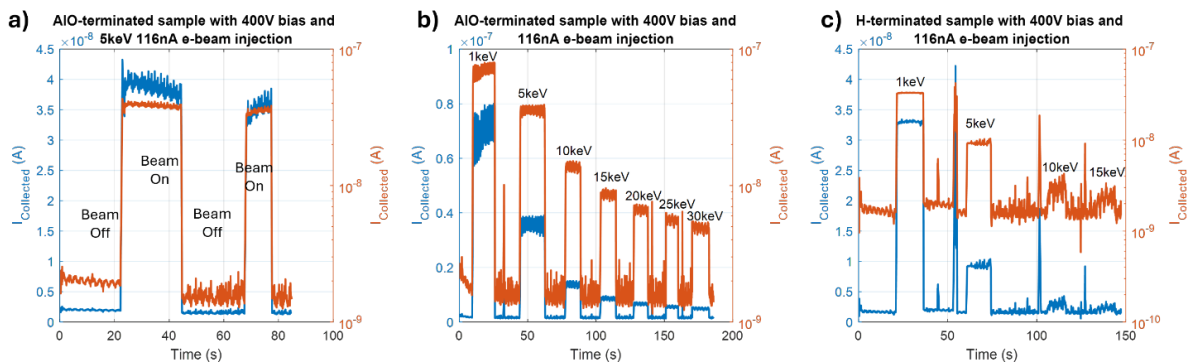


Figure 16: a) AIO-terminated sample's response with turning the e-beam on and off, b) $I-t$ measurements with different energy e-beam injection to AIO-terminated sample, c) $I-t$ measurements with different energy e-beam injection to H-terminated sample

This suggests that the surface may have lost its NEA state and changed to a PEA (Positive Electron Affinity). As a result, the diamond surfaces likely trapped the injected electrons, and these traps worked against the internal electric field that should have facilitated secondary electron transport to the terminated surface. This indicates that, either due to surface contamination or improper treatment, the expected NEA termination was not achieved. We are currently investigating the cause of this issue.

5) Fabrication of Cold Cathodes for Comparison to HELAC and VHELAC

We have iterated on our Spindt cathode fabrication; the updated process can be seen in figure 17. For this process, we have changed the initial tip formation approach to using ICP-RIE instead of RIE so that we can create a high-density plasma independent of the forward power used. This allows the process to be isotropic and has allowed us to form sharper tips. We have also introduced an Al_2O_3 layer deposited using ALD. This is used to improve the dielectric by introducing a high-quality dielectric compared to the PECVD deposited SiO_x . The process maintains its self-aligning property. Previously, we reported leakage current and emission currents reaching 500uA and 15 nA respectively under a 30V device bias. Additionally, the extraction anode was biased at 500 V and placed 6mm from the device. Our latest batch has shown drastic improvements on the emission current using an anode place 8 mm away from the device and biased at 100 V.

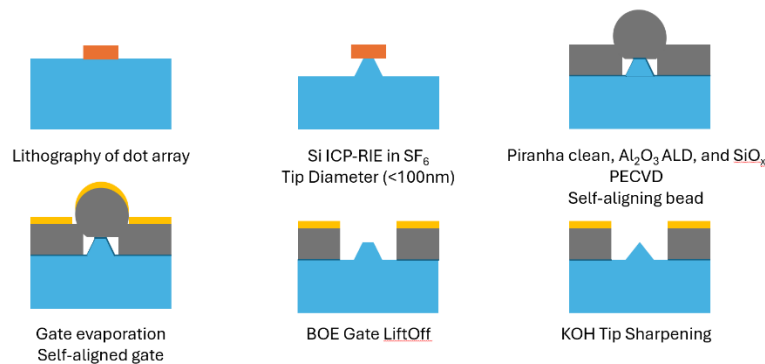


Figure 17: Spindt cathode (sharp tip field emitter array) fabrication process used for Spindt cathode reported here.

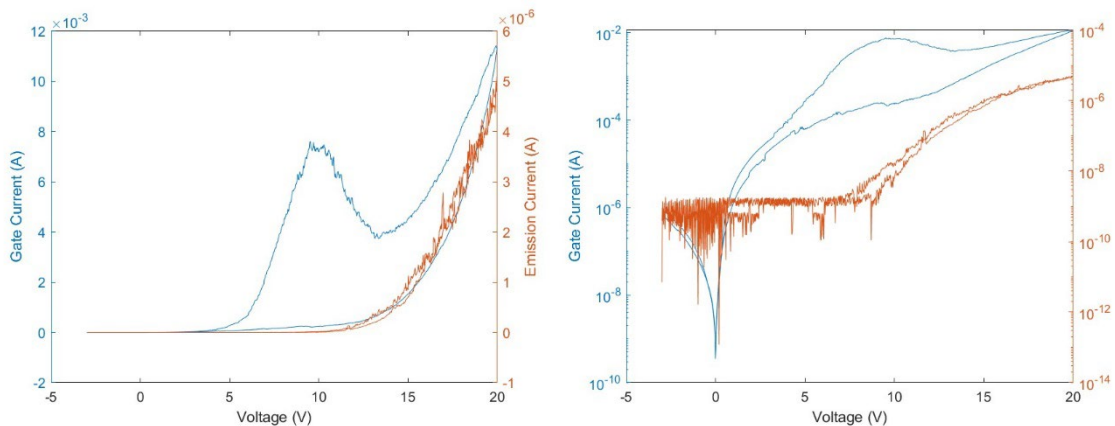


Figure 18: Gate and emission current of Spindt cathode plotted in linear (left) and log (right) scale.

We have achieved emission currents of 5 uA at 20 V device bias with relatively dull tips. Figure 18 shows the gate and emission current measured. Compared to the device reported previously, this

device appears to have a larger gate current by nearly two orders of magnitude; however, the emission current improved by over 3 orders of magnitude. It is also important to highlight that the threshold for a 1 μA of emitted current is only 16 V. After obtaining the behavior observed, we decided to explore the limits of this array. Shortly after applying 25 V, the gate current increased and the emission current decreased significantly. From this, tip failure was suspected.

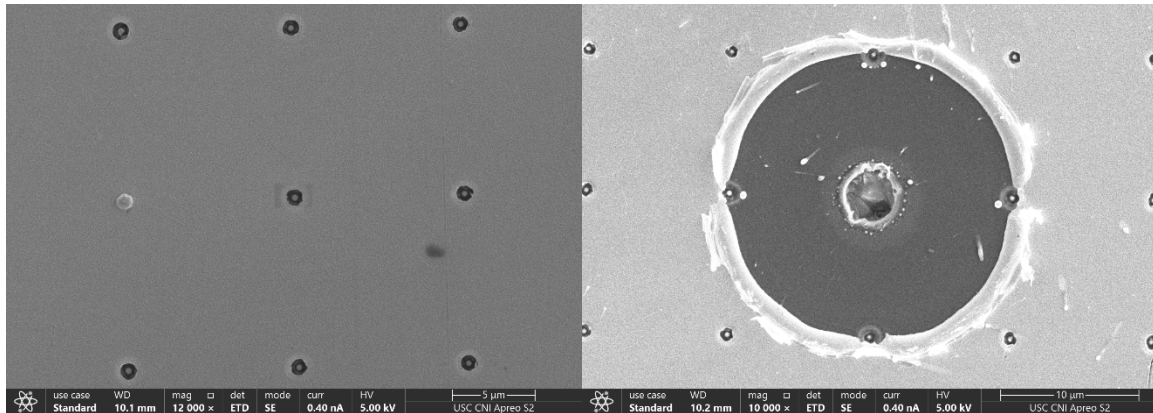


Figure 19: A subset of the field emitter array before (left) and after (right) tip failure.

Tip failure is a common fault in Spindt cathodes. The tip diameter is controlled by the etching time. Several batches were made under various etching times to observe the effect of tip diameter on the emission characteristics. The results shown thus far pertain to dull tips etched for 20 seconds which resulted in a height of ~ 500 nm and a diameter of ~ 200 nm. Figure 19 shows a portion of the cathode before and after tip failure. The tip failure in figure 19 reveals that tip failure results in a reduction of current as both the tip that fails and the neighboring tips are affected. Additionally, tip failure has been observed to cause a decrease in gate current. This can be attributed to the fact that the gate area is reduced when a tip fails. Tip failure is not uniform in the array. Our next task is to investigate where in the fabrication variation is introduced and how to mitigate it. We would also like to increase the anode voltage to extract more current from the emitter.

While addressing fabrication challenges for vacuum HELACs, a novel device concept emerged that aims to achieve similar effects. This concept is inspired by recent advancements in vacuum channel transistors, where a vacuum gap replaces the traditional solid-state channel. In these devices, emitted electrons are collected at the anode terminal, allowing for the design of high-frequency optically modulated electron-beam emitters. The active layer's structure in such devices closely resembles that of traditional HELACs, with the critical difference being the creation of a triple junction where the vacuum intersects the Si/SiO₂ junction. Upon applying sufficient voltage to induce an inversion region in the Si, a two-dimensional electron gas (2DEG) forms. This sheet of charge, when subjected to adequate voltage resulting in local field enhancement, results in electron emission from the exposed 2DEG edge. The device structure is shown in figure 20.

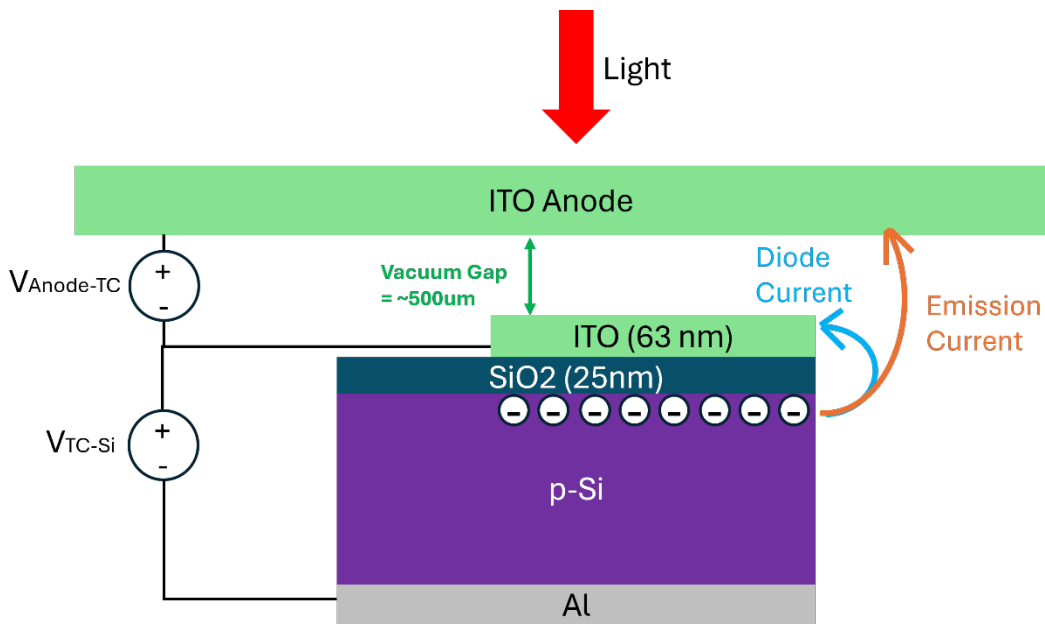


Figure 20: 2DEG emission device structure showing the two different current paths and measurement setup

In previous device measurements, it was observed that the diode current was saturating due to poor optical transmission through the 35nm Al top contact. Only 2-3% of the total optical power was transmitted and absorbed in the Si. This limited carrier generation and insufficient formation of the two-dimensional electron gas (2DEG) led to unreliable and inconsistent emission currents. The saturating diode currents were primarily due to electrons tunneling through the oxide itself, contrary to the desired outcome, which can be considered a leakage current for this device. To address this issue, a 63nm layer of indium tin oxide (ITO) was deposited in place of the Al to enhance optical transparency, thereby improving carrier generation and resulting in stable emission observations depicted in figures 21 and 22.

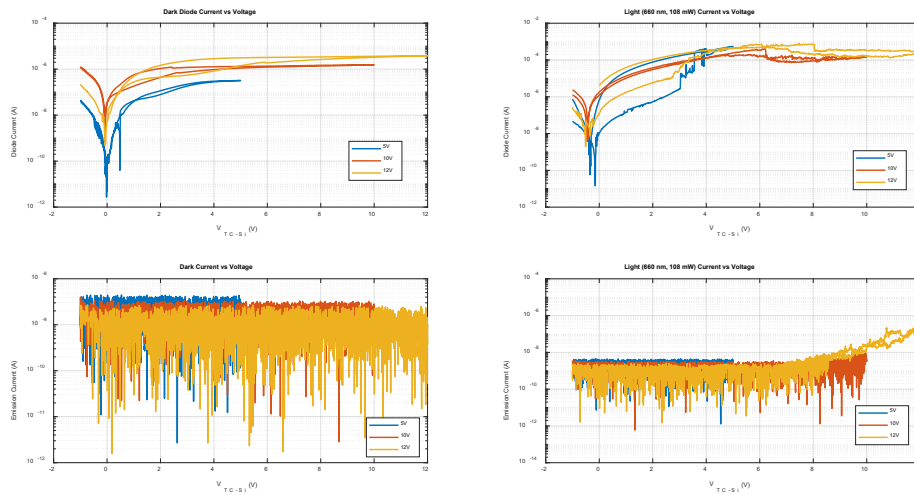


Figure 21: Device I-V characteristics. Diode Current vs. biasing voltage (top) observed in the top contact terminal, Emission Current vs. biasing voltage (bottom) observed in the Anode terminal under light and dark conditions.

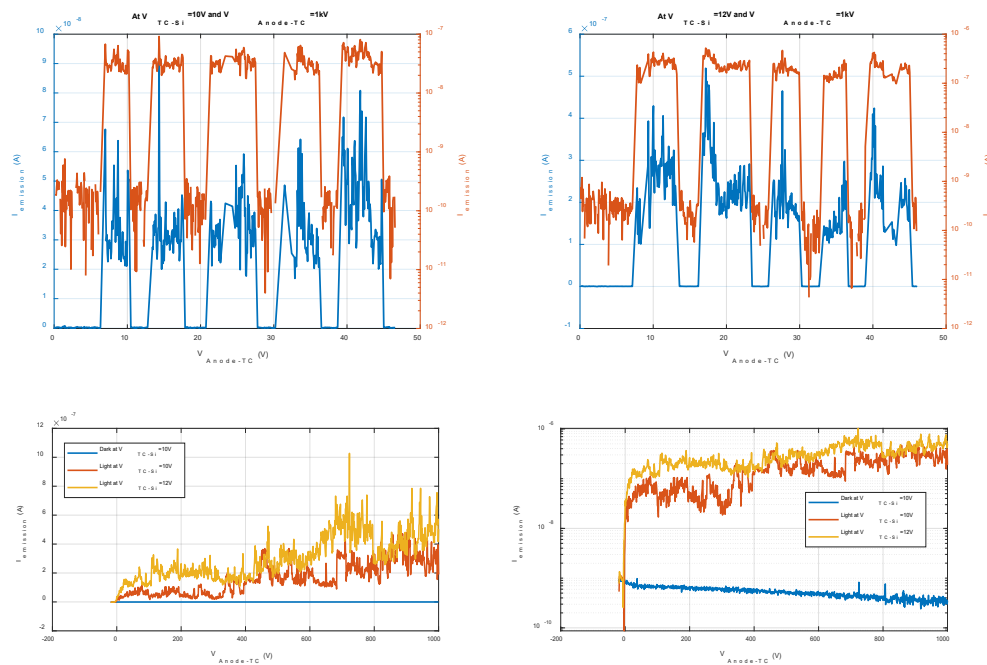


Figure 22: Device I-t characteristics (top). Emission current vs time characteristics for different anode voltages applied. The device was exposed to periodic 660nm LASER pulses. Device I-V characteristics (bottom) for anode voltage sweep, linear scale plot (left), log scale plot (right).

The results presented in Figure 22 indicate that while the emission current is significantly influenced by the biasing voltage applied between the top and bottom contacts of the device, the

extraction voltage applied to the anode has a minimal impact. This can be attributed to the fact that the formation of the inversion layer or two-dimensional electron gas (2DEG) is predominantly affected by the voltage applied to the top contact and generated carriers are getting depleted due to extraction, so fundamentally, it becomes generation limited phenomena and here mainly the extraction is driven by the top contact voltage as the electric field present there is much larger compared to the extraction field created by the anode voltage.

3. Findings and Conclusions

Throughout the reported performance period, we focused on developing a robust photocathode device characterized by high quantum efficiency and rapid response time, which is also capable of exhibiting electrostatically tunable negative electron affinity and demonstrates resilience under suboptimal vacuum conditions, distinguishing it from conventionally available photocathodes.

- HELAC:

The core of this research has been the design and fabrication of a photocathode by deconstructing its required functionalities and assigning them to the most suitable materials, which were subsequently integrated to achieve the desired performance. We began the process with Silicon (Si), a well-studied and readily available semiconductor that serves as a transducer to convert incident photons into electron-hole pairs. A thin SiO₂ insulating layer was then incorporated to facilitate electron transport and enable the injection of electrons into the emission layer with the appropriate energy. Finally, graphene was introduced as the top layer to apply the necessary voltage for creating the electric field or band bending required to achieve negative electron affinity (NEA) and to serve as the emitting surface.

Thus far, we have partially optimized the Si/SiO₂/Gr structure by exploring various design parameters, achieving a current density of approximately 0.56 mA/cm² and an external quantum efficiency (EQE) of ~0.5%, with demonstrated stability under poor vacuum pressures as low as 1 mTorr. However, simulation results indicate the potential for improvement by nearly three orders of magnitude. So we are continuing our work on this domain, exploring alternative materials that may offer enhanced performance for different parts of the device.

- VHELAC:

Our extensive experiments on the HELAC devices have helped identify key limitations on device performance. First, breakdown of the tunneling oxide reduces tunneling probabilities. Second, response time increases due to the effective mass of electrons in the insulator and the drift-diffusion mechanisms that the carriers undergo in both illuminated and dark conditions. These challenges can be effectively mitigated by replacing the insulator with a vacuum gap to eliminate breakdown issues and facilitate ballistic transport. This serves as the primary motivation for developing vacuum HELACs (VHELACs). We have explored several fabrication approaches for VHELACs

and have demonstrated field emitted currents from a subset of these. From the various iterations we have attained a greater understanding of the points of failure of VHELACs and made progress towards reducing their impact. Through simulations we have also investigated the theoretical limits of VHELAC performance across a broad frequency range as a function of applied electric field, device geometry, and incident optical power. 1GHz bandwidth Silicon VHELAC devices can be achieved by applying a vacuum field of 4.2 V/nm. In this case with an optical intensity of ~2000 W/sq-cm, the EQE of the device will be ~80%.

- **LM-IOT:**

We have continued to make progress towards the development of an LM-IOT system by exploring several components such as the electron gun, resonant cavity, and electron beam through simulations, theory, or experiment. We used particle in cell (PIC) simulations to develop a light modulated electron gun which we later demonstrated experimentally using HELACs as the cathode. We also investigated the beam-cavity interaction of existing models of IOT systems and simulated the same interaction for a density-modulated electron beam. From these simulations, we gained an understanding of the optimal beam characteristics needed such as beam energy, frequency, and current for a cylindrical cavity. We are currently working on building the LM-IOT.

- **Diamond Amplifier:**

Integration of diamond into photoemission devices offers a promising approach for achieving high efficiency, high brightness photocathodes. Diamond can function as an electron amplifier, where the injected high-energy electron beam loses energy through scattering, generating thermalized secondary electron-hole pairs. These electrons can be re-emitted from the diamond surface if the surface gets modified to exhibit negative electron affinity (NEA). Our experiments have shown e-beam amplification factors of 350x to 4500x, depending on beam energy and current and we are currently focusing on achieving stable NEA via hydrogen termination of the diamond surface, forming a dipole layer that lowers the work function and enables efficient re-emission. So far we have observed the NEA formation and remission of electrons from diamond but it requires further optimization of the NEA surface quality.

- **Other Cold Cathodes:**

We have also fabricated and characterized 2D-electron gas (2DEG) and Spindt field emitter array (FEA) cold emitters in addition to our HELAC and VHELAC devices. Our aim is to swap cathodes in our IOT and other vacuum emission test chambers and draw comparisons on the bandwidth, emitted current profile, IOT gain, and more.

4. Plans and Upcoming Events

We plan to continue our efforts on developing HELAC, vacuum HELAC devices, and diamond amplifiers, alongside constructing the LM-IOT setup for future experiments as outlined earlier.

In addition to these, we are developing a high-frequency photoemission test setup. We have tested out a pulsed laser-based setup for the high-frequency measurements (>80 MHz). The pulsed laser generates high-intensity optical delta pulses 12.5 ns apart in the time domain. This means that in the frequency domain, the pulsed laser produces delta pulses that are 80 MHz apart. The HELAC receives light from the pulsed laser, and we look at the frequency domain of the device's output to figure out the cut-off frequency of the device. We made sure that all the components of the measurement setup (bias tee, SMA cables, oscilloscope) have very high bandwidth (>10 GHz). Therefore, the dominant pole of the whole system comes from the device. Thus, in the frequency response, when the amplitude of the delta train is reduced by -3dB, that is the cut-off frequency of the device. For measuring frequencies below 80 MHz, we have decided to use our CW laser setup that can be modulated by an RF signal. We measure the amplitude of the device's output with different frequency RF light pulses. Again, we made sure that all the components in the setup had a bandwidth above 80 MHz. Therefore, when the device's output amplitude in the frequency domain falls around -3dB from the maximum amplitude, we can conclude that is the bandwidth of the device.

5. Transitions and Impacts

We presently do not have any transitions, but aim to share the emission devices fabricated in our group beyond the present collaborations as noted in section 8.

6. Recommendations for Future Work:

None

7. Personnel

<u>Principal Investigator</u>			
Full Name	Approximate Level of Effort – LOE - (Hours This FY)	Country of Residence	National Academy Member? (Y/N)
Rehan Kapadia	2	United States	N
<u>Performer Business Contact(s)</u>			
Full Name	Role	Country of Residence	
Cindy Huynh		United States	N
<u>Additional (Non-Student) Team Members</u>			

Full Name	Approximate Level of Effort – LOE - (Hours This FY)	Country of Residence	National Academy Member? (Y/N)
<u>Subcontractors</u>			
Full Name and Organization	Approximate Level of Effort – LOE - (Hours This FY)	Country of Residence	National Academy Member? (Y/N)

8. Collaborations

Full Name	Organization	Collaboration Summary
Peng Zhang	University of Michigan Ann Arbor	We are exploring how structured electron beams from optically modulated cathodes can be used to generate radiation. This collaboration is also aided by the support of Dr. Carter Armstrong, who periodically joins our meetings and offers invaluable suggestions on how we can do DoD and industrially relevant work.
John Booske	University of Wisconsin Madison	We send them HELAC devices for use in x-ray generation devices for the purposes of communications. We have sent them some multiple generations of HELACs, and they are doing testing on those devices. There have been interesting results on thermionic emission from these devices as a result of this collaboration.
Nader Behdad	University of Wisconsin Madison	We send them HELAC devices for use in x-ray generation devices for the purposes of communications. We have sent them some multiple generations of HELACs, and they are doing testing on those devices. There have been interesting results on thermionic emission from these devices as a result of this collaboration.

9. Students

<u>Doctoral Student(s)</u>			
Full Name	University	Graduated?	Graduation Year
Anika Tabassum Priyoti	University of Southern California	N	N/A
Juan Sanchez Vazquez	University of Southern California	N	N/A
Shafayeth Jamil	University of Southern California	N	N/A
<u>Masters Student(s)</u>			
Full Name	University	Graduated?	Graduation Year
<u>Undergraduate Student(s)</u>			
Full Name	University	Graduated?	Graduation Year

10. Technology Transfer

We have previously applied for a patent on the general HELAC structure, U.S. Serial No. 17/940,113, but have not applied for any more this year.

11. Products, Publications, Patents, License Agreements, etc.

Publications resulting from this project for the reporting period:

Archival Publications

#	Citation	Acknowledged ONR Support Received? (Y/N)	Peer Reviewed? (Y/N)
1	1. R. Ahsan, A. T. Priyot, J. Meng, R. Jacobs, J. Booske and R. Kapadia, "Hot Electron Photoemission from Tunable Electron Affinity Semiconductor Cathodes", ACS Applied Materials & Interfaces, Under Review	Y	Y

Conference Papers

#	Citation	Acknowledged ONR Support Received? (Y/N)	Peer Reviewed? (Y/N)
1	1. A. T. Priyoti, R. Ahsan, H. U. Chae, J. S. Vazquez and R. Kapadia, "Semiconductor Physics and Characteristics of Tunable Negative Electron Affinity Photocathode with High Quantum Efficiency," <i>2024 Joint International Vacuum Electronics Conference and International Vacuum Electron Sources Conference (IVEC + IVESC)</i> , Monterey, CA, USA, 2024, pp. 1-2, doi: 10.1109/IVECIVESC60838.2024.10694892.	Y	N
	1. R. Ahsan, A. T. Priyoti, H. U. Chae and R. Kapadia, "Performance Limits of Electrostatically Controllable Negative Electron Affinity Photoemitters," <i>2024 Joint International Vacuum Electronics Conference and International Vacuum Electron Sources Conference (IVEC + IVESC)</i> , Monterey, CA, USA, 2024, pp. 1-2, doi: 10.1109/IVECIVESC60838.2024.10694983.	Y	N

Books

No information to report.

Book Chapter

No information to report.

Theses

No information to report.

Websites

No information to report.

Patents

No information to report.

Other Products:

No information to report.

12. Point of Contact in U.S. Navy / Marine Corps

<u>Navy Point(s) of Contact Student(s)</u>			
Full Name	Organization	Email	Date of Last Contact
Zachary Drikas	Naval Research Laboratory	Y	[12/12/2024

Multi-frequency High Power Microwave Generation and Amplification via Optically Gated Electron Beams

Grant No. N00014-20-1-2681

Annual Report for Fiscal Year 2024

Period of Performance: October 1, 2023 to May 17, 2024

Prepared by:

Prof. Peng Zhang, Principal Investigator
Department of Electrical and Computer Engineering
Michigan State University
428 S. Shaw Ln
East Lansing, MI 48824
Tel: 517-353-3654
Email: pz@egr.msu.edu



Acknowledgement/Disclaimer: This work was sponsored by the Office of Naval Research (ONR), under grant/contract number N00014-20-1-2681. The views and conclusions contained herein are those of the authors only and should not be interpreted as representing those of ONR, the U.S. Navy or the U.S. Government.

Section I: Project Summary

1. Overview of Project

Executive Summary:

Electron beam based high power microwave (HPM) devices are critical to a variety of defense applications for Navy and more broadly the Department of Defense (DOD). This project explores the fundamental physics of density modulation of electron beam emission via combined mechanisms of thermionic/field/photo-emission and the interaction of such premodulated beams with circuits for HPM generation and amplification. This report provides an executive summary of our recent theoretical modeling efforts during the period of 10/1/2023 – 5/17/2024. We analyze quantum pathways interference in two-color coherent control of photoemission using exact quantum theory. We explore the tuning of quantum pathway interference in two-color laser photoemission using DC bias. Our analysis explicitly shows how DC bias shifts the possible pathways, changes the weight of each pathway and interference among them, and modulates photoemission current. In collaboration with Sandia National Labs, we characterize the effects of cathode photoemission leading to electrical discharges in argon gas. We find that when the applied voltage is insufficient for ion-induced secondary electron emission to sustain the plasma, laser driven photoemission can still create a breakdown where a sheath is formed. Our discharge model is able to accurately predict the experimentally measured breakdown voltage curves. We also perform parametric analysis on enhancement of THz Smith-Purcell radiation (SPR) by two layer-grating structure. Our results will be useful to the development of advanced cathodes, electron sources, and electromagnetic interaction circuits with density modulation, enabling new advances for the development of high power electromagnetic sources and amplifiers.

Objective:

The objective of this project is to provide a foundational understanding of the underlying physics in optically gated electron emission and its interaction with microwave circuits. The goal is to provide a guideline for the design of compact HPM devices with the ultimate high-power output and extremely flexible frequency tunability. The ultrafast electron emission due to pulsed lasers, or optical gating, would potentially provide unrivaled precision in phase-control of electromagnetic signals from electron based HPM devices. The potential of selective gating of multiple beams would provide strong flexibility for multi-frequency HPM applications.

Naval Relevance:

The research on multi-frequency high power microwave (HPM) generation and amplification via optically gated electron beams directly contributes to directed energy, which is crucial to a wide range of defense applications for Navy and DOD. HPM based directed energy creates beams of electromagnetic energy over a broad spectrum of known radio and microwave frequencies, causing either temporary or permanent effects on electronics within targeted systems at scalable effects. HPM using premodulated high current electron beams via optical means will not only enhance the power output and multiple-frequency accessibility within a single device, but also provide unique abilities for precise temporal control of the effects induced by directed energy.

The investigator's research on general emission physics and high current diodes are also well in alignment with the ongoing research activities at NRL (e.g. in the Vacuum Electronics Branch, Electronic Science and Technology Division, and the Plasma Physics Division). Our general quantum model for electron emission may be ultimately integrated with the NRL models to give better predictions of electron emission and beam modulation. In the future, it is envisioned to build a hybrid model around our exact analytical solution for simulating electron emission in practical geometries, such as sharp metal tips or cathodes with surface roughness, where effects such as the electron emission angle and space charge can be incorporated. The time-dependent field distribution near the emitter can be first calculated using a Maxwell solver. Our exact model may then be applied along the surface of the emitter to give the instantaneous emission current. The emitted electrons can be loaded into particle-in-cell pusher to account for the detailed space charge effects and electron dynamics. Once such a tool becomes available, it would find immense applications in various areas, such as solid state physics, strong fields, ultrafast sciences, vacuum electronics, and accelerators and beams, many of which are important to future Naval and more broadly DOD directed energy needs.

The proposed research on prebunched beam-circuit interaction provides answers to some of the fundamental questions on vacuum electron devices for HPM, including the fundamental limits on HPM amplification, threshold current for oscillation, and multi-frequency operation. Maximizing the HPM power output increases the system effectiveness of directed energy. Multifrequency HPM sources are crucial for directed energy applications, since different frequencies can be coupled more effectively with a larger set of targets of varying geometries. The proposed multifrequency excitation in a single device will enable the development of compact systems with reduced cost. Implementing both power and frequency tunability in HPM devices will provide Navy and DOD a critical disruptive directed energy capability using high power microwaves.

Introduction/Background:

Traveling wave devices utilize the collective interaction of an electron beam with a periodic structure to convert electron beam energy into electromagnetic radiation. They are key elements in telecommunication systems, satellite-based transmitters, military radar, communication data links, and electronic countermeasures. There continues to be strong interests in increasing the output power, frequency tunability, and bandwidth of traveling wave devices, for uses as radiation sources and power amplifiers, from GHz to THz and beyond. For the development of coherent radiation sources, it is desirable to minimize the threshold beam current for triggering oscillation. In contrast, for high power traveling wave tube (TWT) amplifiers, unwanted oscillations pose a major threat to their operation. For novel contemporary traveling wave devices, such as metamaterial-, photonic crystal- and advanced Smith-Purcell-based traveling wave devices, improving efficiency remains a major challenge.

In vacuum microwave tubes, the energy conversion from electron beams into electromagnetic radiation relies on beam modulation, by either density modulation or velocity modulation. Density modulation is achieved by controlling the electron emission from the cathode. Velocity modulation is achieved by passing the electrons through an RF electric field that modulates the velocities of the electrons. At present, TWTs mainly rely on velocity modulation of the electron beam for power amplification. After the electron velocities are modulated, there is a substantial delay before velocity modulation becomes density modulation, until useful gain is produced. Significant improvements in TWT performance can be enabled by density modulation during emission. In particular, with density modulation, velocity dispersion in the beam can be minimized and the

substantial portion of the interaction circuit for the purpose of converting velocity modulation into density modulation can be eliminated. This would result in compact devices with reductions in overall dimensions and weight, through the elimination of the premodulation circuit. Furthermore, density modulation during emission would eliminate the launching loss of the input RF signal, which is a serious intrinsic problem in TWTs based on velocity modulation.

In this project, we explore density modulation in optically gated electron emission. This is motivated by the recent rapid development in ultrafast lasers and photonics, which has opened up unprecedented advances to control electron beam dynamics at ultrashort spatial-temporal scales. The research on implementing both high power and frequency tunability in HPM devices will provide a critical disruptive capability using high power microwaves. The theory will also be valuable to neighboring fields such as novel miniaturized electromagnetic radiation sources, nano-optoelectronics, ultrafast physics, material science, and accelerator technology.

The idea of using direct current modulation of electron beams in microwave amplifiers has existed for decades. Historically, density modulation was accomplished with a grid that lays over the surface of a thermionic emitter to control the electron emission. Because of the finite transit time of the electrons across the cathode-grid space, this modulation technique is only effective up to 2 GHz for state-of-the-art devices. With the advancement of vacuum microelectronics and field emitter arrays (FEAs), the gate-to-emitter spacing has been reduced into submicron scale, which significantly decreases the electron transit time. Density modulation about 5 GHz by gate modulating of the FEA has been demonstrated; however, there are significant challenges for using FEAs in high power tubes, because the premature failure due to arcing often occurs at current levels much smaller than the design requirements. Breakdown is a major challenge for FEAs because of the high fields within the structure and the thin-film gate electrode. An electrical short between the gate and any individual emitter will burn out the entire FEA and render it unusable. While shields can be added to mitigate the damaging effects of the electrical shorts, high operating voltage is needed to field emitter arrays to draw sufficient current.

Photoemission provides an alternative method to generate premodulated electron beams, which relaxes the requirement of high operating voltage in field emission, thus eliminating possible arcing and circuit breakdown. More importantly, pulsed laser induced (or assisted) electron emission offers the possibility of manipulation and control of coherent electron motion in ultrashort spatiotemporal scales. These advantages would greatly benefit the development of advanced compact HPM devices.

2. Activities and Accomplishments

The main new activities and accomplishments during this performance period (1 October 2023 to 17 May 2024) include: 1) tuning quantum pathway interference in two-color laser photoemission using DC bias; 2) pulsed photoemission induced plasma breakdown; and 3) parametric analysis on enhancement of THz Smith-Purcell radiation (SPR) by two layer-grating structure.

TUNING QUANTUM PATHWAY INTERFERENCE IN TWO-COLOR LASER PHOTOEMISSION USING DC BIAS

We have conducted theoretical analysis on tuning quantum pathway interference in two-color laser photoemission using DC bias [1]. Photoemission or photon assisted field-/thermionic- emission plays an important role in high power high frequency electromagnetic radiation generation. The

strongly modulated electron sources triggered by laser fields are important to the development of compact radiation sources and free-electron lasers. We analyzed the effects of DC field on two-color laser photoemission using quantum pathways interference with the exact analytical solutions of the time-dependent Schrödinger equation (TDSE). Our analysis explicitly shows how DC bias shifts the possible pathways, changes the weight of each pathway and interference among them, and modulates photoemission current.

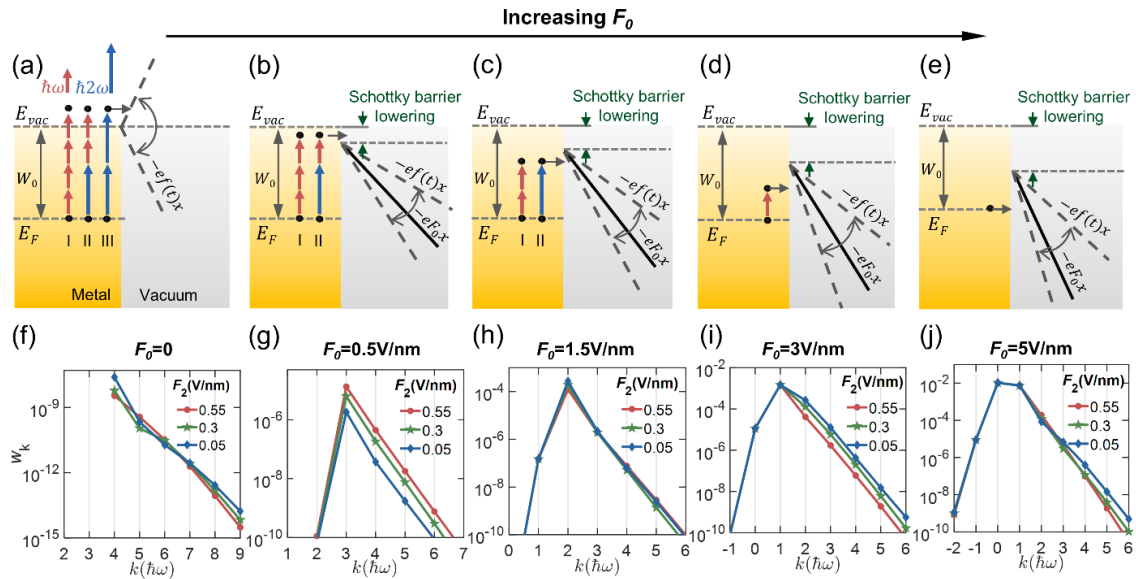


Figure 1. (a)-(e) Energy diagram for photoemission from metal surfaces induced by two-color laser fields $f(t) = F_1 \cos(\omega t) + F_2 \cos(2\omega t + \theta)$ under an increasing DC field F_0 . Red and blue arrows depict the dominant quantum pathways under given DC and laser fields. Red arrow: absorption of a fundamental photon $\hbar\omega$; blue arrow: absorption of a second-harmonic photon $\hbar(2\omega)$. (f)-(j) Electron transmission probability from initial energy $\varepsilon = E_F$, $w_k(\varepsilon = E_F)$, through k -photon ($\hbar\omega$) processes, with phase delay $\theta = 0$, $F_1 = 2.6$ V/nm, and $F_2 = 0.55, 0.3$, and 0.05 V/nm corresponding to lines in red, green and blue.

The 1D model is illustrated in Figs. 1(a)-(e) for photoemission under various combinations of DC bias field F_0 and two-color laser field $f(t) = F_1 \cos \omega t + F_2 \cos(2\omega t + \theta)$, where F_1 and F_2 are the magnitudes of the fundamental and second harmonic laser fields respectively, ω is the angular frequency of the fundamental laser, θ is the relative phase between the two laser fields. Figures 1(f)-(j) show the electron emission probability from Fermi level $w_k(\varepsilon = E_F)$ through k -photon ($\hbar\omega$) processes under a DC field of 0, 0.5, 1.5, 3, and 5 V/nm, respectively, with the fundamental laser field $F_1 = 2.6$ V/nm, the second harmonic laser field $F_2 = 0.55, 0.3, 0.05$ V/nm corresponding to lines in red, green and blue, and the relative phase $\theta = 0$. The metal is assumed to be gold, with $W_0 = 5.1$ eV and $E_F = 5.53$ eV. The fundamental laser has a wavelength of 800 nm ($\hbar\omega = 1.55$ eV), and the dominant emission process is equivalent 4 $\hbar\omega$ -photon absorption when $F_0 = 0$, as shown in Fig. 1(f). Increasing the applied DC field shifts the dominant k -photon process to lower order multiphoton absorption photoemission ($k < 4$, Figs. 1(b) and 1(g)), photo-assisted tunneling (Figs. 1(c), 1(h) and 1(d), 1(i)) or direct tunneling (Figs. 1(e) and 1(j)), resulting in different dominant photon absorption pathways. The possible multiphoton absorption pathways include single color

photon absorption pathways, e.g., pathways I and III in Fig. 1(a), and multicolor pathways, e.g., pathway II in Fig. 1 (a). Interference occurs among different pathways, resulting in coherent modulation of photoemission current with higher frequencies.

It has been shown that a maximum modulation depth of 99.4% can be achieved when $F_0 = 0.5$ V/nm, $F_1 = 2.6$ V/nm and $F_2 = 0.25$ V/nm for a gold emitter with a fundamental laser wavelength of 800 nm, as shown in Fig. 2.

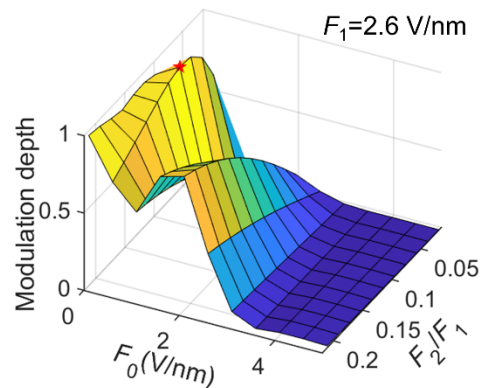


Figure 2. Modulation depth as a function of F_0 and the ratio of F_2/F_1 , with $F_1 = 2.6$ V/nm.

PULSED PHOTOEMISSION INDUCED PLASMA BREAKDOWN

We characterize the effects of cathode photoemission leading to electrical discharges in argon gas [2]. We perform breakdown experiments under pulsed laser illumination of a flat cathode and observe Townsend to glow discharge transitions. The breakdown process is recorded by high-speed imaging, and time-dependent voltage and current across the electrode gap are measured for different reduced electric fields and laser intensities. We employ a 0D transient discharge model to interpret the experimental measurements. The fitted values of transferred photoelectron charge are compared with calculations from a quantum model of photoemission. The breakdown voltage is found to be lower with photoemission than without. When the applied voltage is insufficient for ion-induced secondary electron emission to sustain the plasma, laser driven photoemission can still create a breakdown where a sheath (i.e., a region near the electrode surfaces consisting of positive ions and neutrals) is formed. This photoemission induced plasma persists and decays on a much longer time scale (~ 10 μ s) than the laser pulse length (30 ps). The effects of different applied voltages and photon energies on the breakdown voltage and current waveforms are investigated. The discharge model can accurately predict the measured breakdown voltage curves, despite the existence of discrepancy in quantitatively describing the transient discharge current and voltage waveforms.

Figure 3(a) shows a schematic of the experimental setup. Discharges were generated between two parallel aluminum plate electrodes (22 mm x 13 mm) separated by a 3.5 mm gap. The electrodes were enclosed within a vacuum chamber with optical access for imaging using an intensified

charge-coupled device (ICCD) and illumination of the cathode by a pulsed laser source. Figure 3(b) shows an image of the discharge acquired by the ICCD (Andor Technology, iStar DH334T).

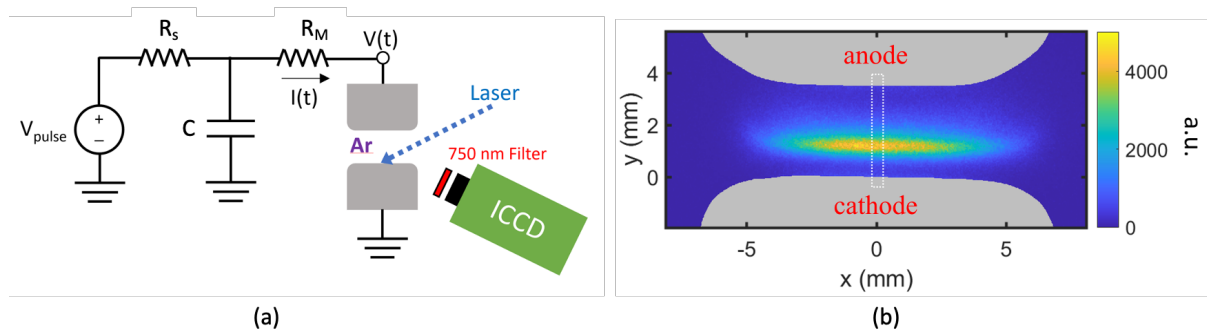


Figure 3: (a) Schematic of the circuit and optical imaging setup. Pulsed laser light incident on the cathode induces photoemission and plasma breakdown. (b) Linear-scale image of the plate-to-plate discharge acquired with the ICCD at $pd = 1$ Torr-cm. The region designated by the dotted white lines was spatially integrated along the x dimension to examine the breakdown evolution.

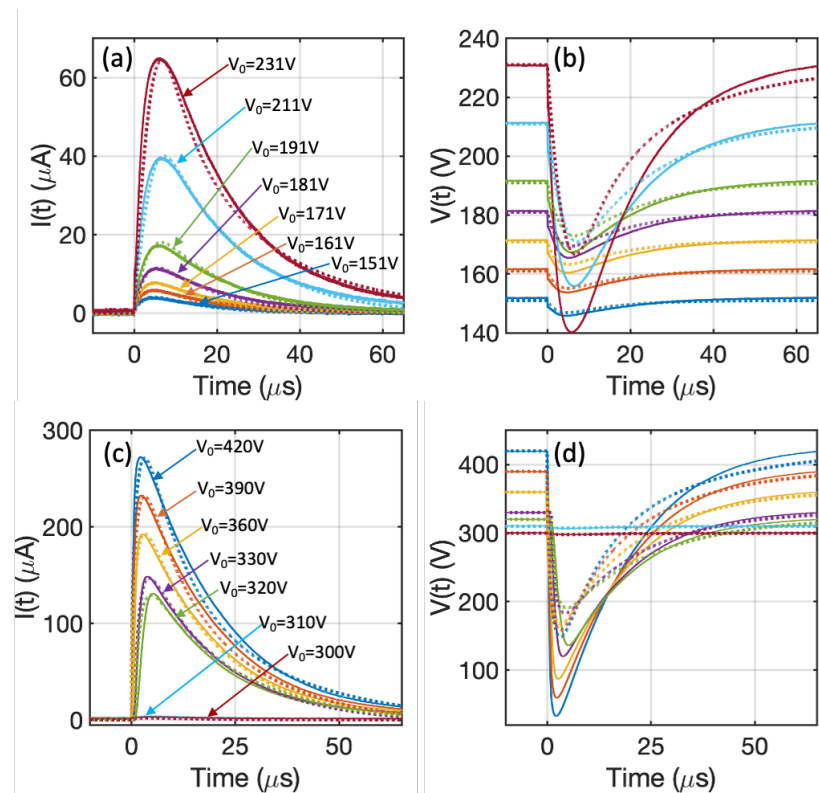


Figure 4: Top row: Transient (a) current and (b) voltage waveforms for $pd = 1$ Torr-cm resulting from the photoemission due to a 230 nm (5.39 eV), 36 μ J pulsed laser incident on the cathode at time $t = 0$ μ s, with different amplitudes of the applied voltage pulse, V_0 . The solid curves are obtained from the experiments with $C = 206$ pF, $d = 0.35$ cm, $R_s = 76$ Ω and $R_M = 1$ M Ω , respectively. The dotted curves are the results of calculations using our theory. Bottom row: Transient (c) current and (d) voltage waveforms for $pd = 10$ Torr-cm with the same parameters as those in the top row.

Figure 4 shows the transient current (Figs. 4(a) and (c)) and voltage (Figs. 4(b) and (d)) waveforms for different amplitudes (V_0) of the applied DC voltage (i.e., V_{pulse} in Fig. 1(a)) obtained from the experimental measurements (solid curves) and numerical calculations (dotted curves) for $pd = 1$ Torr-cm (top row) and 10 Torr-cm (bottom row) when a 230 nm (5.39 eV), 36 μJ pulsed laser is incident on the cathode at time, $t = 0 \mu\text{s}$. In the numerical calculation, the photoelectric current (I_p) produced by irradiation is approximated with a gaussian shaped simulation pulse. Excellent agreement between the theory and experiments is noted.

PARAMETRIC ANALYSIS ON ENHANCEMENT OF THZ SMITH-PURCELL RADIATION (SPR) BY TWO LAYER-GRATING STRUCTURE

We have also performed parametric analysis on enhancement of THz Smith-Purcell radiation (SPR) by two layer-grating structure. SPR is a specific form of a backward wave oscillator (BWO). Previously, using particle-in-cell (PIC) simulations, two-layer gratings (Fig. 5) have been shown to enhance SPR growth rates and reduce the starting currents at certain grating parameters [3]. However, our study shows such an enhancement is not universal and its effectiveness depends on the specific operating point and, significantly, the spatial growth rate, which is intricately tied to the grating parameters such as width and heights. High power, efficient, and low-cost electromagnetic sources have significant uses in high resolution imaging, biomedical scanning, material analysis, security systems, high-data-rate communications, and so on. As a special case of a BWO, Smith-Purcell radiation (SPR) has attracted strong interest in producing high frequency (THz) radiation.

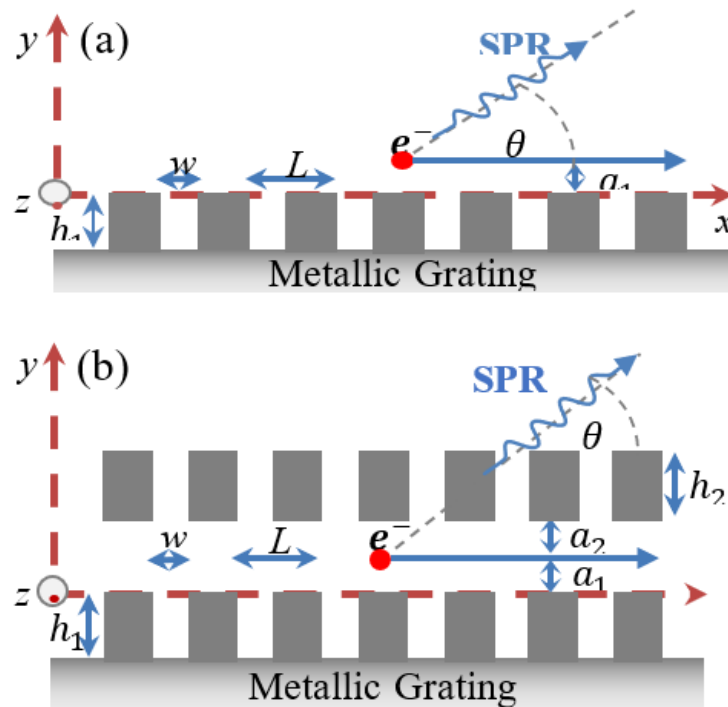


Figure 5. Schematic of Smith-Purcell (a) single-layer and (b) two-layer grating configuration.

Theoretically, the operation frequency of SPR in a two-layer grating is obtained by its cold-tube dispersion relation, and the spatial growth rate is determined by the hot-tube dispersion relation. Higher spatial growth rate directly correlates with lower starting current, both of which shows a similar scaling on the dependence of grating parameters [4]. It is found that the use of a second-layer grating shifts the spatial growth rate band towards lower beam energies, enabling higher growth rates and facilitating starting current reduction in SPR for lower beam energies by offering improved parameter control. Our parametric analysis identifies the domain in which a two-layer or a single-layer grating structure should be chosen to enhance SPR and reduce the starting current [5].

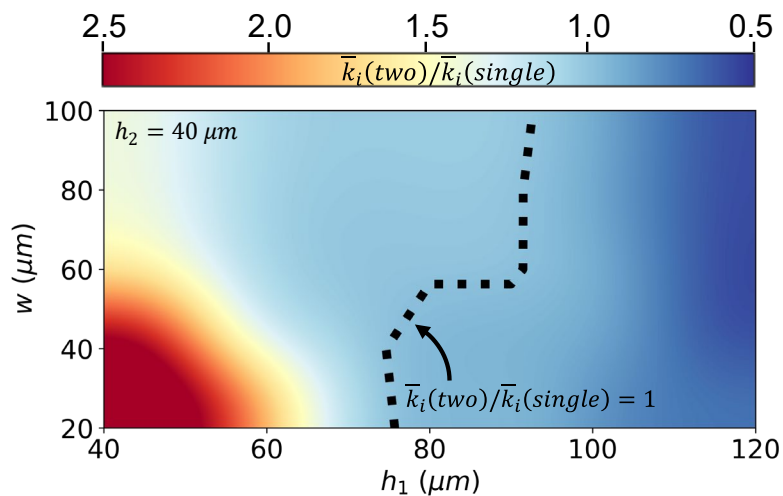


Figure 6. Contour plot of spatial growth rate ratio $\bar{k}_i(\text{two})/\bar{k}_i(\text{single})$ between a two-layer and a single-layer grating structure with fixed values of $h_2 = 40 \mu\text{m}$ and beam energy of 50 keV. The calculations of the imaginary part of the complex wave numbers (\bar{k}_i) were performed using a beam current of 5000A/m, with the other parameters in [4].

Figure 6 shows the contour map for the ratio of spatial growth rate between two- and single-layer grating structure as a function of w and h_1 , with fixed values of $h_2 = 40 \mu\text{m}$ and $a_2 = 10 \mu\text{m}$, for a fixed electron beam energy of 50 keV. For a given set of grating parameters, the two-layer grating structure requires a smaller starting current when $\bar{k}_i(\text{two})/\bar{k}_i(\text{single}) > 1$, whereas the single-layer grating structure is favorable due to a smaller starting current when $\bar{k}_i(\text{two})/\bar{k}_i(\text{single}) < 1$.

This reduction in beam current yields several advantageous effects, such as minimizing beam loss, prolonging cathode lifetime, and mitigating the heating of beam-carrying components.

GUEST EDITING AND BOOK WRITING ON HPM

During this performance period, the PI has served as a Guest Editor for the Special Issue on Plenary, Invited, and Selected Minicourse Papers from ICOPS 2023 [6].

The PI has also been coauthoring the fourth edition of the classical book: J. Benford, J. A. Swegle, E. Schamiloglu, J. Stephens, and P. Zhang, *High Power Microwaves*, 4th ed. (CRC Press), which is expected to be published in December 2024.

- [1] Y. Zhou, and Peng Zhang, "Tuning quantum pathway interference in two-color laser photoemission using DC bias", *New J. Phys.* 25, 113027 (2023).
- [2] A. Iqbal, B. Bentz, Y. Zhou, K. Youngman and Peng Zhang, "Pulsed photoemission induced plasma Breakdown", *J. Phys. D: Appl. Phys.* 56, 505204 (2023).
- [3] M. A. Faisal and P. Zhang, Smith-Purcell Radiation by a Two Layer Grating Structure, in 2023 24th International Vacuum Electronics Conference (IVEC) (2023), pp. 1–2.
- [4] M. A. Faisal, and P. Zhang, "Grating Optimization for Smith–Purcell Radiation: Direct Correlation Between Spatial Growth Rate and Starting Current", *IEEE Trans. Electron Devices* 70, 2860 (2023).
- [5] M. A. Faisal, and P. Zhang, "Parametric Analysis on Enhancement of THz Smith-Purcell Radiation by Two Layer-Grating Structure", under review, 2024.
- [6] J. Stephens, and Peng Zhang, "Guest Editorial - Special Issue on Plenary, Invited, and Selected Minicourse Papers From ICOPS 2023", *IEEE Trans. Plasma Sci.*, 52, 1081 (2024).

3. Findings and Conclusions

We have analyzed quantum pathways interference in two-color coherent control of photoemission using exact quantum theory. We explored the tuning of quantum pathway interference in two-color laser photoemission using DC bias. Our analysis explicitly shows how DC bias shifts the possible pathways, changes the weight of each pathway and interference among them, and modulates photoemission current. In collaboration with Sandia National Labs, we characterized the effects of cathode photoemission leading to electrical discharges in argon gas. We found that when the applied voltage is insufficient for ion-induced secondary electron emission to sustain the plasma, laser driven photoemission can still create a breakdown where a sheath is formed. Our discharge model is able to accurately predict the experimentally measured breakdown voltage curves. We also performed parametric analysis on enhancement of THz Smith-Purcell radiation (SPR) by two layer-grating structure. Our results will be useful to the development of advanced cathodes, electron sources, and electromagnetic interaction circuits with density modulation, enabling new advances for the development of high power electromagnetic sources and amplifiers.

4. Plans and Upcoming Events

We are currently applying our newly developed models for emission current density modulation in RF field emitters to study their effects on beam-structure interaction for radiation generation. In particular, we would like to find out the scaling dependence of RF output power on the input parameters for a given operation frequency, including emitter properties, laser and RF fields. We have been looking at Inductive Output Tubes (IOTs) as an initial example and analyzing the effect of beam bunching on efficiency and output power. The results will be used to determine the optimized combination of input parameters (emitter properties, laser, and RF fields) to give the desired level of density modulation to maximize the efficiency and performance for a given device.

Based on this initial study of density modulated IOTs, we plan to focus on travelling wave tubes (TWTs) and backward wave oscillators (BWOs) using emission modulated beams from photo/light assisted emission. As the PI will be joining University of Michigan (UM), Ann Arbor in January 2025, we plan to have extensive modeling-experiment collaboration with UM colleagues. Besides,

we have existing collaborations with experimentalists at AFRL, University of Southern California, and Sandia National labs. We have also been discussing with experimentalists at Texas Tech University, France, and Singapore to identify possible collaboration opportunities. We plan to explore the possibility of tailoring the emission energy spread using optical fields. We also plan to develop new, general theory for beam-circuit interaction for density modulated beams using optical means. Our goal is to identify the optimized parameter combinations relative to beam dynamics and RF output. We will further explore the space charge effects and explore waveform controllability using emission modulated beams. We also plan to run CST and XOOPIC simulations to test the beam-circuit theory and provide guidance to the source and circuit design of amplifiers and oscillators.

5. Transitions and Impacts

Not Applicable.

6. Recommendations for Future Work:

Optical control of electron beams is envisioned to provide unprecedented new advances in the development of novel high power electromagnetic radiation sources owing to its ultrafast and precise control electron bunching with extremely high spatiotemporal resolution. Integration of existing device platforms with economical lasers will significantly enhance their performance and enable new capabilities. We plan to pursue along such a direction for HPM development beyond the current YIP project.

7. Personnel

Principal Investigator			
Full Name	Approximate Level of Effort – LOE - (Hours This FY)	Country of Residence	National Academy Member? (Y/N)
Peng Zhang	LOE Hours 160	USA	N
Co-Investigator(s) or Co-PI(s)			
Full Name	Approximate Level of Effort – LOE - (Hours This FY)	Country of Residence	National Academy Member? (Y/N)
N.A.	N.A.	N.A.	N.A.
Performer Business Contact(s)			
Full Name	Role	Country of Residence	
Jason Sanders	0	USA	N
Additional (Non-Student) Team Members			
Full Name	Approximate Level of Effort – LOE - (Hours This FY)	Country of Residence	National Academy Member? (Y/N)
Asif Iqbal	LOE Hours 160	USA	N
Lan Jin	LOE Hours 160*6	USA	N
Md Faisal	LOE Hours 160*3	USA	N
Subcontractors			

Full Name and Organization	Approximate Level of Effort – LOE - (Hours This FY)	Country of Residence	National Academy Member? (Y/N)
N.A.	N.A.	N.A.	N.A.

8. Collaborations

Full Name	Organization	Collaboration Summary
John Luginsland	AFOSR	Emission physics, beam-circuit interaction
Steve Fairchild	Air Force Research Laboratory	Emission physics
Jacob Stephens	Texas Tech University	Emission physics, beam-circuit interaction
Edl Schamiloglu	University of New Mexico	beam-circuit interaction, HPM
Jim Benford	Microwave Sciences	beam-circuit interaction, HPM
John A. Swegle	J-Two ROB, LLC	beam-circuit interaction, HPM
L. K. Ang	Singapore University of Technology and Design	Emission physics
Lin Wu	Singapore University of Technology and Design	Emission physics
Y. Y. Lau	University of Michigan	Emission physics, beam-circuit interaction
Nick Jordan	University of Michigan	Emission physics, beam-circuit interaction
John Verboncoeur	Michigan State University	Emission physics, beam-circuit interaction
Rehan Kapadia	University of Southern California	Emission physics, beam-circuit interaction
Sneha Banerjee	Sandia National Labs	Emission physics
Brain Bentz	Sandia National Labs	Emission physics
Yang Zhou	Argonne National Lab	Emission physics

9. Students

Doctoral Student(s)			
Full Name	University	Graduated?	Graduation Year
Lan Jin	Michigan State University	N	2026
Md Faisal	Michigan State University	N	2026
Masters Student(s)			
Full Name	University	Graduated?	Graduation Year

N.A.	N.A.	N.A.	N.A.
Undergraduate Student(s)			
Full Name	University	Graduated?	Graduation Year
N.A.	N.A.	N.A.	N.A.

10. Technology Transfer

We have filed the following US Patent:

1. P. Zhang, L. Jin, and Y. Zhou, "Optically gated field emission cathodes", US Patent Provisional filed on 8/14/2023; converted to nonprovisional United States application on 8/9/2024.

11. Products, Publications, Patents, License Agreements, etc.

Publications resulting from this project for the reporting period:

Archival Publications

#	Citation	Acknowledged ONR Support Received? (Y/N)	Peer Reviewed? (Y/N)
1	Y. Zhou, and Peng Zhang, "Tuning quantum pathway interference in two-color laser photoemission using DC bias", <i>New J. Phys.</i> 25, 113027 (2023).	Y	Y
2	A. Iqbal, B. Bentz, Y. Zhou, K. Youngman and Peng Zhang, "Pulsed photoemission induced plasma Breakdown", <i>J. Phys. D: Appl. Phys.</i> 56, 505204 (2023).	Y	Y
3	M. A. Faisal, and P. Zhang, "Parametric Analysis on Enhancement of THz Smith-Purcell Radiation by Two Layer-Grating Structure", under review, 2024	Y	Y
4	J. Stephens, and Peng Zhang, "Guest Editorial - Special Issue on Plenary, Invited, and Selected Minicourse Papers From ICOPS 2023", <i>IEEE Trans. Plasma Sci.</i> , 52, 1081 (2024).	N	N

Conference Papers

#	Citation	Acknowledged ONR Support Received? (Y/N)	Peer Reviewed? (Y/N)
1	[Invited Talk] Peng Zhang , B. Bentz, A. Iqbal, Y. Zhou, K. Youngman, "EM1.00009: Pulsed laser induced photoemission and its effects in plasma discharge", 76th Annual Gaseous Electronics Conference (GEC) (October 9-13, 2023, Ann	Y	N

	Arbor, MI, USA).		
2	[Invited Talk] Peng Zhang , “GF2.00003: Modeling of surface electron emission with plasma interaction and space charge waves”, 76th Annual Gaseous Electronics Conference (GEC) (October 9-13, 2023, Ann Arbor, MI, USA).	Y	N
3	Y. Heri, and Peng Zhang, “Space Charge Limited Current Scaling for Short-Pulse Beam in a Vacuum Diode with Different Pulse Shapes”, Combined 25th Annual IEEE International Vacuum Electronics Conference + 15th Annual International Vacuum Electron Sources Conference (April 22-25, 2024, Monterey, CA, USA). [Poster]	Y	N
4	L. Jin, and Peng Zhang, “Effects of Laser Pulse Length on Photoemission Spectra from a Biased Metal Surface”, Combined 25th Annual IEEE International Vacuum Electronics Conference + 15th Annual International Vacuum Electron Sources Conference (April 22-25, 2024, Monterey, CA, USA). [Oral]	Y	N
5	M. Rahman, and Peng Zhang, “The Effect of Space Charge on the Performance of Linear Beam Devices”, Combined 25th Annual IEEE International Vacuum Electronics Conference + 15th Annual International Vacuum Electron Sources Conference (April 22-25, 2024, Monterey, CA, USA). [Poster]	Y	N
6	M. Faisal, and Peng Zhang, “Analysis of THz Smith-Purcell Radiation in Single- and Two-Layer Gratings Utilizing Hot-Tube Dispersion Relation”, Combined 25th Annual IEEE International Vacuum Electronics Conference + 15th Annual International Vacuum Electron Sources Conference (April 22-25, 2024, Monterey, CA, USA). [Oral]	Y	N
7	M. Faisal, and Peng Zhang, “Analyzing Spatial Growth Rate and Starting Current in Smith-Purcell Radiation using Single- and Two-Layer Grating Structures”, 14th Annual MIPSE Graduate Student Symposium (November 15, 2023, Ann Arbor, MI, USA). [Poster]	Y	N
8	L. Jin, Y. Zhou, and Peng Zhang, “Beam Density	Y	N

	Modulation During Emission Using RF and Laser Fields”, 14th Annual MIPSE Graduate Student Symposium (November 15, 2023, Ann Arbor, MI, USA). [Poster]		
9	M. Rahman, and Peng Zhang, “The Effect of Space Charge on the Performance of Linear Beam Device for High Frequency Radio Waves”, 14th Annual MIPSE Graduate Student Symposium (November 15, 2023, Ann Arbor, MI, USA). [Poster]	Y	N
10	Y. Heri, and Peng Zhang, “Space Charge Effects on Short-Pulse Beam Dynamics in Vacuum Diodes”, 14th Annual MIPSE Graduate Student Symposium (November 15, 2023, Ann Arbor, MI, USA). [Poster]	Y	N
11	Y. Zhou and Peng Zhang, “Effects of DC Bias on Quantum Pathways Interference in Two-color Laser Induced Photoemission”, Postdoctoral Research and Career Symposium, Argonne (November 9, 2023, Argonne National Laboratory, Lemont, IL, USA). [poster]	Y	N
12	Y. Heri, and Peng Zhang, “IT4.00008: Space Charge Effects on Short-Pulse Beam Dynamics in Vacuum Diodes”, 76th Annual Gaseous Electronics Conference (GEC) (October 9-13, 2023, Ann Arbor, MI, USA). [Poster]	Y	N
13	M. Rahman, and Peng Zhang, “IT4.00010: Space Charge Effects on Beam-Wave Interaction at the Output Gap of Vacuum Electron Tube”, 76th Annual Gaseous Electronics Conference (GEC) (October 9-13, 2023, Ann Arbor, MI, USA). [Poster]	Y	N
14	M. Faisal, and Peng Zhang, “IW5.00008: Reducing Starting Current of Smith-Purcell Radiation with a Two-Layer Grating Structure”, 76th Annual Gaseous Electronics Conference (GEC) (October 9-13, 2023, Ann Arbor, MI, USA). [Poster]	Y	N
15	L. Jin, Y. Zhou, and Peng Zhang, “IW5.00009: Beam density modulation during emission under RF and laser fields”, 76th Annual Gaseous Electronics Conference (GEC) (October 9-13, 2023, Ann Arbor, MI, USA). [Poster]	Y	N

Books

#	Citation	Acknowledged ONR Support Received? (Y/N)	Peer Reviewed? (Y/N)
1	J. Benford, J. A. Swegle, E. Schamiloglu, J. Stephens, and P. Zhang, High Power Microwaves, 4 edition. in the press: Taylor and Francis, 2025.	N	N

Book Chapter

#	Citation	Acknowledged ONR Support Received? (Y/N)	Peer Reviewed? (Y/N)
1	No information to report	N/A	N/A

Theses

#	Citation	Acknowledged ONR Support Received? (Y/N)	Peer Reviewed? (Y/N)
1	No information to report	N/A	N/A

Websites

#	Citation	Acknowledged ONR Support Received? (Y/N)	Peer Reviewed? (Y/N)
1	No information to report	N/A	N/A

Patents

#	Citation	Acknowledged ONR Support Received? (Y/N)	Peer Reviewed? (Y/N)
1	P. Zhang, L. Jin, and Y. Zhou, "Optically gated field emission cathodes", US Patent Provisional filed on 8/14/2023; converted to nonprovisional United States application on 8/9/2024.	Y	Y

Other Products:

#	Product Description	Acknowledged ONR Support Received? (Y/N)	Peer Reviewed? (Y/N)
1	No information to report	N/A	N/A

12. Point of Contact in U.S. Navy / Marine Corps

Navy Point(s) of Contacts			
Full Name	Organization	Email	Date of Last Contact
Kevin Jensen	NRL/UMD	Y	04/20/2024
Matt Franzi	Sandia	Y	08/01/2024
Brad Hoff	AFRL	N	10/01/2024
Allen Garner	Navy/Purdue	Y	09/01/2024
Zachary Drikas	NRL	Y	06/05/2024

ONR Early Career Grant (ECG)

Infrared Optics with Engineered Materials

Grant No. N00014-20-1-2297

Annual Report for Fiscal Year 2024

Period of Performance: October 1, 2023 to September 30, 2024

Prepared by:

Professor Mikhail Kats, Principal Investigator
University of Wisconsin-Madison
Engineering Hall, 1415 Engineering Drive, Room 3441, Madison, WI, USA - 53706
Tel: 608 890 3984
Email: mkats@wisc.edu



Kats Group



Acknowledgement/Disclaimer: This work was sponsored by the Office of Naval Research (ONR), under grant/contract number N00014-20-1-2297. The views and conclusions contained herein are those of the authors only and should not be interpreted as representing those of ONR, the U.S. Navy or the U.S. Government.

Section I: Project Summary

1. Overview of Project

Executive Summary:

The major goals of this project are to discover, engineer, and characterize both existing and emerging infrared (IR) optical materials to enable next-generation IR optics for emitting, manipulating, absorbing, and detecting IR radiation. During FY24, the project achieved key advances in understanding and harnessing colossal optical birefringence in inorganic crystal systems, in exploring VO₂-based metasurfaces for optical limiting and switching, and in refining measurement and metrology techniques critical for IR optical materials. The work included working with crystal-grower colleagues to analyze larger single crystals of BaTiS₃ and BaTiSe₃, conducting spectroscopic ellipsometry and polarization-resolved measurements to elucidate the origins of their extraordinary IR anisotropy, and performing ultrafast spectroscopy and other studies on defect-engineered VO₂ films. On the metrology side, important progress was made in temperature-dependent characterization of amorphous SiO₂, in particular so that it can be used as a reference material for temperature-dependent IR spectroscopy. A key result on electrically tunable metasurfaces for mid-infrared switching, limiting, and nonlinear isolation primarily obtained during the previous year was published during this reporting period in *Nature Photonics*.

Objective:

The proposal had three key sections (chapters). In Chapter 1, we proposed new approaches to modify materials properties, focusing on spatial control of infrared optical properties, such that they can be engineered into devices. In Chapter 2, we proposed the development of new and improved methods of materials metrology to better understand infrared optical materials and to better characterized engineered optical structures. In Chapter 3, we proposed new infrared optical and optoelectronic devices for polarization control and infrared photodetection, based on materials-engineering and characterization techniques (to be) developed in Chapters 1 and 2. Specifics goals included the development of new spectroscopic techniques for materials analysis, new types of flat and thin optical components for imaging and beam control, more-robust control over polarization of infrared light, new optical protective technologies, and new optical technology for thermoregulation using engineered thermal radiation.

Naval Relevance:

The ability to emit, manipulate, absorb, and detect IR light underpins Naval sensing and surveillance needs. Modern naval platforms rely on IR imaging and detection systems for threat identification, target acquisition, and situational awareness. At the same time, adversaries may attempt to disable or deceive IR sensors with high-power lasers. By discovering, engineering, and analyzing materials and structures that offer superior IR performance, and by developing devices that can protect sensitive detectors or extend sensor functionality, the Navy can maintain a technological edge. Thermal management, a perennial challenge in maritime environments, also stands to benefit from engineered IR emissivity and absorptivity control. Although the current work is basic research, it is directed at establishing fundamental principles and materials that can ultimately be translated into applied systems supporting Naval missions.

Introduction/Background:

Recent progress in structured materials and phase-change materials has opened new avenues for IR optical control. Traditional IR optics, which rely heavily on a limited set of bulk materials and conventional lens designs, as well as reflective optics, are often bulky and lack adaptability. The discovery of materials like BaTiS₃ and BaTiSe₃, with giant optical anisotropy in the IR, and the tunability of the phase transition of VO₂, provide new pathways to create compact, robust, and multifunctional IR optical elements. Earlier successes by our team demonstrated promising anisotropic properties and phase-change responses. Our approach in this project is to carry out an interdisciplinary, integrated program where we simultaneously investigate new spectroscopic techniques for materials characterization, new ways of modifying materials, and new devices, with the devices building on the materials innovations developed within the project.

2. Activities and Accomplishments

During FY24, the project made significant strides in multiple areas of infrared materials engineering.

We worked closely with collaborators at USC and WUSTL to achieve major advancements in understanding and expanding the scope of ABX₃ materials exhibiting giant optical anisotropy in the mid-infrared. This material class has shown great promise for infrared optical applications, and our work focused on three specific materials: BaTiS₃, BaTiSe₃, and Sr_{9/8}TiS₃. Through detailed experimental characterization and theoretical modeling, we unveiled the intricate physical mechanisms behind their record-breaking birefringence, exceeding previously known limits by a significant margin. In BaTiS₃, the first material in which we observed giant optical anisotropy previously, we identified picoscale atomic displacements of Ti atoms as a crucial contributor to the enhanced anisotropy. This discovery represents a fundamental advance in our understanding of the structure-property relationships in these materials. Beyond understanding the underlying physics, we also made progress towards practical applications. Recognizing the limitations of small sample sizes produced by chemical vapor transport, we worked with collaborators at USC who investigated flux growth techniques for BaTiS₃, successfully producing larger single crystals suitable for integration into more complex optical devices. Furthermore, our exploration extended to BaTiSe₃, a related selenide compound, which we found also exhibits substantial birefringence, broadening the library of available anisotropic materials for infrared optics.

Figure 1 shows polarization-resolved FTIR transmittance spectra from a BaTiSe₃ crystal. The very different spectral behavior for ordinary and extraordinary polarizations is a consequence of the extreme anisotropy in the material. Such anisotropy is of immediate interest for IR polarization-based sensing and optical components like waveplates that can be much thinner than those made with more-conventional anisotropic materials.

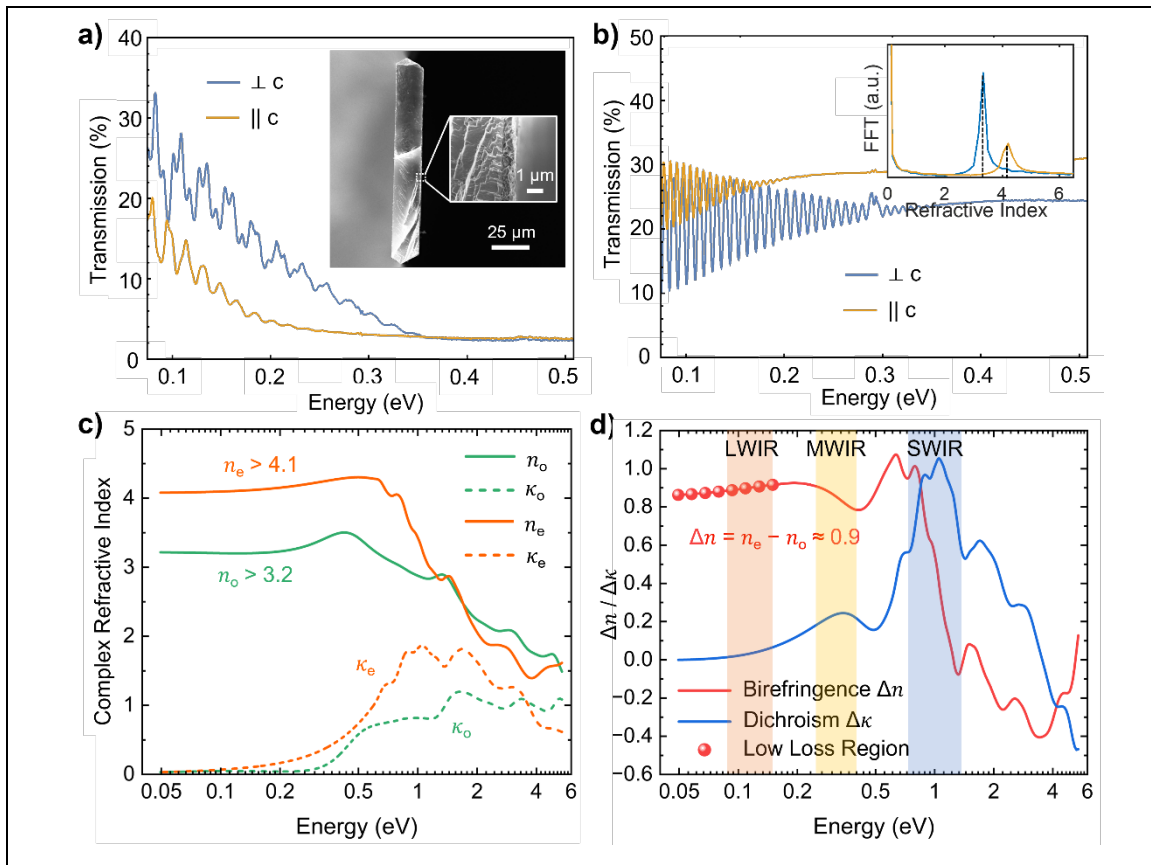
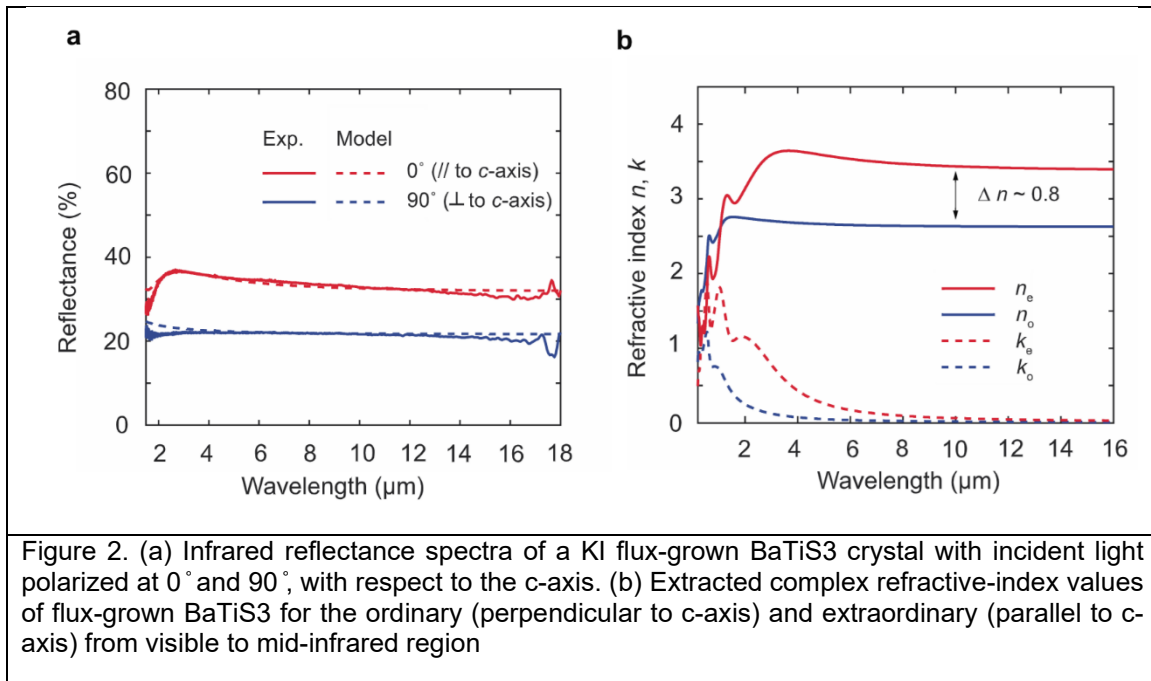
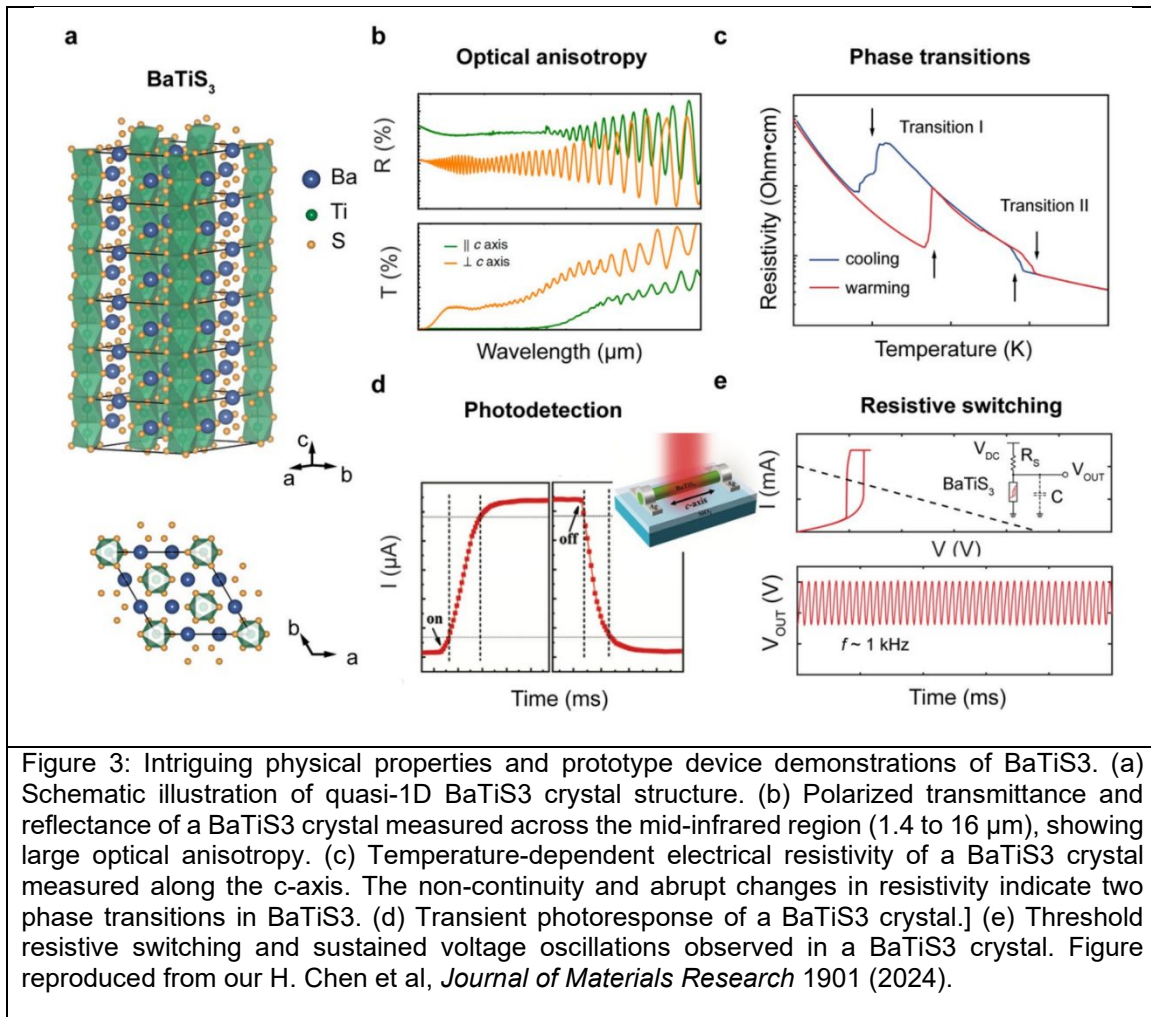


Figure 1. Optical anisotropy of BaTiSe₃. Polarization resolved FTIR (a) transmittance and (b) reflectance spectra show great MWIR to LWIR anisotropy between the ordinary (⊥ c) and the extraordinary (∥ c) polarization. The absorption energy of ordinary and extraordinary are observed at 0.21 eV and 0.31 eV, consistent energy as the weakening of Fabry-Perot fringes. (c) Optical properties obtained from combining FTIR and ellipsometry, both real (n) and imaginary (k) part of the ordinary and extraordinary linear polarization. (d) The large dichroism ($\Delta\kappa = \kappa_o - \kappa_e$) peak across SWIR leaves behind a giant birefringence ($\Delta n = n_e - n_o$) up to 0.9 across the MWIR to LWIR wavelengths.

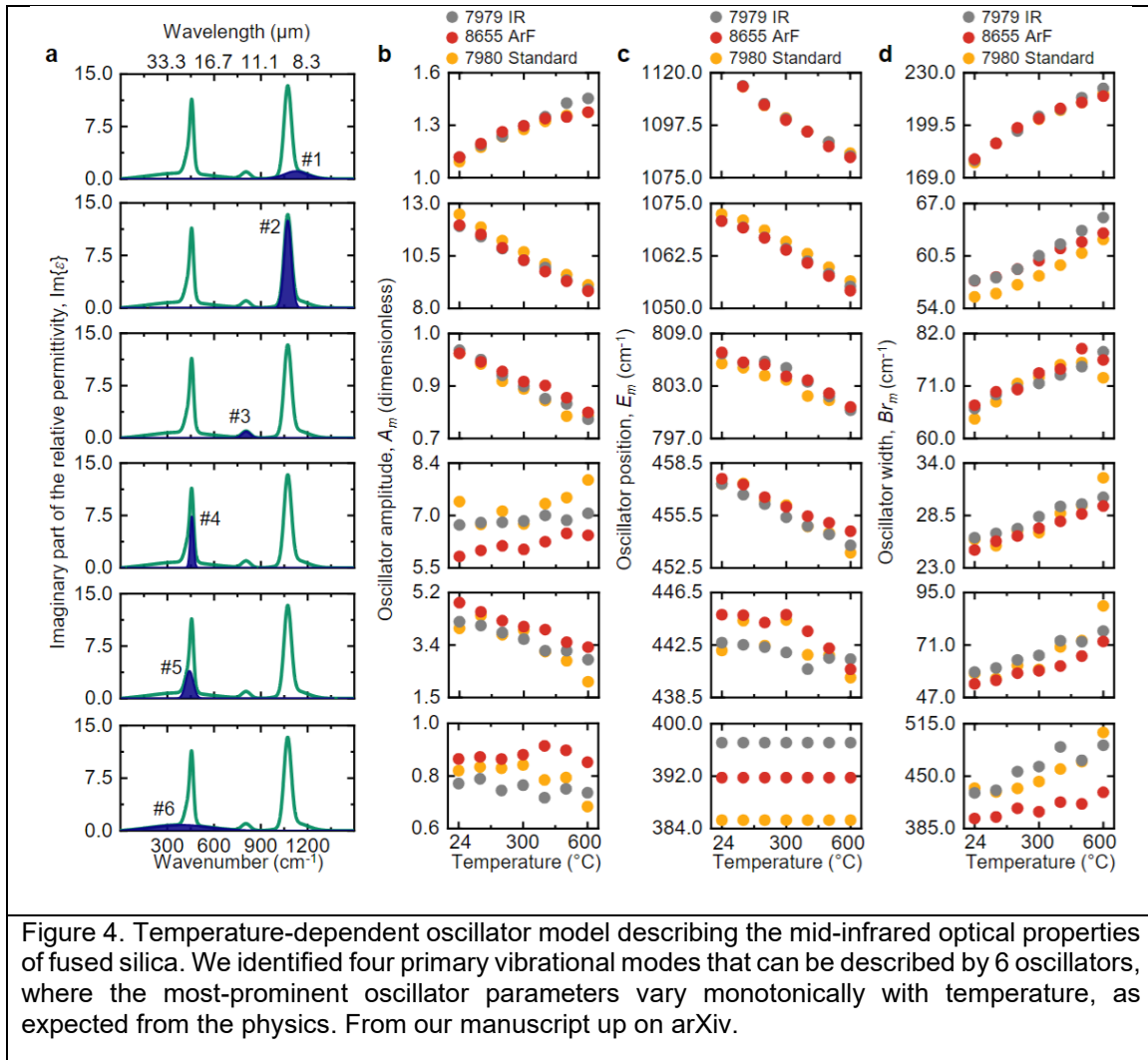
One important enabling result led by our USC collaborators was the development of flux-based crystal growth that enabled the production of larger BaTiS₃ single crystals on the millimeter scale. Previously, only sub-millimeter crystals were available, limiting the experiments and device demonstrations that were possible. We performed detailed optical characterization of these samples (Fig. 2), demonstrating similar birefringence to what we demonstrated in previous experiments on BaTiS₃ grown by vapor transport, which resulted in much smaller crystals. With larger crystals, it is now possible to explore integration into optical testbeds and assess compatibility with optical coatings or metastructures, which we have begun to design.



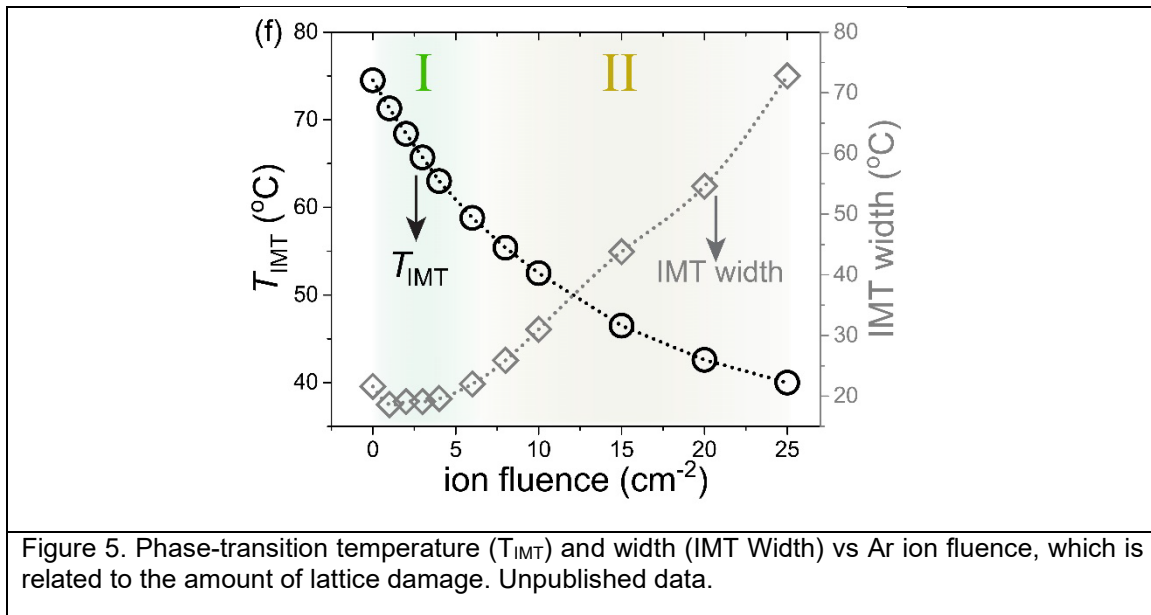
We are excited not only about the giant anisotropy in these materials, but for the possibility of optoelectronic devices. For example, our collaborators have explored both photodetection and the presence of phase transitions in these materials (Fig. 3).



In parallel, we worked on characterizing temperature-dependent infrared properties of amorphous SiO₂. A crucial aspect of accurate infrared measurements is the availability of reliable reference materials with well-characterized optical properties. Amorphous SiO₂ is commonly used as a reference material in the infrared, especially by our group as we have established some of the best thermal-emission spectroscopy measurements in the world. However, the temperature-dependent optical properties of SiO₂ are not well-established, which means we cannot use it as a reliable reference for high-temperature measurements. We addressed this gap by carefully measuring the temperature-dependent reflectance and transmittance of amorphous SiO₂ across a broad infrared spectral range, making sure that our fitted data was not overfit using a new approach where we look for the temperature evolution of fitting oscillator parameters that describe vibrational modes within the material (Fig. 4). The resulting dataset and the fitting methodology provide a valuable resource for calibrating infrared measurements and extracting accurate information from experimental data. The dataset has been shared with research groups working on hypersonic materials characterization and thermal emission measurements, demonstrating its broader impact. A preprint of this work is now up on arXiv, though we are making some changes before submitting it to a peer-reviewed journal.



The project also advanced defect-engineering in VO₂. By introducing controlled defects through ion bombardment, it became possible to systematically tune the metal-insulator phase transition temperature and widen or narrow the transition window (Fig. 5). Preliminary pump-probe spectroscopy—currently being refined to overcome technical issues and therefore not directly shown in this report—suggests that defects not only shift the equilibrium properties but also influence the ultrafast response. This tunability is directly relevant to IR optical limiters and switches, where one might want to design a device that responds sharply at a particular intensity or wavelength. While the completion of pump-probe experiments has been delayed, the partial data are already guiding future experiments and device design concepts.

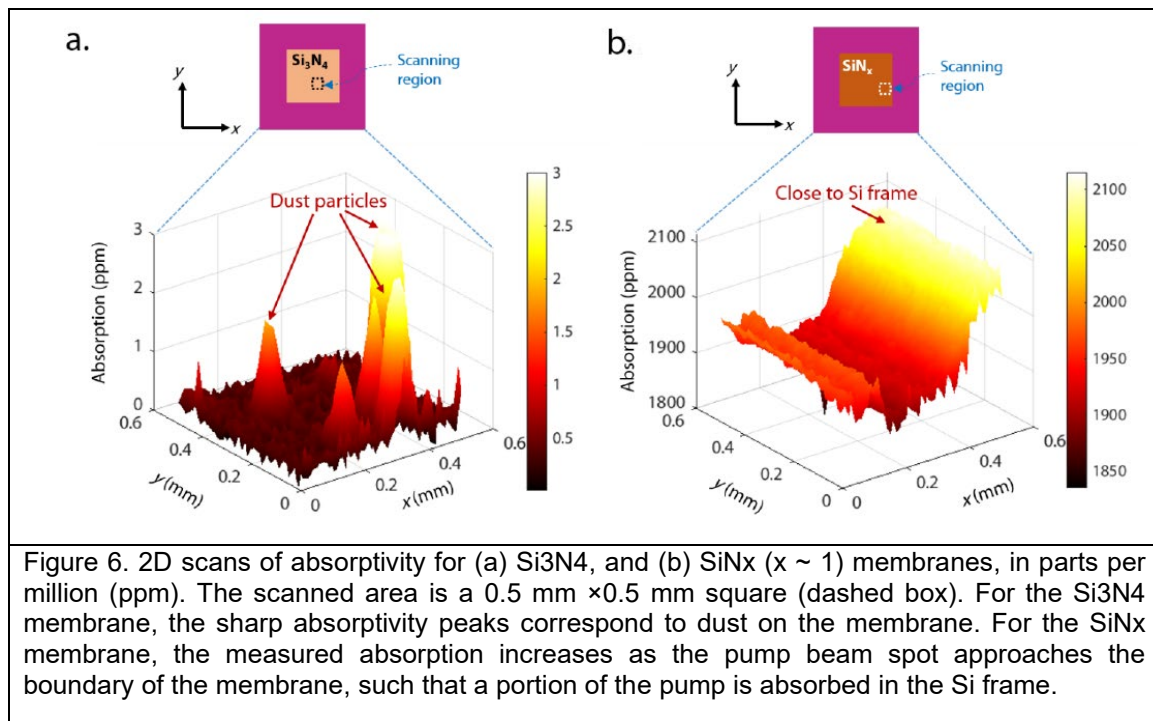


On the metrology front, our original plan to obtain a custom-built photothermal common-path interferometry (PCI) system via an ONR DURIP received this year was delayed and had to be adapted due to vendor-related issues, in particular the primary PCI system configuration is no longer available. Instead, we are now finalizing a purchase of an alternate system which we believe will be yet more powerful at performing wavelength-dependent measurements of absorption losses in low-loss materials. We are excited to investigate a number of infrared optical materials, in particular the ones described above, with this new PCI system. At the same time, we collaborated with researchers at the University of Minnesota to learn more about PCI, performing experiments that have recently been posted as preprint on arXiv, describing the optical losses of silicon nitride in the near infrared (Fig.6).

Finally, during this period, our manuscript describing electrically tunable metasurfaces for mid-infrared switching, limiting, and nonlinear isolation received has been published in *Nature Photonics*, and highlighted with a “News & Views” article in the same journal. The paper describes successful design, fabrication, and characterization of a multifunctional mid-infrared metasurface device. This device integrates a metasurface with a vanadium dioxide (VO₂) thin film, whose phase transition properties are leveraged to achieve dynamic control of infrared light. By applying electrical currents, we can modulate the state of the VO₂, switching it between its insulating and metallic phases. This switching behavior allows the device to function as a current-gated switch, a tunable optical limiter, and a nonlinear isolator. The calculated switching time scale, down to 10 microseconds, offers exciting possibilities for high-speed limiting. The nonlinear isolation functionality is particularly significant, demonstrating the breaking of reciprocity. This combination of functionalities in a single compact device represents a significant step towards advanced infrared optical systems.

Our dissemination efforts included preparing manuscripts for peer-reviewed journals and presenting at international conferences. Draft data sets for temperature-dependent SiO₂ IR properties and anisotropic ABX₃ materials have been circulated to collaborators, fostering

discussions that may lead to broader adoption of these results. Furthermore, we initiated discussions with the Air Force Research Laboratory (AFRL), visiting their Materials and Manufacturing Directorate (RX) and exploring possible technology transitions. These engagements ensure that the knowledge and capabilities developed under this program can influence the future of optical materials for defense applications.



3. Findings and Conclusions

We have identified the microscopic origin of giant birefringence in several ABX₃ materials contributes to a deeper understanding of anisotropic infrared physics, and suggesting that other layered chalcogenides or related compounds could be engineered to exhibit similarly extreme properties, both anisotropy and potential dynamic tunability via phase transitions, guiding future materials discovery. Notably, taking together both the work this year and in previous years, we have now identified at minimum two very different mechanisms by which ABX₃ chalcogenides acquire giant anisotropy, both of which were nearly impossible to predict ahead of time and had to be found experimentally. We have also continued to work with our collaborators at USC, now leading to BaTiS₃ crystals on the multi-millimeter scale. By offering fine control over polarization and absorption, these materials will be enabled the development of new types of IR components—potentially integrated into metasurface platforms—that enhance surveillance, targeting, and countermeasure capabilities.

On the metrology front, we have created a robust reference for the measurement of temperature-dependent IR properties by precisely measuring the temperature-dependent optical properties of

SiO₂ of different grades, enabling the use of such wafers as references for high-temperature measurements.

While the work on VO₂ defect engineering is ongoing, we are excited about the devices that will soon be presented, using defect engineering to modify the transition temperature of tunable optical metasurfaces after the initial fabrication is completed and the device is characterized.

The expected commissioning of the PCI system will address a key need in IR metrology: reliably detecting small absorption levels and spatial nonuniformities. This will facilitate quality control, device design optimization, and fundamental studies of how material quality and processing conditions influence IR performance.

In sum, these findings and conclusions address the project's objectives by strengthening the link between fundamental science of optical materials and the engineering of new types of high-performance IR optics for Naval applications.

4. Plans and Upcoming Events

The next steps will focus on completing pending pump-probe spectroscopy experiments on defect-engineered VO₂ to fully characterize the ultrafast dynamics and confirm the tunability of its transition. With PCI assembly well underway, we plan to bring the system online and conduct a series of absorption measurements on ABX₃ crystals, VO₂ films, and reference materials. These measurements will also involve micropatterned heaters to allow localized thermal stimulation and dynamic studies of temperature-dependent IR properties. We are also continuing to work on our design of a VO₂-based IR imager.

Moving forward, integration studies will seek to incorporate ABX₃ crystals into at least one prototype metasurface architecture. We are working with partners in South Korea to develop anti-reflection coatings and other thin-film layers compatible with ABX₃ materials.

To broaden impact, we will continue discussions with AFRL and potentially explore other DoD laboratories, looking for opportunities where our materials and methods can address identified capability gaps. One planned milestone is a possible demonstration of a wave plate based on anisotropic crystals with the aforementioned anti-reflection coatings.

5. Transitions and Impacts

Recently, our publications were noticed by several scientists and group leaders at the Air Force Research Lab (AFRL) Materials and Manufacturing Directorate (RX). They reached out to us and expressed significant interest in following up on this research via collaborations and other tech transfer efforts. In particular, the AFRL researchers are interested in enabling tunable optical anisotropy, which may be possible with this group of ABX₃ materials. AFRL invited me to visit them, which I accepted. My collaborator Jayakanth Ravichandran (USC) and traveled to Dayton and spent two days discussing with their scientists and engineers in the RX and RY (Sensors) directorates. This was on Oct 2-3, 2024.

6. Recommendations for Future Work:

In this project, we have made exciting progress in the discovery and understanding of ABX₃ chalcogenide materials with giant infrared anisotropy. The physical underpinnings of the giant

anisotropy are unique and varied, demonstrating that the ABX₃ chalcogenide family of materials holds many mysteries and opportunities. In particular, recent work suggests that some of these materials may have significant phase transitions, enabling new approaches to tunable infrared optics.

I would like to recommend that a major multi-PI effort be formed to investigate this family of optical materials and the imaging, polarization, detection, and switching devices that can be enabled by these new materials with exotic physics. In particular, a MURI-type effort would be highly appropriate.

7. Personnel

Principal Investigator			
Full Name	Approximate Level of Effort – LOE - (Hours This FY)	Country of Residence	National Academy Member? (Y/N)
Mikhail Kats	None	USA	N

8. Collaborations

Full Name	Organization	Collaboration Summary
Shriram Ramanathan	Rutgers	Research collaboration (unfunded) on phase-transition materials. Notably, Ramanathan and I (+ Yu/Columbia) started a non-overlapping but somewhat related project funded by DARPA on tunable visible nickelates
Jayakanth Ravichandran	USC	Research collaboration (unfunded) on highly anisotropic perovskites. Notably, we were also co-PIs on a proposal to ONR to develop MWIR and LWIR detectors, which unfortunately was not selected for an award
Rohan Mishra	Washington University	Research collaboration (unfunded) on theory to understand anisotropy in highly anisotropic perovskites
Carsten Ronning	University of Jena	Research collaboration (unfunded) on use of ion beams to engineer materials
Jun Xiao	UW-Madison	Research collaboration (unfunded) on ultrafast measurements of phase-transition materials
Joseph Talghader	U. Minnesota	Talghader operates a PCI system that we were learning on, before building our own PCI system at UW-Madison. We are writing a joint manuscript about PCI of SiN membranes.

Michelle Povinelli	USC	Had some initial discussion on infrared measurements of hypersonic materials using our techniques
--------------------	-----	---

9. Students

Doctoral Student(s)			
Full Name	University	Graduated?	Graduation Year
Jonathan King	UW-Madison	Y	2024
Hongyan Mei	UW-Madison	Y	2024
Shenwei Yin	UW-Madison	N	2024

10. Technology Transfer

A patent filed originally in 2020 was issued: Y. Xiao, C. Wan, J. Salman, M. A. Kats, "Planck spectrometer", Patent application filed Dec 2020, published 2022. Issued Jan 2024. US Patent 11,879,783 B2.

Recently, our publications were noticed by several scientists and group leaders at the Air Force Research Lab (AFRL) Materials and Manufacturing Directorate (RX). They reached out to us and expressed significant interest in following up on this research via collaborations and other tech transfer efforts. In particular, the AFRL researchers are interested in enabling tunable optical anisotropy, which may be possible with this group of ABX3 materials. AFRL invited me to visit them, which I accepted. My collaborator Jayakanth Ravichandran (USC) and I traveled to Dayton and spent two days discussing with their scientists and engineers in the RX and RY (Sensors) directorates. This was on Oct 2-3, 2024.

11. Products, Publications, Patents, License Agreements, etc.

Publications resulting from this project for the reporting period:

Archival Publications

#	Citation	Acknowledged ONR Support Received? (Y/N)	Peer Reviewed? (Y/N)
1	J. King, C. Wan, T. J. Park, S. Deshpande, Z. Zhang, S. Ramanathan, M. A. Kats, "Electrically tunable VO ₂ -metal metasurface for mid-infrared switching, limiting, and nonlinear isolation", <i>Nature Photonics</i> 18, 74 (2024)	Y	Y
2	B. Zhao, G. Ren, H. Mei, V. C. Wu, S. Singh, G.-Y. Jung, H. Chen, R. Giovine, S. Niu, A. S. Thind, J. Salman, N. S. Settineri, B. C. Chakoumakos, M. E. Manley, R. P. Hermann, A. R. Lupini, M. Chi, J. A. Hachtel, A. Simonov, S. J. Teat, R. J. Clément, M. A. Kats, J. Ravichandran, R. Mishra, "Giant modulation	Y	Y

	of refractive index from picoscale atomic displacements," <i>Advanced Materials</i> 2311559 (2024)		
3	B. Zhao, H. Mei, Z. Du, S. Singh, T. Chang, J. Li, N. S. Settineri, S. J. Teat, Y.-S. Chen, S. B. Cronin, M. A. Kats, and J. Ravichandran, "Infrared optical anisotropy in quasi-1D hexagonal chalcogenide BaTiSe ₃ ," <i>Advanced Optical Materials</i> 12, 2400327 (2024)	Y	Y
4	H. Chen, S. Singh, H. Mei, G. Ren, B. Zhao, M. Surendran, Y.-T. Wang, R. Mishra, M. A. Kats, J. Ravichandran, "Molten flux growth of single crystals of quasi-1D hexagonal chalcogenide BaTiS ₃ ", <i>Journal of Materials Research</i> 39, 1901 (2024)	Y	Y
5	S. Yin, J.-W. Cho, D. Feng, H. Mei, T. Kumar, C. Wan, Y. Jin, M. Kim, M. A. Kats, "Preventing overfitting in infrared ellipsometry using temperature dependence: fused silica as a case study," arXiv:2409.05323 (2024)	Y	N

Conference Papers

#	Citation	Acknowledged ONR Support Received? (Y/N)	Peer Reviewed? (Y/N)
1	J. L. King, Y. Xiao, M. A. Kats, "Planck-enhanced filter spectroscopy: Using temperature-dependent thermal radiation to improve the spectral resolution of filter-based spectroscopy systems", SPIE Optics + Photonics, San Diego (2024)	Y	N
2	S. Yin, D. Feng, J.-W. Cho, T. Kumar, C. Wan, H. Mei, M. A. Kats, "Using the temperature degree of freedom to prevent overfitting in infrared spectroscopic ellipsometry", <i>Frontiers in Optics</i> , Denver (2024)	Y	N
3	J. L. King, J.-W. Cho, D. Quach, M. Hafermann, K. Paz, H. Mei, S. Yin, T. Kumar, J. Andrade, C. Hessel, C. Ronning, D. Woolf, M. A. Kats, "Impact of lattice strain on vanadium dioxide transition temperature, induced via defects and doping", <i>Novel Optical Materials and Applications</i> , Quebec (2024)	Y	N
4	J.-W. Cho, J. L. King, D. Quach, M. Hafermann, K. Paz, H. Mei, S. Yin, T. Kumar, J. Andrade, C. Hessel, C. Ronning, D. Woolf, M. A. Kats, "Engineering of vanadium dioxide for reconfigurable optics by combining metal doping and defect engineering", <i>Optica Advanced Photonics Congress</i> , Quebec (2024)	Y	N

5	H. Mei, G. Ren, B. Zhao, J. Salman, G.-Y. Jung, H. Chen, A. Thind, S. Singh, N. Settineri, S. Teat, B. Chakoumakos, J. Ravichandran, R. Mishra, M. Kats, "Infrared optics with highly anisotropic Materials", Materials Research Society Fall Meeting, Boston (2023)	Y	N
6	S. Yin, D. Feng, J.-W Cho, T. Kumar, C. Wan, H. Mei, M. A. Kats, "Preventing overfitting in infrared ellipsometry using temperature dependence: fused silica as a case study", Materials Research Society Fall Meeting, Boston (2023)	Y	N
7	T. Kumar, D. Feng, S. Yin, P. Lin, M. Mah, M. Fortman, G. R. Jaffe, C. Wan, C. Fang, R. Warzoha, V. W. Brar, J. J. Talghader, M. A. Kats, "Optical Loss Measurements of Silicon-Nitride Membranes using Photothermal Common-Path Interferometry", Materials Research Society Fall Meeting, Boston (2023)	Y	N

Books

No information to report.

Book Chapter

No information to report.

Theses

#	Citation	Acknowledged ONR Support Received? (Y/N)	Peer Reviewed? (Y/N)
1	Mid-infrared spectroscopy, camouflage, and sensor protection	Y	N
2	Reinventing infrared optical systems with advanced materials and engineering methods	Y	N

Websites

No information to report.

Patents

#	Citation	Acknowledged ONR Support Received? (Y/N)	Peer Reviewed? (Y/N)
1	Y. Xiao, C. Wan, J. Salman, M. A. Kats, "Planck spectrometer", Patent application filed Dec 2020, published 2022. Issued Jan 2024. US Patent 11,879,783 B2.	Y	N

Other Products:

No information to report.

12. Point of Contact in U.S. Navy / Marine Corps

None at this time

ONR Industry Contract

Implementation of tunable dielectric and multiferroic materials for high power microwave applications

Grant No. N00014-22-1-2694

Annual Report for Fiscal Year 2024

Period of Performance: October 1, 2023 to January 1, 2024

Prepared by:

Dr. Somnath Sengupta, Principal Investigator

Powerhouse Consulting Group

Tel: (443) 820-7798

Email: somnath@powerhouseconsultinggroup.com



Powerhouse Consulting Group

Better Lives through Science and Technology



This work was sponsored by the Office of Naval Research (ONR), under grant/contract number N00014-22-1-2694. The views and conclusions contained herein are those of the authors only and should not be interpreted as representing those of ONR, the U.S. Navy or the U.S. Government.

Section I: Project Summary

1. Overview of Project

The purpose of this report is to provide an overall summary of the goals, objectives, and achievements of the three subsequent grants and then the overall program technical details for GRANT# N00014-22-1-2694. It is not meant to be a compilation of the monthly reports, rather a broad view of the implementation related successes and issues over the past four years of a class of low loss tunable dielectric materials for high power RF systems. In August 2019, Powerhouse was awarded the first of three grants towards a systematic approach of assessment, scalability, and then implementation of low loss, electronically tunable high permittivity dielectric material for directed energy applications. The first grant (N00014-19-1-2599) focused on the **ASSESSMENT** of this family of materials for directed energy applications while the subsequent second grant in 2021 (N00014-21-1-2019) was aimed towards examining the **SCALABILITY** of the material family in various form factors. Each phase met the deliverables and technical milestones to justify the next phase that led to this current grant in 2022 (N00014-22-1-2694). for **IMPLEMENTATION** of the material as a simple yet effective component for HPM generation. *The success of this trifecta of grants has brought us to the point of decision for a laboratory demonstration prototype.*

The development of a time-domain, agile capability will enable a waveform-agile source that is scalable in an array, or that can be distributed. This is so because the ability to fine-tune delays allows the creation of different waveforms on target due to pre-designed constructive and destructive interference.

2. Activities and Accomplishments

1. Synthesis of tunable dielectric composites for coaxial delay line measurements; *A 40% change in delay was observed during the experiment when we went from 0V to 2000V.*
2. Synthesis of BST based magnetoelectric ceramic formulations and measurement of magnetoelectric (ME) and converse magnetoelectric coefficients (cME). We have demonstrated that even in its paraelectric phase, the low loss tunable dielectric exhibit magnetoelectric coupling with hexagonal ferrites like Barium Ferrite. The small coupling coefficient of our composites can be optimized but it goes to show that Powerhouse can fabricate, just like its family of low loss tunable dielectrics, a wide range of coupled ME composites too.
3. Tunable delay was also observed in the magnetoelectric compounds

Sample ID	Delay	Length of sample	Delay per unit length
copper 50 ohm line; 6 mm diameter	0.27 ns	2.90 inches	~0.09 ns per inch
BST/60 wt% OxIII	0.36 ns	1.49 inches	~0.24 ns per inch
50wt% of BST/60 wt% OxIII and 50 wt% of Ferrite	0.40	0.93 inches	~0.43 ns per inch

3. Findings and Conclusions

1. Tunable delay line was demonstrated. Since these materials can handle MWs of pulsed power; it suffices to say that tunable delay lines designed and integrated into DE systems will provide the agility for scanning antennas and waveform generators.
2. As for the magnetoelectric materials, the coupling of the electric and magnetic phases open up the possibility of designs of new structures of nonlinear transmission lines.

4. Plans and Upcoming Events

The project has concluded. All activities between Jan 31, 2024 and June 2024 can be reported if there is a follow-on request for annual report. Otherwise, all activities of the entire grant have been summarized in our final report.

5. Transitions and Impacts

Since the project has concluded and no follow-on work exists, it is not possible to respond to this section.

6. Recommendations for Future Work:

Since the high-power tunable ceramics are the specialty of Powerhouse and we will not be performing any further phases, it is not possible to recommend future work.

7. Personnel

Principal Investigator			
Full Name	Approximate Level of Effort – LOE - (Hours This FY)	Country of Residence	National Academy Member? (Y/N)
Somnath Sengupta	190	USA	N
Performer Business Contact(s)			
Full Name	Role	Country of Residence	
Somnath Sengupta	Business Contact	USA	N

8. Collaborations

Full Name	Organization	Collaboration Summary
Zachary Drikas	High Power Microwave Section, Naval Research Laboratory, Code 5745	The HPM team (Dr. Drikas) has been the cornerstone of our work with regards to HPM applications; locating adequate measurement facilities within NRL, and discussing future applications to steer the work towards meaningful data collection.
Matthew Laskoski	Advanced Materials Section, Naval Research Laboratory, Code 6127	The Code 6127 team has been a great collaborator during the fledgling days of this program and through the COVID-19 ordeal. Under a CRADA, the team has provided help

		with sintering, X-Ray Diffraction (XRD), and other analysis techniques. The data for the sintering steps, density measurements, and XRD were obtained in Dr. Laskoski's laboratory. We are currently exploring the opportunity of designing and fabricating extremely high epsilon materials for conformal antenna applications.
Robert Sternowski	Softronics, Ltd	Softronics is a radio manufacturer. They have extensive experience in the measurements of properties like intermodulation distortion and high bias field performances. All IMD3 data were collected in collaboration with Softronics. They have also provided a third-party validation of the material.

9. Students

Not Applicable

10. Technology Transfer

None has occurred

11. Products, Publications, Patents, License Agreements, etc.

Not Applicable

12. Point of Contact in U.S. Navy / Marine Corps

Zachary Drikas, NRL Code 5745; Last day of contact for this part of the work is January 2024.

ONR SBIR/STTR contracts

Contract Number: N68335-24-C-0493, SBIR Phase I, Topic Number: N241-062
Project Title: Low Profile, Foldable, High Power Microwave Antenna
Period of Performance: 15 July 2024 to 15 Jan 2025
Principle Investigator: Michael Kranz, 256-261-1260, mike.kranz@engeniushmicro.com
Organization: EngeniusMicro, LLC.

EngeniusMicro is developing reflectarray technology to realize compact and foldable antennas for High-Power Microwave systems. Reflectarrays are a promising approach to the problem of antenna form factor and weight reduction. These phased array structures provide much of the performance of traditional dish antennas, but in a planar form factor that can be easily fabricated, mounted, stacked, and/or folded. Reflectarrays can also be electronically or mechanically reconfigured, providing the potential for electronic beam steering and dynamic beam adjustment.

The effort has investigated multiple reflectarray unit cells for systems based on both linear and circular polarization. In particular, the investigation has demonstrated the application of three-dimensional reflectarray elements in the reduction of field enhancement, leading to higher power handling of reflectarray systems. The effort also demonstrated methods of fabricating, through both traditional methods and additive manufacturing techniques, arrays of 3D elements in addition to miniaturized actuators for rotating those elements to reconfigure the array. The effort demonstrated a reflectarray feed arrangement that yields antenna compactness, as well as multiple folding mechanisms that yield small stowable configurations that can be easily packaged for transport and storage, and then easily deployed in the field.

Contract Number: N68335-24-C-0496, SBIR Phase I, Topic Number: N241-062
Project Title: Collapsible Radiating Antenna For Trivial Easy Deployment (CRAFTED)
Period of Performance: 15 July 2024 to 15 Jan 2025
Principle Investigator: Johana Yan Zorn, johana@maxentric.com
Organization: MaXentric Technologies, LLC

The Navy is seeking innovative concepts for high power microwave antenna with foldable reduced footprint for stowaway and easy deployment. In response, MaXentric proposes the *Collapsible Radiating Antenna For Trivial Easy Deployment (CRAFTED)* system. The *CRAFTED* solution will make use of cleverly designed rigid panels for a wideband antenna that can be easily collapsible into a small form factor. The structure will be lightweight, yet it will be able to endure wind loading, vibrations, and physical shocks typical to a shipboard application. The low stowage size and weight along with ease of deployment will greatly improve the utility of HPMS in shipboard applications and give the United States a greater edge against its adversaries.

The project successfully completed the proof-of-concept design phase, achieving several critical milestones. The high-level design for the antenna, including materials, skin, and frame configurations, was finalized to meet performance and structural requirements. A thorough tradespace analysis determined the optimal antenna parameters, ensuring an efficient and robust design. The mode converter and feed network were carefully designed to support the system's operational needs. Comprehensive power-handling analyses were conducted to ensure the design could withstand operational demands. Collaboration with vendors established feasible fabrication techniques for the antenna's construction. Additionally, detailed mechanical analyses confirmed the structural integrity of the design, validating its readiness for subsequent development phases.

Contract Number: N68335-24-C-0495, SBIR Phase I, Topic Number N241-062
Project Title: Innovative Low Profile, Foldable, High Power Microwave Antenna
Period of Performance: 15 July 2024 to 15 Jan 2025
Principle Investigator: Andrew Foley, afoley@nanohmics.com
Organization: Nanohmics Inc.

High-power microwaves (HPM) systems offer a leverage point against marine, ground, and air platforms by directly targeting electronics systems with precision strike capability. System size and precision (i.e. directionality and steerability) in most cases compete in direct tradeoffs. However, a stowable system might be broken down and stored when not in use to provide a minimal profile for marine vessels or ground vehicles. To meet this interest, Nanohmics is developing a stowable metasurface lens solution for improving antenna gain in HPM antenna systems. During the Phase I, Nanohmics demonstrated a sub-module hardware of a system that may be scaled to achieve a precisely focused beam with a compact form factor. These antennas are of immediate interest for the DoD's directed energy development endeavors. Commercial and civilian applications include wireless power transmission, WLAN, 5G/6G communication, and mine clearing.

Contract Number: N68335-24-C-04, SBIR Phase I, Topic Number: N241-062
Project Title: Deployable High-Power Microwave Reflectarray
Period of Performance: 15 July 2024 to 15 Jan 2025
Principle Investigator: Michael Geiler, mgeiler@psicorp.com
Organization: Physical Sciences Inc.

Physical Sciences Inc. (PSI) proposes to develop a deployable Element Steering Reflect-Array (ESRA) antenna for high power microwave applications. The HPM antenna is based on a rotational phase shift element and is capable of +/-45 degrees of beam steering at speeds of 360 degrees per second, ten times faster than a solid parabolic or dish reflector with equivalent aperture size. The system is lightweight and collapsible for stowage and transportation, as well to help maximize usability of available surfaces on the platform. ESRA is designed to operate at levels of 100 MW or higher with an aperture of 10 m² and gain of more than 40dBi making it an effective tool in naval counter UAV/USV operations.

Contract Number: N68335-24-C-0407, STTR Phase I, Topic Number: N24A-T024
Project Title: Low-Void Density Additive Ferroic Composites
Period of Performance: 15 July 2024 to 15 Jan 2025
Principle Investigator: Mohammad Abdul-Moqueet, mabdulmoqueet@nanohmics.com
Organization: Nanohmics Inc.

High-power microwave (HPM) systems offer a leverage point against marine, ground, and air platforms by directly targeting electronics systems with precision strike capability and minimizing collateral damage. HPMs are ideal for neutralizing threats from remote operated drones, which rely on a continuous data uplink from a comms system for operational instructions. Additional HPM applications include disabling electronic infrastructure, vehicle stopping, mine clearing, radar countermeasures, intercepting missiles, and, if the technology matures sufficiently, long-range power transfer from a satellite network to long-term/open-ocean missions. This is a particularly challenging application space due to the reduced SWaP, non-planar topography, and often extreme

operational temperature requirements for these onboard systems. Currently, these ceramic and ferrite materials must be machined from bulk resulting in expensive prototyping and limitations to design geometries due to material brittleness. Leveraging new developments in additive manufacturing and 3D printing that enable rapid testing and fabrication of RF components could produce a commercially viable platform for incorporating ferroelectric and/or ferromagnetic materials in challenging environments and form factors. Nanohmics in collaboration with university partners as experience developing nanopowders. The team has extensive experience preparing feed material and designing and fabricating RF components. By manufacturing the materials in-house, the team can quickly formulate nanopowders, paints, and inks for application by dry brushing, ink-jet printing, screen printing, and airbrushing. The team is additionally in the process of expanding in-house capabilities of electrospinning nanofibers and producing embedded PLA filaments of listed materials.

Contract Number: N68335-24-C-0408, STTR Phase I, Topic Number: N24A-T024

Project Title: Additive Manufacturing of Multi-functional Ferroic Composites

Period of Performance: 15 July 2024 to 15 Jan 2025

Principle Investigator: Thomas Allen, tallen@nanovox.com

Organization: NanoVox LLC

NanoVox is advancing high-voltage composite manufacturing through additive techniques that integrate ferroelectric and ferromagnetic nanomaterials into engineered polymer matrices. Using fluidic direct-print methods, we fabricate complex, spatially graded structures with tailored electromagnetic (EM) properties optimized for high-power microwave (HPM) and nonlinear transmission line (NLTL) applications. Our multi-material, multi-physics additive manufacturing (AM) platform enables the co-fabrication of functional devices by integrating dielectrics, magnetics, conductors, and structural polymers into a single digitally controlled process. Combining high-resolution inkjet, direct-write, and photonic-curing technologies, we achieve precise spatial control of electrical, magnetic, thermal, and mechanical properties at the voxel level. Composites feature high-density inclusions such as barium titanate (BTO) and nickel zinc ferrite (NZFO), chemically modified for uniform dispersion, robust interfacial adhesion, and controlled nanostructure.



Additively manufactured high-breakdown-voltage flange designed for high-power microwave (HPM) applications, fabricated using nanocomposite materials with enhanced dielectric strength and dimensional precision.

Engineered interfaces ensure uniform field distribution, suppress charge migration, and minimize defects—yielding dielectric breakdown strengths exceeding those of conventional ceramics, along with tunable permittivity, broadband permeability, and excellent mechanical performance. Through nanoscale interfacial engineering and radial grading of permittivity and permeability, we enhance

impedance matching, field uniformity, and GHz-frequency performance. Our inkjet-printed Rogowski capacitors and coaxial NLTLs demonstrate >90% of bulk material properties with sub-wavelength accuracy and scalable throughput. Together, these capabilities enable scalable, high performance manufacturing for defense and commercial systems requiring compact, high-voltage, frequency-agile components—including HPM devices, NLTLs, antennas, capacitors, and wavefront shaping elements.

Contract Number: N68335-24-C-0406, STTR Phase I, Topic Number: N24A-T024

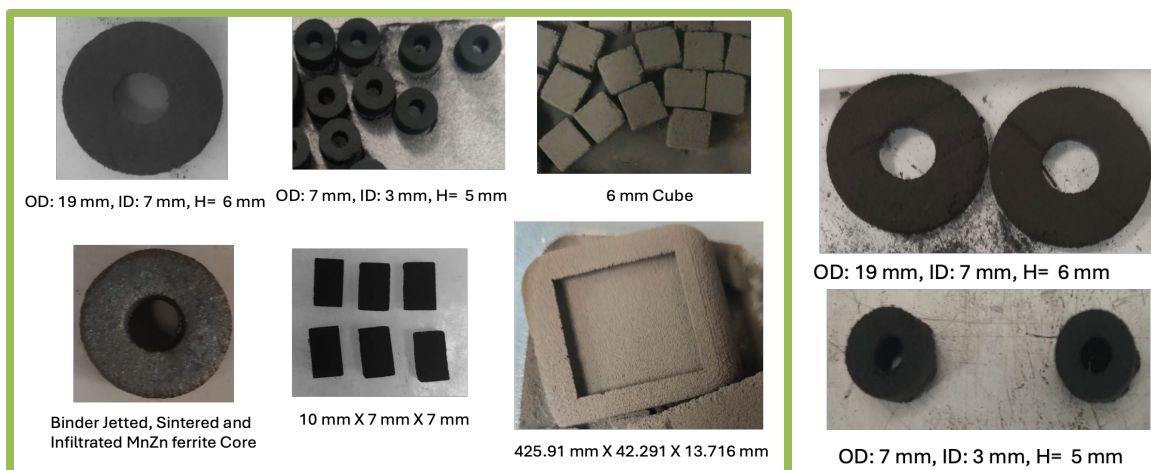
Project Title: Jet based Additive Manufacturing of Ni-Zn Ferrite Composites Enabling High Power Microwave (HPM) Directed Energy Weapons (DEW)

Period of Performance: 15 July 2024 to 15 Jan 2025

Principle Investigator: Eric Hepburn, eric.hepburn@hepburnandsons.com

Organization: Hepburn and Sons LLC

Hepburn and Sons LLC has partnered with the University of Pittsburgh to provide the US Navy with additively manufactured functional ceramic materials, capable of supporting high power microwaves, for use in directed energy weapons and pulse circuits. The primary objectives of this effort are to print functional prototypes, refine the printing and characterization process, and use the learnings and evaluation to generate information and design tools for the US Navy and the broader community. In the Phase I Base Period, the team has validated the capabilities of the printing concept, to realize large scale elements with using existing well-established printing procedures for well characterized, commercially available powder feedstock. This accelerates learning and prepares for first of its kind, high frequency capable ferromagnetic and ferroelectric material prints. Through these initial feasibility studies, the team has achieved i.) candidate powder feedstock identification, selection, and characterization, ii.) initial ceramic feasibility printing, iii.) characterization of printed parts with further refinement of print and powder parameters to scale to the Navy's target geometries, and iv.) validated that the target geometries provided by the US Navy could be successfully printed. Phase II efforts will build on these initial successes to translate manufacturable and scalable processing to relevant high frequency functional ceramic systems of greatest interest to the Navy. Examples of program successes are shown below.



Contract Number: N68335-24-C-0355, STTR Phase I, Topic Number: N24A-T024
Project Title: Digital Design and Additive Manufacturing Strategy for Ferroelectric-Polymer Composites
Period of Performance: 15 July 2024 to 15 Jan 2025
Principle Investigator: Jacob Zorn, PhD., jacob.zorn@corvidtec.com
Organization: Corvid Technologies

Corvid Technologies, along with our research partners, has worked to develop a digital design and additive manufacturing pipeline toward the production of novel high-performance electrical components. Utilizing computational techniques, in particular the Phase-Field Method (PFM) and Bi-Directional Evolution Structural Optimization (BESO), a variety of composite architectures were generated and their permittivity, conductivity (thermal and electrical), and elastic properties were computed. From these properties, the team was able to derive a preliminary figure of merit for the electrical breakdown strength of the resulting fully-connected and periodic architectures. Further, in collaboration with our research partners, the team has begun the procedure of optimizing various stereolithography (SLA) additive manufacturing process parameters, in particular the rheology of the necessary ferroelectric-polymer slurry necessary for SLA production. Future work within this realm will consist of printing of the ferroelectric ceramic architectures followed by appropriate polymer infiltration and the necessary testing to mature this combined computational-digital-manufacturing pipeline.

Contract Number: N6833524C0404, STTR Phase I, Topic Number: N24A-T024
Project Title: High Impedance Ferro-materials for use in Additive Manufacturing (HiFAM)
Period of Performance: 15 July 2024 to 15 Jan 2025
Principle Investigator: Giuseppe Brunello, PhD, gbrunello@upt-usa.com and Subrecipient Principal Investigator: Dr. Zachary D. Harris, zdh13@pitt.edu
Organization: United Protective Technologies, LLC and STTR Partner: University of Pittsburgh

High Impedance Ferromagnetic Materials for Additive Manufacturing (HiFAM) is currently in Phase I of an STTR effort. The HiFAM project aims to create a novel material with electrical permeability independent of its electrical conductivity and suitable for additive manufacturing. This is done by functionalizing a chosen feedstock material. During the project, the feedstock's electrical resistivity was increased over fifteen orders of magnitude, demonstrating that customized electromagnetic materials can be transformed into electrically resistive materials. This enables novel materials for high Q-factor inductors or high-frequency transformers, which are critical components for more efficient and sensitive RF communication. The HiFAM process also imparts significant chemical and mechanical resistance to the feedstock: a material sample processed with HiFAM has successfully withstood 36 hours in a salt-fog chamber.

The remaining challenges include densifying the feedstock of an additively manufactured part without affecting material properties. Alternative processing methods and composite matrix materials are being investigated to improve processability. These investigations will be the focus of Phase II of the project.

Contract Number: N68335-22-C-0642, SBIR Phase II
Project Title: Next-Gen Solid-State Power Module for High Power Microwave Drivers
Period of Performance: 29 Aug 2022 to 22 July 2026
Principle Investigator: Jacob Young, 719-302-3117 x8638, jyoung@sara.com
Organization: Scientific Applications & Research Assoc., Inc.

SARA is actively developing a next-generation solid-state modulator designed for driving high-power microwave (HPM) sources, addressing many of the limitations associated with traditional spark gap switched pulse generators. The chosen architecture for the modulator is a linear transformer driver (LTD), which offers several key advantages, including ultrafast rise times, long operational lifetimes exceeding one million shots, high repetition rates ranging from tens to hundreds of kHz, and sub-nanosecond jitter. The primary enabling technology is the optimization of solid-state device characteristics and packaging techniques tailored toward pulsed power applications that can result in smaller lighter and more efficient systems than can currently be achieved with commercially available devices. The system is ultimately expected to generate pulses on the order of 100 kV, with a rise time under 10 ns, and peak power reaching 200 MW. This effort aims to push the boundaries of modulator switching speed and timing precision, targeting jitter levels of less than 100 ps to enable phased array operation.

To date, the project has developed a custom gate drive technology capable of achieving current rise rates exceeding 30 kA/ μ s when paired with a single 6.5 kV SiC MOSFET. This technology has been successfully integrated into a sub-scale LTD prototype, which has demonstrated the ability to switch up to 2 kA, effectively emulating full-load conditions. Currently, a larger sub-scale prototype is under development and is scheduled for demonstration early in 2025. Following this, the system will undergo further refinement and an additional expansion in the spring. Future objectives include demonstrating advanced capabilities such as arbitrary wave shaping, ultra-low jitter performance, and high repetition-rate operation in burst mode.

Contract Number: N68335-21-C-0435, SBIR Phase II
Project Title: Solid-state, Sub-nanosecond Pulse Sharpener for Generating High Power Impulses
Period of Performance: 1 February 2023 to 31 December 2024
Principle Investigator: Dr. Jason Sanders, 310-212-3030, jason@transientplasmasystems.com
Organization: Transient Plasma Systems, Inc.

The Office of Naval Research issued this SBIR topic to fund the development of a solid-state closing switch capable of producing high power ultra-wideband (UWB) electrical pulses. This effort has researched the fabrication of Semiconductor Avalanche Shaping (SAS) device structures in both Si and SiC, with Si being viewed as the conservative approach for achieving the threshold specifications of this topic. SiC material properties suggest it is likely well suited for impact-ionization avalanche switching inherent to SAS, which does not rely on long minority carrier lifetime for practical implementation in the same way that other wideband opening switches, such as Drift Step Recovery Diodes (DSRDs), do. Devices have been designed and simulated during Phase I. In Phase II solid-state devices capable of switching kW-MW power pulses with risetimes faster than 300 ps at high pulse repetition rate are in development. Both Si and SiC parts were fabricated in 2023 and tested using a testbed developed by TPS for characterizing switching performance and durability. Si parts, which are expected to provide nearest-term capability for NAVY requirements, fabricated at TPS facilities are currently producing multi-kV pulses with risetimes that are hundreds of picoseconds. Initial durability testing, measured in shots fired, has

also been promising, with no failures recorded to date. In 2024 progress has been made in stacking and packaging SiC SAS parts, which have been fabricated and are being tested. On-going investigations are exploring the best way to drive SiC parts to achieve sufficiently fast risetime (faster than 1 nanosecond). In 2025 TPS will continue to work with NAVY through the end of the Phase II Option to mature this technology and identify future DOD customers.

Contract Number: N68335-23-C-0010, SBIR Phase II

Project Title: Improved Marx Pulse Generator for HPM Systems

Period of Performance: 9 March 2023 to 17 September 2025

Principle Investigator: Sam Dickerson, sdickerson@sara.com, 719-302-3117

Organization: Scientific Applications & Research Associates, Inc.

SARA is working to contribute to the next wave of US sourced high-power microwave (HPM) systems by developing an innovative, solid-state, semiconductor opening switch (SOS) based pulse generator. The pulse generator is made up of an SOS driver and the opening switch. The driver system adequately pumps the opening switch diodes enabling generation of very high peak power, fast risetime pulses. Unlike other SOS systems, the driver under development here relies on only a single stage of magnetic compression and consists of a solid-state Marx generator, saturating transformer, and pumping capacitor.

Currently, the Phase II base effort is in progress, and is focused on experimental testing and demonstration of the solid-state Marx generator. The optimal solid-state switching device was down selected, and an advanced power semiconductor module housing both the Marx generator switching semiconductors and the charging elements, has been designed, fabricated, and independently tested. Individual stages of the Marx generator have been assembled and are presently undergoing laboratory testing. Preliminary test results are encouraging and suggest the Marx generator topology will make a very strong SOS driver, as well as a strong candidate for many other pulsed power and HPM applications. Additionally, to aid system design efforts, sample lots of US sourced SOS devices have been acquired and experimentally evaluated. The results of that evaluation have been fed into system designs, and a conceptual design for a full-scale gigawatt (GW) class SOS based pulse generator have been developed.

In the next phase, the Phase II Option, the effort will focus on development and experimental demonstration of the full-scale pulse generator. Following an early design phase, the pulse generator will be assembled using the latest US-sourced SOS diodes. Full scale demonstrations will show the pulse generator's capability to generate pulses over 300 kV with risetimes under 10 nanoseconds at pulse repetition frequencies surpassing 300 Hz.